THEORETICAL EVALUATIONS OF ELECTRON-TRANSFER PROCESSES IN ORGANIC SEMICONDUCTORS

A Dissertation
Presented to
The Academic Faculty

By

Chad Michael Risko

In Partial Fulfillment
Of the Requirements for the Degree
Doctor of Philosophy in the
School of Chemistry and Biochemistry

Georgia Institute of Technology

August 2005

THEORETICAL EVALUATIONS OF ELECTRON-TRANSFER PROCESSES IN ORGANIC SEMICONDUCTORS

Approval:

Dr. Jean-Luc Brédas, Advisor
School of Chemistry & Biochemistry
Georgia Institute of Technology

Dr. Seth R. Marder
School of Chemistry & Biochemistry
Georgia Institute of Technology

Dr. Rigoberto Hernandez
School of Chemistry & Biochemistry
Georgia Institute of Technology

Dr. Joseph W. Perry
School of Chemistry & Biochemistry
Georgia Institute of Technology

Dr. Bernard Kippelen
School of Electrical & Computer Engineering
Georgia Institute of Technology

Date Approved: July 7th, 2005

ACKNOWLEDGEMENTS

I am indebted to a great number of people whose knowledge and willingness to share have made this experience more than I could have ever imagined. Throughout the duration of my graduate work, I have had the fortunate opportunity to be exposed to a unique blend of people and cultures that have helped cultivate within me a broader view of science and the world. I would first like to thank Professor Jean-Luc Brédas who has provided me with this tremendous opportunity for study. When I initially approached Professor Brédas as a first-year graduate student, I knew nothing of the impact that he had had within the scientific community; I only saw a man who possessed a great deal of knowledge and who seemed to be a genuinely nice person. As I later realized the greater impact, I learned some of my most important lessons – be thorough in your investigations; respect the science and the people with which you work; be humble; and, most importantly, remain excited. So, it is with a great deal of gratitude that I thank Professor Brédas for taking a chance on someone with no experience in this wonderful field of quantum chemistry.

I would also like to thank all of the people within the Brédas group – the "Bredators" – for sharing their knowledge and know-how, as well as providing a unique group of friends, during my studies. In particular, I would like to thank: Dr. Veaceslav Coropceanu for his guidance, wisdom, and teaching me to keep questioning; Dr. Egbert Zojer for sharing his knowledge in optical processes and solid-state physics; Dr. Demetrio da Silva Filho for his technical and computer assistance; Dr. Massimo Malagoli

for his computer assistance; Dr. Tommy Ohyun Kwon for his knowledge in quantum-chemistry; and, Dr. Karin Schmidt for our struggles through TURBOMOLE and Dushin. I would like to thank Amalia Leclercq for her friendship over the last four years. I would also like to acknowledge the other post-doctoral fellows, graduate students, and visitors that have made this a unique experience: Dr. Mattias Hjort, Dr. Georg Heimel, Dr. Terttu Hukka, Kelly Lancaster, PaDreyia Lawson, Sigi Sanchez-Carrera, Peter Pacher, Lorenz Romaner, Christian Fink, and Mattis Gruber. For their support and assistance, I am also grateful to Alyceson Andrews and Leslie Jones.

In addition, I would like to acknowledge the "Brédateurs" of the Service de Chimie des Matériaux Nouveaux et Centre de Recherche en Electronique et Photonique Molêcules au Université de Mons-Hainaut, Mons, Belgium. In particular, I am grateful to Dr. Jérôme Cornil and Dr. David Beljonne for sharing their knowledge and making my stay in Mons very pleasant. I would also like to acknowledge Dr. Victor Geskin, Dr. Roberto Lazzaroni, and Angès Leclercq.

Because of the nature of the work with which I have been involved, I am also indebted to a great number of people for their experimental collaborations. First, Professor Seth R. Marder and his group at the Georgia Institute of Technology have provided me with a unique opportunity to work with a number of gifted scientists. In particular, I would like to thank Professor Marder for his direction through my research and Dr. Stephen Barlow for his guidance and willingness to answer my chemistry questions. I would also like to acknowledge Dr. Xiaowei Zhan and Dr. Simon C. Jones for the rewarding collaboration

efforts. I would like to thank Professor Bernard Kippelen and Dr. Benoit Domercq at the Georgia Institute of Technology for teaching me a few things about organic electronic devices. Finally, I would also like to acknowledge for their fruitful collaborations: Dr. Zakya Kafafi and Dr. Gary Kushto at the Office of Naval Research; Professor Antoine Kahn and his group at Princeton University; and Professor Cristoph Lambert and his group at the Institut für Organische Chemie, Julius-Maximilians-Universität Würzburg (Würzburg, Germany).

Additionally, I would like to acknowledge my Dissertation committee members: Professors Brédas, Marder, and Kippelen, Professor Joseph W. Perry, and Professor Rigoberto Hernandez.

I am also grateful to Dr. Gary Giachino at Baker University. As an undergraduate, he saw something – potential, I guess – and urged me to pursue chemistry. It is because of Dr. "G" that I am involved in the chemical sciences. Along these lines, I would also like to thank Wayne Nyberg, my friend and colleague, whose words "An education is something that no one can take away from you" provided inspiration for my graduate work.

Finally, it is with the utmost reverence that I acknowledge my family and friends whose faith, love, and compassion have guided me throughout. First, to my wife Sonya, I am indebted for her unwavering love, devotion, and support as I pursued this dream. To my Father, Steve, you have always been there for me no matter the circumstance to provide for me everything you had, and more. To my Mother, Karen, you have given me a love

that only a Mom can. To Dave and Alicia – who have elected to put up with my Mother and Father – thank you for everything you have given and taught me over the years. To Aric and Megan, great things lie ahead in your future as long as you keep hold of the things that matter most. To my Grandparents, Uncles, and Aunts, it is your distinctive qualities and accomplishments in life that have laid the foundation for my goals by providing me with a unique set of heroes. Finally, to Jason and Clint, my two longest and dearest friends, it is with you that I learned about love and heartbreak, winning and losing, and everything else that only friends can teach each other. We have experienced so many great things so far; I am certain, though, that the best is yet to come.

TABLE OF CONTENTS

LIST OF TABLES

LIST OF FIGURES

LIST OF ABBREVIATIONS

34PS	1,1-dimethyl-3,4-diphenylsilole
AEA(IP)	Adiabatic Electron Affinity (Ionization Potential)
Alq_3	Tris(quinolin-8-olato) aluminum(III)
AM1	Austin Model 1
BLA	Bond Length Alternation
BS	Broken Symmetry
CAS	Complete Active Space
CI	Configuration Interaction
CIS	Configuration Interaction Singles
CNDO	Complete Neglect of Differential Overlap
CR	Charge Resonance
CV	Cyclic Voltammetry
DFT	Density Functional Theory
DOS	Density of States
EA	Electron Affinity
ESR	Electron Spin Resonance
ETM	Electron-Transport Material
FWHM	Full-Width at Half-Maximum
GGA	Generalized Gradient Approximation
GMH	Generalized Mulliken-Hush

HF	Hartree-Fock
HOMO	Highest-Occupied Molecular Orbital
HTM	Hole-Transport Material
INDO	Intermediate Neglect of Diatomic Overlap
IP	Ionization Potential
IPES	Inverse Photoemission Spectroscopy
IR	Infrared
IV	Intervalence
IVCT	Intervalence Charge Transfer
KS	Kohn-Sham
KT	Koopmans' Theorem
LCAO	Linear Combination of Atomic Orbitals
L(S)DA	Local (Spin) Density Approximation
LUMO	Lowest-Unoccupied Molecular Orbital
MNDO	Modified Neglect of Diatomic Overlap
MP2	Møller-Plesset Perturbation Theory 2
MV	Mixed Valence
NDDO	Neglect of Diatomic Differential Overlap
NMR	Nuclear Magnetic Resonance
OFET	Organic Field-Effect Transistor
OLED	Organic Light-Emitting Diode
OPC	Organic Photovoltaic Cell
PES	Photoelectron Spectroscopy

PKS	Piepho-Krausz-Schatz
PL	Photoluminescence
PPSPP	2,5-di-(3-biphenyl))-1,1-dimethyl-3,4-diphenylsilole
PSP	1,1-dimethyl-2,3,4,5-tetraphenylsilole
PyPySPyPy	2,5-bis(6'-(2',2"-bipyridyl))-1,1-dimethyl-3,4-diphenylsilole
PySPy	1,1-dimethyl-2,5-bis(2'-pyridyl)-3,4-diphenylsilole
SCF	Self-Consistent Field
SOMO	Singly-Occupied Molecular Orbital
TDDFT	Time-Dependent Density Functional Theory
TMB	Tetramethylbenzidine
TMPD	Tetramethyl-*p*-phenylenediamine
TPD	N,N'-diphenyl-N,N'-bis(3-methylphenyl)-([1,1'-biphenyl])-4,4'-diamine
UPS	Ultraviolet Photoelectron Spectroscopy
UV/vis	Ultraviolet/Visible
VEA(IP)	Vertical Electron Affinity (Ionization Potential)
Vis/NIR	Visible/Near Infrared
XPS	X-ray Photoelectron Spectroscopy
ZDO	Zero Differential Overlap
ZINDO	Zerner's Intermediate Neglect of Differential Overlap

SUMMARY

The field of organic electronics, in which π-conjugated, organic molecules and polymers are used as the active components (*e.g.*, semiconductor, light emitter/harvester, etc.), has lead to a number a number of key technological developments that have been founded within fundamental research disciplines. In the Dissertation that follows, the research involves the use of quantum-chemical techniques to elucidate fundamental aspects of both intermolecular and intramolecular electron-transfer processes in organic, π-conjugated molecules. The Dissertation begins with an introduction and brief review of organic molecular systems used as electron-transport semiconducting materials in device applications and/or in the fundamental studies of intramolecular mixed-valence processes. This introductory material is then followed by a brief review of the electronic-structure methods (*e.g.*, Hartree-Fock theory and Density Functional Theory) and electron-transfer theory (*i.e.*, semiclassical Marcus theory) employed throughout the investigations.

The next three Chapters deal with investigations related to the characterization of non-rigid, π-conjugated molecular systems that have amorphous solid-state properties used as the electron-transport layer in organic electronic and optoelectronic devices. Chapters 3 and 4 involve studies of silole- (silacyclopentadiene)-based materials that possess attractive electronic and optical properties in the solid state. Chapter 5 offers a

preliminary study of dioxaborine-based molecular structures as electron-transport systems.

In Chapters 6 – 8, the focus of the work shifts to investigations of organic mixed-valence systems. Chapter 6 centers on the examination of tetraanisylarylenediamine systems where the inter-redox site distances are approximately equal throughout the series. Chapter 7 examines the bridge-length dependence of the geometric structure, charge-(de)localization, and electronic coupling for a series of vinylene- and phenylene-vinylene-bridged bis-dianisylamines. In Chapter 8, the role of symmetric vibrations in the delocalization of the excess charge is studied in a dioxaborine radical-anion and a series of radical-cation bridged-bisdimethylamines. Finally, Chapter 9 provides a synopsis of the work and goals for future consideration.

CHAPTER 1

INTRODUCTION

Organic, π -conjugated materials display semiconducting properties that allow for the low-cost fabrication of new generations of thin-film electronic, optoelectronic, and electrooptic devices such as light-emitting diodes (OLEDs), photovoltaic cells (OPCs), field-effect transistors (OFETs), and photorefractive cells.[1, 2] Encompassing a vast array of scientific disciplines – including synthetic chemistry, theoretical chemistry/physics, applied physics, materials science, and device engineering[3] – the relatively recent advancements in organic electronic technologies have relied upon strong connections between research in basic and applied sciences. However, in order to understand many of the intrinsic processes involved within these complex systems (*e.g.*, charge injection and collection processes at the electrode-organic-semiconductor interface and charge transport through thin-films of the organic material (*vide infra*)), investigations within the general framework of electron-transfer chemistry have been vital to the material advancement.

Being of fundamental importance in numerous aspects of chemistry, physics, and biology;[4-6] the understanding and control of electron-transfer reactions have been an intense area of research activity for a number of decades.[7, 8] Electron-transfer reactions are distinctive in that they can be investigated in a variety of environments (*e.g.*, gas-phase and (in)homogenous solution and solid-state media)[6] and involve central chemical

issues such as energetics, dynamics, and geometric and electronic structure.[6] Covering a diverse spectrum, the study of electron-transfer reactions encompass investigations in such systems as: isolated molecules; clusters; electrochemical electron transfer; electron transfer at surfaces and interfaces; and solid-state electron transfer.[4]

Many of the organic, π-conjugated systems – which are assisted by the extended variety of organic synthetic procedures that allow for a multitude of potential redox systems – that have found interest in electronic device applications allow for the investigation of both intermolecular and intramolecular (*i.e.*, mixed-valence processes) electron-transfer reactions. Though seemingly different, an intermolecular process can become an intramolecular process through the addition of a bridge between the independent redox sites,[9] and both processes can be described through the semiclassical Marcus theory of electron transfer (see Chapter 2).[5, 8, 10, 11] This relationship can be understood if one considers two redox sites with one in the radical-anion state (donor) and the other in the neutral state (acceptor), see Figure 1.1. Without a covalent bond between the redox sites, the electron transfer from donor to acceptor is an intermolecular process; however, simple introduction of a covalent tether between the two moieties transforms the process to an intramolecular one. Thus, it can be seen that the two processes are inherently related. It is within this realm that we briefly introduce current research in molecular materials for organic electronic devices – in particular those for the transport of electrons (versus holes) – and organic mixed-valence systems in order to provide the motivation for the work that follows.

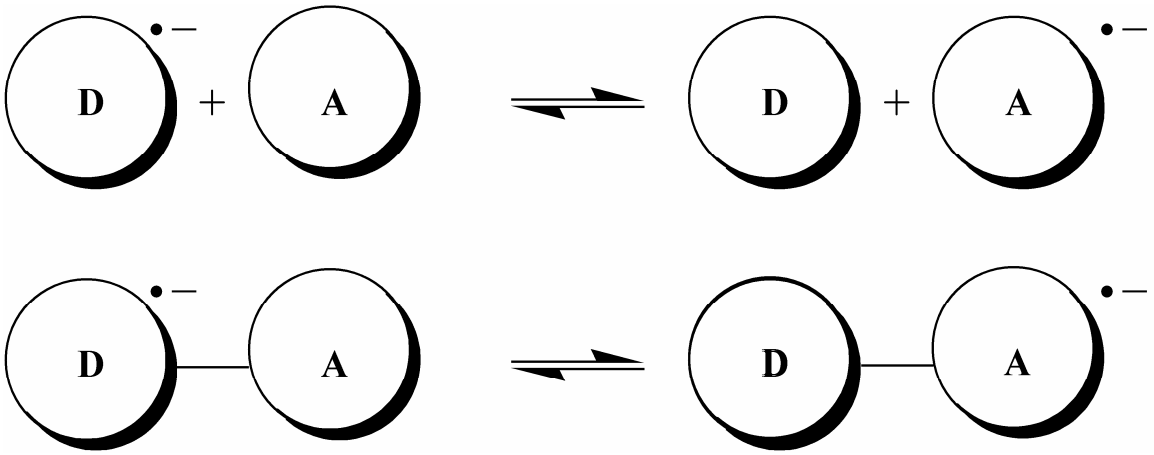

Figure 1.1 Intermolecular [top] and intramolecular [bottom] electron transfer between donor and acceptor redox sites.

1.1 Organic molecular systems for electron transport

Versus typical inorganic semiconductors, organic, π-conjugated materials possess a number of unique properties that allow for their implementation in a wide variety of applications. Organic materials, in either molecular or polymeric forms, offer the ability for device processing at low-temperatures[12] by techniques that offer ease of mass production (*e.g.*, conventional and ink-jet printing techniques). Secondly, organic systems can be designed for physical flexibility, which allows for deposition on both rigid and flexible (*e.g.*, polymeric) substrates. Such processing diversity and ease allows for amenability to small production runs and suitability to large-area depositions.[12-14] Thirdly, the ability to utilize tailored synthetic procedures allows for the capability to design organic molecular systems with varying semiconducting and light emission (*e.g.*, differentiation between red, green, and blue emission) properties. Additionally, organic

materials offer the possibility of devices with lower power consumption versus their inorganic counterparts, especially in the areas of displays and large-area lighting.[15]

1.1.1 Device structure

1.1.1.1 OLEDs and OPCs

OLEDs and OPCs possess rather similar device structure even though they are responsible for the inverse processes of creation of an excited state (exciton) via charge recombination (in the case of OLEDs) or the dissociation of a photoexcited state via charge separation (in the case of OPCs). For both applications, the simplest device configuration is that of a single bipolar (*i.e.*, both p-type and n-type conduction, *vide infra*) organic layer sandwiched between a transparent anode and a cathode, all of which lie on top of a transparent substrate (*e.g.*, glass or flexible polymer),[16] see Figure 1.2. Multilayer and blended devices allow for the use of customized materials for hole transport (HTM), electron transport (ETM), and light emission/absorption. The energy level diagrams of Figure 1.2 reveal some of the electronic structure parameters involved in both single-layer and multilayer device configurations. The solid-state electron affinity, EA, (often equated to the energy of the lowest-unoccupied molecular orbital [LUMO]) and the ionization potential, IP, (often equated to the energy of the highest-occupied molecular orbital [HOMO]) relative to the metal work functions of the cathode Φ_C and anode Φ_A determine the charge injection/collection properties of the particular device.[16]

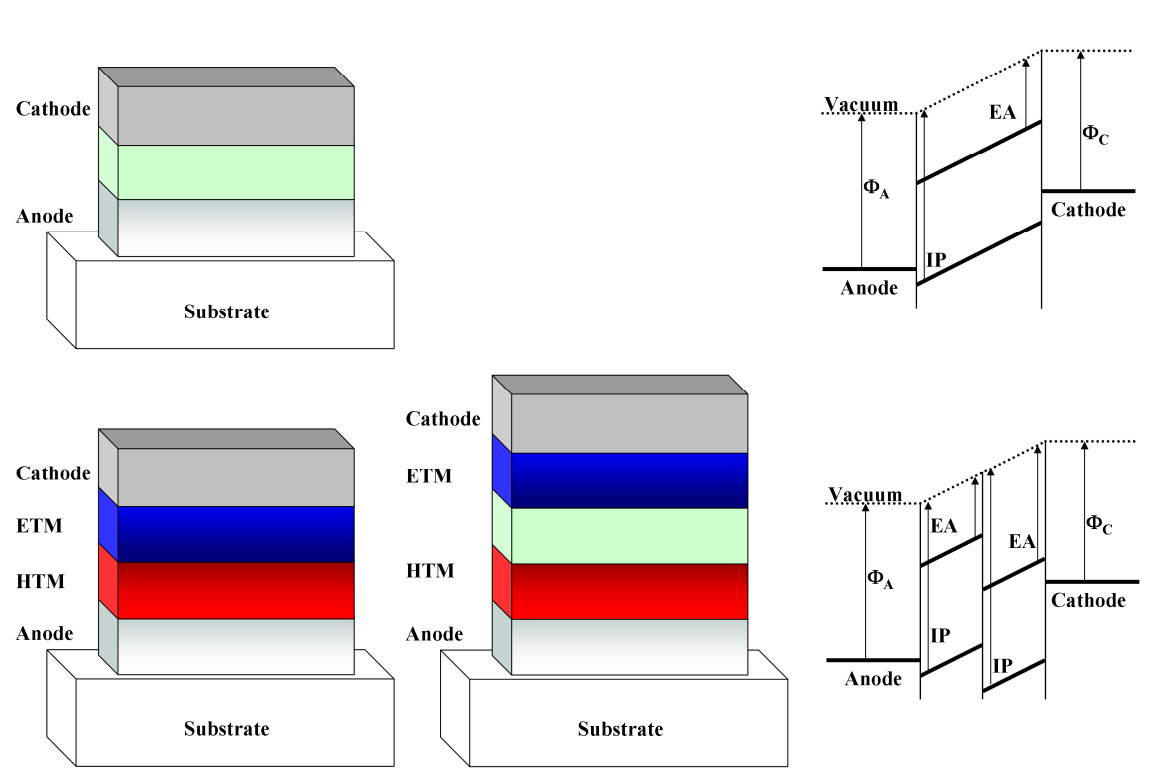

Figure 1.2 Schematic device configurations for single-layer [top] and multilayer [bottom] OLEDs and OPCs [left], along with representative energy level diagrams under the influence of a bias [right].[16]

For an OLED, there are in general four primary steps in device operation. First, holes from the anode (via oxidation) and electrons from the cathode (via reduction) are injected into the neighboring organic media. As can be seen from Figure 1.2, the ease of injection is regulated by the offset of the IP and EA with respect to the work function of the anode and cathode, respectively. It is of note that a situation in which their exists unbalanced injection of holes and electrons can result in an excess of one charge carrier, which in turn can lead to an increase in non-radiative recombination due to interactions of the excited states with the excess charge carriers.[17] The second step involves charge migration through the organic media by means of successive hops (via individual

oxidation [holes] and reduction [electrons] reactions between neighboring molecules) of the charge carrier; in general, electron mobility is orders of magnitude lower than that for holes.[16] It is of importance to note that injection and transport are the limiting factors in the determination of both the operating voltage and luminance efficiency, with hole current being often limited by injection and electron current strongly influenced by the presence of traps.[17] The third step entails charge recombination and the creation of an excited state (exciton formation). When the oppositely-charged carriers interact, the charges neutralize each other and form either singlet or triplet excited states. Spin statistics would dictate that the favorable singlet excited state necessary for radiative decay is formed only 25% of the time, thus bringing forth a significant limitation to device efficiency; however, a number of means to circumvent this limitation, including the use of triplet emitters, are currently under investigation. The final process is that of radiative decay of the singlet excited state with subsequent light extraction from the device. Light extraction is determined by the device structure and the refractive indices of the individual layers;[17] these device characteristics can cause such problems as self-absorption of the radiated photon and prevention of photon emission in the proper direction.

For OPCs, the individual steps, and inherent efficiency limitations, are similar to those for OLEDs. First, photoexcited states (excitons) are formed through the absorption of light from an external source (*i.e.*, the solar spectrum). The bound electron-hole pairs then dissociate into the individual charge carriers, a process that requires the electron and hole to be able to overcome the mutual Coulombic attraction that leads to charge

recombination.[18] The dissociated electron and hole then migrate through the organic media under the influence of an electric field generated by the equalization of the Fermi energies of the two electrodes.[18] The charges are then collected at the respective electrodes.

1.1.1.2 OFETs

OFETs utilize organic, π-conjugated materials as the semiconducting component in the standard transistor applications of signal amplification and opening/closing of an electrical circuit. In general, OFET performance is typically determined by three key figures of merit.[12] The on-current to off-current ratio (I_{ON}/I_{OFF}) measures the source-drain current gain when the device is in the on-state,[14] and is indicative of the switching performance.[19] The field-effect mobility (μ_{FET}) describes the average charge carrier drift velocity per unit electric field in the active layer under the influence of an electric field.[14] For a high-performance OFET, μ_{FET} and I_{ON}/I_{OFF} should both be as high as possible.[20] Finally, the threshold voltage (V_T)[12] is the minimum voltage applied across the device at which a current is first observed; ideally, the threshold voltage should be as low as possible.

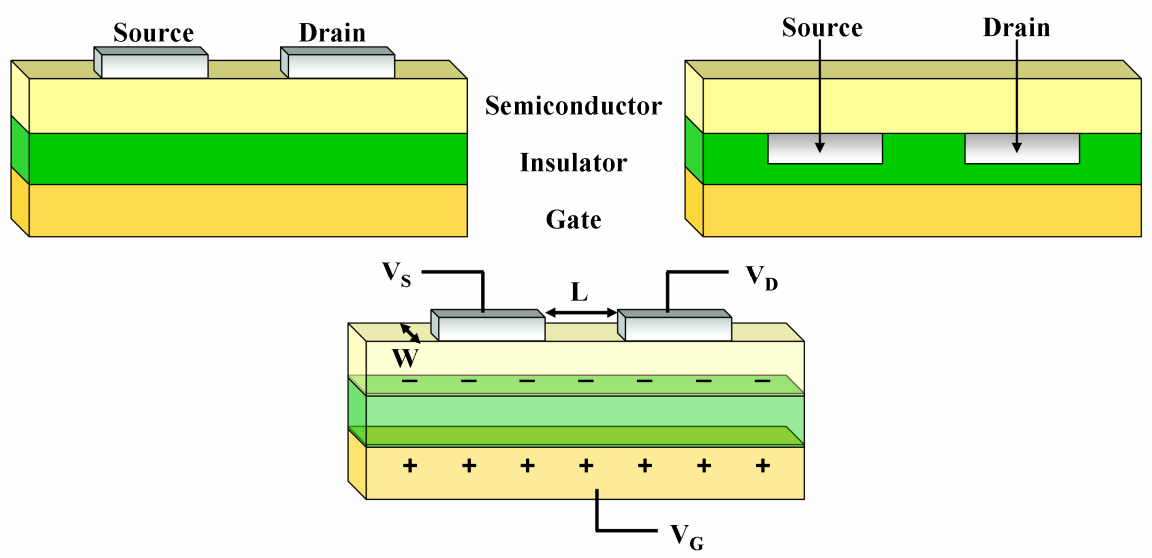

Figure 1.3 Top- [left] and bottom-contact [right] device configurations [top] and relevant voltages for OFETs [bottom].[12]

In an OFET, the organic semiconductor is deposited such that it is in direct contact with a gate/insulator structure and metallic source and drain electrodes, see Figure 1.3. The gate/insulator assembly consists of a metal (or doped semiconductor) electrode coated with an insulating material.[12] The semiconductor material is required to have high charge-carrier mobility for either holes (p-type) or electrons (n-type). The semiconductor film and gate electrode are capacitively coupled such that, when a bias, V_G, is applied to the gate electrode, charge formation is induced within the semiconductor;[12] this gate-induced charging is known as the field effect. OFET devices are differentiated by the relative positioning of the source and drain electrodes: i) bottom-contact in which the electrodes are deposited directly on the gate/insulator assembly before the organic semiconductor and ii) top-contact in which the source and drain electrodes are deposited on the organic semiconductor. The mobile charge carriers induced in the semiconductor

through the field effect move in response to the application of a voltage between the source and drain, V_D;[12] when V_D is applied, the device is said to be in the 'on' state, while when there is no bias between the source and drain the device is in the 'off' state.

1.1.2 Molecular electron-transport (n-type) materials

A constant theme for the successful commercial implementation of the devices described above is the requirement for materials with large carrier mobilities of both holes and electrons. In the design of such materials, it is of importance to consider the optimization of such physico-chemical properties as redox potentials, radical-ion stabilities, relaxation energies, and luminescence yields.[21] While hole-transport materials have been relatively ubiquitous in the development and investigation of organic-based electronic devices, molecular electron-transport materials have only recently undergone a substantial increase in consideration and design[22-24] due to a number of key difficulties facing their development, including: i) most organic, π-conjugated materials tend to be better hole than electron transporters;[14, 25] ii) a need for electrochemical stability of the radical-anion versus molecular oxygen and water under ambient operating conditions;[21, 22] iii) a lack of general design guidelines;[14] and, iv) difficulty in the optimization of EAs [LUMO energies] to complement the Fermi energies of a variety of cathode materials in order to facilitate the injection of electrons.[2]

In general, a number of factors need to be considered in the design process of electron-transport materials, including:

i) reversible electrochemical reduction to facilitate the electron transport, which can be considered to be a series of reductions between neighboring molecules in the film;[16]

ii) large magnitude electron affinities to allow for the use of air-stable cathode metals[12] and to prevent trapping by molecular oxygen and water to allow for nondispersive electron transport;[25]

iii) minimal intermolecular distances in the solid-state to allow for wavefunction overlap (strong intermolecular electronic coupling) on adjacent molecules to increase the intermolecular charge-transfer rate;[12]

iv) large glass-transition temperatures (T_g) and thermal stability to withstand heating (*i.e.*, Joule heating) encountered with large electric fields and current densities;[16]

v) good film-forming properties including the ability to form uniform, pin-hole free films and prevent the formation of crystallites;[12, 16]

vi) chemical purity and chemical stability versus various degradation pathways.[12, 16]

To date, the design of molecular systems for electron transport has focused on distinct building blocks in only a few model chemistries: i) metal chelates; ii) perfluorinated compounds, and iii) π-conjugated systems composed of electron-deficient rings.[3, 12, 16, 17] It is within these chemistries that we briefly review some of the more recent molecular architectures.

Metal chelates have been intensely explored for both their electron-transport and emission properties since the seminal work of Tang and van Slyke in 1987[26] that demonstrated efficient electroluminescence from tris(quinolin-8-olato) aluminum(III)

(Alq_3), see Figure 1.4.[16, 26] Alq_3, to date, is the most widely used electron-transport material owing to its thermal and morphological stability in thin films, the ability to form pinhole-free films upon vacuum evaporation, ease of synthesis and purification, and relatively large EA.[16, 17] One of the principal drawbacks with Alq_3, however, is that under exposure to ambient conditions, the electron transport becomes highly dispersive suggesting electron trapping by molecular oxygen.[16] A variety of other metals (*e.g.*, zinc, gallium, indium, and beryllium) and ligands (*e.g.*, derivatized quinolate, 10-hydroxybenzo[h]quinolate, and 2-(2-hydroxyphenyl)benzothiazolate) have also been utilized with limited success.[16]

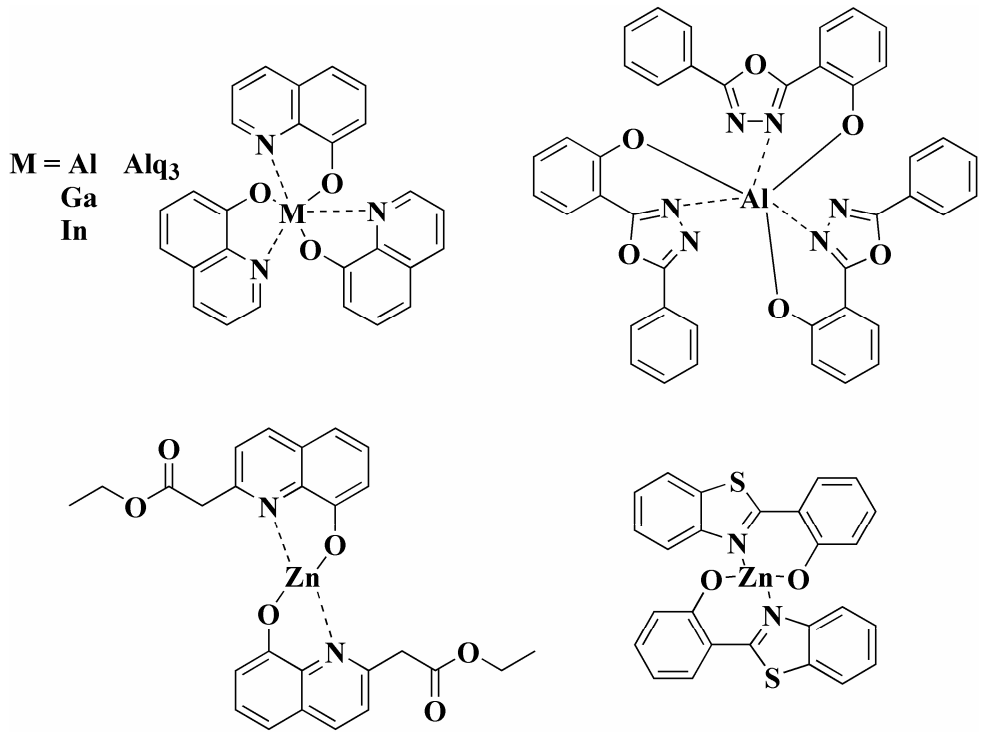

Figure 1.4 Molecular structures of example metal chelates used as electron-transport materials.[16, 17]

Perfluorinated molecular systems, in which the hydrogen atoms of π-conjugated hydrocarbons are replaced by fluorine atoms, possess higher EAs due to the highly electronegative nature of the fluorine atoms. Both linear[27] and branched[28] perfluorinated oligo(p-phenylene)s have been investigated as electron-transport materials. While linear perfluorinated oligo(p-phenylene)s show electron mobilities that are two-orders of magnitude larger than Alq_3, they are insoluble, highly crystalline solids with no glass transitions.[27] Branching of the perfluorinated oligo(p-phenylene)s has produced amorphous solids with decent glass transition temperatures; nondispersive transport has been realized in the branched systems.[16] Additionally, perfluorination of the excellent hole-transport system pentacene has been shown to provide n-type transport in OFET structures.[29]

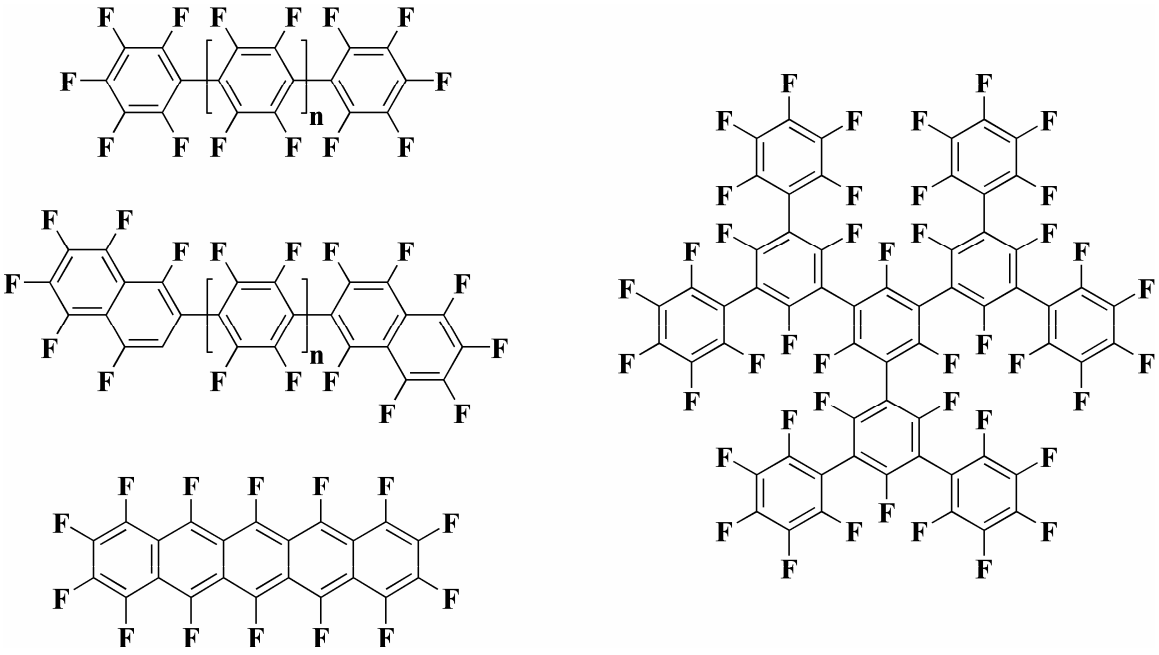

Figure 1.5 Molecular structures of example perfluorinated compounds used as electron-transport materials.[16, 29]

Probably the widest variety of molecular materials synthesized for electron transport are those that fall within the realm of π-conjugated systems composed of electron-deficient rings. Among the most widely studied materials within this area are based upon oxadiazole.[16] Several studies indicate that oxadiazole-based systems, see Figure 1.6, have both efficient electron-transport and hole-blocking properties in a variety of

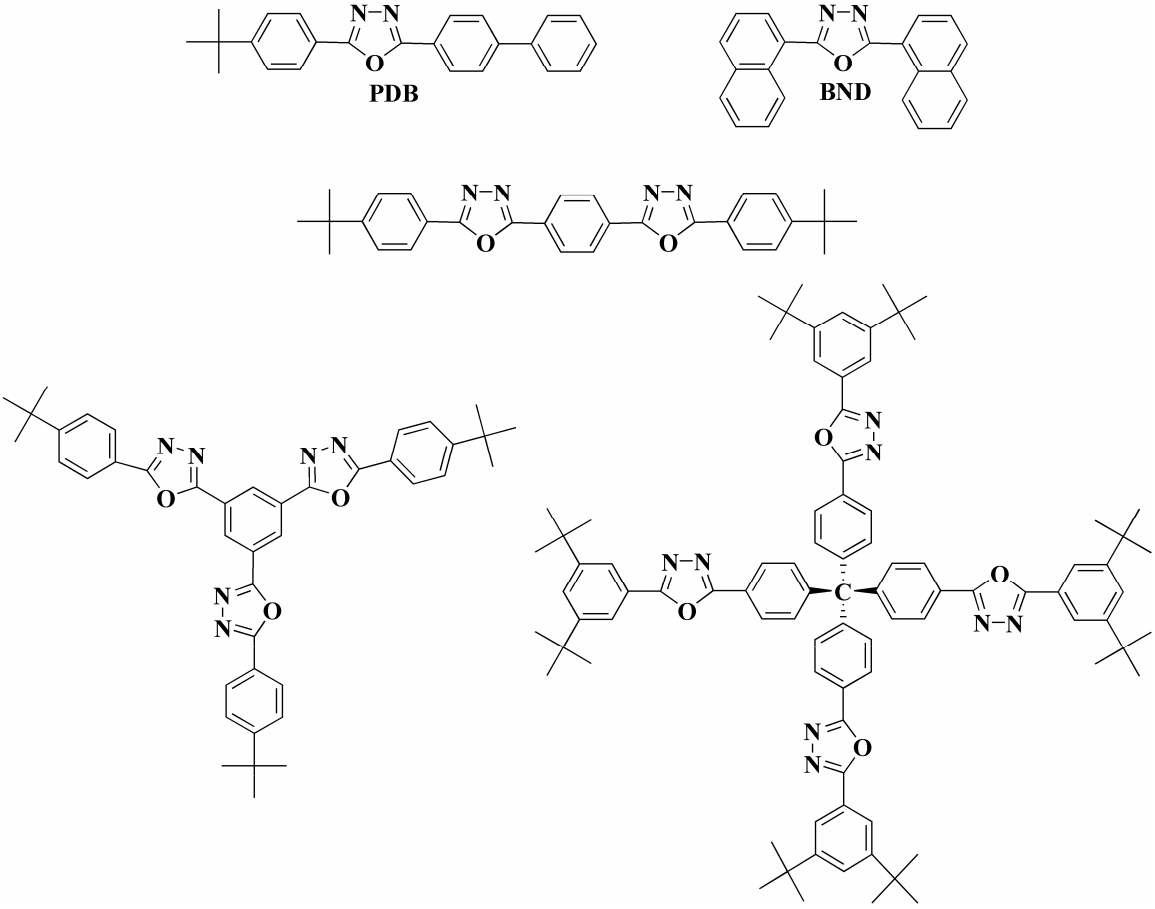

Figure 1.6 Molecular structures of example oxadiazoles used as electron-transport materials.[3, 16]

molecular architectures, including small molecule[30], polymer,[31] and dendritic forms.[32]

2,5-diaryl-1,3,4-oxadiazoles, including the widely studied 5-(4-biphenyl)-2-(4-tert-butylphenyl)-1,3,4-oxadiazole (PBD) have been exploited as electron-transport materials in electroluminescent devices due to their electron-deficient nature, high thermal stability and high photoluminescence quantum yield.[3] Bilayer OLEDs using PDB were among the first to show that external quantum efficiencies of OLEDs could be significantly improved with the addition of a separate electron-transport layer;[16] however, amorphous PDB films displayed tendencies to crystallize over time.[16] A second diaryl-substituted oxadiazole is 2,5-bis(4-naphthyl)-1,3,4-oxadiazole (BND); the relatively high electron mobilities of both PDB and BND have been attributed to the planar molecular shapes that allow for preferential stacking and close intermolecular interactions.[16] To deal with the crystallization issue, dimeric and branched/starburst oxadiazoles have been synthesized with the intent to raise the glass transition temperature.[16]

Silole- (silacyclopentadiene)-based systems, see Figure 1.7, have recently garnered much attention as electron-transport materials due to the presence of a low-lying LUMO.[33] The σ*-π* conjugation in the ring due to interaction between the σ*-orbitals of the two exocyclic silicon-carbon bonds with the π*-orbital of the butadiene moiety provide the stable features of the LUMO level.[34] The low-lying LUMO provides silole-based systems with large electron affinities coupled with redox stability in air.[25, 33-35] These intrinsic characteristics have led to very high electron mobilities and, in some cases, nondispersive and air-stable electron transport. For instance, 2,5-bis(6'-(2',2"-bipyridyl)-1,1-dimethyl-3,4-diphenylsilole (PyPySPyPy) exhibits very high, nondispersive, air-stable time-of-flight electron mobility that is a two-order of magnitude improvement versus Alq_3.[25, 35]

Recent studies on organic light-emitting diodes based on PyPySPyPy and its biphenyl analog 2,5-di-(3-biphenyl)-1,1-dimethyl-3,4-diphenylsilole (PPSPP) have demonstrated that these two chemically similar molecular systems display distinctly different solid-state properties. While PPSPPP has superior luminescence properties in the solid state, single-layer electron-only devices reveal that PyPySPyPy exhibits a higher current flow than devices made with PPSPP; these results suggest that PyPySPyPy has higher electron conductivity signifying both higher electron mobility and a lower barrier to electron injection than PPSPP.[36, 37] Additionally, dithenesiloles have been shown to have reduction properties comparable to Alq_3.[16]

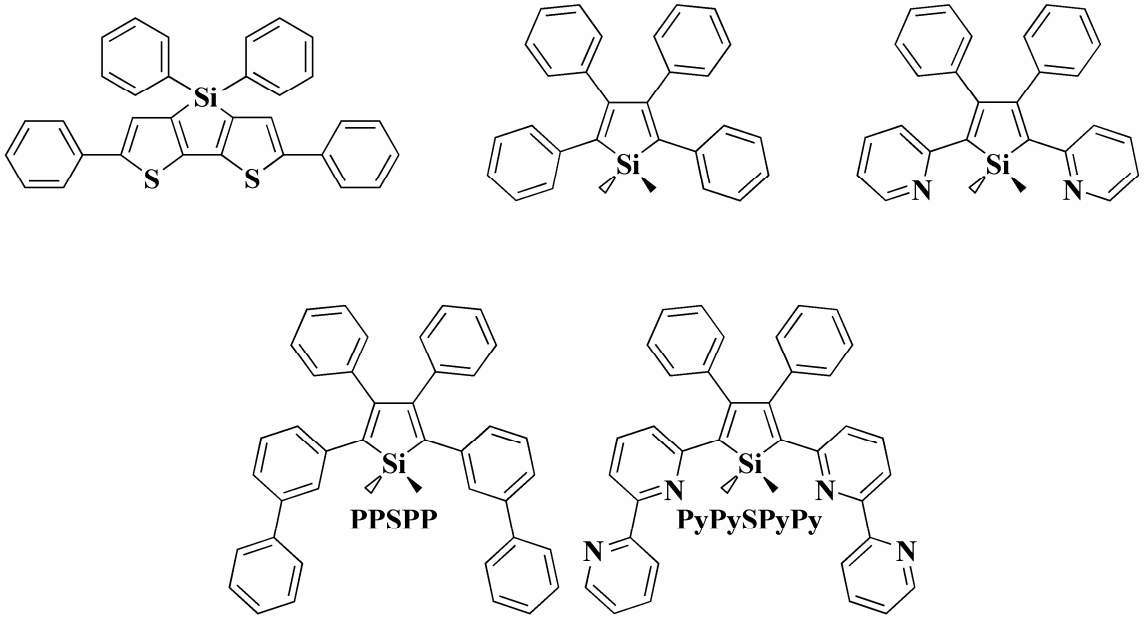

Figure 1.7 Molecular structures of example siloles used as electron-transport materials.[16, 33]

Another series of electron-deficient molecular systems receiving substantial attention are based upon substituted oligothiophenes. While oligothiophenes are typically used as hole-transport materials, the introduction of strongly electron-withdrawing groups,

electron-deficient nitrogen-containing moieties, and cyano groups significantly enhances the EA, see Figure 1.8 .[38] Diperfluorooctyl-substituted phenylene-thiophene oligomers were shown to possess n-type conductivity in OFET geometries with large I_{ON}/I_{OFF} ratios;[14] with good mobilities and I_{ON}/I_{OFF} ratios, the largest transistor memory effect ever reported for an organic material was demonstrated with these compounds.[14] A perfluoroarene-modified oligothiophene has been shown to possess n-type activity; a mobility of 0.8 cm^2/Vs is the highest mobility to date reported for n-type thiophenes.[39] Of interest, however, is that displacement of the perfluoroarene groups inside of the thiophene units brings forth p-type transport.[39] Cyano end-capped sexithiophene has also been shown to possess current-voltage results compatible with electron transport.[38] Additionally, dimesitylborylthiophenes have also shown promise as electron-transport materials in OLED applications.[40]

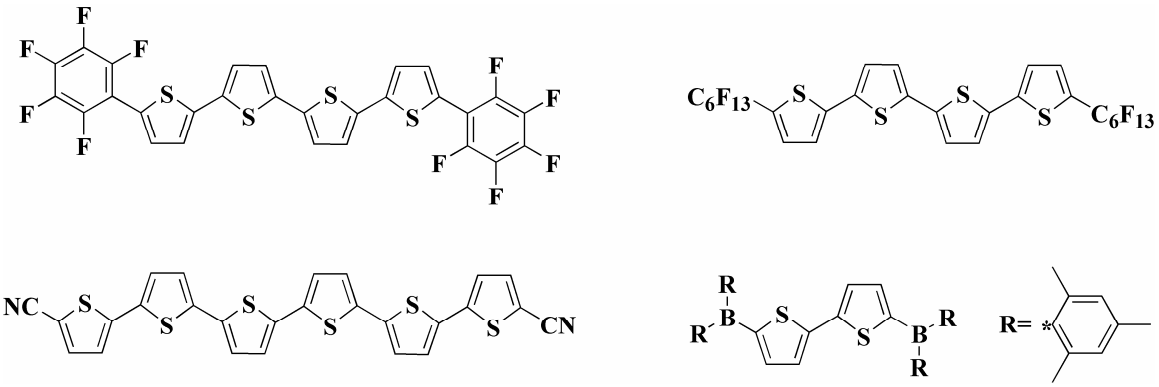

Figure 1.8 Molecular structures of example substituted oligothiophenes used as electron-transport materials.[14, 20, 38, 40]

In addition to the oxadiazole, silole, and thiophene chemistries listed above, there exist a significant number of other π-conjugated systems with electron-deficient rings that have been utilized in electron-transport applications. These molecular architectures include azole-, triazine-, quinoxaline- and phenylquinoxaline-, anthrazoline-, phenanthroline-, and quinoline-based systems, see Figure 1.9.[3, 16] As can be seen from the diversity of the structures involved, the inclusion of heterocyclic, conjugated rings into the molecular structure allow for the tailoring of numerous device properties.

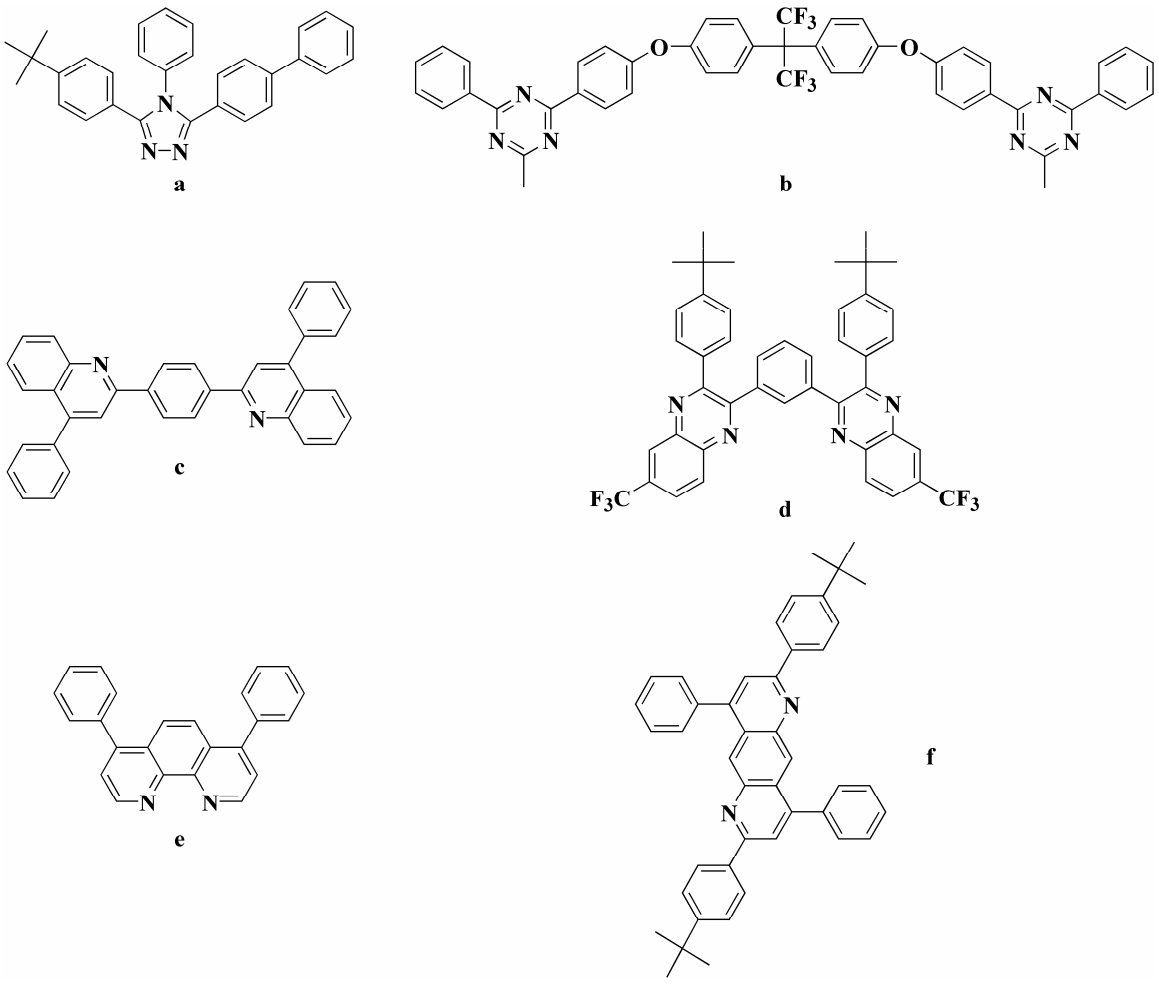

Figure 1.9 Representative examples of additional electron-deficient molecular structures – a) azole-, b) triazine-, c) quinoline-, d) quinoxaline-, e) phenanthroline-, and f) anthrozoline-based – electron-transport materials.[3, 16]

1.2 Organic molecular systems for mixed-valence investigations

Traditionally studied in inorganic/organometallic systems, investigations of mixed-valence (MV) processes in organic molecular structures have increased dramatically over the last two decades. MV, or intervalence (IV), compounds can be characterized in a very generalized manner as at minimum two redox centers of differing oxidation state (*i.e.*, donor and acceptor) linked by a bridge that mediates electron transfer between the sites.[41] Consisting of only two charge-bearing units, dimeric MV compounds constitute some of the simplest systems for the study of intramolecular electron transfer,[42] an area of study that has found great interest in the realms of supramolecular chemistry[43] and electron transport in unimolecular electronic devices.[44] One of the more interesting features of MV systems is the appearance of an absorption band in the visible and/or near-infrared that cannot be attributed to the redox centers or the bridge;[45] this band is referred to as the intervalence charge-transfer (IVCT) band, or charge-resonance (CR) band in strongly electronically-coupled systems. Through Hush analysis (see Chapter 2) of the IVCT band, it is possible to estimate both the degree of electronic coupling between the bridge-separated redox sites as well as the reorganization energy parameter that are of importance in the Marcus theory of electron transfer.[46]

1.2.1 Electronic coupling strength

The properties of MV systems depend strongly upon the extent of communication, or electronic coupling, between the individual redox centers. A classification scheme introduced by Robin and Day[47] is generally utilized to distinguish systems by the magnitude of this electronic coupling.[48] In Class I MV systems, the interaction between the redox centers is either null or extremely weak – generally due to such factors as large inter-redox-site distance, lack of conjugation, and forbiddance of inter-redox interaction because of spin or symmetry principles – making the system exhibit properties of the isolated redox units.[41, 48]

Systems in the Class II régime possess weak to moderate degrees of electronic coupling.[41] While the weak/moderate coupling has little to no effect on the potential energy surfaces near the equilibrium geometries, there can exist significant mixing near the crossing point.[41] In Class II, the molecular system remains vibrationally charge-localized (or valence-trapped), and the electron transfer over the activation barrier can range from being nonadiabatic (*i.e.*, optical excitation to an upper potential surface can be used to overcome the activation energy) to strongly adiabatic (*i.e.*, thermal energy can promote the electron transfer along a single lower surface);[48] see Chapter 2 for a more complete description of diabatic, nonadiabatic, and adiabatic electron transfer.

Finally, Class III molecular systems consist of strong electronic coupling between the redox centers.[41] The interaction between the donor and acceptor redox sites is so large

that the two minima that remained in Class II systems are no longer discernable and the lower-energy surface is a single well.[48] Because the charge is completely delocalized, the properties of the individual redox centers are no longer observable and the molecular system takes on the identity of the delocalized species.[41]

1.2.2 Organic mixed-valence compounds

One of the primary focal points in the study of mixed-valency in dimeric, organic structures has been the influence of the bridge on the degree of electronic coupling. The first system in which Hush analysis of the IVCT band could be directly compared with thermal electron transfer rates determined by electron spin resonance (ESR) spectroscopy was a bis(hydrazine) radical cation with four σ-bonds separating the dinitrogen units, see Figure 1.10.[49, 50] Though preliminary studies on bis(diazenium) radical cations with four σ-bonds in the bridge showed IVCT bands, the electron-transfer rates did not fall within timescales measurable by ESR;[49, 51, 52] addition of alkyl groups to form bis(alykylhydrazine) units, as well as extension of the bridge to six σ-bonds for the bis(diazenium) radical cations, however, did allow for subsequent ESR study of the electron-transfer rate.[51, 52]

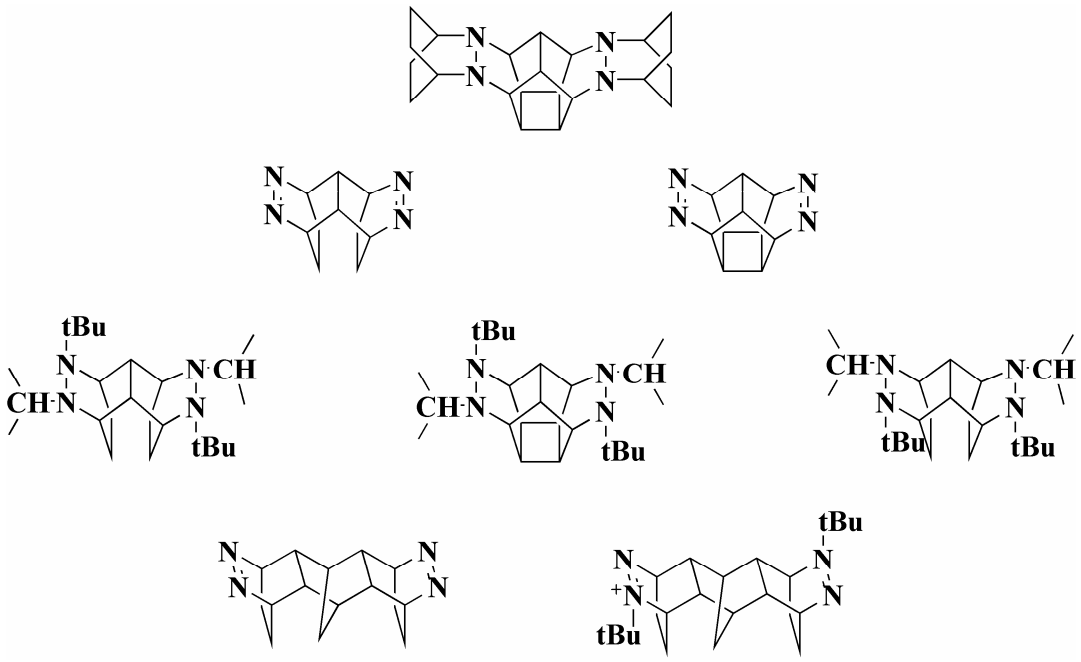

Figure 1.10 Chemical structures of σ-bridged bis(diazenium), bis(alkylhydrazyl), and bis(hydrazine) MV compounds.[49-52]

A significant enhancement in the diversity of bridge influences has been achieved through the introduction of aromatic bridges. Tetramethyl-p-phenylenediamine (TMPD), see Figure 1.11, was the first organic radical cation prepared, as well as the first to be studied by ESR.[53, 54] With TMPD as a template, a series of elegant studies on aromatic-bridged bis(hydrazine) systems were commenced by Nelsen *et al*., see Figure 1.11.[54-63] Unlike the charge-delocalized TMPD, the p-phenylene-bridged bis(hydrazine) was shown to be charge-localized due to large intramolecular reorganization energies upon oxidation. The role of the steric interactions in the orientation of the hydrazine units with respect to one another was introduced by addition of methyl groups to the phenylene bridge (*i.e.*, p-xylene and p-durene); the increased steric interactions decreased the electronic coupling.[55] Additionally, the mono- and dications of the p-phenylene and p-

durene analogs were used to study the relationships between the one-electron electronic coupling parameter and the two-electron magnetic superexchange coupling.[58]

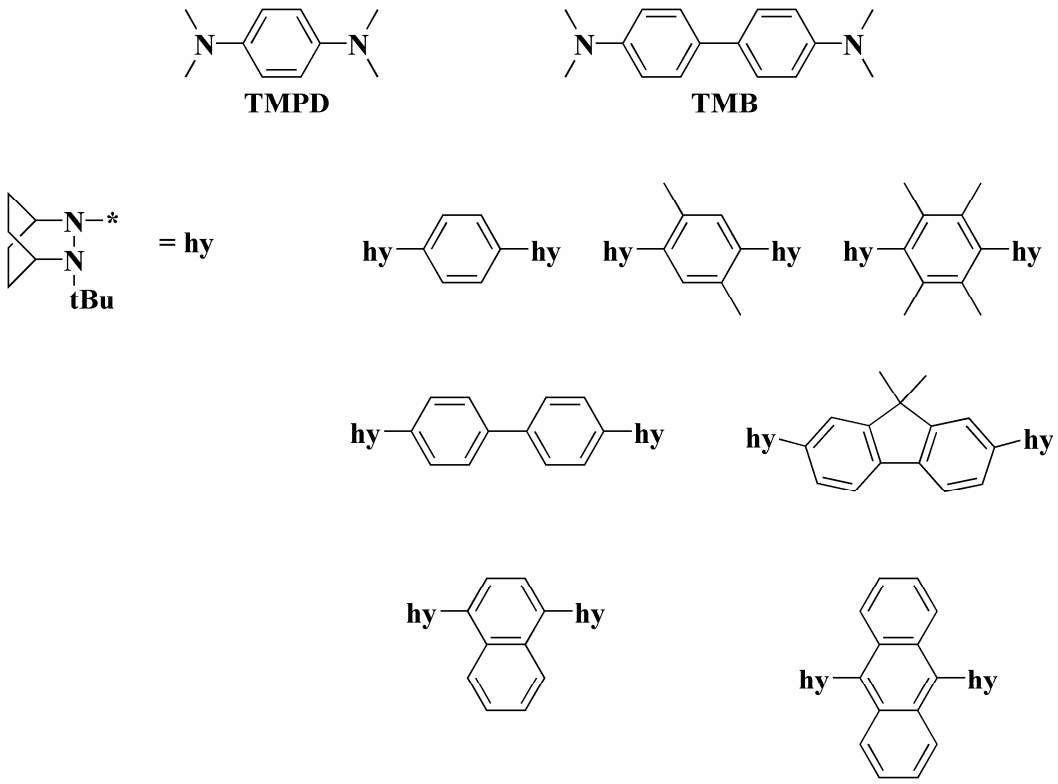

Figure 1.11 Chemical structures of tetramethyl-p-phenylenediamine (TMPD), tetramethylbenzidine (TMB), and aromatic-bridged bis(hydrazine) MV compounds.[53-63]

In addition to the various phenylene-bridged bis(hydrazines), other bridges (*e.g.*, p-biphenylene, p-fluorene, p-naphthylene, p-anthrylene) have been utilized to study the influence of bridge orientation and electronic levels on the electronic coupling. Extension of the aromatic bridge with p-naphthylene and p-anthrylene bridges allowed for better electronic communication between the hydrazine units versus the p-phenylene bridge.[57,

[59] It is worth noting that an optical peak that originates from charge-localization on the bridge lies only a few kcal/mol above the IVCT band in the p-anthrylene system; thus, if this transition is small enough to be an intermediate on the ground-state energy surface, the energy gap to the transition state for electron transfer is very small.[57] Likewise, the more planar p-fluorene-bridged structure allows for stronger electronic coupling than the twisted p-biphenylene system.[59] In addition, these aromatic-bridged bis(hydrazine)s have also been studied theoretically by a variety of Hartree-Fock, Density Functional Theory, and semi-empirical methods to determine parameters such as the electron-transfer distance, intramolecular reorganization energy, and electronic coupling.[60, 61, 63]

Kochi *et al*. have performed studies on radical-cation systems with similar structural motifs to those of Nelsen *et al*. that, instead of being predominately charge-localized, bridge Class II and Class III, see Figure 1.12.[43, 64, 65] Using 2,5-dimethoxy-4-methylphenyl, similar steric and bridge-length studies were performed using a variety of analytical techniques. In these studies, X-ray crystallography was shown for the first time to successfully delineate the charge distribution between a pair of aromatic redox centers in a MV system.[64]

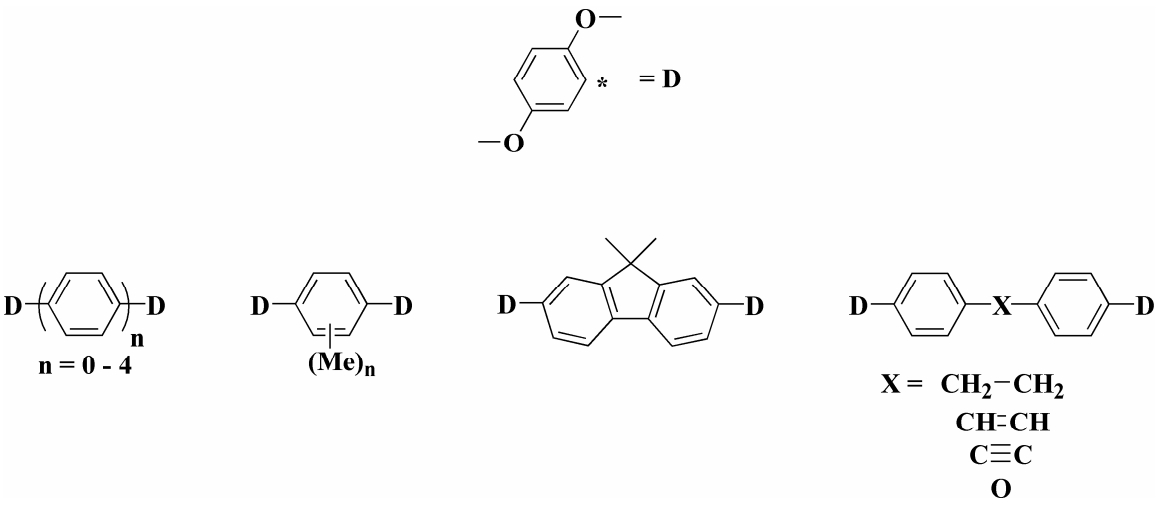

Figure 1.12 Chemical structures of bis(2,5-dimethoxy-4-methylphenyl) MV compounds.[43, 64, 65]

Bis(triarylamine) systems have been utilized extensively to investigate the dependence of bridge length on the electronic coupling, see Figure 1.13.[42, 66-72] In these systems, the distance between the redox centers range from a few Ångstroms to 2 nm. Vis/NIR, X-ray, gas-phase ultraviolet photoelectron spectroscopy (UPS), and theoretical results indicate that in the case of bis(triarylamine) compounds, both the p-phenylene and p-biphenylene systems are charge delocalized.

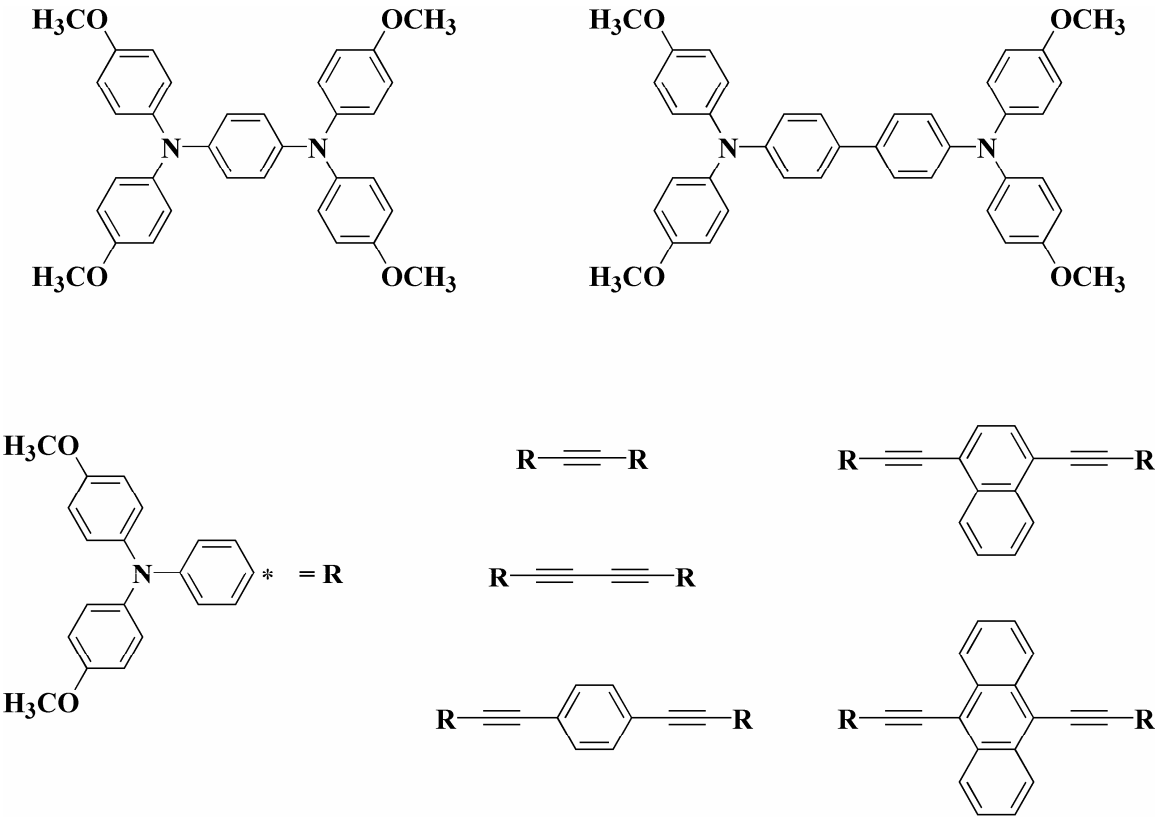

Figure 1.13 Chemical structures of bis(triarylamine) MV compounds.[66-68]

Although a majority of the studied organic MV compounds are of radical-cation ground states, there has been a definitive increase in the investigation of systems in other electronic states, see Figure 1.14. An exploratory theoretical study on neutral systems based upon structures formally consisting of one neutral, paramagnetic nitroxide and one cationic, diamagnetic nitroxide have been shown to possess electronic coupling strengths that fall within all three Robin and Day classifications.[73] The first synthesized and photophysically studied neutral MV compound consisted of a triarylamine redox center

Neutral:

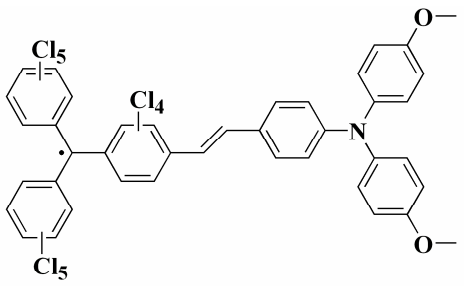

Radical-anion:

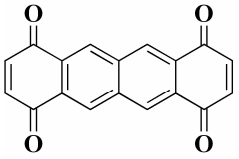

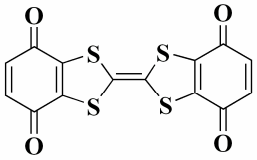

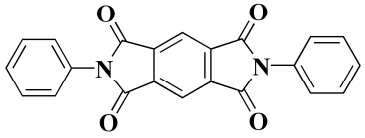

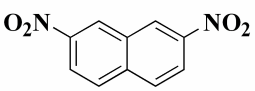

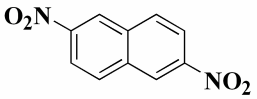

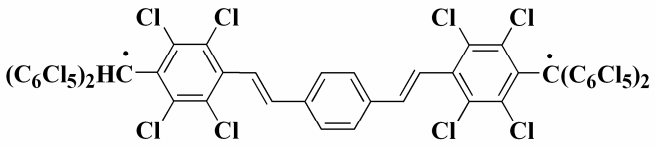

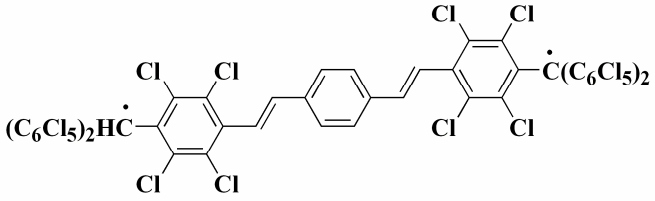

Excited State:

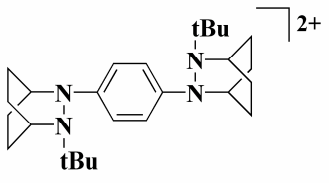

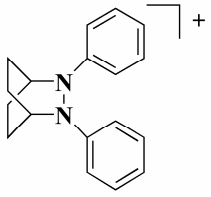

Figure 1.14 Chemical structures of example neutral, radical-anion, and excited-state MV compounds.[41, 44, 73-79]

linked to a perchlorinated triarylmethyl radical center.[74] Radical-anion systems include diquinones;[41, 44] diimides;[41] Class II 2,7-dinitronaphthalene and Class III pseudo p-substituted dinitronaphthalene;[77, 78] and bis(perchlorinated triarylmethyl) radicals.[41, 79] Additionally, excited-state MV systems, in which the first excited-state possesses MV character, have also become an interesting topic of research. Two systems, the dication of the durene-bridged bis(hydrazine) compound[75] and the monocation of 2,3-diphenyl-2,3-diazabicyclo[2.2.2]octane,[76] show potential for mixed-valence properties after excitation.

MV systems with more than two redox sites offer the possibility to study in a controlled manner structures that display more than one electron-transfer pathway,[80] as well as offer high-spin systems via the formation of multi-ion states. In a tris(triarylamine) system, the mono- and dication were shown to possess IVCT bands at the same energy, signifying the difficulty in trying to distinguish the case when two electrons move toward one hole (monocation) and when one electron moves toward two holes (dication).[81, 82] The perchlorinated 2,4,6-trichloro-α,α,α',α',α",α"-hexakis(pentachloro-phenyl)mesitylylyne was the first purely organic MV molecule with a high-spin ground state to show moderate intramolecular electron-transfer phenomena;[83] this small analog served as a precursor to a larger branched perchlorinated-phenylene system.[41] Additionally, several hexaarylbenzene systems with six triarylamine redox sites have been investigated for concerted multi-electron processes, though all have been shown to consist of consecutive one-electron transfer steps.[68, 80]

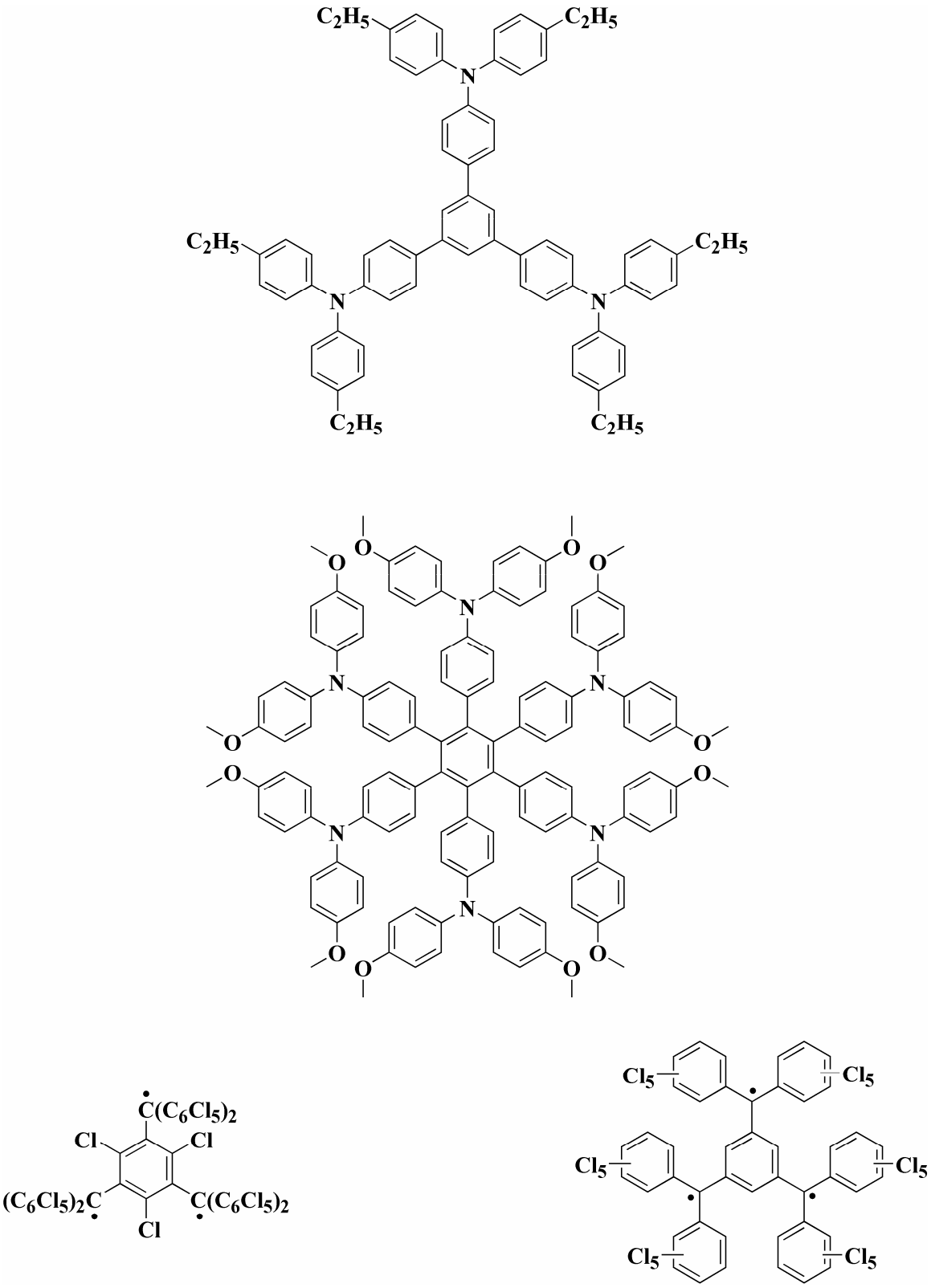
C2H5
C2H5
N
C2H5
C2H5
N
N
C2H5
C2H5
O
O
O

In addition to the various redox site and bridge effects on electronic coupling, the role of symmetric and asymmetric vibrational modes in charge (de)localization processes in MV systems has also been an intense area of investigation. The Piepho-Krausz-Schatz (PKS) vibronic-coupling model[84] (see Chapter 2) was developed for use in understanding mixed-valence systems that fall between Class II and Class III. At this borderline region, a failure in the Hush relations occurs due to a breakdown of the adiabatic Born-Oppenheimer approximation. Recent theoretical investigations of bis(triarylamine) (*vide supra*) have implemented the PKS model to analyze the IVCT band shape.[46, 71, 72] These studies have shown that symmetric vibrational modes are of significant importance in the delocalization of the charge in Class III compounds.[42, 72] Additionally, these studies have been successfully used in the reproduction of the dependence of the IVCT band on temperature.[71]

From an experimental standpoint, the role of vibrational modes has been studied via Raman spectroscopy in a number of systems. Initial studies on the σ-bridged bis(alkylhydrazyl)s revealed that six vibrational modes were coupled to the intramolecular charge transfer, with the two strongest modes assigned to the vibrations within the dinitrogen units.[85] Resonance Raman spectroscopy of the Class III bis(3-oxo-9-azabicyclo-[3.3.1]non-9-yl)benzene structure showed that symmetric vibrational modes are strongly coupled to the IV transition.[86] Additionally, resonance Raman studies have been used on poly(aryl)amine compounds.[87, 88]

1.3 Thesis objectives and outline

The primary emphasis of the work described herein is centered on theoretical investigations concerned with the elucidation of fundamental aspects of both intermolecular and intramolecular electron transfer in organic, π-conjugated molecular systems. The common denominator found throughout these investigations is the determination of structure-property relationships via quantum-chemical characterizations of geometric and electronic structures as well as optical properties. These theoretically-assessed parameters are then correlated with a multitude of empirical data.

In Chapter 2, a brief review of the basic models used in the theoretical characterization of electron-transfer processes will be provided. First, a synopsis of the basic quantum-mechanical problem (*i.e.*, the Schrödinger equation) is provided along with details of approximate methods (*i.e.*, Hartree-Fock theory, semiempirical methods, post-Hartree-Fock methods, Density Functional Theory) currently in use. Second, a review of the Marcus equations, and extensions thereof, used for the description of electron-transfer processes in the weak electronic-coupling régime is given. Finally, a two-state, two-mode vibronic-coupling model that is utilized for investigations of intramolecular mixed-valence processes is introduced.

Chapter 3 and Chapter 4 deal with investigations of the properties of silole molecular systems as they relate to electron-transport materials. In Chapter 3, two siloles – 2,5-bis(6'-(2',2"-bipyridyl))-1,1-dimethyl-3,4-diphenylsilole and 2,5-di-(3-biphenyl))-1,1-

dimethyl-3,4-diphenylsilole – are compared as they possess significantly different electron-transport and optical properties in solid-state films, though they are structurally and chemically very similar. In Chapter 4, a series of 1,1-diaryl-2,3,4,5-tetraphenylsiloles are studied in order to determine the geometric, electronic, and optical effects of the differing substituents. Chapter 5 introduces a relatively new series of compounds thought to be of interest for electron-transport materials – dioxaborines. Initial characterizations of a variety of molecular architectures are provided along with a comparison to some simple oxadiazole and silole systems.

With Chapter 6, the focus shifts to the investigation of mixed-valence systems. Chapter 6 centers on the investigation of a series of tetraanisylarylenediamine systems where the aryl bridge is changed from phenylene to naphthylene to anthrylene; somewhat unexpectedly, the electronic coupling is discovered to decrease with increasing ionization potential of the bridge. In Chapter 7, we investigate the bridge-length dependence of a series of vinylene- and phenylene-vinylene-bridged bis-dianisylamines. Finally in Chapter 8, the role of symmetric vibrations in the delocalization of the excess charge is studied in a dioxaborine radical-anion and a series of bridged-bisdimethylamines.

1.4 References

(1) Friend, R. H.; Gymer, R. W.; Holmes, A. B.; Burroughes, J. H.; Marks, R. N.; Taliani, C.; Bradley, D. D. C.; dos Santos, D. A.; Brédas, J. L.; Logdlund, M.; Salaneck, W. R., *Nature* **1999,** 397, 121.

(2) Dimitrakopoulos, C.; Malenfant, P., *Adv. Mater.* **2002,** 14, 99.

(3) Hughes, G.; Bryce, M. R., *J. Mater. Chem.* **2005,** 15, 94.

(4) Jortner, J.; Bixon, M., In *Advances in Chemical Physics: Electron Transfer - from Molecules to Biomolecules*, ed.; Jortner, J.; Bixon, M., Ed. John Wiley and Sons, Incorporated: New York, 1999; Vol. 1.

(5) Barbara, P.; Meyer, T.; Ratner, M., *J. Phys. Chem.* **1996,** 100, 13148.

(6) Newton, M. D., Control of Electron Transfer Kinetics: Models for Medium Reorganization Energy and Donor-Acceptor Coupling. In *Advances in Chemical Physics: Electron Transfer - from Molecules to Biomolecules*, ed.; Jortner, J.; Bixon, M., Ed. John Wiley and Sons, Incorporated: New York, 1999; Vol. 1.

(7) Pourtois, G.; Beljonne, D.; Cornil, J.; Ratner, M. A.; Brédas, J. L., *J. Am. Chem. Soc.* **2002,** 124, 4436.

(8) Marcus, R. A., *Rev. Mod. Phys* **1993,** 65, 599.

(9) Coropceanu, V.; André, J. M.; Malagoli, M.; Brédas, J. L., *Theor. Chem. Acc.* **2003,** 110, 56.

(10) Marcus, R. A., *J. Chem. Phys.* **1956,** 24, 966.

(11) Brédas, J. L.; Beljonne, D.; Coropceanu, V.; Cornil, J., *Chem. Rev.* **2004,** 104, 4971.

(12) Newman, C. R.; Frisbie, C. D.; da Silva Filho, D. A.; Brédas, J. L.; Ewbank, P. C.; Mann, K. R., *Chem. Mater.* **2004,** 16, 4436.

(13) Crone, B.; Dodabalapur, A.; Lin, Y. Y.; Filas, R. W.; Bao, Z.; LaDuca, A.; Sarpeshkar, R.; Katz, H. E.; Li, W., *Nature* **2000,** 403, 521.

(14) Fachetti, A.; Letizia, J.; Yoon, M. H.; Mushrush, M.; Katz, H. E.; Marks, T. J., *Chem. Mater.* **2004,** 16, 4715.

(15) Borchardt, J. K., *Materials Today* **2004,** 9, 42.

(16) Kulkarni, A. P.; Tonzola, C. J.; Babel, A.; Jenekhe, S. A., *Chem. Mater.* **2004,** 16, 4556.

(17) Hung, L. S.; Chen, C. H., *Mater. Sci. Eng., A* **2002,** 39, 143.

(18) Lemaur, V.; Steel, M.; Beljonne, D.; Brédas, J. L.; Cornil, J., *J. Am. Chem. Soc.* **2005,** 127, 6077.

(19) Reese, C.; Roberts, M.; Ling, M. M.; Bao, Z., *Materials Today* **2004,** 9, 20.

(20) Fachetti, A.; Mushrush, M.; Yoon, M. H.; Hutchinson, G. R.; Ratner, M. A.; Marks, T. J., *J. Am. Chem. Soc.* **2004,** 126, 13859.

(21) Würthner, F., *Angew. Chem. Int. Ed.* **2001,** 40, 1037.

(22) de Leeuw, D. M.; Simenon, M. M. J.; Brown, A. R.; Einerhand, R. E. F., *Synth. Met.* **1997,** 87, 53.

(23) Tokuhisa, H.; Era, M.; Tsutsui, T., *Adv. Mater.* **1998,** 10, 404.

(24) Zhang, Y. D.; Jespersen, K. G.; Kempe, M.; Kornfield, J. A.; Barlow, S.; Kippelen, B.; Marder, S. R., *Langmuir* **2003,** 19, 6534.

(25) Murata, H.; Malliaras, G. G.; Uchida, M.; Shen, Y.; Kafafi, Z. H., *Chem. Phys. Lett.* **2001,** 339, 16 1.

(26) Tang, C. W.; van Slyke, S. A., *Appl. Phys. Lett.* **1987,** 51, 913.

(27) Heidenhain, S. B.; Sakamoto, Y.; Suzuki, T.; Miura, A.; Fujikawa, H.; Mori, T.; Tokito, S.; Taga, Y., *J. Am. Chem. Soc.* **2000,** 122, 10240.

(28) Komatsu, S.; Sakamoto, Y.; Suzuki, T.; Tokito, S., *J. Solid State Chem.* **2002,** 168, 470.

(29) Sakamoto, Y.; Suzuki, T.; Kobayashi, M.; Gao, Y.; Fukai, Y.; Inoue, Y.; Sato, F.; Tokito, S., *J. Am. Chem. Soc.* **2005,** 126, 8138.

(30) Adachi, C.; Tsutsui, T.; Saito, S., *Appl. Phys. Lett.* **1989,** 55, 1489.

(31) Brocks, G.; Tol, A., *J. Chem. Phys.* **1997,** 106, 6418.

(32) Bettenhausen, J.; Greczmiel, M.; Jandke, M.; Strohriegl, P., *Synth. Met.* **1997,** 91, 223.

(33) Tamao, K.; Uchida, M.; Izumizawa, T.; Furukawa, K.; Yamaguchi, S., *J. Am. Chem. Soc.* **1996,** 118, 11974.

(34) Yamaguchi, S.; Itami, Y.; Tamao, K., *Organometallics* **1998,** 17, 4910.

(35) Murata, H.; Malliaras, G. G.; Uchida, M.; Shen, Y.; Kafafi, Z. H., *Appl. Phys. Lett.* **2001,** 80, 189.

(36) Palalis, L. C.; Uchida, M.; Kafafi, Z. H., *IEEE J. Sel. Top. Quantum Electron.* **2004,** 10, 79.

(37) Palalis, L. C.; Mäkinen, A. J.; Murata, H.; Uchida, M.; Kafafi, Z. H., In *Organic Light-Emitting Materials and Devices Vi. Proceedings of the Spie - the International Society for Optical Engineering*, ed.; Kafafi, Z. H., Ed. SPIE: Bellingham, WA, 2003; Vol. 4800.

(38) Yassar, A.; Demanze, F.; Jaafari, A.; El Idrissi, M.; Coupry, C., *Adv. Funct. Mater.* **2002,** 12, 699.

(39) Fachetti, A.; Yoon, M. H.; Stern, C.; Katz, H. E.; Marks, T. J., *Angew. Chem. Int. Ed.* **2003,** 42, 3900.

(40) Noda, T.; Shirota, Y., *J. Am. Chem. Soc.* **1998,** 120, 9714.

(41) Ruiz-Molina, D.; Sedó, J.; Rovira, C.; Veciana, J., Intramolecular Electron-Transfer Phenomena in Organic Mixed-Valence Compounds. In *Handbook of Advanced Electronic and Photonic Devices: High Tc Superconductors and Organic Conductors*, ed.; Nalwa, H. S., Ed. Academic Press: 2001; Vol. 3.

(42) Coropceanu, V.; Malagoli, M.; André, J. M.; Brédas, J. L., *J. Am. Chem. Soc.* **2002,** 124, 10519.

(43) Sun, D.; Lindeman, S. V.; Rathore, R.; Kochi, J. K., *J. Chem. Soc., Perkin Trans. 2* **2001**, 1585.

(44) Gautier, N.; Dumur, F.; Lloveras, V.; Vidal-Gancedo, J.; Veciana, J.; Rovira, C.; Hudhomme, P., *Angew. Chem. Int. Ed.* **2003,** 42, 2765.

(45) Dehareng, D.; Dive, G.; Moradpour, A., *Int. J. Quantum Chem.* **2000,** 76, 552.

(46) Coropceanu, V.; Malagoli, M.; André, J. M.; Brédas, J. L., *J. Am. Chem. Soc.* **2002,** 124, 10519.

(47) Robin, M. B.; Day, P., In *Advances in Inorganic Chemistry and Radiochemistry*, ed.; Ed. Academic Press: New York, 1967; Vol. 10.

(48) Sutin, N., In *Advances in Chemical Physics: Electron Transfer - from Molecules to Biomolecules*, ed.; Jortner, J.; Bixon, M., Ed. John Wiley and Sons, Incorporated: New York, 1999; Vol. 1.

(49) Nelsen, S. F.; Adamus, J.; Wollf, J. J., *J. Am. Chem. Soc.* **1994,** 116, 1589.

(50) Nelsen, S. F., *J. Am. Chem. Soc.* **1996,** 118, 2047.

(51) Nelsen, S. F.; Ramm, M. T.; Wollf, J. J.; Powell, D. R., *J. Am. Chem. Soc.* **1997,** 119, 6863.

(52) Nelsen, S. F.; Trieber, D. A.; Wollf, J. J.; Powell, D. R.; Rogers-Crowley, S., *J. Am. Chem. Soc.* **1997,** 119, 6873.

(53) Roth, H. D., *Tetrahedron Lett.* **1986,** 42, 5097.

(54) Nelsen, S. F.; Ismagilov, R. F.; Powell, D. R., *J. Am. Chem. Soc.* **1996,** 118, 6313.

(55) Nelsen, S. F.; Ismagilov, R. F.; Powell, D. R., *J. Am. Chem. Soc.* **1997,** 119, 10213.

(56) Nelsen, S. F.; Tran, H. Q.; Nagy, M. A., *J. Am. Chem. Soc.* **1998,** 120, 298.

(57) Nelsen, S. F.; Ismagilov, R. F.; Powell, D. R., *J. Am. Chem. Soc.* **1998,** 120, 1924.

(58) Nelsen, S. F.; Ismagilov, R. F.; Teki, Y., *J. Am. Chem. Soc.* **1998,** 120, 2200.

(59) Nelsen, S. F.; Ismagilov, R. F.; Gentile, K. E.; Powell, D. R., *J. Am. Chem. Soc.* **1999,** 121, 7108.

(60) Nelsen, S. F.; Newton, M. D., *J. Phys. Chem. A* **2000,** 104, 10023.

(61) Blomgren, F.; Larsson, S.; Nelsen, S. F., *J. Comput. Chem.* **2001,** 22, 655.

(62) Nelsen, S. F.; Li, G.; Konradsson, A., *Org. Lett.* **2001,** 3, 1583.

(63) Nelsen, S. F.; Blomgren, F., *J. Org. Chem.* **2001,** 66, 6551.

(64) Lindeman, S. V.; Rosokha, S. V.; Sun, D.; Kochi, J. K., *J. Am. Chem. Soc.* **2002,** 124, 843.

(65) Rosokha, S. V.; Sun, D.; Kochi, J. K., *J. Phys. Chem. A* **2002,** 106, 2283.

(66) Lambert, C.; Nöll, G., *J. Am. Chem. Soc.* **1999,** 121, 8434.

(67) Lambert, C.; Amthor, S.; Schelter, J., *J. Phys. Chem. A* **2004,** 108, 6474.

(68) Lambert, C.; Nöll, G., *Chem. Eur. J.* **2004,** 8, 3467.

(69) Lambert, C.; Nöll, G.; Schelter, J., *Nat. Mater.* **2002,** 1, 69.

(70) Coropceanu, V.; Gruhn, N. E.; Barlow, S.; Lambert, C.; Durivage, J. C.; Bill, T. G.; Nöll, G.; Marder, S. R.; Brédas, J. L., *J. Am. Chem. Soc.* **2004,** 126, 2727.

(71) Coropceanu, V.; Lambert, C.; Nöll, G.; Brédas, J. L., *Chem. Phys. Lett.* **2003,** 373, 153.

(72) Coropceanu, V.; Malagoli, M.; André, J. M.; Brédas, J. L., *J. Chem. Phys.* **2001,** 115, 10409.

(73) Rassat, A.; del Re, G.; Peluso, A., *Chem. Phys. Lett.* **1999,** 313, 582.

(74) Heckman, A.; Lambert, C.; Goebel, M.; Wortmann, R., *Angew. Chem. Int. Ed.* **2004,** 43, 5851.

(75) Lockard, J. V.; Zink, J. I.; Konradsson, A.; Weaver, M. N.; Nelsen, S. F., *J. Am. Chem. Soc.* **2003,** 125, 13471.

(76) Lockard, J. V.; Zink, J. I.; Trieber, D. A.; Konradsson, A.; Weaver, M. N.; Nelsen, S. F., *J. Phys. Chem. A* **2005,** 109, 1205.

(77) Nelsen, S. F.; Konradsson, A.; Telo, J. P., *J. Am. Chem. Soc.* **2005,** 127, 920.

(78) Nelsen, S. F.; Weaver, M. N.; Konradsson, A.; Telo, J. P.; Clark, T., *J. Am. Chem. Soc.* **2004,** 126, 15431.

(79) Rovira, C.; Ruiz-Molina, D.; Elsner, O.; Vidal-Gancedo, J.; Bonvoisin, J.; Launay, J. P.; Veciana, J., *Chem. Eur. J.* **2001,** 7, 240.

(80) Lambert, C.; Nöll, G.; Hampel, F., *J. Phys. Chem. A* **2001,** 105, 7751.

(81) Bonvoisin, J.; Launay, J. P.; van der Auweraer, M.; de Schryver, F. C., *J. Phys. Chem.* **1994,** 98, 5052.

(82) Bonvoisin, J.; Launay, J. P.; van der Auweraer, M.; de Schryver, F. C., *J. Phys. Chem.* **1996,** 100, 17079.

(83) Sedó, J.; Ruiz-Molina, D.; Vidal-Gancedo, J.; Rovira, C.; Bonvoisin, J.; Launay, J. P.; Veciana, J., *Adv. Mater.* **1996,** 9, 748.

(84) Piepho, S. B.; Krausz, E. R.; Schatz, P. N., *J. Am. Chem. Soc.* **1978,** 100, 2996.

(85) Williams, R. D.; Hupp, J. T.; Ramm, M. T.; Nelsen, S. F., *J. Phys. Chem. A* **1999,** 103, 11172.

(86) Bailey, S. E.; Zink, J. I.; Nelsen, S. F., *J. Am. Chem. Soc.* **2003,** 125, 5939.

(87) Littleford, R. E.; Paterson, M. A. J.; Low, P. J.; Tackley, D. R.; Jayes, L.; Dent, G.; Cherryman, J. C.; Brown, B.; Smith, W. E., *Phys. Chem. Chem. Phys.* **2004**, 3257.

(88) Szeghalmi, A. V.; Erdmann, M.; Engel, V.; Schmitt, M.; Amthor, S.; Kriegisch, V.; Nöll, G.; Stahl, R.; Lambert, C.; Leusser, D.; Stalke, D.; Zabel, M.; Popp, J., *J. Am. Chem. Soc.* **2004,** 126, 7834.

CHAPTER 2

OVERVIEW OF THEORETICAL METHODS FOR THE DESCRIPTION OF ELECTRON-TRANSFER PROCESSES

In this Chapter, we briefly review the electronic-structure, electron-transfer, and vibronic-coupling theories used for the quantum-chemical description of electron-transfer processes in molecular systems. We first introduce the Hartree-Fock (and related post-Hartree-Fock and semi-empirical methods) and Density Functional Theory methods to electronic-structure calculations. This is followed by a description of the development of electron-transfer theory from classical principles to the involvement of quantum-mechanical principles. Finally, we present a two-state, two-mode vibronic-coupling model relevant to electron transfer in mixed-valence compounds.

2.1 Electronic-structure theories

We present in this Section a brief discussion of the electronic-structure methods derived from quantum mechanics that find use in the description of molecular systems. These methods provide the key parameters for the electron-transfer and vibronic-coupling theories presented below. The notation and terminology presented herein are primarily taken from the following texts: Levine,[1] Cohen-Tannoudji,[2] Szabo and Ostlund,[3] Jensen,[4] Cramer,[5] and Koch and Holstein.[6]

2.1.1 The Schrödinger equation

To describe the electronic structure of a stationary organic molecular system, the principal quantum-mechanical tool is the non-relativistic, time-independent Schrödinger equation:

$$\hat{H}\left|\Psi_i\left(\vec{r}_1,\vec{r}_2,\vec{r}_3\ldots\vec{r}_N;\vec{R}_1,\vec{R}_2,\vec{R}_3\ldots\vec{R}_M\right)\right\rangle = E\left|\Psi_i\left(\vec{r}_1,\vec{r}_2,\vec{r}_3\ldots\vec{r}_N;\vec{R}_1,\vec{R}_2,\vec{R}_3\ldots\vec{R}_M\right)\right\rangle \quad (2.1)$$

where $\hat{H}$ is the Hamiltonian operator for any *N*-electron and *M*-nuclei system described by position vectors $\vec{r}_i$ and $\vec{R}_A$, respectively. In atomic units, the Hamiltonian operator in differential form is:

$$\hat{H} = -\frac{1}{2}\sum_{i=1}^{N}\nabla_i^2 - \frac{1}{2}\sum_{A=1}^{M}\frac{1}{M_A}\nabla_A^2 - \sum_{i=1}^{N}\sum_{A=1}^{M}\frac{Z_A}{r_{iA}} + \sum_{i=1}^{N}\sum_{j>1}^{N}\frac{1}{r_{ij}} + \sum_{A=1}^{M}\sum_{B>1}^{M}\frac{Z_A A_B}{R_{AB}} \quad (2.2)$$

where $r_{iA} = |r_i - R_A|$ is the distance between the *i*th electron and *A*th nucleus, $r_{ij} = |r_i - r_j|$ is the distance between the *i*th electron and *j*th electron, $R_{AB} = |R_A - R_B|$ is the distance between the *A*th nucleus and *B*th nucleus, M_A is the ratio of the mass of nucleus *A* to the mass of an electron, Z_A is the atomic number of nucleus *A*, and the Laplacian operators ∇_i^2 and ∇_A^2 involve differentiation with respect to the coordinates of the *i*th electron and *A*th nucleus, respectively. In the Hamiltonian operator, the first two terms represent the kinetic energies of the electrons and nuclei, respectively; the third term represents the electrostatic interactions (Coulomb interactions) between the electrons and nuclei; and the fourth and fifth terms represent electron-electron and nuclear-nuclear repulsion, respectively.

Due to the large mass difference between the protons and electrons (~1840:1), one can approximate that the electrons move within a stationary field of fixed nuclei; this assumption is known as the Born-Oppenheimer approximation. Thus, in the Hamiltonian operator presented in Equation 2.2, the second term can be neglected while the last term representing the nuclear-nuclear interactions can be considered a constant. The remaining terms define the electronic Hamiltonian:

$$\hat{H}_e = -\frac{1}{2}\sum_{i=1}^{N}\nabla_i^2 - \sum_{i=1}^{N}\sum_{A=1}^{M}\frac{Z_A}{r_{iA}} + \sum_{i=1}^{N}\sum_{j>1}^{N}\frac{1}{r_{ij}} \tag{2.3}$$

Additionally, the total wavefunction can be reduced to the electronic wavefunction $\psi_e = \psi_e\left(\vec{r}_i, \vec{R}_A\right)$ to describe the motion of the electrons with the electronic Hamiltonian; the electronic wavefunction explicitly depends on the electronic coordinates and only parametrically on the nuclear coordinates. This leads to the electronic Schrödinger equation:

$$\hat{H}_e\left|\psi_e\left(\vec{r}_i, \vec{R}_A\right)\right\rangle = E_e\left(\vec{R}_A\right)\left|\psi_e\left(\vec{r}_i, \vec{R}_A\right)\right\rangle \tag{2.4}$$

Note that $\psi_e\left(\vec{r}_i, \vec{R}_A\right)$ is not observable; the only physical interpretation comes from the probability to find an electron within a defined volume, as defined by $\left|\psi_e\left(\vec{r}_1\vec{r}_2\vec{r}_3\ldots\vec{r}_N\right)\right|^2 d\vec{r}_1 d\vec{r}_2 d\vec{r}_3 \ldots d\vec{r}_N$. The total energy for a system of fixed nuclei must also include the nuclear repulsion

$$E_{total}\left(\vec{R}_A\right) = E_e\left(\vec{R}_A\right) + \sum_{A=1}^{M}\sum_{B>A}^{M}\frac{Z_A Z_B}{R_{AB}} \tag{2.5}$$

This total energy function provides a potential energy surface for nuclear motion.

The nuclei in the Born-Oppenheimer approximation are confined to movement along a potential energy surface that is obtained by solving the electronic Schrödinger equation. The Hamiltonian for the motion of nuclei in an average field of the fast-moving electrons is:

$$\hat{H}_n = -\frac{1}{2}\sum_{A=1}^{M}\frac{1}{M_A}\nabla_A^2 + E_{total}\left(\vec{R}_A\right) \tag{2.6}$$

The corresponding nuclear Schrödinger equation

$$\hat{H}_n\left|\Psi_n\left(\vec{R}_A\right)\right\rangle = E_n\left|\Psi_n\left(\vec{R}_A\right)\right\rangle \tag{2.7}$$

describes the vibrational, translational, and rotational modes of the molecular system.

In addition to the spatial wavefunction $\psi_e\left(\vec{r}_i,\vec{R}_A\right)$, spin wavefunctions $\alpha(\omega)$ and $\beta(\omega)$ representing the non-classical term for spin must be introduced to completely describe an electron in the nonrelativistic theory. An electronic wavefunction that describes both the spatial and spin components is defined as a spin orbital $\chi(\vec{x})$, where $\vec{x}$ indicates both the space and spin coordinates. The combination of the spatial and spin functions leads to two configurations of the spin orbitals:

$$\chi(\vec{x}) = \left\{\psi_e(\vec{r})\alpha(\omega), \psi_e(\vec{r})\beta(\omega)\right\} \tag{2.8}$$

Due to the fact that the Hamiltonian operator makes no reference to spin, an additional requirement to the wavefunction for an N-electron system needs to be addressed. The antisymmetry principle, a very general statement of the Pauli exclusion principle, states that a many-electron wavefunction must be antisymmetric with respect to interchange of $\vec{x}_i$ for any two electrons:

$$\Phi\left(\vec{x}_1,\ldots,\vec{x}_i,\ldots\vec{x}_j,\ldots,\vec{x}_N\right) = -\Phi\left(\vec{x}_1,\ldots,\vec{x}_j,\ldots\vec{x}_i,\ldots,\vec{x}_N\right) \tag{2.9}$$

It is important to note that the antisymmetry principle does not distinguish between electrons.

2.1.2 The Hartree-Fock approximation

Though the Born-Oppenheimer approximation greatly simplifies the Schrödinger equation, solutions to the electronic Schrödinger are still complex. Introduction of the concept of molecular orbitals through the Hartree, or independent-particle, approximation allows for the total wavefunction to be approximated by a product of orthonormal wavefunctions:

$$\psi_{HP}(\vec{r}_1,\vec{r}_2,\ldots,\vec{r}_N)=\phi_1(\vec{r}_1)\phi_2(\vec{r}_2)\ldots\phi_N(\vec{r}_N) \tag{2.10}$$

Such an expression is known as the Hartree product. Unfortunately, the Hartree product does not satisfy the indistinguishability requirement of the antisymmetry principle.

To deal with the antisymmetry problem, Fock showed that a Hartree product could be made antisymmetric through the proper addition and subtraction of all possible permutations of the Hartree product. Thus, in Hartree-Fock (HF) theory, the generalized wavefunction for an N-electron system is expressed as a single Slater determinant of the form:

$$\Psi(\vec{x}_1,\vec{x}_2,\ldots\vec{x}_N)=(N!)^{-1/2}\begin{vmatrix} \chi_1(\vec{x}_1) & \chi_2(\vec{x}_1) & \cdots & \chi_N(\vec{x}_1) \\ \chi_1(\vec{x}_2) & \chi_2(\vec{x}_2) & \cdots & \chi_N(\vec{x}_2) \\ \cdots & \cdots & \ddots & \vdots \\ \chi_1(\vec{x}_N) & \chi_2(\vec{x}_N) & \cdots & \chi_N(\vec{x}_N) \end{vmatrix} \tag{2.11}$$

where the factor $(N!)^{-1/2}$ normalizes the wavefunction. The Slater determinant form of the wavefunction ensures the indistinguishability as each electron is associated with every spin orbital of the wavefunction; additionally, the antisymmetry principle is satisfied with respect to the interchange of any two electrons (*e.g.*, the interchange of any two coordinates ($\vec{x}_i$) exchanges two rows of the determinant bringing forth a change in sign of the wavefunction). The Slater determinant introduces both exchange (due to the requirement that the probability be invariant to the exchange of space and spin coordinates of any two electrons) and correlation (the motion of two electrons with parallel spins is correlated) effects; however, since the motion of electrons with opposite spins is uncorrelated in single-determinant wavefunctions, the Slater determinant is said to be an uncorrelated wavefunction.

2.1.2.1 The Hartree-Fock energy expression

For any arbitrary wavefunction in which the Hamiltonian is known, but not necessarily the eigenvalues, the variational principle imparts that the expectation value of the Hamiltonian is:

$$\left\langle \hat{H} \right\rangle = \frac{\left\langle \Psi \middle| \hat{H} \middle| \Psi \right\rangle}{\left\langle \Psi \middle| \Psi \right\rangle} \geq E_0 \tag{2.12}$$

with the equality occurring if and only if the wavefunction is an eigenvector of the Hamiltonian with eigenvalue E_0. Keeping the rules of the variational principle in mind,

the HF energy can be written in terms of one- and two-electron integrals and the nuclear repulsion energy, as:

$$E_{HF} = \sum_{i=1}^{N} \left\langle \chi_i(\vec{x}_i) \middle| \hat{h}(i) \middle| \chi_i(\vec{x}_i) \right\rangle + \frac{1}{2} \sum_{ij}^{N} \left(\hat{J}_{ij} - \hat{K}_{ij} \right) + V_{NN} \tag{2.13}$$

where the first summation corresponds to one-electron integrals:

$$\left\langle \chi_i(\vec{x}_i) \middle| \hat{h}(i) \middle| \chi_i(\vec{x}_i) \right\rangle = \int d\vec{x}_1 \chi_i^*(\vec{x}_1) \hat{h}(r_1) \chi_i(\vec{x}_1) \tag{2.14}$$

representing the one-electron contribution for a single electron in a field of nuclei, while the second summation is composed of the two-electron Coulomb $\hat{J}$ and exchange $\hat{K}$ integrals:

$$\hat{J}_{ij} = \int d\vec{x}_1 d\vec{x}_2 \chi_i^*(\vec{x}_1) \chi_j^*(\vec{x}_2) \frac{1}{r_{12}} \chi_i(\vec{x}_1) \chi_j(\vec{x}_2) \tag{2.15}$$

$$\hat{K}_{ij} = \int d\vec{x}_1 d\vec{x}_2 \chi_i^*(\vec{x}_1) \chi_j^*(\vec{x}_2) \frac{1}{r_{12}} \chi_j(\vec{x}_2) \chi_i(\vec{x}_1) \tag{2.16}$$

While the Coulomb term, interpreted as the electrostatic interaction of an electron in a spatially-averaged one-electron potential of all other electrons, is a local term, the exchange term, arising from the asymmetric nature of the determinental wavefunction, is a non-local term since there does not exist a simple potential uniquely defined at a local point in space $\vec{x}_i$. Note that $h(i)$ is a one-electron operator defined as

$$\hat{h}(i) = -\frac{1}{2} \nabla_i^2 - \sum_A \frac{Z_A}{r_{iA}} \tag{2.17}$$

that allows for simplification of the electronic Hamiltonian to

$$\hat{H}_e = \sum_i \hat{h}(i) + \sum_{i>j} \frac{1}{r_{ij}} + V_{NN} \tag{2.18}$$

where V_{NN} is the nuclear-nuclear repulsion term, which is a constant for fixed nuclear-nuclear distance.

2.1.2.2 Restricted closed-shell Hartree-Fock and the Roothan Equations

In the ground state, the *N*-electrons of a closed-shell neutral system are paired such that there are *N/2* occupied orbitals. Spin can be eliminated from the orbital picture by writing the spin orbitals in terms of their spin and spatial parts:

$$\chi_i(\vec{x}_1) = \begin{cases} \psi_j(\vec{r}_1)\alpha(\omega) \\ \psi_j(\vec{r}_1)\beta(\omega) \end{cases} \tag{2.19}$$

thus giving the closed-shell ground state the form:

$$|\psi_0\rangle = |\chi_1(\vec{x}_1)\ldots\chi_i(\vec{x}_i)\ldots\chi_N(\vec{x}_N)\rangle = |\psi_1(\alpha)\psi_1(\beta)\ldots\psi_i(\alpha)\psi_i(\beta)\ldots\psi_{N/2}(\alpha)\psi_{N/2}(\beta)\rangle \tag{2.20}$$

For a closed-shell and restricted set of orbitals, the spatial HF equation can be written:

$$\hat{f}(\vec{r}_1)|\psi_i(\vec{r}_1)\rangle = \varepsilon_i|\psi_i(\vec{r}_1)\rangle \tag{2.21}$$

where the Fock operator $\hat{f}$ is defined as:

$$\hat{f}(\vec{r}_1) = \hat{h}(\vec{r}_1) + \sum_j^{N/2} 2\hat{J}_j(\vec{r}_1) - \hat{K}_j(\vec{r}_1) \tag{2.22}$$

The closed-shell Coulomb and exchange operators are now defined in terms of spatial orbitals as:

$$\hat{J}_j(\vec{r}_1)\psi_i(\vec{r}_1) = \left[\int d\vec{r}_2 \psi_j^*(\vec{r}_2)\frac{1}{r_{12}}\psi_j^*(\vec{r}_2)\right]\psi_i(\vec{r}_1) \tag{2.23}$$

$$\hat{K}_j(\vec{r}_1)\psi_i(\vec{r}_1) = \left[\int d\vec{r}_2 \psi_j^*(\vec{r}_2)\frac{1}{r_{12}}\psi_i^*(\vec{r}_2)\right]\psi_j(\vec{r}_1) \tag{2.24}$$

To solve the spatial HF equation, a set of *K* known basis functions is introduced and expressed as a linear combination of these basis functions, *i.e.*, the linear combination of atomic orbitals (LCAO) approximation; thus, the HF equation becomes a set of algebraic equations. The expansion of the unknown molecular orbitals ($\psi_i \equiv \psi_i(\vec{r}_i)$) in the selected basis φ_μ is given by:

$$\psi_i = \sum_\mu C_{i\mu}\phi_\mu \quad i = 1,2,\ldots,K \tag{2.25}$$

where $C_{i\mu}$ are a set of unknown expansion coefficients. Substituting ψ_i into the spatial HF equation yields a set of *K* equations known as the Roothan equations, which can be written into matrix form as:

$$\mathbf{FC} = \mathbf{SC}\varepsilon \tag{2.26}$$

where **F**, the Fock matrix, is a Hermitian $K \times K$ matrix with the elements:

$$F_{\mu\nu} = \int d\vec{r}_1 \varphi_\mu^*(\vec{r}_1) f(\vec{r}_1) \phi_\nu(\vec{r}_1) \tag{2.27}$$

C, the coefficient matrix, is a Hermitian $K \times K$ matrix, **S**, the overlap matrix, is also a Hermitian $K \times K$ matrix with elements:

$$S_{\mu\nu} = \int d\vec{r}_1 \varphi_\mu^*(\vec{r}_1) \phi_\nu(\vec{r}_1) \tag{2.28}$$

and ε is a $K \times K$ diagonal matrix consisting of orbital energies ε_i. The solution to the Roothan equations is performed through an iterative procedure.

2.1.2.3 Unrestricted Hartree-Fock wavefunctions

With restricted spin orbitals and determinants, the spatial orbitals are constrained to be identical for both α and β spins. In order to allow for spin polarization effects derived

from the interaction of electrons with like spins, it is necessary to permit the spins to occupy different regions of space and treat them individually in the construction of the molecular orbitals; note that while the β orbital may be spatially similar and analogous to the α orbital, it need not be identical. The separation of the two spins into two different determinants leads to the unrestricted Hartree-Fock (UHF) formalism. While the unrestricted wavefunctions allow for spin polarization, they are generally not eigenfunctions of the spin operator $\hat{S}^2$. Additionally, by allowing the spatial parts of the different spin orbitals to differ, the final wavefunction can be contaminated by the inclusion of higher spin states (*e.g.* triplet, pentet, etc. states for singlet wavefunctions and quartet, sextet, etc. states for doublet wavefunctions). While unrestricted singlet wavefunctions frequently collapse to the corresponding restricted singlets, the unrestricted formalism is typically a good approximation for doublets and triplets because unrestricted wavefunctions have lower energies than their restricted counterparts.

2.1.2.4 Post Hartree-Fock methods

Within Hartree-Fock theory, the fundamental assumption is made that each electron moves in a static electric field that is created by all other electrons. Hence, instantaneous electron-electron repulsion processes, or the correlated motions of electrons, are not taken into account. Two post-Hartree-Fock methods that have widely been utilized to address these issues are configuration interaction (CI) and the second-order Møller-Plesset perturbation theory (MP2).

2.1.2.4.1 Configuration interaction

In configuration interaction (CI), the exact wavefunction is represented as a linear combination of *N*-electron trial functions:

$$\left|\phi_0\right\rangle = C_0\left|\psi_0\right\rangle + \sum_{ar} C_a^r\left|\psi_a^r\right\rangle + \sum_{\substack{a<b\\r<s}} C_{ab}^{rs}\left|\psi_{ab}^{rs}\right\rangle + \sum_{\substack{a<b<c\\r<s<t}} C_{abc}^{rsr}\left|\psi_{abc}^{rst}\right\rangle + \sum_{\substack{a<b<c<d\\r<s<t<u}} C_{abcd}^{rstu}\left|\psi_{abcd}^{rstu}\right\rangle + \cdots \quad (2.29)$$

This is the form of the full configuration wavefunction, which represents the exact solution within the Born-Oppenheimer approximation. In practice, the expansion has to be truncated at a certain point (*e.g.*, the second term leading to single configuration interaction [SCI], the third term leading to single and double configuration interaction [SDCI], etc.) resulting in an improved, but not exact, solution to the Schrödinger equation.

2.1.2.4.2 Møller-Plesset perturbation theory

Perturbation theory is applicable when the Hamiltonian of a system can be written as:

$$\hat{H}(\lambda) = \hat{H}_0 + \lambda\hat{H}' \quad (2.30)$$

where the eigenstates and eigenvalues of $\hat{H}_0$ are known and where $\hat{H}'$ is the perturbation; by definition, $\hat{H}'$ is much smaller than $\hat{H}_0$. λ is a parameter that can vary between zero and one. In Møller-Plesset perturbation theory (MPPT), the unperturbed electronic Hamiltonian is defined as the sum of one-electron Fock operators:

$$\hat{H}_0 = \sum_{i=1}^{N} \hat{f}(\vec{x}_i) \tag{2.31}$$

The zeroth-order energy is given by:

$$E^{(0)} = \langle \psi_e | \hat{H}_0 | \psi_e \rangle \tag{2.32}$$

while the first-order energy correction is given by:

$$E^{(1)} = \langle \psi_e | \hat{H}' | \psi_e \rangle \tag{2.33}$$

where the perturbation is given by the difference between the sum of the Fock operators and the real electronic Hamiltonian:

$$\hat{H}' = \hat{H} - \hat{H}_0 = \hat{H} - \sum_{i=1}^{N} \hat{f}(\vec{x}_i) \tag{2.34}$$

Summation of the zeroth-energy and first-order energy correction gives:

$$E^{(0)} + E^{(1)} = \langle \psi_e | \hat{H}_0 | \psi_e \rangle + \langle \psi_e | \hat{H}' | \psi_e \rangle = \langle \psi_e | \hat{H}_0 + \hat{H}' | \psi_e \rangle = \langle \psi_e | \hat{H} | \psi_e \rangle \tag{2.35}$$

which is simply the HF energy.

In order to improve upon the perturbation, a second-order energy correction is made. Application of Brillouin's theorem and Condon-Slater rules reveals that only doubly-excited determinants contribute to the MP2 correction. The second-order correction takes the form:

$$E^{(2)} = \frac{1}{4} \sum_{i>j}^{occ} \sum_{a>b}^{virt} \frac{\left[\langle \chi_i \chi_j | \chi_a \chi_b \rangle - \langle \chi_i \chi_j | \chi_b \chi_a \rangle \right]^2}{(\varepsilon_i + \varepsilon_j) - (\varepsilon_a + \varepsilon_b)} \tag{2.36}$$

where:

$$\langle \chi_i \chi_j | \chi_a \chi_b \rangle = \int \chi_i^*(\vec{x}_1) \chi_j^*(\vec{x}_2) \frac{1}{r_{12}} \chi_a(\vec{x}_1) \chi_b(\vec{x}_2) d\vec{x}_1 d\vec{x}_2 \tag{2.37}$$

$$\langle \chi_i \chi_j | \chi_b \chi_a \rangle = \int \chi_i^*(\vec{x}_1) \chi_j^*(\vec{x}_2) \frac{1}{r_{12}} \chi_b(\vec{x}_1) \chi_a(\vec{x}_2) d\vec{x}_1 d\vec{x}_2 \quad (2.38)$$

In these equations, χ_i and χ_j are occupied spin orbitals, χ_a and χ_b are virtual spin orbitals, and ε_i, ε_j, ε_a, and ε_b are the energies of the respective spin orbitals. The MP2 method scales as K^5 because the integral transformation from the atomic orbital to the molecular orbital basis where the MP2 energies are calculated scales as K^5.

2.1.2.5 Semi-empirical methods

Due to the fact that Hartree-Fock calculations scale formally to the fourth power of the number of basis functions, semi-empirical methods have been introduced early on to reduce the number of integrals and allow for the study of large molecular systems. Semi-empirical methods reduce the computational cost by considering only valence electrons explicitly, utilizing only minimal basis sets, and typically use exponential basis functions in these limited descriptions. The central assumption of semi-empirical methods is the Zero Differential Overlap (ZDO) approximation, which neglects all basis functions depending on the same electron coordinates when located on different atoms. Under the ZDO approximation, the overlap matrix (**S**) is reduced to a unit matrix, all one-electron integrals involving three centers (two from the basis functions and one from the operator) are set to zero, and all three- and four-center two-electron integrals are neglected. The remaining integrals are parameterized based upon assignment on the basis of calculation or experiment to compensate for the approximations.

In the Neglect of Diatomic Differential Overlap (NDDO) method, ZDO is applied exclusively between atomic orbitals centered on distinct atoms. Further parameterizations of the NDDO model lead to the Modified Neglect of Diatomic Overlap (MNDO), Austin Model 1 (AM1), and Modified Neglect of Diatomic Overlap Parametric Number 3 (PM3) methods; the parameterizations employed are only in terms of atomic variables. The three methods differ only in the treatment of core-core repulsions. Of importance in this work is the AM1 method, which was developed in order to address deficiencies of MNDO. In AM1, the core-core function was modified by addition of Gaussian functions to the model, which was then reparameterized. The AM1 method is known to accurately reproduce heats of formation and geometries for a wide variety of organic compounds.

Further approximations to the ZDO are made through both Intermediate and Complete Neglect of Differential Overlap (INDO and CNDO, respectively). In the INDO model, all two-center two-electron integrals that are not of the Coulomb type are neglected. In addition, to preserve rotational invariance, some of the integrals are made independent of the orbital type. In the CNDO approximation, only the Coulomb one-center and two-center two-electron integrals remain. Thus, the main difference between NNDO, INDO, and CNDO methods is the treatment of the two-electron integrals; while CNDO and INDO reduce these to just two parameters, all one- and two-center integrals are kept in the NDDO approximation.

2.1.3 Density Functional Theory

An alternative method to those based upon the Hartree-Fock equations is found within Density Functional Theory (DFT). The basis for DFT is the proof by Hohenberg and Kohn[7] that the ground-state electronic energy of a molecular system is determined completely by the electron density. The important feature of DFT methods is that they take into account electron correlation from the outset, a factor only available in computationally-expensive post-Hartree-Fock methods.

2.1.3.1 Electron and pair densities

The electron density $\rho(\vec{r})$ is defined as a multiple integral over the spin coordinates of all electrons and over all but one of the spatial variables

$$\rho(\vec{r}_i) = N\int\ldots\int\left|\Psi(\vec{x}_1,\vec{x}_2,\ldots,\vec{x}_N)\right|^2 ds_1 d\vec{x}_2\ldots d\vec{x}_N \tag{2.39}$$

where $\rho(\vec{r}_i)$ determines the probability of finding any of the *N* electrons within a volume element $d\vec{r}_i$ but with arbitrary spin while the other *N-1* electrons have arbitrary positions and spin. Note that $\rho(\vec{r})$ vanishes at infinity as well as integrates to the total number of electrons. Additionally, unlike a wavefunction, $\rho(\vec{r})$ is observable.

The pair density $\rho_2(\vec{x}_1,\vec{x}_2)$ allows for the extension of the probability of finding any one electron within a particular volume element to finding a second electron within that same space:

$$\rho_2(\vec{x}_1,\vec{x}_2) = N(N-1)\int\ldots\int|\Psi(\vec{x}_1,\vec{x}_2,\ldots,\vec{x}_N)|^2 d\vec{x}_3\ldots d\vec{x}_N \tag{2.40}$$

$\rho_2(\vec{x}_1,\vec{x}_2)$ is of importance in that it actually contains all information pertaining to electron correlation. For instance, when two electrons have the same spin ($\vec{x}_1 = \vec{x}_2$):

$$\rho_2(\vec{x}_1,\vec{x}_2) = -\rho_2(\vec{x}_1,\vec{x}_2) \tag{2.41}$$

which is only true for $\rho_2(\vec{x}_1,\vec{x}_2) = 0$; thus, the probability of finding two electrons of the same spin at the same point in space is zero. Hence, electrons of like spin do not move independently of each other. This does not hold for electrons of different spins, an effect known as exchange or Fermi correlation; however, this effect is included in the antisymmetry of the Slater determinant.

2.1.3.2 Hohenberg-Kohn theorems

The first Hohenberg-Kohn theorem states that *the external potential $V_{ext}(\vec{r})$ is, within a constant, a unique functional of $\rho(\vec{r})$; since, in turn $V_{ext}(\vec{r})$ fixes the Hamiltonian, the full many-particle ground state is a unique functional of $\rho(\vec{r})$*. In other words, since $\rho(\vec{r})$ uniquely determines the Hamiltonian operator, all properties of the system are determined as well. Thus, the average value of any observable can be written as a functional of the electron density ($\langle A\rangle = A[\rho(\vec{r})]$). The total energy of the electronic system, in much the same way, can be expressed as a functional of the electron density:

$$E_v[\rho] = T[\rho] + E_{eN}[\rho] + E_{ee}[\rho] \tag{2.42}$$

where $T[\rho]$ represents the kinetic energy of the system, and $E_{eN}[\rho]$ and $E_{ee}[\rho]$ are the nuclear-electron and electron-electron electrostatic interactions, respectively. The sum of

the kinetic and the electron-electron terms is called the universal functional of Hohenberg and Kohn:

$$F_{HK}[\rho] = T[\rho] + E_{ee}[\rho] \tag{2.43}$$

Equation 2.43 is the most important equation in DFT; if $F_{HK}[\rho]$ were known exactly, the Schrödinger equation could be solved *exactly*. Within the universal functional, the Coulomb integral $J[\rho]$ can be extracted from the electron-electron term, thus allowing the functional to be written as:

$$F_{HK}[\rho] = T[\rho] + J[\rho] + E_{ncl}[\rho] \tag{2.44}$$

where $E_{ncl}[\rho]$ incorporates the non-classically defined electron-electron interactions of self-interaction, exchange, and electron correlation effects. Note that only $J[\rho]$ is known.

The second Hohenberg-Kohn theorem states that $F_{HK}[\rho]$ *delivers the lowest energy if and only if the input density is the true ground-state density,* ρ_0. In essence, the second theorem is a restatement of the variational principle, which in the current context, can be written as:

$$E_0 \leq E_v[\rho] = T[\rho] + E_{eN}[\rho] + E_{ee}[\rho] \tag{2.45}$$

It is important to note that in order to find ρ_0, one must look at all wavefunctions associated to ρ_0 and select that for which $E_{\Psi \to \rho_0}$ is lowest. Since it is impossible to access all wavefunctions, there is no way to identify the correct wavefunction; hence, it is reasonable to assert that there is no wavefunction in DFT. Though the correct wavefunction is not accessible, a related wavefunction exists that can be used for qualitative interpretation.

2.1.3.3 The Kohn-Sham equations

Within the variational principle of the second Hohenberg-Kohn theorem, a difficulty arises in that any candidate Hamiltonian needs to account for the various electron-electron interactions. In order to circumvent this difficulty, Kohn and Sham hypothesized that the Hamiltonian would be simpler if it were one for a system of non-interacting electrons that has the same density of some system where the electrons do interact. For such a system of non-interacting electrons, the kinetic energy is the sum of the individual electronic kinetic energies:

$$T_S = -\frac{1}{2}\sum_i^N \langle \phi(\vec{x}_i) | \nabla^2 | \phi(\vec{x}_i) \rangle \tag{2.46}$$

where $\phi(\vec{x}_i)$ are Kohn-Sham (KS) orbitals (in complete analogy to HF orbitals) that are components of a Slater determinant that represents the ground-state wavefunction:

$$\Theta_S(\vec{x}_1, \vec{x}_2, \ldots \vec{x}_N) = (N!)^{-1/2} \begin{vmatrix} \phi_1(\vec{x}_1) & \phi_2(\vec{x}_1) & \cdots & \phi_N(\vec{x}_1) \\ \phi_1(\vec{x}_2) & \phi_2(\vec{x}_2) & \cdots & \phi_N(\vec{x}_2) \\ \cdots & \cdots & \ddots & \vdots \\ \phi_1(\vec{x}_N) & \phi_2(\vec{x}_N) & \cdots & \phi_N(\vec{x}_N) \end{vmatrix} \tag{2.47}$$

The KS orbitals are related to the ground-state density of the real interacting electrons through:

$$\rho_S(\vec{r}) = \sum_i^N \sum_S |\phi_i(\vec{r}, s)|^2 = \rho_O(\vec{r}) \tag{2.48}$$

Note that the KS orbitals and their eigenvalues, in the strictest sense, have no physical significance; the only connection to physical reality is that the sum of the orbitals squared adds up to the exact density.

Though the kinetic energy expression for the non-interacting reference system has the same density as the real, interacting one, the non-interacting kinetic energy does not equal the true kinetic energy. Kohn and Sham accounted for the discrepancy by re-expressing the universal equation as:

$$F[\rho] = T_S[\rho] + J[\rho] + E_{XC}[\rho] \tag{2.49}$$

where $E_{XC}[\rho]$, the *exchange-correlation energy*, incorporates both the residual part of the true kinetic energy $T_C[\rho]$ and the non-classical electrostatic interactions and is defined as:

$$E_{XC}[\rho] \equiv (T[\rho] - T_S[\rho]) + (E_{ee}[\rho] - J[\rho]) = T_C[\rho] + E_{ncl}[\rho] \tag{2.50}$$

Thus, the total energy for the system can be expressed as:

$$E[\rho] = T_S[\rho] + J[\rho] + E_{eN}[\rho] + E_{XC}[\rho] \tag{2.51}$$

With the introduction of orbitals, the minimized energy can be found through solving the pseudo-eigenvalue equation:

$$\hat{h}_i^{KS}\phi_i = \varepsilon_i\phi_i \tag{2.52}$$

where the one-electron KS operator is defined as:

$$\hat{h}_i^{KS} = -\frac{1}{2}\nabla_i^2 - \sum_A^M \frac{Z_A}{r_{1A}} + \int \frac{\rho(\vec{r}_2)}{r_{12}} d\vec{r}_2 + V_{XC}(\vec{r}_1) \tag{2.53}$$

and

$$V_{XC} \equiv \frac{\delta E_{XC}}{\delta \rho} \tag{2.54}$$

V_{XC} is the exchange-correlation potential which is best described as the one-electron operator for which the expectation value of the KS Slater determinant is E_{XC}; because it is not known how to express $E_{XC}[\rho]$, there is no explicit form for V_{XC}.

2.1.3.4 Approximate exchange-correlation functionals

In order to make DFT a viable option for electronic-structure calculations, reasonable approximations need to be made for a form of the exchange-correlation energy. Due to the fact that the form of the exact exchange-correlation functional is unknown, there is no real guidance in the search for approximate forms. To date, the three most commonly used approximations are the localized density approximation, generalized gradient approximation, and the formation of hybrid functionals through the incorporation of part of the exact HF exchange in the DFT functionals.

One note, however, on the role of approximate functionals and the concept of self-interaction. The classical electrostatic repulsion term

$$J[\rho] = \iint \frac{\rho(\vec{r}_1)\rho(\vec{r}_2)}{r_{12}} d\vec{r}_1 d\vec{r}_2 \tag{2.55}$$

does not completely vanish for a one-electron system because the density interacts with itself. This can be nullified, however, by setting $E_{XC}[\rho]$ exactly minus $J[\rho]$. However, since $E_{XC}[\rho]$ is never exact and independent of $J[\rho]$, then the above relation should not be expected to hold. Thus, there will generally be residual energy due to self-interaction effects.

2.1.3.4.1 Local density approximation (LDA)

Virtually all exchange-correlation functionals are based upon the notion of a uniform electron gas. Electrons move on a positive background charge distribution such that the total ensemble is electrically neutral; the number of electrons, as well as the volume of the gas, is allowed to approach infinity, while the electron density is finite. Such a model allows for E_{XC} to be written as:

$$E_{XC}^{LDA}[\rho] = \int \rho(\vec{r})\varepsilon_{XC}\rho(\vec{r})d\vec{r} \tag{2.56}$$

where ε_{XC} is the exchange-correlation energy per particle of a uniform electron gas of density $\rho(\vec{r})$. This definition for E_{XC} is known as the local density approximation (LDA). We note that the unrestricted case can be developed through the introduction of spin into Equation 2.56; this is known as the local spin-density approximation (LSDA). The term ε_{XC} can be segmented into exchange and correlation contributions:

$$\varepsilon_{XC}(\rho(\vec{r})) = \varepsilon_X(\rho(\vec{r})) + \varepsilon_C(\rho(\vec{r})) \tag{2.57}$$

The exchange portion is generally expressed as:

$$\varepsilon_X(\rho(\vec{r})) = -\frac{3}{4}\sqrt[3]{\frac{\rho(\vec{r})}{\pi}} \tag{2.58}$$

and is, apart from a pre-factor, equal to the form used in HF theory. As for the correlation contribution, no such explicit expression is known, with analytical expressions typically derived from highly accurate simulations of a homogeneous electron gas.

2.1.3.4.2 Generalized gradient approximation (GGA)

In a molecular system, the electron density is typically not spatially uniform. To improve upon this limitation in the LDA/LSDA approach, information pertaining to the gradient of the charge density $\nabla\rho(\vec{r})$ is supplemented to the density $\rho(\vec{r})$ at a particular point $\vec{r}$. Such an approach is known as either gradient corrected (GCA) or generalized gradient approximation (GGA). In general, GGA functionals are constructed with a correction added to the original LDA/LSD term:

$$\varepsilon_{X/C}^{GGA}\left[\rho(\vec{r})\right] = \varepsilon_{X/C}^{LDA/LSDA}\left[\rho(\vec{r})\right] + \Delta\varepsilon\left[\frac{\nabla\rho(\vec{r})}{\rho^{4/3}(\vec{r})}\right] \tag{2.59}$$

where the subscript *x/c* indicates that the same functional form holds for either exchange or correlation.

In principle, any exchange and correlation functionals developed under the GGA formalism can be added together to form the full exchange-correlation functional:

$$E_{XC}^{GGA} = E_{X}^{GGA} + E_{C}^{GGA} \tag{2.60}$$

The most popular GGA exchange functional was developed by Becke (often denoted B or B88),[8] which has the correct asymptotic behavior at long range for the energy density. Popular correlation functionals include those developed by Perdew (P86),[9] Perdew and Wang (PW91),[10] and Lee, Yang, and Parr (LYP).[11]

2.1.3.4.3 Hybrid functionals

In general, exchange contributions are significantly larger than correlation effects; thus, an accurate expression for the exchange energy is a requirement for a meaningful exchange-correlation functional. Thus, a direct means of obtaining an accurate exchange-correlation energy is to use the exact HF exchange expression and approximate only the electron correlation:

$$E_{XC} = E_X^{exact} + E_C^{KS} \tag{2.61}$$

Such an expression is known as a hybrid functional, since it incorporates both HF and DFT energies. Though such a function works well for atoms, the artificial splitting of the exchange and correlation terms breaks down in terms of molecular systems; this is due to the fact that the separation of the terms does not represent the dependence of each term on the other. A more reasonable means to express the exchange-correlation energy is

$$E_{XC} = aE_X^{HF} + (1-a)E_{XC}^{KS} \tag{2.62}$$

where a is a constant that varies between zero and one. For instance, if a = 0.5, then the functional is known as 'half and half' (H and H).

It is within this manner that one of the more popular exchange-correlation functionals in current use, and one that is used predominately throughout the remainder of this text, was constructed – the three-parameter B3LYP functional:[11-14]

$$E_{XC}^{B3LYP} = (1-a)E_X^{LSDA} + aE_X^{HF} + b\Delta E_X^B + (1-c)E_C^{LSDA} + cE_C^{LYP} \tag{2.63}$$

which incorporates the exact HF exchange, exchange and correlation terms derived from LSDA, and the Becke exchange and LYP correlation terms; the values optimized for a, b,

and *c* are 0.20, 0.72, and 0.81, respectively.[12] In addition to the three-parameter B3LYP functional, there are numerous other parameter and parameter-free hybrid methods available. It is important to note that the parameters utilized in the above expression are derived from atomization and ionization energies and proton and electron affinities computed within 1 kcal/mol of experimental results for 125 reference molecules containing main group elements in the Gaussian-2 (G2) model database; thus, there is clearly some semi-empirical nature in hybrid functionals.

2.1.3.5 Time-dependent density functional theory

Excitation energies within the DFT methodology are determined through time-dependent DFT (TDDFT). TDDFT employs the fact that the frequency-dependent linear response of a finite system with respect to a time-dependent perturbation has discrete poles at the exact, correlated excitation energies of the unperturbed system. In the KS formalism, the orbital eigenvalue differences of the ground state act as a first approximation to the excitation energies. TDDFT is usually most successful for low-energy excitations, because the high-lying KS virtual orbitals are typically poor.

2.1.4 Basis sets

As expressed above, a linear combination of different basis functions is used to represent the different molecular orbitals. Thus, the quality of a calculation depends upon the

number of basis functions used. Expansion of an unknown function is not an approximation if the basis set chosen is complete; however, a complete basis set requires an infinite number of functions to be used, which is impossible in actual calculations. In general, the smaller the basis, the poorer the representation; however, if the type of basis functions is able to accurately reproduce the unknown function, then fewer basis functions may be used for achieving a given level of accuracy.

2.1.4.1 Slater and Gaussian type orbitals

Two types of orbitals are typically used in electronic-structure calculations. The first, Slater-Type Orbitals (STOs), have the form:

$$\chi_{\zeta,n,l,m}(r,\theta,\varphi) = NY_{l,m}(\theta,\varphi)r^{n-1}e^{-\zeta r} \tag{2.64}$$

where N is a normalization constant and $Y_{l,m}$ are spherical harmonic functions. Gaussian-Type Orbitals (GTOs) can be written in terms of both polar and Cartesian coordinates:

$$\chi_{\zeta,n,l,m}(r,\theta,\varphi) = NY_{l,m}(\theta,\varphi)r^{(2n-2-l)}e^{-\zeta r^2} \tag{2.65}$$

$$\chi_{\zeta,l_x,l_y,l_z}(x,y,z) = Nx^{l_x}y^{l_y}z^{l_z}e^{-\zeta r^2} \tag{2.66}$$

where the sum of l_x, l_y, and l_z determine the type of orbital. Note that though the equations of the two GTO coordinate systems appear similar, the number of components produced can differ, *e.g.*, a d-type GTO written in terms of spherical coordinates has five components while Cartesian coordinates have six; in general, the six Cartesian components can be transformed into five spherical d-type functions and one additional s-type function. Versus their STO counterparts, GTOs have two complicating factors due to

the r^2-dependence. First, at the nucleus, GTOs have zero slope versus the 'cusp' of the STO, thus GTOs have difficulty representing the behavior of the wavefunction near the nucleus. Second, GTOs fall off too rapidly at distances far from the nucleus. In order to overcome these issues, additional GTOs are necessary to achieve the same level of accuracy as STOs. However, the ease by which the GTOs can be integrated (the product of two Gaussians being a Gaussian) compensates for the addition of functions to improve the accuracy.

In practice, basis functions near the core of the nucleus are important for the description of the energetics of the system. However, these functions play little role in describing the chemical phenomena for which the calculations are of interest; the important chemical region is in the outer valence. In order to gain accurate insight into both the energetic and chemical parameters, several GTOs are combined to form contracted GTOs (CGTOs). As the core orbitals change little upon different bonding situations, the variational constants in front of these inner basis functions are fixed, *i.e.*, held constant. This allows for the remaining functional variability to be spent on the description of the valence orbitals.

2.1.4.2 Basis set nomenclature

A minimal basis set is one that uses one basis function per atomic orbital of the electronic shells occupied in the free atom. Improvement upon this rather simplistic model is made through a double-zeta basis set; the term *zeta* arises from the Greek notation used for the

exponent in the STO and GTO functions (denoted ζ). A double-zeta basis set employs two basis functions per atomic orbital. Further extension of the basis sets is done through triple-zeta, quadruple-zeta, quintuple-zeta, etc. basis sets. In addition to the incorporation of more functions per atomic orbital, split-valence basis sets employ extra functions for each valence orbital, *e.g.*, the split-valence double-zeta basis sets, which are now routinely used, employ one basis function per core atomic orbital and two basis functions per valence orbital.

Basis sets can also be extended through the addition of polarization and diffuse functions. Atomic orbitals often become distorted (polarized) under the influence of other atoms within a molecular system. To account for these effects, polarization functions (often denoted '*') with higher angular momentum terms are added to the basis sets. Diffuse functions, *i.e.*, basis functions with small exponents (often denoted '+'), are added to account for properties that extend far away from the atomic nucleus, *e.g.*, for the proper description of loosely bound electrons in radical anions and molecular polarizability (dependent on the wavefunction tail). Thus, variations in the combination of these functions provide the ability to create the diverse assortment of basis sets utilized throughout the literature, including such examples as 3-21G, 6-31G*, 6-31+G*, 6-311G**, etc.

2.1.5 Software

At this time, we note that it is not the intent of the work that follows to either improve or implement the electronic-structure methodology described above. Therefore, the electronic-structure methods discussed throughout the remainder of this Dissertation are used as implemented in the following commercially-available software packages: Gaussian98 (Revision A.11) [HF, MP2, AM1, INDO, ZINDO/CIS, DFT, TDDFT] ;[15] AMPAC 6.55 [AM1, AM1/CI];[16] and TURBOMOLE 5.6 [DFT, TDDFT].[17]

2.2 Electron-transfer theory

We now delve into the basics of electron-transfer theory with an emphasis on self-exchange reactions. Though electron transfer is one of the most ubiquitous chemical reactions, it can also be one of the most complex. There are, in general, three electron transfer processes of chemical interest: i) thermally-activated electron transfer through the crossing region; ii) optical electron transfer occurring vertically from the equilibrium configuration of the initial state; and iii) photo-initiated electron transfer involving charge separation and charge recombination;[18] the first two are of interest in this work and are expanded somewhat further. We assume throughout that the reactions described herein fall within the weak electronic-coupling regime.

2.2.1 Thermally-activated electron transfer

Electron transfer initiates a change in chemical structure.[19] For a one-electron transfer between a donor (*D*) and an acceptor (*A*):

$$D^- + A \rightarrow D + A^- \tag{2.67}$$

we can depict the reactant and product sides of the chemical reaction as non-interacting diabatic states (Ψ_R and Ψ_P, respectively) under the harmonic approximation; note that these states are never uniquely defined and generally correspond to charge-localized structures.[18] The potential energy surfaces under the parabolic approximation, thusly, can be expressed as:

$$V_R = \frac{1}{2} f (q - q_R)^2 \tag{2.68}$$

$$V_P = \frac{1}{2} f (q + q_P)^2 + \Delta G^\circ \tag{2.69}$$

where f is the force constant (which is assumed to be equal for the reactants and products), ΔG° is the standard free energy of the reaction, and q_R and q_P are the minima locations for the reactant and product diabatic curves, respectively, see Figure 2.1. Though the potential surfaces are rather simple functions of vibrational coordinates, they are complicated functions of the numerous solvent coordinates in the many-coordinate dimensional space.[20] Additionally, the potential energy surfaces are uniquely defined for any set of physical displacements within the system of interest.

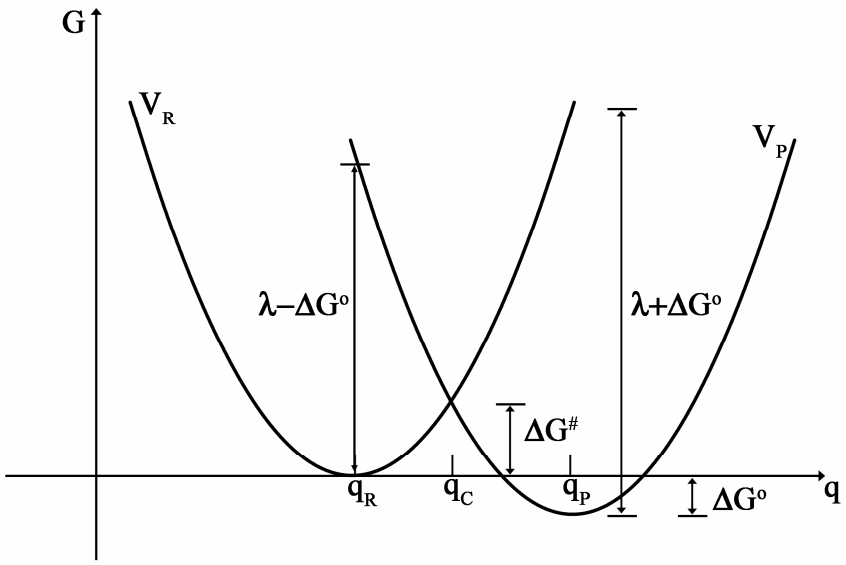

Figure 2.1 Electron transfer reaction depicted by diabatic potential energy curves.[19]

At the crossing point (q_C) of the potential surfaces,

$$V_R(q_C) = V_P(q_C) \tag{2.70}$$

which represents the coordinate position of the free energy barrier $\Delta G^{\#}$ for the electron-transfer reaction, which can be defined as:

$$\Delta G^{\#} = \frac{1}{2} f(q_C - q_R)^2 \tag{2.71}$$

Using the definition of the potential energy curves:

$$\frac{1}{2} f(q_C - q_R)^2 = \Delta G° + \frac{1}{2}(q_C + q_P)^2 \tag{2.72}$$

We solve for the crossing point:

$$q_C = \frac{\Delta G°}{f}\left(\frac{1}{q_P - q_R}\right) + \frac{(q_P - q_R)}{2} \tag{2.73}$$

It is important at this time to define λ, known as reorganization energy, by:

$$\lambda = \frac{1}{2} f\left(q_R - q_P\right)^2 \tag{2.74}$$

The reorganization energy increases with increasing separation between the diabatic minima.

As mentioned earlier, the free energy barrier $\Delta G^{\#}$ is defined at the crossing point. Substitution of q_C into the free energy barrier expression gives:

$$\Delta G^{\#} = \frac{1}{4\lambda}\left(\lambda + \Delta G^{\circ}\right)^2 \tag{2.75}$$

Substitution of the free energy barrier expression into the Arrhenius equation for the reaction rate constant gives:

$$k_{ET} = A \exp\left(\left[-\frac{\left(\lambda + \Delta G^{\circ}\right)^2}{4\lambda k_B T} \right]\right) \tag{2.76}$$

where A is the Arrhenius pre-exponential factor, k_B is the Boltzmann constant, and T is the temperature. This expression was first postulated by R.A. Marcus in his seminal work in 1956;[21] it is for this expression and subsequent work that R.A. Marcus won the Nobel Prize in Chemistry in 1992.[20]

2.2.2 Reorganization energy

The reorganization energy is composed of both a solvation (λ_o) and intramolecular (λ_i) component:

$$\lambda = \lambda_o + \lambda_i \tag{2.77}$$

The role of the solvent in electron-transfer reactions is rather complex. The influence that can be imparted by the surrounding media on the electron-transfer rate can be viewed as both long range (*e.g.*, dielectric continuum) and short range (*e.g.*, hydrogen bonding).[18] In the original model proposed by Marcus[20] to handle the surrounding medium, which was developed under the dielectric continuum approximation, the solvent reorganization is written as:

$$\lambda_0 = (\Delta e)^2 \left[\frac{1}{2a_1} + \frac{1}{2a_2} - \frac{1}{R} \right] \left[\frac{1}{\varepsilon_\infty} - \frac{1}{\varepsilon_0} \right] \tag{2.78}$$

where a_1 and a_2 are the ionic radii of the donor and acceptor, R is the center-to-center distance of the reactants, Δe is the amount of charge transferred, and ε_∞ and ε_0 are the optical and static dielectric constants of the solvent, respectively. Though useful, the dielectric continuum model can be problematic due to the neglect of the properties of the individual solvent molecules, *e.g.*, polarization, volume, etc.[19] Other models based upon both spherical and elliptical cavities, in which the charge distributions are placed in dielectric cavities, are having some success. Direct calculations of free energies using the Onsager/Kirkwood cavity models have shown that λ_o is strongly distance dependent, larger for anions versus cations, and sensitive to conformational and geometric changes.[19]

The intramolecular reorganization energy, λ_i, combines the relaxation energies of the electron-donor molecule (λ_D) and of the electron-acceptor molecule (λ_{A^-}), see Figure 2.2, upon the electron-transfer reaction. Assuming in this instance the transfer of an electron from donor to acceptor, the electron-transfer process can be formally divided into two processes: i) simultaneous oxidation of the donor and reduction of the acceptor

through a vertical process from the initial states of the reactants, and ii) subsequent relaxation to the product nuclear geometries. It is important to note that both the Franck-Condon principle and energy conservation principle should be satisfied for electron transfer to occur.[22]

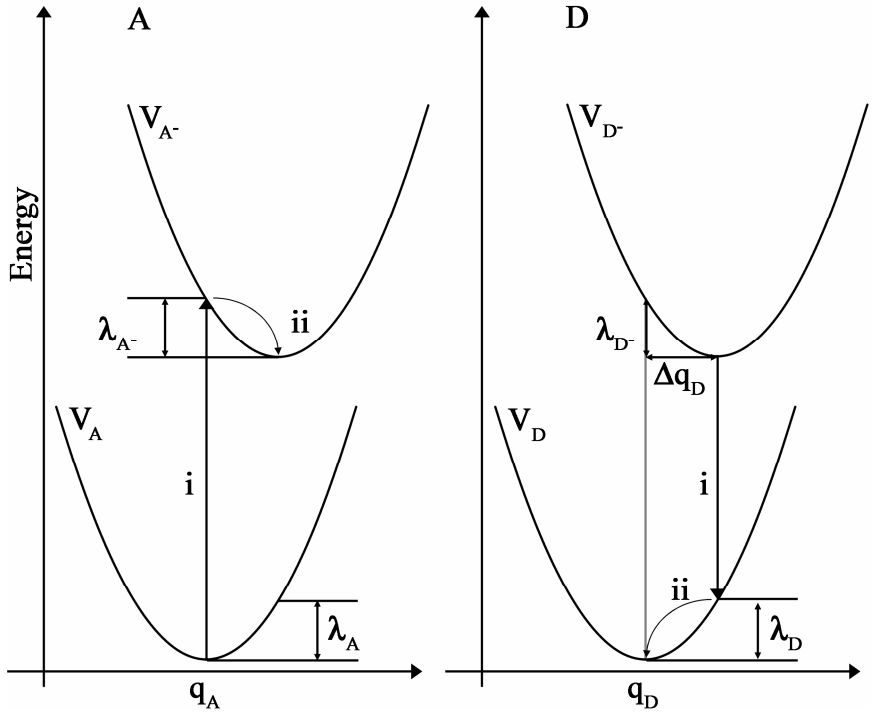

Figure 2.2 Sketch of the potential energies of electron-acceptor (*A*) and electron-donor (*D*) species in an electron-transfer process, illustrating the acceptor (λ_{A^-}) and donor (λ_D) relaxation energies.[22]

2.2.3 Quantum-mechanical modifications

One of the problems with the classical picture depicted above is that it cannot account for electron transfer at very low temperatures. The problem arises from the fact that the quantum-mechanical tunneling through the free energy barrier is not accounted for in the original representation. The extent to which tunneling plays a role depends upon the amount of vibrational overlap between the initial and final states and the extent of electronic coupling.[19]

The probability for a transition from a discrete initial state to a discrete final state in accordance to first-order perturbation theory is given by:

$$P_{RP} = \frac{1}{\hbar^2}\left|\left\langle \Psi_R \middle| \hat{H} \middle| \Psi_P \right\rangle\right|^2 \left[\frac{\sin(\omega_{RP} t/2)}{\omega_{RP}/2}\right] \tag{2.79}$$

where H is the system Hamiltonian, $\hbar\omega_{RP}$ is the transition energy between the initial and final states (*e.g.*, reactant and product states), and t is the time.[22] In order to account for the continuous distribution of final, vibrationally coupled, electronic states, the probability can be recast in the form of the density of states $\rho(E_A)$ and summed over all probabilities. Assuming that $\left\langle \Psi_R \middle| \hat{H}' \middle| \Psi_P \right\rangle \rho(E_A)$ varies slowly with energy, the transition probability takes on the Golden Rule form:

$$k_{ET} = \frac{2\pi}{\hbar}\left|\left\langle \Psi_R \middle| \hat{H} \middle| \Psi_P \right\rangle\right|^2 \rho(E_A) \tag{2.80}$$

Noting that vibrational motions drive reactions, and recasting the initial and final states in terms of reactants and products, we arrive at the semi-classical Marcus equation:

$$k_{ET} = \frac{2\pi}{\hbar}\left|H_{RP}\right|^2 (FCWD) \tag{2.81}$$

where $H_{RP} = \left\langle \Psi_R \middle| \hat{H} \middle| \Psi_P \right\rangle$ is the electronic coupling matrix and *FCWD* denotes the Franck-Condon-weighted density of states. In the high-temperature regime, the *FCWD* obey a standard Arrhenius-type equation:

$$FCWD = \sqrt{\frac{1}{4\pi\lambda k_B T}} \exp\left[-\frac{(\lambda + \Delta G^\circ)^2}{4\lambda k_B T} \right] \tag{2.82}$$

When the reorganization energy is cast into both classical modes for the surrounding medium and intramolecular high-frequency quantum modes, the Bixon and Jortner model[23] expresses the rate as:

$$k_{ET} = \frac{2\pi}{\hbar}\left|H_{RP}\right|^2 \sqrt{\frac{1}{4\pi\lambda_0 k_B T}} \sum_{n=0}^{\infty} \exp(-S_i)\frac{S_i^n}{n!} \exp\left[-\frac{(\lambda_0 + \Delta G^\circ + n\hbar\omega_i)^2}{4\lambda_0 k_B T} \right] \tag{2.83}$$

where a single effective quantum mode ω_i is assumed to contribute to λ_i.[22] Note that the electronic coupling element H_{RP} is predicted to falloff exponentially with distance because of the exponential character of the radial part of the wavefunctions through the relationship:

$$H_{RP} = V_0 \exp\left[-\beta \frac{(R - R_0)}{2} \right] \tag{2.84}$$

where V_0 is the electronic coupling matrix element at van der Waals radius R_0 and β is a constant that determines the rate of falloff.[19] The dimensionless Huang-Rhys factor, *S*, which is a measure of the electron-vibrational coupling, is defined as:

$$S_i = \frac{\lambda_i}{\hbar\omega_i} \tag{2.85}$$

In general, only a few modes can be treated; thus, vibrations in a given range are averaged to give an averaged mode of *S*:

$$S = \sum_i S_i \tag{2.86}$$

with an effective frequency:[19]

$$\hbar\omega = \frac{\sum_i S_i \hbar\omega_i}{\sum_i S_i} \tag{2.87}$$

2.2.4 Adiabatic and nonadiabatic régimes

In the weak electronic-coupling limit, the electronic coupling of arbitrary strength falls within the non-adiabatic (very weak coupling) and adiabatic regimes (stronger coupling), see Figure 2.3.[24] The quantum-mechanically-modified Arrhenius expression for electron-transfer rate constant can be re-expressed as:

$$k_{ET} = \kappa_{el} \nu_n \exp\left(-\frac{\Delta G^{\#}}{k_B T}\right) \tag{2.88}$$

where κ_{el} is the electronic transmission coefficient and ν_n is the nuclear vibration frequency that takes the system from reactants to products through the crossing point.[25] In the framework of Landau-Zerner theory, the electronic transmission coefficient is given by:[25]

$$\kappa_{el} = \frac{1 - \exp\left(-\nu_{el} / 2\nu_n\right)}{1 - \frac{1}{2}\exp\left(-\nu_{el} / 2\nu_n\right)} \tag{2.89}$$

where the electron hopping frequency ν_{el} is

$$\nu_{el} = \frac{2\pi}{\hbar}|H_{DA}|^2 \sqrt{\frac{1}{4\pi\lambda k_B T}} \tag{2.90}$$

Taking the inverse of ν_n and ν_{el} gives vibrational and electronic characteristic times, t_n and t_{el}, respectively. The two limits $t_n >> t_{el}$ and $t_{el} >> t_n$ are referred to as the adiabatic

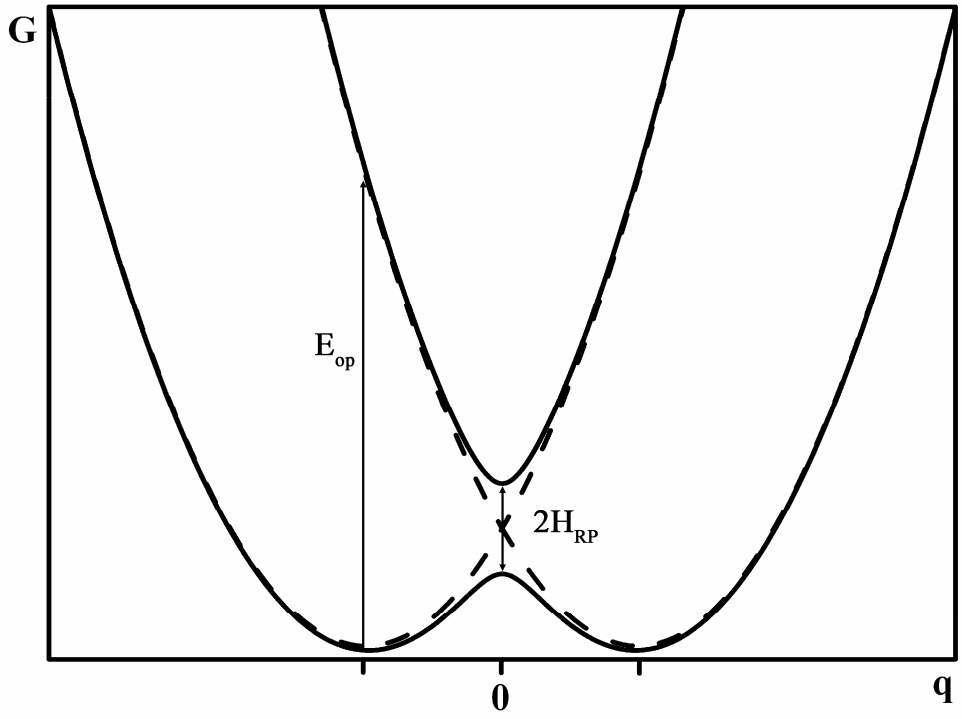

Figure 2.3 Transition from diabatic [dashed] to (non-)adiabatic [solid] potential energy surfaces for a self-exchange reaction. When the coupling between the two states is zero, the electron transfer occurs between the two diabatic states. In the weak-coupling regime, non-adiabatic (very weak coupling) processes generally requires movement between both lower and upper surfaces, while adiabatic (stronger coupling) electron transfers follow only the lower surface.

and non-adiabatic régimes.[25] In the adiabatic régime, the electronic states are localized over the donor-acceptor complex and the electron transfer occurs solely along the lower

potential surface, generally in a broad reaction zone.[24] In the non-adiabatic limit, the vibrational motion is much faster than the electron motion, and the motion through the crossing point is so fast that the electronic wavefunction does not have enough time to move completely from the donor to the acceptor.[25] Non-adiabatic dynamics intrinsically involve more than one energy surface and generally occur suddenly in a narrow reaction zone during relatively rare events; the system either hops between diabatic states or can progress along the lower surface over the crossing point.[24]

2.2.5 Inverted region

One of the original hypotheses of Marcus[20] that took a great deal of time to observe experimentally dealt with the concept of the "inverted" region. Chemical intuition holds that as the driving force of a reaction, in this case the standard free energy (ΔG°), is increased then the reaction rate should increase. Indeed, Marcus theory predicts that in the "normal" region (I in Figure 2.4), where the reorganization energy (λ) is greater than the absolute value of the standard free energy ($|\Delta G^\circ|$), that there should be an increase in the reaction rate. This continual increase in reaction rate continues to the maximum point at which $\lambda = |\Delta G^\circ|$ (II in Figure 2.4); at this point, the activation energy ($\Delta G^\#$) is zero. Continuing the increase in driving force past this point, however, leads to an actual decrease in the reaction rate (III in Figure 2.4); III is known as the "inverted" region. As can be seen in Equations 2.75 and 2.76, a standard free energy of reaction larger than the reorganization energy leads to the reemergence of an activation energy and subsequent decrease in electron-transfer rate. The inclusion of Franck-Condon factors in the rate

constant allows for quantum-mechanical tunneling that avoid this classical activation barrier; these tunneling processes allow reactions in the "inverted" region to become effectively activationless.[18]

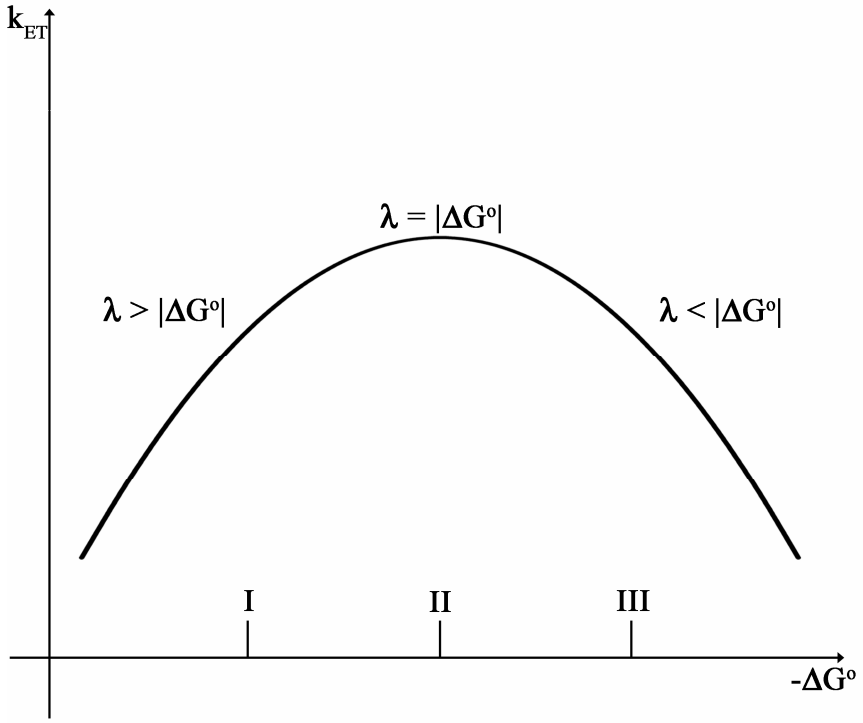

Figure 2.4 Diagram of k_{ET} versus -ΔG° depicting the normal (I) and inverted (III) regions. The peak of curve (II) represents the equivalence point of λ and |ΔG°|.

2.2.6 Optical electron-transfer processes

Optical electron transfer is related to thermally-activated electron transfer through the assumption that the electronic coupling matrix element H_{RP} is the same for both

processes. Through perturbation theory arguments, Hush determined that the energy at the maximum of the charge-transfer band (E_{op}), see Figure **2.3**, due to the transfer of an electron in the weak electronic-coupling régime is equal to the Marcus reorganization energy:

$$E_{op} = h\nu_{\max} = \lambda \tag{2.91}$$

and the intensity of the transition is related to the electronic coupling by:

$$H_{RP} = \frac{0.0206}{r}\left(\nu_{\max}\varepsilon_{\max}\nu_{1/2}\right)^{1/2} \tag{2.92}$$

where *r* is the effective distance between the donor and acceptor (in Å), $\varepsilon_{\max}$ is the molar extinction coefficient (in M^{-1} cm^{-1}), and $\nu_{1/2}$ is the full-width at half-maximum (in cm^{-1}); H_{RP} and $\nu_{\max}$ are also in cm^{-1}. The photon energy is used to balance the electronic mismatch associated with the vertical transition from equilibrium. Through the dipole moment operator $\hat{\mu}$, the electronic coupling element may be expressed as:

$$H_{RP} = \frac{\left|\hat{\mu}_{12}\right|E_{op}}{\Delta\hat{\mu}_{RP}} \tag{2.93}$$

where $\hat{\mu}_{12}$ is the adiabatic transition dipole moment and $\Delta\hat{\mu}_{RP}$ is the change in diabatic state dipole moments;[18] this expression is termed the Generalized Mulliken-Hush equation. Defining the effective donor-acceptor distance *r* as:

$$r = \left|\frac{\Delta\hat{\mu}_{RP}}{e}\right| \tag{2.94}$$

where *e* is the amount of charge transferred, the electronic coupling can be re-expressed:

$$H_{RP} = \frac{\left|\hat{\mu}_{12}\right|E_{op}}{er} \tag{2.95}$$

This equation has been further generalized through the expression of $\Delta\hat{\mu}_{RP}$ entirely in terms of the matrix elements of the dipole moment of the adiabatic basis:

$$\left|\Delta\hat{\mu}_{RP}\right| = \left[\left(\Delta\hat{\mu}_{12}\right)^2 + 4\left(\hat{\mu}_{12}\right)^2\right]^{1/2} \tag{2.96}$$

to give:[26]

$$H_{RP} = \frac{\left|\hat{\mu}_{12}\right| E_{op}}{\left[\left(\Delta\hat{\mu}_{12}\right)^2 + 4\left(\hat{\mu}_{12}\right)^2\right]^{1/2}} \tag{2.97}$$

Thus, all components of the electronic coupling element can be determined from both theoretical calculations and adiabatic observables.

2.3 Two-state, two-mode vibronic-coupling model

The intervalence charge-transfer band in mixed-valence compounds cannot be attributed to the individual components of the molecular system or the bridging ligands; instead, the band is associated with electron transfer arising from the coupling of the redox sites.[27] Through the Hush model and the Generalized Mulliken-Hush equation for optical electron transfer (*vide supra*), the intervalence band allows for the direct estimation of the electronic coupling element and the intramolecular reorganization energy components of the Marcus equation.[28] However, the Mulliken-Hush model is inapplicable to mixed-valence systems that are intermediate between Class II and Class III; the failure arises from the breakdown of the Born-Oppenheimer approximation when both electronic and vibronic coupling terms are strong.[28] Thus, a vibronic model is needed in order to overcome the deficiency. In the following, we focus on a two-electron-state, Ψ_+ and Ψ_-,

one-electron model that is derived from molecular orbital theory.[27] Though the original the Piepho-Krausz-Schatz (PKS) model[29] was cast in the valence-bond approach, the two models have been shown to be equivalent for both one- and two-electron-transfer cases.[30]

2.3.1 Vibronic Hamiltonian

The full molecular Hamiltonian introduced in Equation 2.2 can be rewritten simply as:

$$\hat{H} = \hat{H}_e + T_Q + V(r,Q) \tag{2.98}$$

where $\hat{H}_e$ is the electronic Hamiltonian, T_Q is the kinetic energy of the nuclei, and $V(r,Q)$ is the operator for electron-nuclear interactions and inter-nuclear repulsions with electron r and nuclear Q coordinates. Performing a Taylor expansion on the operator $V(r,Q)$ using the normal coordinates Q_α gives:

$$V(r,Q) = V(r,Q_0) + \sum_\alpha \left(\frac{\partial V}{\partial Q_\alpha}\right)_{Q_0} + \frac{1}{2}\sum_{\alpha\beta}\left(\frac{\partial V^2}{\partial Q_\alpha \partial Q_\beta}\right)_{Q_0} \tag{2.99}$$

where Q_0 is the reference geometry and refers to the symmetric nuclear configuration of the molecule. The linear vibronic interaction is defined by the matrix elements of the second term in Equation 2.99

$$l_\alpha^i = \left\langle \Psi_i \left| \frac{\partial V}{\partial Q_\alpha} \right| \Psi_i \right\rangle \tag{2.100}$$

$$l_\alpha^{ij} = \left\langle \Psi_i \left| \frac{\partial V}{\partial Q_\alpha} \right| \Psi_j \right\rangle \tag{2.101}$$

where l_α^i and l_α^{ij} are the diagonal and off-diagonal linear vibronic constants, respectively.[28] Through selection rules, the diagonal vibronic coupling constant is a function of totally symmetric vibrations only, while the off-diagonal term is a function of antisymmetric vibrations.[27]

Considering a simple two-mode model where Q_+ and Q_- represent single symmetric and antisymmetric modes, respectively, the vibronic Hamiltonian can be written as:

$$\hat{H}_{vib} = \begin{pmatrix} T_{Q_+} + T_{Q_-} + \frac{1}{2}\left(k_- Q_-^2 + k_+ Q_+^2\right) & l_- Q_- \\ l_- Q_- & T_{Q_+} + T_{Q_-} + \frac{1}{2}\left(k_- Q_-^2 + k_+ Q_+^2\right) + \Delta + l_+ Q_+ \end{pmatrix} \quad (2.102)$$

where k_+ and k_- are the force constants (assumed to be the same for the two electronic states).[28] The energy difference between the two electronic states $\Delta = \varepsilon_+ - \varepsilon_-$ is related to the electronic coupling element between the donor and acceptor moieties by:

$$\Delta = 2H_{DA} \quad (2.103)$$

The full dynamic solution of the vibronic Hamiltonian can only be solved numerically. However, modification of the basis and limitations to the vibrational quanta[28] can provide transition vibronic moments and eigenvalues of the dynamic matrix that can be used to simulate the shape and intensity of the charge-transfer band.

2.3.2 Off-diagonal vibronic constant

Because the symmetric and antisymmetric coordinates are decoupled from each other,[30] the linear vibronic coupling constants may be treated independently. Assuming that $l_- \neq 0$ and $l_+ = 0$, two static solutions exist. If the electronic coupling is weak, then:

$$\frac{l_-^2}{k_-} > H_{DA} \tag{2.104}$$

and a pseudo-Jahn-Teller instability of the reference symmetric geometry gives two equivalent broken-symmetry adiabatic minima, see Figure 2.5.[28] The states correspond to a situation in which the excess charge is localized on one of the redox sites. The vibronic coupling element is related to the intramolecular reorganization energy by:

$$\lambda = 2\frac{l_-^2}{k_-} \tag{2.105}$$

If the electronic coupling is strong, then:

$$\frac{l_-^2}{k_-} \leq H_{DA} \tag{2.106}$$

and the lower surface possesses only one minimum; the symmetric equilibrium structure is stable with respect to antisymmetric vibrations.

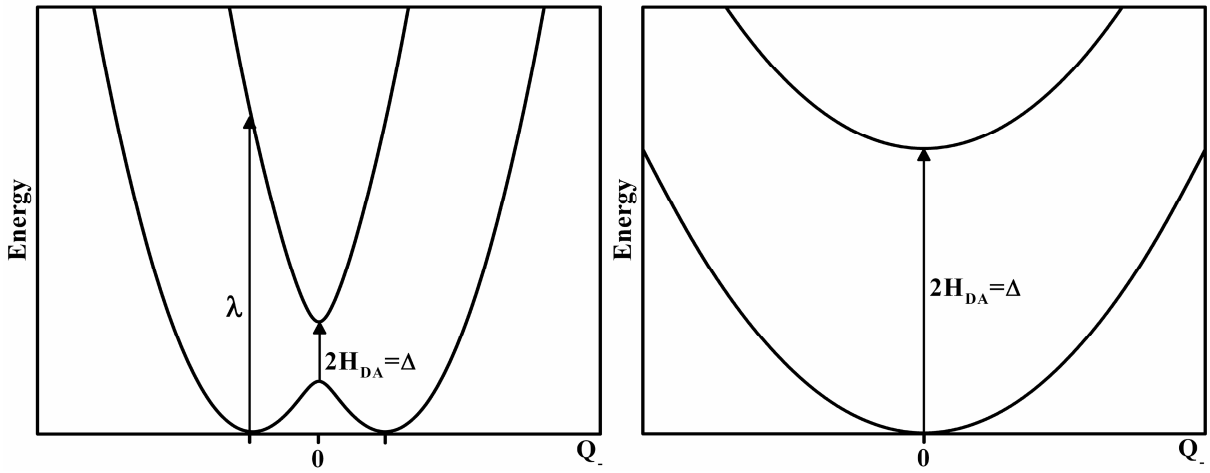

Figure 2.5 Adiabatic potential surfaces for off-diagonal vibronic coupling for Class II [left] and Class III [right] mixed-valence systems.

2.3.3 Diagonal vibronic constant

When only the diagonal vibronic coupling constant is taken into account ($l_- = 0$ and $l_+ \neq 0$), the upper surface is displaced with respect to the ground adiabatic surface, see Figure 2.6; the displacement is due to the sensitivity of the molecular geometry to the change in electron distribution upon excitation.[28] Thus, the energy of the intervalence transition can be written as:

$$E_{op} = \Delta = \Delta_0 + L \tag{2.107}$$

where Δ_0 is energy difference between the excited state at its equilibrium geometry and the same geometry on the ground state energy surface and:

$$L = k_+ \left(\delta Q_+\right)^2 / 2 \tag{2.108}$$

L, generally referred to as the relaxation energy, is a function of:

$$\partial Q_+ = \frac{l_+}{Q_+} \tag{2.109}$$

which is the displacement of the two potential energy curves. The relevance of the diagonal vibronic coupling term is that if the interaction of the symmetric vibrational modes is strong, then the shape of the intervalence band can be broad even for Class III systems.[28]

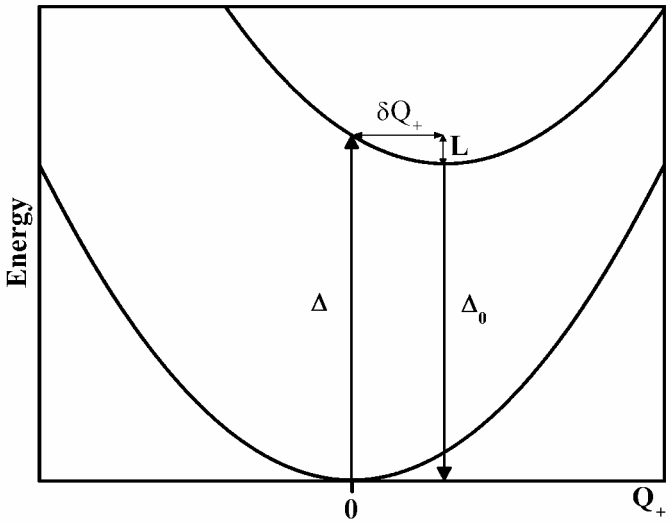

Figure 2.6 Adiabatic potential surface for diagonal vibronic coupling.

2.4 References

(1) Levine, I. N., *Quantum Chemistry*. 5 ed.; Prentice-Hall, Inc.: Upper Saddle River, NJ, 2000.

(2) Cohen-Tannoudji, C.; Diu, B.; Laloë, F., *Quantum Mechanics*. John Wiley and Sons: New York, 1977; Vol. 1-2.

(3) Szabo, A.; Ostlund, N. S., *Modern Quantum Chemistry: Introduction to Advanced Electronic Structure Theory*. Dover Publications, Inc.: Mineola, NY, 1989.

(4) Jensen, F., *Introduction to Computational Chemistry*. John Wiley and Sons, Ltd.: Chichester, UK, 1999.

(5) Cramer, C. J., *Essentials of Computational Chemistry: Theories and Models*. 2nd ed.; John Wiley and Sons, Ltd.: Chichester, UK, 2004.

(6) Koch, W.; Holthausen, M. C., *A Chemist's Guide to Density Functional Theory*. 2nd ed.; Wiley-VCH: Weinheim, 2001.

(7) Hohenberg, P.; Kohn, W., *Phys. Rev.* **1964,** 136, B864.

(8) Becke, A. D., *Phys. Rev. A: At., Mol., Opt. Phys.* **1988,** 38, 3098.

(9) Perdew, J. P., *Phys. Rev. B: Condens. Matter Mater. Phys.* **1986,** 33, 8822.

(10) Burke, K.; Perdew, J. P.; Wang, Y., In *Electronic Density Functional Theory: Recent Progress and New Directions*. Dobson, J. F.; Vignale, G.; Das, M. P., Eds. Plenum: 1998.

(11) Lee, C.; Yang, W.; Parr, R. G., *Phys. Rev. B: Condens. Matter Mater. Phys.* **1988,** 37, 785.

(12) Becke, A. D., *J. Chem. Phys.* **1993,** 98, 5648.

(13) Vosko, S. H.; Wilk, L.; Nusair, M., *Can. J. Phys.* **1980,** 58, 1200.

(14) Stephens, P. J.; Devlin, F. J.; Chabalowski, C. F.; Frisch, M. J., *J. Chem. Phys.* **1994,** 98, 11623.

(15) Frisch, M. J.; Trucks, G. W.; Schlegel, H. B.; Scuseria, G. E.; Robb, M. A.; Cheeseman, J. R.; Zakrzewski, V. G.; Montgomery, J., J.A.; Stratmann, R. E.; Burant, J. C.; Dapprich, S.; Millam, J. M.; Daniels, A. D.; Kudin, K. N.; Strain, M. C.; Farkas, O.; Tomasi, J.; Barone, V.; Cossi, M.; Cammi, R.; Mennucci, B.; Pomelli, C.; Adamo, C.; Clifford, S.; Ochterski, J.; Petersson, G. A.; Ayala, P. Y.; Cui, Q.; Morokuma, K.; Salvador, P.; Dannenberg, J. J.; Malick, D. K.; Rabuck, A. D.; Raghavachari, K.; Foresman, J. B.; Cioslowski, J.; Ortiz, J. V.; Baboul, A. G.; Stefanov, B. B.; Liu, G.; Liashenko, A.; Piskorz, P.; Komaromi, I.; Gomperts, R.; Martin, R. L.; Fox, D. J.; Keith, T.; Al-Laham, M. A.; Peng, C. Y.; Nanayakkara, A.; Challacombe, M.; Gill, P. M. W.; Johnson, B.; Chen, W.; Wong, M. W.; Andres, J. L.; Gonzalez, C.; Head-Gordon, M.; Replogle, E. S.; Pople, J. A. *Gaussian98, Rev. A.11*, 1998.

(16) Semichem *Ampac 6.55*, Shawnee, KS, 1997.

(17) Ahlrichs, R.; Bär, M.; Baron, H.-P.; Bauernschmitt, R.; Böcker, S.; Deglmann, P.; Ehrig, M.; Eichkorn, K.; Elliott, S.; Furche, F.; Haase, F.; Häser, M.; Horn, H.; Hättig, C.; Huber, C.; Huniar, U.; Kattannek, M.; Köhn, A.; Kölmel, C.; Kollwitz, M.; May, K.; Ochsenfeld, C.; Öhm, H.; Schäfer, A.; Schneider, U.; Sierka, M.; Treutler, O.; Unterreiner, B.; von Arnim, M.; Weigend, F.; Weis, P.; Weiss, H. *Turbomole*, 5.6; 2003.

(18) Newton, M. D., In *Advances in Chemical Physics: Electron Transfer - from Molecules to Biomolecules*. Jortner, J.; Bixon, M., Eds. John Wiley and Sons, Inc.: New York, 1999; Vol. 1.

(19) Barbara, P. F.; Meyer, T. J.; Ratner, M. A., *J. Phys. Chem.* **1996,** 100, 13148.

(20) Marcus, R. A., *Rev. Mod. Phys.* **1993,** 65, 599.

(21) Marcus, R. A., *J. Chem. Phys.* **1956,** 24, 966.

(22) Brédas, J. L.; Beljonne, D.; Coropceanu, V.; Cornil, J., *Chem. Rev.* **2004,** 104, 4971.

(23) Jortner, J.; Bixon, M., In *Advances in Chemical Physics: Electron Transfer - from Molecules to Biomolecules*. Jortner, J.; Bixon, M., Eds. John Wiley and Sons, Inc.: New York, 1999; Vol. 1.

(24) Newton, M. D., *Coord. Chem. Rev.* **2003,** 238-239, 167.

(25) Coropceanu, V.; André, J. M.; Malagoli, M.; Brédas, J. L., *Theor. Chem. Acc.* **2000,** 110, 56.

(26) Creutz, C.; Newton, M. D.; Sutin, N., *J. Photochem. Photobio. A* **1994,** 82, 47.

(27) Piepho, S. B., *J. Am. Chem. Soc.* **1988,** 110, 6319.

(28) Coropceanu, V.; Malagoli, M.; André, J. M.; Brédas, J. L., *J. Am. Chem. Soc.* **2002,** 124, 10519.

(29) Piepho, S. B.; Krausz, E. R.; Schatz, P. N., *J. Am. Chem. Soc.* **1978,** 100, 2996.

(30) Schatz, P. N., .In *Mixed Valency Systems: Applications in Chemistry, Physics, and Biology*. Prassides, K., Ed. Kluwer Academic Publishers: Netherlands, 1991.

CHAPTER 3

GEOMETRIC AND ELECTRONIC STRUCTRE OF SILOLE-BASED ORGANIC SEMICONDUCTORS

3.1 Introduction

As discussed in Chapter 1, silole- (silacyclopentadiene)-based materials have attracted significant recent attention as electron-transport and electroluminescent materials in OLED applications. Two of the more intriguing candidates, and among the most widely studied systems, for such applications are 2,5-bis(6'-(2',2"-bipyridyl))-1,1-dimethyl-3,4-diphenylsilole (PyPySPyPy) and its biphenyl analogue 2,5-di-(3-biphenyl))-1,1-dimethyl-3,4-diphenylsilole (PPSPP), see Figure 3.1. Recent OLED studies have demonstrated that these two chemically similar molecular systems display distinctly different solid-state properties. PyPySPyPy has shown very high, nondispersive, air-stable time-of-flight electron mobility of $2x10^{-4}$ cm^2/Vs, a two-order of magnitude improvement compared to the well-established electron transporter tris(quinolin-8-olato) aluminum(III) (Alq_3).[1, 2] Polycrystalline films of PyPySPyPy and PPSPP display green (2.46 eV) and blue (2.61 eV) fluorescence with absolute photoluminescence (PL) quantum yields of 28±3% and 85±5%, respectively;[3, 4] the PL quantum yield for PPSPP is among the highest reported for neat organic films.[2, 3] In addition, two-layer films of PPSPP or PyPySPyPy with the hole-transport material N,N'-diphenyl-N,N'-(2-naphtyl)-(1,1'-phenyl)-4,4'-diamine (NPB) show exciplex PL quantum yields of 62% (PPSPP) and 21% (PyPySPyPy); the NPB:PPSPP exciplex PL quantum yield is the highest reported to date.[3] As for their use

as electron-transport materials, single-layer electron-only devices fabricated using PyPySPyPy exhibit a higher current flow than devices made using PPSPP. This suggests that PyPySPyPy has higher electron conductivity, higher electron mobility, and lower barrier to electron injection than PPSPP.[3, 5]

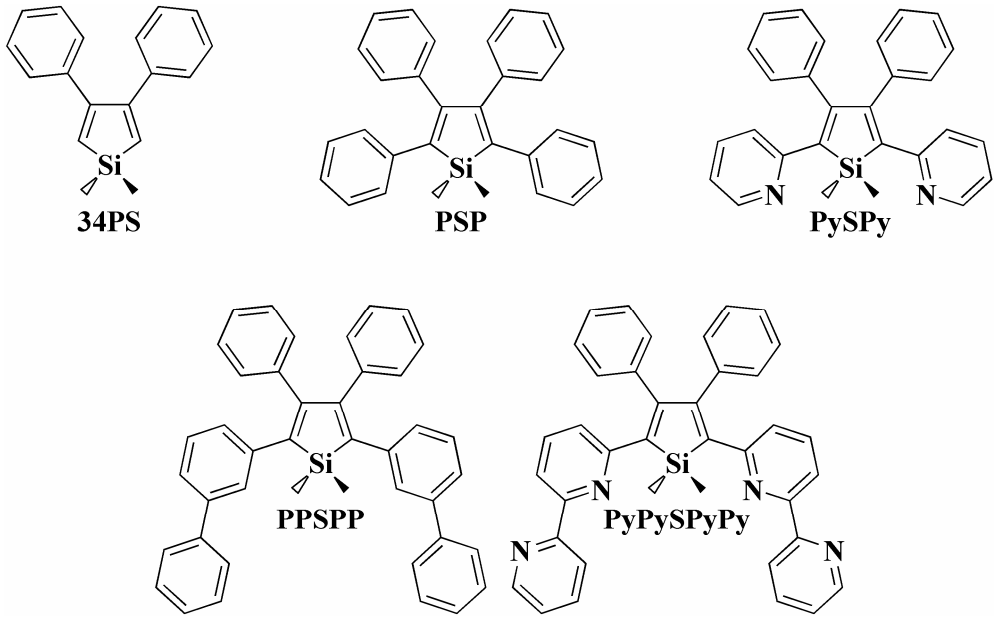

Figure 3.1 Chemical structures of: 1,1-dimethyl-3,4-diphenylsilole (34PS), 1,1-dimethyl-2,5-bis(2'-pyridyl)-3,4-diphenylsilole (PySPy), 1,1-dimethyl-2,3,4,5-tetraphenylsilole (PSP), 2,5-bis(6'-(2',2"-bipyridyl))-1,1-dimethyl-3,4-diphenylsilole (PyPySPyPy), and 2,5-di-(3-biphenyl))-1,1-dimethyl-3,4-diphenylsilole (PPSPP).

The purpose of the present work is to determine theoretically the electronic structure of PyPySPyPy and PPSPP in order to understand the chemical and physical properties that control their remarkably distinctive thin-film electronic properties.[6] Density Functional Theory and correlated semiempirical methods are used to describe the geometric and electronic structures and optical properties of these molecules. Here, our focus will be on:

the geometric structures of both the neutral molecules and their radical-anions; the absorption spectra of the neutral species; and the evaluation of the intramolecular reorganization energies and electron affinities of PyPySPyPy and PPSPP.

3.2 Theoretical methodology

In order to better understand the geometric and electronic structure of the relatively large molecular systems PyPySPyPy and PPSPP, we have assessed as well their constitutive molecular fragments so as to build a complete picture of the roles of the numerous intramolecular interactions. In that context, we have considered the molecular structures of 1,1-dimethyl-3,4-diphenylsilole (34PS), 1,1-dimethyl-2,5-bis(2'-pyridyl)-3,4-diphenylsilole (PySPy), and 1,1-dimethyl-2,3,4,5-tetraphenylsilole (PSP), in addition to PyPySPyPy and PPSPP (see Figure 3.1). The geometries were optimized in two different electronic configurations corresponding to the neutral and reduced radical-anion states. For the sake of completeness, the neutral states of pyridine, benzene, bipyridine, and biphenyl were also investigated.

Geometry optimizations were carried out at the Density Functional Theory (DFT) level using the B3LYP functionals, where Becke's three-parameter hybrid exchange functional[7, 8] is combined with the Lee-Yang-Parr correlation functional,[9] and a 6-31G* split valence plus polarization basis set; the unrestricted formalism was employed in the B3LYP (UB3LYP) investigation of the radical anions. The size of the larger molecular systems limited the basis set from extension with diffuse functions; such basis functions,

which are generally prescribed for the proper description of small molecular anions,[10, 11] proved either to be computationally expensive or not to allow convergence of the iterative procedures; as a result, the energetic values of the anionic systems will only be used here to provide relative values of the intramolecular reorganization energy and the electron affinity. The excitation energies of the low-lying excited states have been calculated with time-dependent DFT (TDDFT) and with Zerner's semiempirical intermediate neglect of differential overlap (ZINDO)[12] method supplemented by a single-configuration interaction (CIS) scheme. All DFT calculations were carried out with the Gaussian98 (Revision A.11) suite of programs.[13]

3.3 Results and discussion

3.3.1 Geometric structure

3.3.1.1 Neutral

The DFT optimized geometries are collected in Tables 3.1 – **3.3**, using the bond numbering scheme presented in Figure 3.2. In all instances, the silole ring is found to be nearly coplanar, with maximum deviations from planarity on the order of 4°. In 34PS, see Table 3.1, the exo-cyclic carbon-silicon bonds (1.893 Å) are slightly longer than the in-ring carbon-silicon bonds (1.875 Å). The *cis*-butadiene portion of the silole ring presents a very large degree of bond-length alternation (BLA) between the single and double carbon-carbon bonds, on the order of 0.163 Å; the single bond is especially long (1.520 Å) for a conjugated system, which is likely a consequence of the steric interactions

between the phenyl rings attached at the 3- and 4-positions. The phenyl groups attached at the 3- and 4-positions have carbon-carbon bridge bond lengths of 1.487 Å; the rings, rotated in-phase, lay approximately 46° out-of-plane with respect to the silole ring. We note that the results obtained for the silole ring are in good agreement with previous computational analyses of silole systems performed at the B3LYP/6-31G*(C,H)/LanL2DZdp(Si),[14] HF/66-31G*(Si)/6-31G*(C)/31G*(H),[15] HF/6-31G*,[16] and HF-AM1[17] levels of theory.

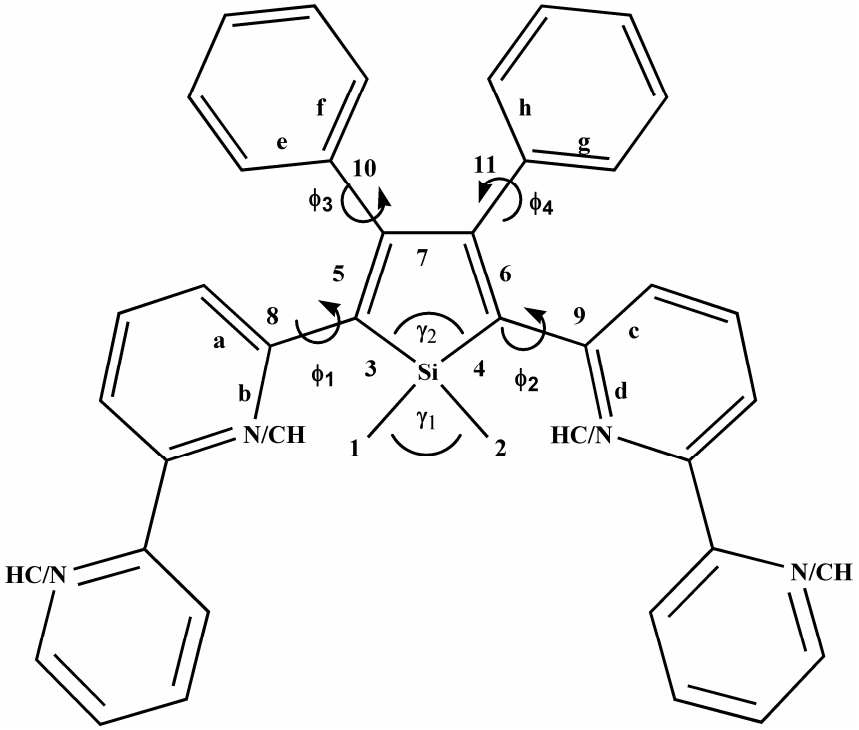

Figure 3.2 Bond numbering scheme used for 34PS, PySPy, PSP, PyPySPyPy, and PPSPP.

Table 3.1 B3LYP/6-31G*-optimized bond lengths (Å) and angles (°) for the neutral and radical-anion electronic configurations of 34PS and PySPy (see Figure 3.2 for bond numbering). Δ (Anion-Neutral) values are provided for each system.

	34PS			PySPy		
	neutral	anion	Δ	neutral	anion	Δ
bond (Å)						
1	1.893	1.923	0.030	1.887	1.901	0.014
2	1.893	1.923	0.030	1.887	1.901	0.014
3	1.875	1.846	-0.029	1.896	1.881	-0.015
4	1.875	1.846	-0.029	1.896	1.881	-0.015
5	1.357	1.402	0.045	1.368	1.414	0.046
6	1.357	1.402	0.045	1.368	1.414	0.046
7	1.520	1.474	-0.046	1.507	1.453	-0.054
8	-----	-----	-----	1.469	1.440	-0.029
a	-----	-----	-----	1.411	1.429	0.018
b	-----	-----	-----	1.357	1.376	0.019
9	-----	-----	-----	1.469	1.440	-0.029
c	-----	-----	-----	1.411	1.429	0.028
d	-----	-----	-----	1.357	1.376	0.019
10	1.487	1.472	-0.015	1.494	1.490	-0.004
e	1.406	1.417	0.011	1.404	1.409	0.005
f	1.405	1.416	0.011	1.404	1.408	0.004
11	1.487	1.472	-0.015	1.494	1.490	-0.004
g	1.406	1.417	0.011	1.404	1.409	0.005
h	1.405	1.416	0.011	1.404	1.408	0.004
angle (°)						
γ_1	109.9	102.8	-7.1	112.6	108.6	-4.0
γ_2	90.9	91.7	0.8	90.6	91.7	1.1
dihedral angle (°)						
ϕ_1	-----	-----	-----	18.6	19.1	0.5
ϕ_2	-----	-----	-----	18.6	19.1	0.5
ϕ_3	46.1	35.4	-10.7	69.3	61.8	-7.5
ϕ_4	46.1	35.4	-10.7	69.3	61.8	-7.5

Extending the 34PS system by addition of either pyridyl (PySPy) or phenyl (PSP) groups at the 2- and 5-positions only slightly alters the overall geometry of the silole core, see Tables 3.1 and 3.2. Both PySPy and PSP maintain exo-cyclic carbon-silicon bond lengths of 1.89 Å; however, the in-ring carbon-silicon bonds differ by 0.01 - 0.02 Å for PySPy

(1.896 Å) and PSP (1.886 Å). The BLA parameter, though somewhat smaller than in 34PS, remains large (0.139 Å in PySPy and 0.146 Å in PSP); the difference in BLA between the two systems is due to a slightly shorter single bond in the *cis*-butadiene moiety for PySPy. The phenyl rings at the 3- and 4-positions acquire more significant torsions for both PySPy (~69°) and PSP (~57°) with bridge bond lengths of 1.49 Å. Interestingly, rather pronounced geometric differences are found at the 2- and 5-aryl substitutions: the pyridyl rings in PySPy lay relatively in-plane with the silole ring (~19°) while the phenyl rings of PSP are rotated by some 50°; in addition, the carbon-carbon bridge bond length is 0.01 Å shorter for PySPy. The geometric distortions in PSP are likely related to the hydrogen present at the 2-position on the phenyl ring that imparts steric interactions with the silicon-substituted methyl groups and, thus, prevents the more planar structure observed for the pyridyl substituents.

Table 3.2 B3LYP/6-31G*-optimized bond lengths (Å) and angles (°) for the neutral and radical-anion electronic configurations of PSP (see Figure 3.2 for bond numbering). Δ (Anion-Neutral) values are provided for each system. X-ray crystallographic[18] values and AM1[17] of neutral PSP are also provided.

	PSP					
		neutral			Anion	
	X-ray[18]		AM1[17]	DFT	DFT	Δ
bond (Å)						
1	1.854(3)	1.863(2)	1.818	1.893	1.913	0.020
2	1.855(3)	1.848(2)	1.818	1.893	1.913	0.020
3	1.865(2)	1.867(2)	1.833	1.886	1.869	-0.017
4	1.865(2)	1.876(2)	1.833	1.886	1.869	-0.017
5	1.354(3)	1.361(3)	1.353	1.367	1.416	0.049
6	1.359(3)	1.357(3)	1.353	1.367	1.416	0.049
7	1.513(2)	1.509(2)	1.486	1.513	1.456	-0.057
8	1.481(2)	1.472(2)	-----	1.479	1.458	-0.021
a	-----	-----	-----	1.409	1.422	0.013
b	-----	-----	-----	1.408	1.423	0.015
9	1.480(2)	1.473(2)	-----	1.479	1.458	-0.021
c	-----	-----	-----	1.409	1.422	0.013
d	-----	-----	-----	1.408	1.423	0.015
10	1.485(3)	1.485(3)	-----	1.492	1.487	-0.005
e	-----	-----	-----	1.405	1.410	0.005
f	-----	-----	-----	1.404	1.409	0.005
11	1.492(3)	1.492(3)	-----	1.492	1.487	-0.005
g	-----	-----	-----	1.405	1.410	0.005
h	-----	-----	-----	1.404	1.409	0.005
angle (°)						
γ_1	110.0(2)	109.7(2)	-----	111.4	105.6	-5.8
γ_2	92.6(1)	92.7(1)	-----	92.5	93.3	0.8
dihedral angle (°)						
ϕ_1	48.5(3)	54.5(3)	-----	50.4	37.6	-12.8
ϕ_2	43.5(3)	36.7(3)	-----	50.4	37.6	-12.8
ϕ_3	57.2(3)	66.3(3)	-----	57.5	55.4	-2.1
ϕ_4	56.6(3)	70.8(3)	-----	57.5	55.4	-2.1

The optimized geometric parameters at the B3LYP/6-31G* level for PSP are in good agreement with the reported x-ray crystal structure determination of Párkányi.[18] The exo-cyclic silicon-carbon bonds are slightly overestimated (0.03 Å), while the in-ring silicon-carbon bonds are underestimated (0.02 Å). Excellent agreement is found for the carbon-carbon bonds within the *cis*-butadiene moiety and, hence, for the degree of BLA. It is of note that the experimental BLA (0.15 Å) of the *cis*-butadiene segment in PSP is larger than that observed for a similar silole system that is hydrogen-substituted at the 3- and 4-positions (0.12 Å);[18] thus, this confirms that relaxation of the steric interactions of the phenyl substituents is achieved through a lengthening of the bonds in the *cis*-butadiene fragment. Additionally, the mean torsional angles of the phenyl groups found in the X-ray structure at both the 3- and 4-positions (~ 63°) and 2- and 5-positions (~48°) are reasonably well reproduced by the DFT optimizations.

No significant modifications to the silole unit are incurred upon addition of the external aryl rings for PyPySPyPy and PPSPP, see Table **3.3**. For the respective larger analogs, the BLA of the *cis*-butadiene segment, as well as the bond lengths and torsion angles of the phenyl substituents at the 3- and 4-positions, are preserved. The substitutions at the 2- and 5-positions for both PyPySPyPy and PPSPP maintain the bridging bond lengths of PySPy and PSP, respectively. However, the torsion angle in PyPySPyPy (32°) does increase somewhat versus the smaller analog (~18°); there is virtually no difference between PPSPP and PSP. Note that the lowest energy conformer for PyPySPyPy is that with the nitrogen atoms of each bipyridyl unit in a *trans*-conformation (the *cis*-conformation is calculated at the DFT level to be 9.6 kcal/mol higher in energy). The

Table 3.3 B3LYP/6-31G*-optimized bond lengths (Å) and angles (°) for the neutral and radical-anion electronic configurations of PyPySPyPy and PPSPP (see Figure 3.2 for bond numbering). Δ (Anion-Neutral) values are provided for each system.

	PyPySPyPy			PPSPP		
	neutral	anion	Δ	neutral	anion	Δ
bond (Å)						
1	1.888	1.903	0.015	1.893	1.912	0.019
2	1.888	1.903	0.015	1.893	1.911	0.018
3	1.892	1.879	-0.013	1.886	1.871	-0.015
4	1.892	1.879	-0.013	1.886	1.870	-0.016
5	1.367	1.414	0.047	1.367	1.415	0.048
6	1.367	1.414	0.047	1.367	1.415	0.048
7	1.509	1.452	-0.057	1.513	1.456	-0.057
8	1.473	1.443	-0.030	1.479	1.457	-0.022
a	1.410	1.430	0.020	1.408	1.423	0.015
b	1.351	1.369	0.018	1.406	1.420	0.014
9	1.473	1.443	-0.030	1.479	1.457	-0.022
c	1.410	1.430	0.020	1.408	1.423	0.015
d	1.351	1.369	0.018	1.406	1.420	0.014
10	1.493	1.490	-0.003	1.493	1.487	-0.006
e	1.404	1.408	0.004	1.404	1.409	0.005
f	1.404	1.407	0.003	1.404	1.409	0.005
11	1.493	1.490	-0.003	1.493	1.487	-0.006
g	1.404	1.408	0.004	1.404	1.409	0.005
h	1.404	1.407	0.003	1.404	1.409	0.005
angle (°)						
γ_1	111.3	108.9	-2.4	110.0	106.1	-3.9
γ_2	91.0	92.0	1.0	92.3	93.3	-1.0
dihedral angle (°)						
ϕ_1	32.0	22.9	-9.1	49.5	36.2	-13.3
ϕ_2	32.0	22.9	-9.1	50.0	36.2	-13.8
ϕ_3	63.2	61.3	-1.9	58.3	56.2	-2.1
ϕ_4	63.2	61.3	-1.9	58.3	56.2	-2.1

torsion angles within the bipyridyl and biphenyl substituents are approximately 7° and 37°, respectively. We note that the DFT-calculated dipole moments for PPSPP and PyPySPyPy are both very small: PPSPP has a dipole moment of 0.26 D in the *syn*-

conformation, while the presence of the nitrogen atoms in the pyridine rings makes the molecular dipole of PyPySPyPy somewhat larger (0.59 D).

3.3.1.2 Radical-anion

Upon reduction to the radical-anion state, the modifications in geometry of the considered molecules are primarily confined to the silole ring and the aryl rings directly bound at the 2- and 5-positions on the silole ring. In 34PS, the silicon-carbon bonds relax rather considerably with the exo-cyclic bonds lengthening by 0.03 Å and the in-ring silicon-carbon bonds shortening by the same extent (0.03 Å). These changes in bond length are related to the fact that reduction to the radical-anion populates the silole LUMO; this population allows for increased antibonding (σ*) interaction between the silicon and exo-cyclic methyl carbons that lengthens these bonds, while bringing forth increased bonding character for the in-ring silicon-carbon bonds through the extended conjugation provided by the interaction of the low-lying silicon p_z-orbital and the π*-orbital of the *cis*-butadiene unit. Population of the LUMO also causes a dramatic decrease by half in the BLA of the *cis*-butadiene moiety; the respective double bonds lengthen by 0.045 Å and the single bond shortens by 0.046 Å. The phenyl rings at the 3- and 4-positions have slightly smaller torsion angles (~35°) and bridging carbon-carbon bond lengths (1.472 Å).

The nature of the changes in the silicon-carbon bonds for PySPy and PSP, though smaller in absolute terms, are similar to those observed for 34PS upon reduction. The lesser

extent of the silicon-carbon bond length modifications is linked to a delocalization of the radical-anion to the aryl rings at the 2- and 5-positions. The *cis*-butadiene portions of the two systems, as well, undergo like transformations: for PySPy [PSP], the double bonds increase by 0.046 [0.049] Å while the single bond decreases by 0.054 [0.057] Å; these changes produce a BLA of 0.039 [0.040] Å, a decrease of over 70%. While some change occurs to the torsion angles of the phenyl groups substituted at the 3- and 4-positions in 34PS, there are only minimal changes in both PySPy and PSP. The 2- and 5-position pyridyl substituents in PySPy undergo virtually no change. The bridging carbon-carbon bond decreases by 0.029 Å while the adjacent carbon-carbon and carbon-nitrogen bonds increase by approximately 0.018 Å; thus, as was seen in the *cis*-butadiene portion of the silole ring, a loss of BLA is continued throughout this portion of the molecular system. Similar types of bond transformations at the 2- and 5-phenyl substitutions are observed for PSP as well. The bridging bond decreases (0.021 Å), while the first carbon-carbon bonds within the ring increase (0.013 – 0.014 Å). However, there is a much more drastic shift towards planarity for this system as the torsion angle at the 2- and 5-positions shifts from 50° to 38°.

Parallel geometric transformations to those for PySPy and PSP are observed upon reduction of PyPySPyPy and PPSPP, respectively. For instance, within the *cis*-butadiene moiety, the BLA decreases to 0.038Å for PyPySPyPy and 0.041Å for PPSPP; a loss of BLA in the bonds in immediate proximity to the 2- and 5-positions on the silole ring occurs as well in both PyPySPyPy and PPSPP (we note that the remaining bonds in both the bipyridyl and biphenyl units change by less than 0.01 Å). The main distinction

between the two radical-anion structures is the relative planarity between the silole ring and the bipyridyl or biphenyl units. The bipyridyl units in PyPySPyPy (23°) become more coplanar with respect to the silole ring; also, the dihedral distortions between the pyridine segments are virtually negligible (1.3°). The biphenyl units in PPSPP undergo slightly larger torsional shifts from 50° in the neutral state to 36° in the radical-anion state, while the torsions between the phenyl rings change by only 2°. Overall, we observe that the geometry relaxations upon reduction are confined to the silole ring and the parts adjacent to it of the aryl rings substituting in the 2- and 5-positions.

3.3.2 Electronic structure

Though PySPy and PyPySPyPy have similar absorption maxima (3.37 eV and 3.28 eV, respectively), the two molecules possess rather different solid-state properties: PySPy is crystalline, while PyPySPyPy is amorphous with a glass transition temperature (T_g) of 77°C.[19] Based on these observations, Uchida et al.[19] suggested that the addition of the extra aryl groups simply serve as a means to add more flexibility to PyPySPyPy while having minimal effect on the HOMO (highest occupied molecular orbital) – LUMO (lowest unoccupied molecular orbital) gap.[19]

To better understand the optical data, we now turn to a description of the main characteristics of the HOMO and LUMO levels, as calculated at the DFT level. Analysis of the HOMO wavefunction for 34PS (-5.68 eV) indicates that it mainly resides on the

cis-butadiene moiety; its bonding – antibonding pattern is consistent with observations in the geometrical analysis of the neutral species, see Figure 3.3. Aryl substitution at the 2- and 5-positions to form PySPy and PSP brings forth electronic interactions between the

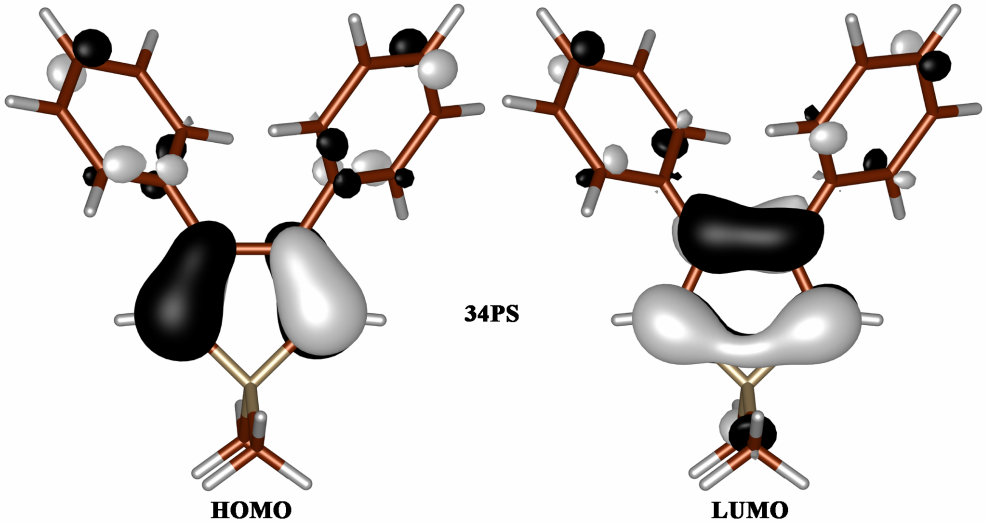

Figure 3.3 B3LYP/6-31G*-calculated highest occupied (HOMO) [bottom] and lowest unoccupied (LUMO) [top] one-electron molecular orbitals for 34PS.

HOMO of 34PS and the highest π-orbitals of pyridine (-7.11 eV) and benzene (-6.70 eV). Because the highest π-orbitals for 34PS and benzene are closer in energy than 34PS and pyridine, a larger energy destabilization is expected *a priori* for the PSP HOMO through a greater degree of orbital splitting produced by more pronounced wavefunction overlap. However, the HOMO energies for PySPy (-5.28 eV) and PSP (-5.29 eV), are nearly identical. This is due, at least partly, to the more planar structure of PySPy, which allows for a greater degree of antibonding orbital interaction (see below) than the more twisted structure of PSP. Examination of the wavefunctions shows that their spatial distributions

are very similar in the two systems, see Figure 3.4; they primarily lie on the silole ring and the aryl rings substituted at the 2- and 5-positions with an antibonding character between the silole ring and the respective aryl substituent.

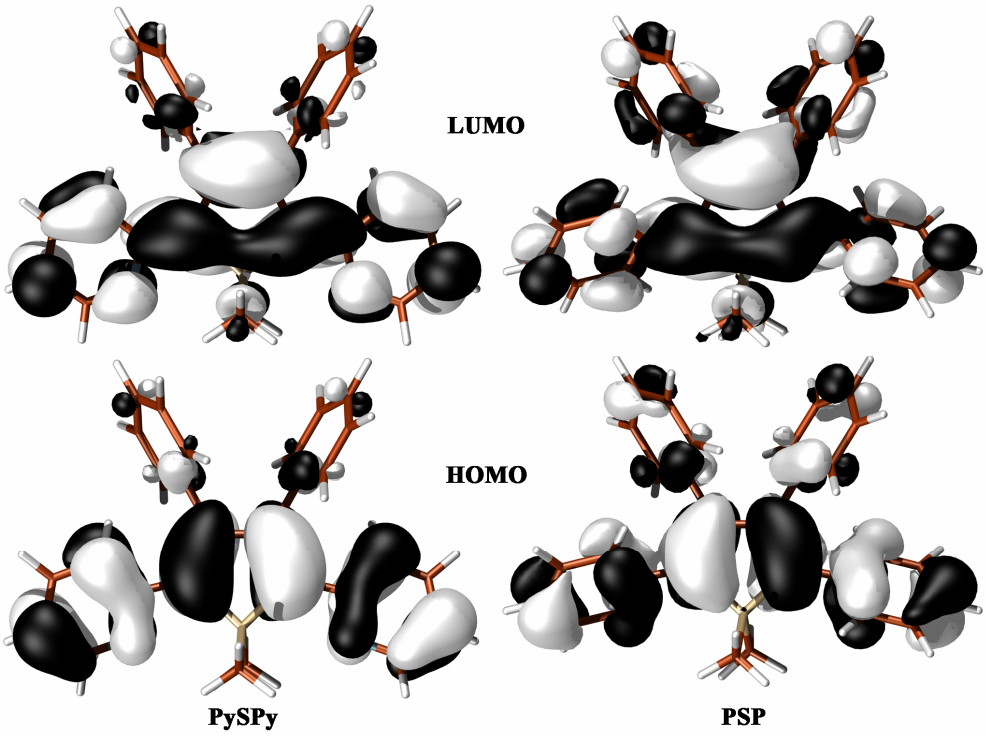

Figure 3.4 B3LYP/6-31G*-calculated highest occupied (HOMO) [bottom] and lowest unoccupied (LUMO) [top] one-electron molecular orbitals for PySPy [left] and PSP [right].

Addition of external aryl groups in PyPySPyPy and PPSPP again produces HOMO levels that have nearly identical energies, -5.33 eV and -5.32 eV, respectively. This is in excellent agreement with the ultraviolet photoelectron spectroscopic (UPS) data that indicate that the solid-state ionization potentials of PyPySPyPy and PPSPP differ by only

0.05 eV (5.94 and 5.89 eV, respectively).[3, 20, 21] As with their smaller analogs, the orbital distributions are nearly identical for the two systems with the majority of the probability density residing on the silole ring and the aryl rings substituted at the 2- and 5-positions, see Figure 3.5. In fact, the HOMO's for the PyPySPyPy/PySPy and PSP/PPSPP pairs are virtually indistinguishable (neglecting the small amount of orbital density on the external aryl rings of the larger systems).

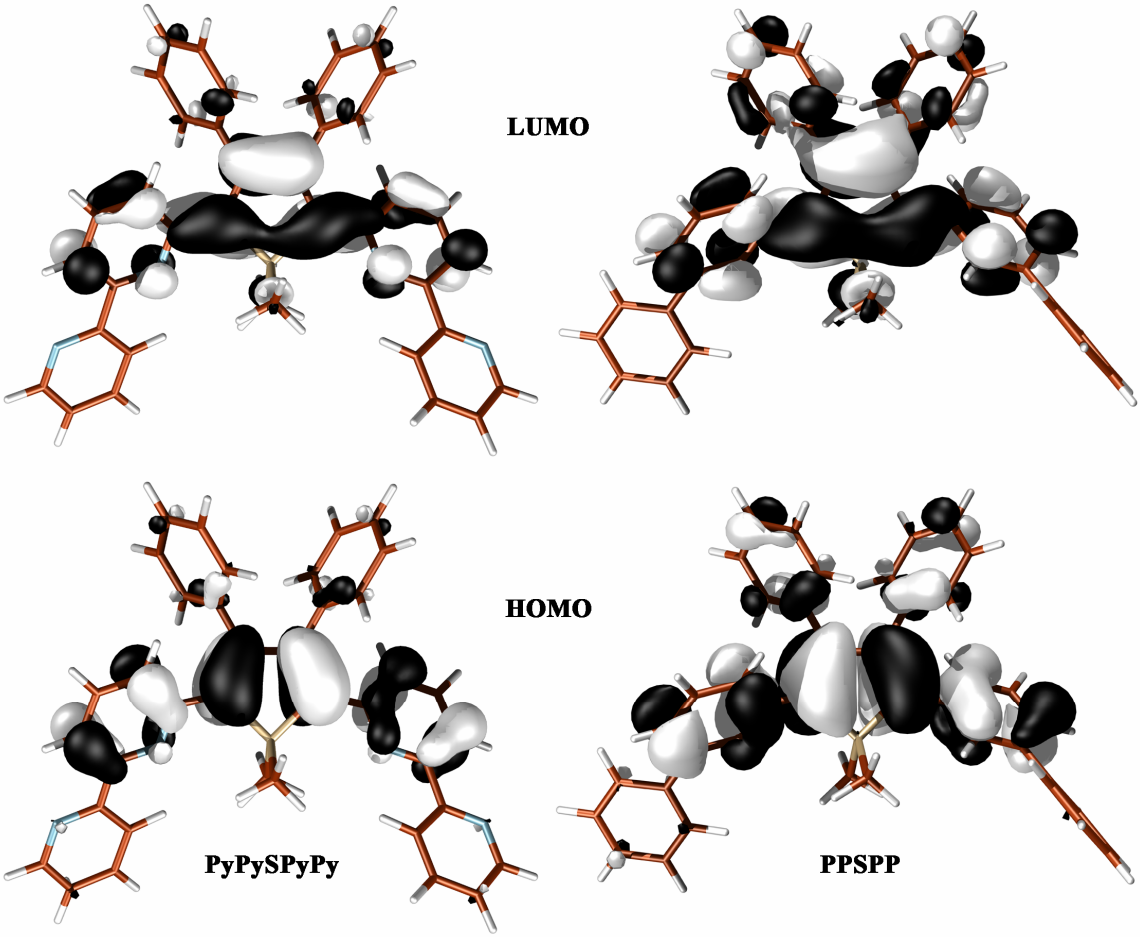

Figure 3.5 B3LYP/6-31G*-calculated highest occupied (HOMO) [bottom] and lowest unoccupied (LUMO) [top] one-electron molecular orbitals for PyPySPyPy [left] and PPSPP [right].

The DFT B3LYP/6-31G* calculations indicate that the LUMO for 34PS lies at -1.37 eV; as with the HOMO, it resides primarily on the silole ring. The LUMO shape maintains the primary characteristics of the isolated silole ring in which interaction between the σ*-orbitals of the two exocyclic σ-bonds on the ring silicon and the π*-orbital of the butadiene moiety composes the σ*- π* conjugation in the ring, see Figure 3.3. Addition of pyridyl and phenyl at the 2- and 5-positions to form PySPy and PSP produces LUMO energies of -1.82 eV and -1.59 eV, respectively (note that the pyridine LUMO is calculated to lie at -0.68 eV, while that of benzene at 0.10 eV). The wavefunctions are very similar for the two systems, see Figure 3.4, and are primarily located on the silole ring and the aryl rings substituted at the 2- and 5-postitions with a bonding character between the silole ring and the substituent. Further extension with outer aryl groups in PyPySPyPy and PPSPP produces LUMO levels at -1.84 eV and -1.63 eV, respectively. Though the DFT LUMO energy results slightly overestimate the difference in the solid-state LUMO levels of PyPySPyPy and PPSPP (0.06 eV) as determined by the combination of UPS and optical-bandgap data,[3, 20, 21] there is concurrence with the fact that the LUMO for PyPySPyPy is energy stabilized versus PPSPP. Again, the orbital distributions are nearly identical for the two systems with the majority of the probability density residing on the silole ring and the aryl rings substituted at the 2- and 5-postitions, see Figure 3.5. As with the HOMO wavefunctions, the LUMO wavefunctions of the larger systems are virtually indistinguishable from the smaller molecules. The approximate 0.2 eV stabilization in the LUMO energy for PyPySPyPy versus PPSPP could be one of the main factors in the electron transport differences of the two molecular systems.

PyPySPyPy and PySPy photoluminesce at 2.53 eV and 2.58 eV in THF after absorption with maxima at 3.28 eV and 3.37 eV, respectively.[19] The photoluminescence and absorption wavelengths vary only slightly for the two materials in thin films with values of 2.50 eV and 3.21 eV for PyPySPyPy and 2.54 eV and 3.26 eV for PySPy.[19] The INDO/CIS evaluation of the absorption energies for PyPySPyPy (3.50 eV) and PySPy (3.48 eV) are in very good agreement with the experimental data and confirm the similarity in the absorption maxima; the INDO/CIS emission energies, calculated on the basis of AM1/CI-optimized geometries of the lowest excited state,[22] are also in good agreement with experiment (2.88 eV for PyPySPyPy and 2.80 eV for PySPy). Optical data for PSP[17] indicates that the system undergoes intense fluorescence in the blue region of the visible spectrum (2.58 eV) after absorption with a maximum at 3.53 eV. INDO/CIS calculations for PSP absorption (3.78 eV) show good agreement with the empirical absorption maximum; the calculated absorption maximum for PPSPP is 3.78 eV, as well. TDDFT results for the absorption maxima of PyPySPyPy (3.07 eV) and PPSPP (3.20 eV) are in good agreement with the INDO/CIS results.

Evaluation of the nature of the excited state through investigation of electron-hole distribution[23,24, 25] for PyPySPyPy, see Figure 3.6, reveals that the photoinduced excited state (exciton) is predominantly located on the silole ring and the pyridine rings directly substituted at the 2- and 5-positions; very similar electron-hole distributions are evaluated for PySPy, PSP, and PPSPP and are thus not shown here. These results indicate that: (i) the addition of the external aryl ring does not effect the location of the exciton, which is consistent with the molecular orbital analysis; and (ii) as a consequence, the electron-hole

distributions are similar, whether taking account of the ground-state geometry or the lowest excited-state geometry;[24, 25] this contrasts with the situation in well-conjugated oligomers (*e.g.*, oligophenylenevinylenes[26]) where the exciton wavefunction is initially significantly delocalized (ground-state geometry) but localizes upon nuclear relaxation (excited-state geometry). For instance, polyfluorene derivatives[27] (where the number of repeat units range from n = 3 – 10) have absorption maxima that continually move to longer wavelengths with increasing repeat unit (λ_{abs} = 348 – 384 nm), but the emission maxima remain virtually unchanged past n = 6 (λ_{em} = 413 – 434 nm, n = 3 – 5; λ_{em} = 445 nm, n = 6 – 10); these results suggest significant geometric changes upon going from the ground state to the relaxed excited state.[27]

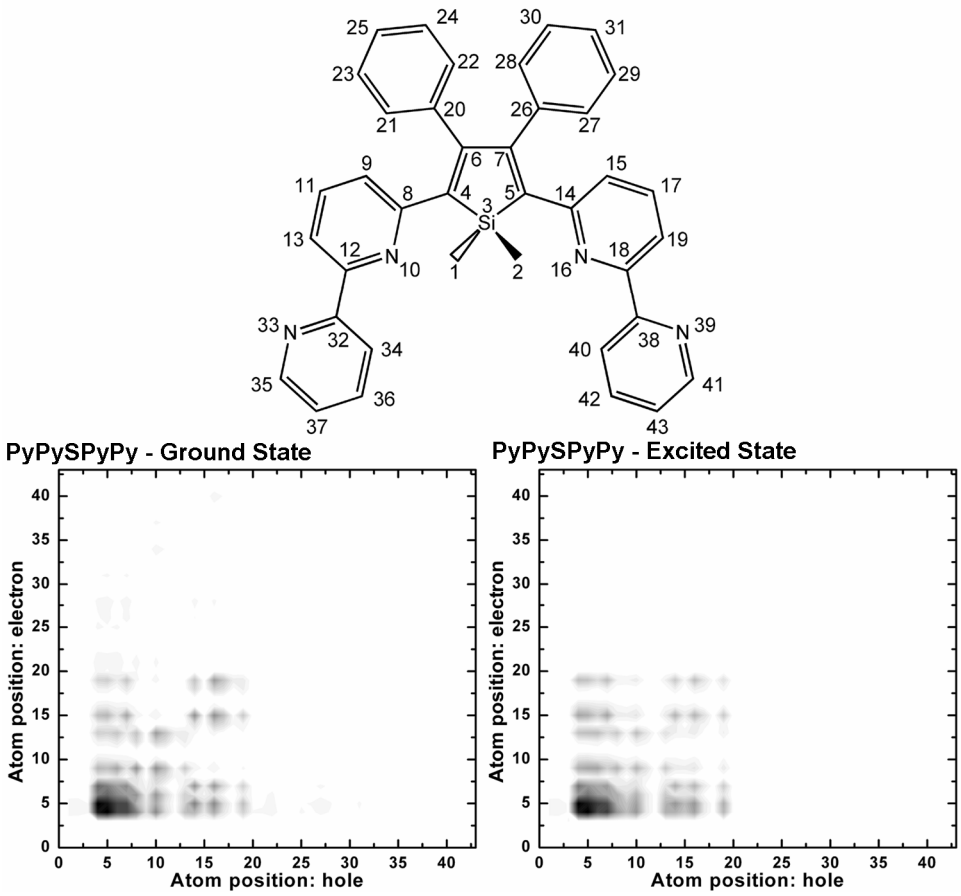

Figure 3.6 Electron-hole distributions and atomic labeling scheme for PyPySPyPy ground and excited-state geometries.

The above quantum-chemical assessments of the orbital energies, orbital shapes, absorption data, and electron-hole distributions confirm the suggestion of Uchida et al.[19] The addition of the aryl ring to PySPy to form PyPySPyPy has no significant effect on the HOMO – LUMO gap (3.46 eV and 3.49 eV, respectively) or on the electron-hole distribution. This is made even clearer by the fact that the calculated transitions for the two systems primarily involve a HOMO → LUMO transition (on the order of 88% and 83%, respectively). The calculated values for PSP and PPSPP are very similar; as a result, analogous absorption characteristics are predicted for these systems.

3.3.3 Intramolecular reorganization energy and electron affinity

When considering the transport properties of radical-anions (negative polarons) as charge carriers through an organic molecular film, the electron-hopping process can be portrayed at the microscopic level as a self-exchange electron-transfer reaction between two neighboring molecules – the acceptor being in the neutral electronic state and the donor in the reduced radical-anion state. A simple analysis of such an electron-transfer reaction can be based on Marcus theory and extensions thereof,[28, 29] as described in Chapter 2. Quantum-chemical calculations allow for the description of both the transfer integral and the intramolecular reorganization energy component of the total reorganization energy. The transfer integral is related to the energetic splitting of the frontier orbitals of the system as it goes from an isolated state to a system of interacting molecules.[30] In the absence of structural data for the relative positions of PyPySPyPy or PPSPP molecules in films, only exploratory evaluations of the transfer integrals can be performed. Analysis at the INDO level of theory of the intermolecular electronic coupling between dimers (with intermolecular distances ranging between 5 – 7 Å and variations in orientation) composed of molecules using the DFT-derived geometries indicates that: (i) the more planar structure of PyPySPyPy appears to allow for shorter intermolecular distances and confirms the potential for larger transfer integrals versus PPSPP; and (ii) the transfer integrals for both electrons and holes are in the range of 10^{-2} – 10^{-3} eV, results that are one to two orders of magnitude lower than in ordered systems, such as crystalline pentacene.[31]

The intramolecular reorganization energy combines the relaxation energies of the electron-donor (initially ionized) molecule, λ_1, and of the electron-acceptor (initially neutral) molecule, λ_2, upon electron-transfer reaction;[32] from the previous discussion (see Chapter 2), it is clear that for electron transfer (carrier hopping) rates to be high, reorganization energies need to be kept as low as possible. The calculated intramolecular reorganization energies, see Table 3.4, for PyPySPyPy (0.50 eV) and PPSPP (0.52 eV) demonstrate that the two systems, again, are very similar in nature. The slightly larger reorganization energy in PPSPP is consistent with the fact that while both PyPySPyPy and PPSPP undergo similar bond length changes upon reduction, PPSPP displays slightly larger torsional modifications. However, the major result is that the intramolecular reorganization energy values, ~0.5 eV, are in both cases very large. They are about twice as large as the calculated values[33, 34] for N,N'-diphenyl-N,N'-bis(3-methylphenyl)-([1,1'-biphenyl])-4,4'-diamine (TPD), a widely used hole-transport material, and four times as big as in pentacene.[35] This is directly related to the very large, strongly localized geometrical changes occurring in the silole ring upon reduction.

Table 3.4 B3LYP/6-31G* relaxation energies (eV) and intramolecular reorganization energies (eV) for PyPySPyPy and PPSPP.

System	neutral (λ_1) [eV]	anion (λ_2) [eV]	total reorganization ($\lambda_1 + \lambda_2$) [eV]
PyPySPyPy	0.236	0.264	0.500
PPSPP	0.241	0.279	0.520

From the energies of the optimized neutral and radical-anion structures, as well as single-point calculations of the neutral geometry on the radical-anion potential surface and the radical-anion geometry on the neutral potential surface, qualitative estimates of the electron affinity for PyPySPyPy and PPSPP can be made (note that the electron affinity is defined here as the energy of the neutral state subtracted from the energy of the radical-anion state; thus, a negative electron affinity reflects an energy stable radical-anion state). The adiabatic electron affinity for PyPySPyPy is -0.95 eV, while that for PPSPP is -0.75 eV. In comparison, the vertical electron affinity is -0.69 eV for PyPySPyPy and -0.47 eV for PPSPP. Both results qualitatively indicate a much more stable radical-anion state for PyPySPyPy.

It is worth noting that calculation of the dianionic state of both PyPySPyPy and PPSPP reveals significant energy destabilization versus the radical-anion and neutral states. For PyPySPyPy, the addition of a second electron to the stable radical-anion requires 2.12 eV; the dianion state is destabilized by 1.17 eV versus the neutral state. Formation of the dianion in PPSPP requires 2.31 eV, a state that is 1.56 eV less stable than the neutral state. The results for PyPySPyPy and PPSPP expose a significant divergence from the silole dianions theoretically studied by Goldfuss and von Ragué Schleyer;[14] whereas silole rings that have undergone deprotonation of the hydrogen atoms present on the ring silicon allow for aromatic stabilization of the dianion, the presence of 1,1-dimethyl groups on the systems described herein do not permit such stabilization.

3.4 Conclusions

While PyPySPyPy and PPSPP have been shown experimentally to display diverse solid-state electronic properties, the quantum-chemical analysis reported in this work indicate that the geometric and electronic structures, nature of the photoabsorption processes, and intramolecular reorganization energies are very similar for the two molecules. A direct answer as to why PyPySPyPy and PPSPP behave differently in the solid state cannot be easily provided based on the present study, since a deep understanding of the solid-state phenomena requires identification and appreciation of the effects of intermolecular interactions. We note that solid-state UPS and X-ray photoelectron spectroscopic (XPS) investigations[20] have uncovered the formation of charge-transfer complexes at the metal (Mg)-silole interface developed through strong chemical interactions; however, charge hopping in the bulk silole film is probably best described through a polaron model. At this stage, one can only speculate that the more planar conformation found around the silole ring and the rings in the 2- and 5-positions in the case of PyPySPyPy might lead to stronger intermolecular interactions and tighter packing of these molecular segments. In general, such packing results in higher carrier mobilities and is conducive to luminescence quenching; this consideration is in qualitative agreement with the comparison of the electron mobilities and photoluminescence quantum yields between films of PyPySPyPy and PPSPP. Finally, we stress that, when considering electron transport, large reorganization energies, on the order of 0.5 eV, are calculated for both PyPySPyPy and PPSPP. Such huge values, which are due to the significant extent and

localized character of the geometry relaxation upon reduction, are detrimental to the achievement of high electron mobilities in the solid state.

3.5 References

(1) Murata, H.; Malliaras, G. G.; Uchida, M.; Shen, Y.; Kafafi, Z. H., *Chem. Phys. Lett.* **2001,** 339, 161.

(2) Murata, H.; Kafafi, Z. H.; Uchida, M., *Appl. Phys. Lett.* **2002,** 80, 189.

(3) Palilis, L. C.; Mäkinen, A. J.; Murata, H.; Uchida, M.; Kafafi, Z. H., *Proceedings of SPIE-The International Society for Optical Engineering* **2003,** 4800, 256.

(4) Palilis, L. C.; Murata, H.; Uchida, M.; Kafafi, Z. H., *Org. Elec.* **2003,** 4, 113.

(5) Palilis, L. C.; Uchida, M.; Kafafi, Z. H., *IEEE J. Sel. Top. Quantum Electron.* **2004,** 10, 79.

(6) Risko, C.; Kushto, G.; Kafafi, Z.; Brédas, J. L., *J. Chem. Phys.* **2004,** 121, 9031.

(7) Becke, A. D., *Phys. Rev. A: At., Mol., Opt. Phys.* **1988,** 38, 3098.

(8) Becke, A. D., *J. Chem. Phys.* **1993,** 98, 5648.

(9) Lee, C.; Yang, W.; Parr, R. G., *Phys. Rev. B: Condens. Matter Mater. Phys.* **1988,** 37, 785.

(10) Rienstra-Kiracofe, J. C.; Barden, C. J.; Brown, S. T.; Schaefer III, H. F., *J. Phys. Chem. A* **2001,** 105, 524.

(11) Rienstra-Kiracofe, J. C.; Tschumper, G. S.; Schaefer III, H. F.; Nandi, S.; Ellison, G. B., *Chem. Rev.* **2002,** 102, 231.

(12) Zerner, M. C.; Loew, G. H.; Kichner, R. F.; Mueller-Westerhoff, U. T., *J. Am. Chem. Soc.* **1980,** 102, 589.

(13) Frisch, M. J.; Trucks, G. W.; Schlegel, H. B.; Scuseria, G. E.; Robb, M. A.; Cheeseman, J. R.; Zakrzewski, V. G.; Montgomery, J., J.A.; Stratmann, R. E.; Burant, J. C.; Dapprich, S.; Millam, J. M.; Daniels, A. D.; Kudin, K. N.; Strain, M. C.; Farkas, O.; Tomasi, J.; Barone, V.; Cossi, M.; Cammi, R.; Mennucci, B.; Pomelli, C.; Adamo, C.; Clifford, S.; Ochterski, J.; Petersson, G. A.; Ayala, P. Y.; Cui, Q.; Morokuma, K.; Salvador, P.; Dannenberg, J. J.; Malick, D. K.; Rabuck, A. D.; Raghavachari, K.; Foresman, J. B.; Cioslowski, J.; Ortiz, J. V.; Baboul, A. G.; Stefanov, B. B.; Liu, G.; Liashenko, A.; Piskorz, P.; Komaromi, I.; Gomperts, R.; Martin, R. L.; Fox, D. J.; Keith, T.; Al-Laham, M. A.; Peng, C. Y.; Nanayakkara, A.; Challacombe, M.; Gill, P. M. W.; Johnson, B.; Chen, W.; Wong, M. W.; Andres, J. L.; Gonzalez, C.; Head-Gordon, M.; Replogle, E. S.; Pople, J. A. *Gaussian98, Rev. A.11*, 1998.

(14) Goldfuss, B.; von Ragué Schleyer, P., *Organometallics* **1997,** 16, 1543.

(15) Khabashesku, V. N.; Balaji, V.; Boganov, S. E.; Nefedov, O. M.; Michl, J., *J. Am. Chem. Soc.* **1994,** 116, 320.

(16) Yamaguchi, S.; Itami, Y.; Tamao, K., *Organometallics* **1998,** 17, 4910.

(17) Ferman, J.; Kakareka, J. P.; Klooster, W. T.; Mullin, J. L.; Quattrucci, J.; Ricci, J. S.; Tracy, J. J.; Vining, W. J.; Wallace, S., *Inorg. Chem.* **1999,** 38, 2464.

(18) Párkányi, L., *J. Organomet. Chem.* **1981,** 216, 9.

(19) Uchida, M.; Izumizawa, T.; Nakano, T.; Yamaguchi, S.; Tamao, K.; Furukawa, K., *Chem. Mater.* **2001,** 13, 2680.

(20) Mäkinen, A. J.; Uchida, M.; Kafafi, Z. H., *Appl. Phys. Lett.* **2003,** 82, 3889.

(21) Mäkinen, A. J.; Uchida, M.; Kafafi, Z. H., *J. Appl. Phys.* **2004,** 95, 2832.

(22) The lowest-lying excited state geometry was optimized using a coupled semi-empirical RHF-AM1/configuration interaction (AM1/CI) scheme as implemented in the AMPAC program package. AMPAC 5.0 Users Manual, Semichem (1994).

(23) We adopt a non-antisymmetrized definition of the electron-hole distribution.

(24) Tretiak, S.; Mukamel, S., *Chem. Rev.* **2002,** 102, 3171.

(25) Rissler, J.; Bässler, J. H.; Gebhard, G.; Schwerdtfeger, P., *Phys. Rev. B: Condens. Matter Mater. Phys.* **2001,** 64, 45122.

(26) Tretiak, S.; Saxena, A.; Martin, R. L.; Bishop, A. R., *Phys. Rev. Lett.* **2002,** 89, 097402.

(27) Klaerner, G.; Miller, R. D., *Macromolecules* **1998,** 31, 2007.

(28) Marcus, R. A., *J. Chem. Phys.* **1956,** 24, 966.

(29) Barbara, P. F.; Meyer, T. J.; Ratner, M. A., *J. Phys. Chem.* **1996,** 100, 13148.

(30) Brédas, J. L.; Calbert, J. P.; da Silva Filho, D. A.; Cornil, J., *Proc. Natl. Acad. Sci. U. S. A.* **2002,** 99, 5804.

(31) Cheng, Y. C.; Silbey, R. J.; da Silva Filho, D. A.; Calbert, J. P.; Cornil, J.; Brédas, J. L., *J. Chem. Phys.* **2003,** 118, 3764.

(32) Coropceanu, V.; André, J. M.; Malagoli, M.; Brédas, J. L., *Theor. Chem. Acc.* **2003,** 110, 59.

(33) Malagoli, M.; Brédas, J. L., *Chem. Phys. Lett.* **2000,** 327, 13.

(34) Lin, B. C.; Cheng, C. P.; Lao, Z. P. M., *J. Phys. Chem. A* **2003,** 107, 5241.

(35) Gruhn, N. E.; da Silva, D. A.; Bill, T. G.; Malagoli, M.; Coropceanu, V.; Kahn, A.; Brédas, J. L., *J. Am. Chem. Soc.* **2002,** 124, 7918.

CHAPTER 4

INFLUENCE OF 1,1-DIARYL SUBSTITUTION ON THE ELECTRONIC PROPERTIES OF SILOLES

4.1 Introduction

The Schottky-Mott limit for metal-semiconductor interfaces allows for simple predictions of electron (hole) injection barriers through alignment at a common vacuum level of the properties of the separate constituents, *i.e.*, the electron affinity, EA, (or ionization potential, IP) of the semiconductor and the metal workfunction.[1, 2] However, such a minimal assumption negates significant contributions from interface dipole moments and the creation of gap electronic states that cause pinning of the Fermi energy. The importance of gap electronic states and the associated pinning of the metal Fermi energy have recently been discussed also for interfaces between metals and organic semiconductors;[1] in the case of silole-based organic semiconductors, Kafafi and co-workers have found gap states formed at the silole/magnesium interface using photoelectron spectroscopy (PES).[3] Additionally, morphological properties at the metal-organic interface due to variations in processing techniques and the physics of the charge transport (thermally-activated hopping) involved in amorphous organic solids add other complications for electronic device structures containing metal-organic interfaces.[4] These interface effects point to the need for detailed understanding of the electronic structure of thin-film organics in order to begin to gain thorough insight into device performance.

In the previous Chapter, we investigated from a quantum-chemical standpoint two siloles that have shown unique solid-state electron mobility and electroluminescence properties; these compounds present two exo-cyclic methyl groups attached to the silicon atom. Now, we examine effects of 1,1-diaryl substitution in 1,1-diaryl-2,3,4,5-tetraphenylsiloles.[5] This class of siloles was selected given that: (i) it has previously been reported that OLEDs based on siloles with R1 = R1' = Ph can be much brighter and more efficient than those based upon siloles with R1 = R1' = alkyl;[6] and (ii) since thermal stability is an important materials parameter for OLEDs, 1,1-diaryl siloles are known to have higher melting points and glass-transition temperatures than their 1,1-dialkyl counterparts. The electronic effects of 1,1-substituents in siloles have previously been probed by electrochemistry,[7, 8] as well as by UV/vis absorption and *ab initio* calculations;[9] however, there is only one report in which two different aryl groups are compared, with this study only comparing UV/vis data.[9] Additionally, despite considerable interest in the electron-transport properties of siloles, no direct measurements of EAs have been published and only a few studies have involved the determination of an IP by PES.[10-12]

In order to probe the effects of the 1,1-diaryl groups on the electronic structure of the siloles in more detail, three new species were synthesized where the aryl groups are 2-(9,9-dimethylfluorenyl) (**III**), 2-thienyl (**IV**), or pentafluorophenyl (**V**) groups; the properties of these compounds were compared to those of the previously reported 1,1-diphenyl-2,3,4,5-tetraphenylsilole (**II)** and 1,1-methyl-2,3,4,5-tetraphenylsilole (**I)**. Density of electronic states derived from Density Functional Theory (DFT) calculations

are used to assess the solid-state PES and inverse photoemission spectroscopy (IPES) spectra of these siloles; these techniques offer the most direct experimental probes of IP and EA, respectively. Calculated adiabatic and vertical EAs and IPs are also compared to the solid-state and electrochemically-derived estimates. We also employ DFT to calculate the intramolecular reorganization energies for the self-exchange electron-transfer reactions between these siloles and their radical ions. Finally, experimental and theoretical optical data and IP and EA data are utilized to estimate the binding energies of excitons in these siloles. [Note: The siloles described herein were synthesized in the group of Professor S. R. Marder at the Georgia Institute of Technology; the cyclic voltammetry (CV) and optical studies were also performed in the group of Professor Marder. The PES and IPES investigations were performed in the group of Professor A. Kahn at Princeton University.]

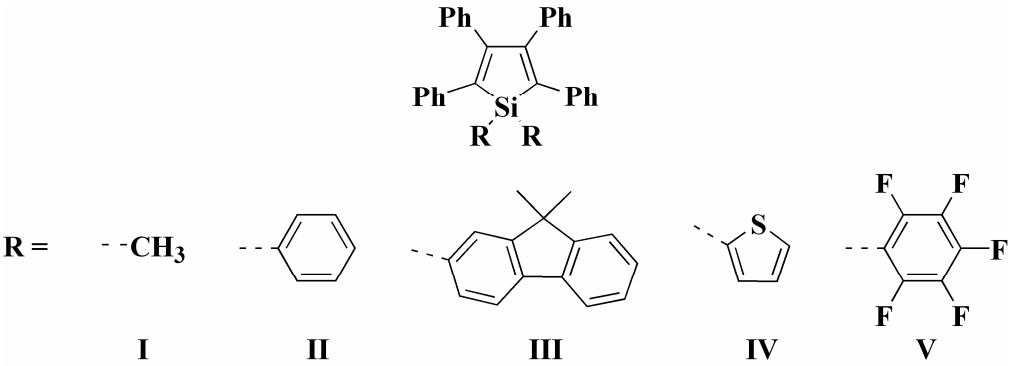

Figure 4.1 Chemical structures of siloles **I-V**.

4.2 Theoretical methodology

The geometries of **I – V** were optimized in the neutral, radical-anion, and radical-cation states via DFT. The DFT calculations were carried-out using the B3LYP functionals, where Becke's three-parameter hybrid exchange functional is combined with the Lee-Yang-Parr correlation functional,[13-15] with a 6-31G* split valence plus polarization basis set. Excitation energies for the low-lying excited states were calculated with time-dependent density functional theory (TDDFT). Simulation of the PES and IPES spectra was accomplished through the density of states (DOS) given by the DFT methodology. In order to account for polarization effects in the solid state, the DOS were rigidly shifted with respect to the binding-energy axis (in **II** by 2.97 eV for PES and 5.22 eV for IPES; in **III** by 2.04 eV for PES and 5.16 eV for IPES; in **IV** by 2.79 eV for PES and 4.64 eV for IPES; and, in **V** by 2.83 eV for PES and 5.20 eV for IPES); the DOS was convoluted with Gaussian functions characterized by a full-width at half-maximum (FWHM) of ca. 0.5 – 0.7 eV in order to replicate the experimental line widths. With the B3LYP functionals that contain correlation effects, neither compression nor expansion of the calculated DOS was deemed necessary, in contrast to previous Hartree-Fock-based simulations of PES and IPES data.[16] All DFT calculations were performed with Gaussian98 (Revision A.11).[17]

4.3 Results and discussion

4.3.1 Geometry

Selected geometric parameters for the neutral, radical-anion, and radical-cation electronic states of **I** – **V** (note that **I** is the same as PSP described in Chapter 3) are collected in Tables 4.1 – 4.5, which use the bond numbering scheme presented in Figure 4.2. Across the series, the determined geometries do not vary significantly amongst the various molecular structures in the different electronic states. In the neutral state, the exo-cyclic silicon-carbon bonds range from 1.87 – 1.90 Å, while the in-ring silicon-carbon bonds range from 1.87 – 1.89 Å. The carbon-carbon bonds within the *cis*-butadiene portion of the silole ring possess bond-length alternation (BLA) patterns on the order of 0.15 Å, similar to what we have seen in Chapter 3. The twists of the phenyl rings at the 2- and 5-positions for **I** – **IV** are on the order of 50°, while those in **V** are 60°; the phenyl rings at the 3- and 4-positions are on the order of 55 - 57°.

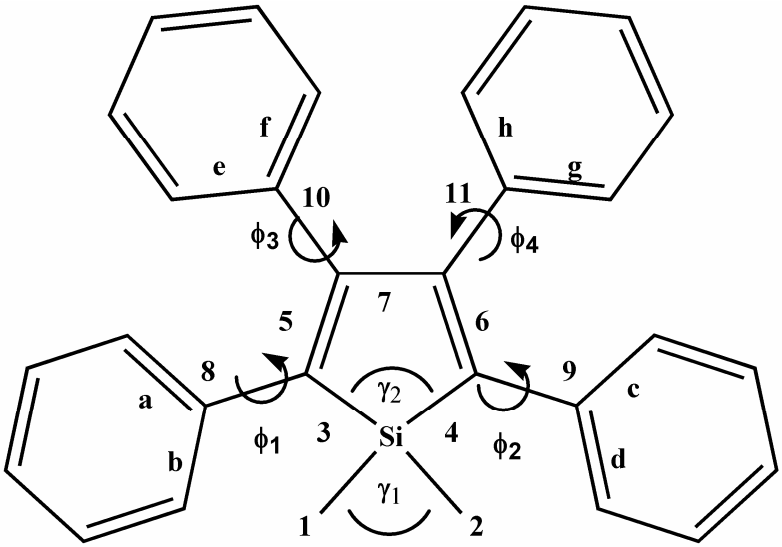

Figure 4.2 Bond and angle numbering scheme.

We find that, as with the reduction processes described in Chapter 3, the geometric modifications upon both reduction and oxidation of the siloles **I** – **V** are primarily confined to the central portion of the molecular structures: the silole ring, the exo-cyclic silicon-carbon bonds, the carbon-carbon bonds of the 2,5-phenyl rings in close proximity to the silole ring, and the torsional angle of the 2,5-phenyl rings with respect to the silole ring. Upon reduction, the exo-cyclic silicon-carbon bonds increase on the order of 0.020 – 0.037 Å, while the in-ring silicon-carbon bonds decrease by 0.017 – 0.028 Å; the changes observed for oxidation, on the other hand, are in the opposite direction – a decrease in the exo-cyclic silicon-carbon bond (0.008 – 0.016 Å) and an increase in the in-ring silicon-carbon bond (0.016 – 0.019 Å). For both reduction and oxidation, there is a significant decrease (in the range of 72 – 75% and 62 – 64%, respectively) in BLA within the *cis*-butadiene moiety versus the neutral state. Additionally, the phenyl rings at

the 2- and 5-positions become more co-planar with the silole ring upon both reduction and oxidation, while the phenyl rings at the 3- and 4-positions adjust only marginally.

Table 4.1 Selected geometric parameters for the neutral, radical-anion, and radical-cation forms of **I** at the B3LYP/6-31G* level.

	neutral	anion	Δ(A-N)	cation	Δ(C-N)
bond (Å)					
1	1.893	1.913	0.020	1.885	-0.008
2	1.893	1.913	0.020	1.885	-0.008
3	1.886	1.869	-0.017	1.902	0.016
4	1.886	1.869	-0.017	1.902	0.016
5	1.367	1.416	0.049	1.409	0.042
6	1.367	1.416	0.049	1.409	0.042
7	1.513	1.456	-0.057	1.462	-0.051
8	1.479	1.458	-0.021	1.450	-0.029
a	1.409	1.422	0.013	1.422	0.013
b	1.408	1.423	0.015	1.421	0.013
9	1.479	1.458	-0.021	1.450	-0.029
c	1.409	1.422	0.013	1.422	0.013
d	1.408	1.423	0.015	1.421	0.013
10	1.492	1.487	-0.005	1.485	-0.007
e	1.405	1.410	0.005	1.407	0.002
f	1.404	1.409	0.005	1.406	0.002
11	1.492	1.487	-0.005	1.485	-0.007
g	1.405	1.410	0.005	1.407	0.002
h	1.404	1.409	0.005	1.406	0.002
angle (°)					
γ_1	111.4	105.6	-5.8	112.9	1.5
γ_2	92.5	93.3	0.8	90.5	-2.0
dihedral (°)					
ϕ_1	50.4	37.6	-12.8	31.6	-18.8
ϕ_2	50.4	37.6	-12.8	31.6	-18.8
ϕ_3	57.5	55.4	-2.1	59.2	1.7
ϕ_4	57.5	55.4	-2.1	59.2	1.7

Table 4.2 Selected geometric parameters for the neutral, radical-anion, and radical-cation forms of **II** at the B3LYP/6-31G* level.

	neutral	anion	Δ(A-N)	cation	Δ(C-N)
bond (Å)					
1	1.889	1.913	0.024	1.875	-0.014
2	1.889	1.913	0.024	1.875	-0.014
3	1.889	1.863	-0.026	1.906	0.017
4	1.889	1.863	-0.026	1.906	0.017
5	1.368	1.417	0.049	1.408	0.040
6	1.368	1.417	0.049	1.408	0.040
7	1.513	1.455	-0.058	1.463	-0.050
8	1.479	1.463	-0.016	1.451	-0.028
a	1.409	1.420	0.011	1.422	0.013
b	1.409	1.420	0.011	1.421	0.012
9	1.479	1.463	-0.016	1.451	-0.028
c	1.409	1.420	0.011	1.422	0.013
d	1.409	1.420	0.011	1.421	0.012
10	1.492	1.487	-0.005	1.486	-0.006
e	1.405	1.409	0.004	1.407	0.002
f	1.404	1.409	0.005	1.406	0.002
11	1.492	1.487	-0.005	1.486	-0.006
g	1.405	1.409	0.004	1.407	0.002
h	1.404	1.409	0.005	1.406	0.002
angle (°)					
γ_1	111.4	106.6	-4.8	114.2	2.8
γ_2	92.5	93.8	1.3	90.4	-2.1
dihedral (°)					
ϕ_1	47.7	40.0	-7.7	33.4	-14.3
ϕ_2	47.9	40.0	-7.9	33.4	-14.5
ϕ_3	57.8	54.8	-3.0	58.8	1.0
ϕ_4	57.8	54.8	-3.0	58.8	1.0

Table 4.3 Selected geometric parameters for the neutral, radical-anion, and radical-cation forms of **III** at the B3LYP/6-31G* level.

	neutral	anion	Δ(A-N)	cation	Δ(C-N)
bond (Å)					
1	1.887	1.913	0.026	1.870	-0.017
2	1.887	1.913	0.026	1.870	-0.017
3	1.890	1.863	-0.027	1.908	0.018
4	1.890	1.863	-0.027	1.908	0.018
5	1.367	1.418	0.051	1.408	0.041
6	1.367	1.418	0.051	1.408	0.041
7	1.513	1.454	-0.059	1.463	-0.050
8	1.479	1.463	-0.016	1.452	-0.027
a	1.409	1.430	0.021	1.420	0.011
b	1.409	1.420	0.011	1.421	0.012
9	1.479	1.463	-0.016	1.452	-0.027
c	1.409	1.430	0.021	1.420	0.011
d	1.409	1.420	0.011	1.421	0.012
10	1.492	1.488	-0.004	1.487	-0.005
e	1.405	1.409	0.004	1.406	0.001
f	1.404	1.408	0.004	1.406	0.002
11	1.492	1.488	-0.004	1.487	-0.005
g	1.405	1.409	0.004	1.406	0.001
h	1.404	1.408	0.004	1.406	0.002
angle (°)					
γ_1	111.9	106.6	-5.3	115.1	3.2
γ_2	92.4	94.0	1.6	90.2	-2.2
dihedral (°)					
ϕ_1	48.1	37.9	-10.2	33.2	-14.9
ϕ_2	48.1	38.0	-10.1	33.2	-14.9
ϕ_3	57.5	56.2	-1.3	59.6	2.1
ϕ_4	57.5	56.3	-1.2	59.6	2.1

Table 4.4 Selected geometric parameters for the neutral, radical-anion, and radical-cation forms of **IV** at the B3LYP/6-31G* level.

	neutral	anion	Δ(A-N)	cation	Δ(C-N)
bond (Å)					
1	1.871	1.899	0.028	1.854	-0.017
2	1.873	1.903	0.030	1.857	-0.016
3	1.886	1.858	-0.028	1.903	0.017
4	1.885	1.858	-0.027	1.903	0.018
5	1.367	1.416	0.049	1.408	0.041
6	1.367	1.418	0.051	1.408	0.041
7	1.515	1.455	-0.060	1.464	-0.051
8	1.479	1.464	-0.015	1.450	-0.029
a	1.409	1.419	0.010	1.421	0.012
b	1.408	1.419	0.011	1.422	0.014
9	1.479	1.463	-0.160	1.450	-0.029
c	1.409	1.419	0.010	1.421	0.012
d	1.408	1.420	0.012	1.422	0.014
10	1.492	1.487	-0.005	1.485	-0.007
e	1.405	1.409	0.004	1.407	0.002
f	1.404	1.408	0.004	1.406	0.002
11	1.492	1.487	-0.005	1.486	-0.006
g	1.405	1.409	0.004	1.406	0.001
h	1.404	1.409	0.005	1.406	0.002
angle (°)					
γ_1	109.8	105.0	-4.8	112.8	3.0
γ_2	92.9	94.3	1.4	90.8	-2.1
dihedral (°)					
ϕ_1	50.1	40.1	-10.0	32.5	-17.6
ϕ_2	47.0	37.6	-9.4	30.2	-16.8
ϕ_3	57.8	55.8	-2.0	59.5	1.7
ϕ_4	57.7	55.2	-2.5	59.5	1.8

Table 4.5 Selected geometric parameters for the neutral, radical-anion, and radical-cation forms of **V** at the B3LYP/6-31G* level.

	neutral	anion	Δ(A-N)	cation	Δ(C-N)
bond (Å)					
1	1.902	1.939	0.037	1.887	-0.015
2	1.902	1.939	0.037	1.887	-0.015
3	1.874	1.846	-0.028	1.893	0.019
4	1.874	1.846	-0.028	1.893	0.019
5	1.366	1.415	0.049	1.408	0.042
6	1.366	1.415	0.049	1.408	0.042
7	1.516	1.454	-0.062	1.463	-0.053
8	1.481	1.464	-0.017	1.448	-0.033
a	1.408	1.418	0.010	1.423	0.015
b	1.407	1.416	0.009	1.421	0.014
9	1.481	1.464	-0.017	1.448	-0.033
c	1.408	1.418	0.010	1.423	0.015
d	1.407	1.416	0.009	1.421	0.014
10	1.490	1.486	-0.004	1.484	-0.006
e	1.405	1.409	0.004	1.407	0.002
f	1.404	1.408	0.004	1.406	0.002
11	1.490	1.486	-0.004	1.484	-0.006
g	1.405	1.409	0.004	1.407	0.002
h	1.404	1.408	0.004	1.406	0.002
angle (°)					
γ_1	108.8	103.9	-4.9	113.2	4.4
γ_2	93.9	95.1	1.2	91.9	-2.0
dihedral (°)					
ϕ_1	60.0	43.6	-16.4	26.5	-33.5
ϕ_2	60.3	43.6	-16.7	26.5	-33.8
ϕ_3	55.0	55.6	0.6	61.3	6.3
ϕ_4	54.9	55.5	0.6	61.3	6.4

4.3.2 IP and EA measurements and simulations

In order to probe the energies of filled and empty orbitals, PES and IPES data were acquired on vapor-deposited thin films of the 1,1-diaryl-substituted siloles, **II – V.**[18] It should be noted that experimental thin-film IPs for small molecules have previously been shown to be as much as 1 – 1.5 eV lower than the experimental gas-phase values due to extra stabilization of the cation in the solid state through polarization of the surrounding medium;[19-21] accordingly, EA values are expected to be more exothermic in the solid state than the gas phase due to polarization stabilization of the anion. The spectra are shown in Figure 4.3, along with simulations based upon DFT calculations that facilitate interpretation and assignment of the spectra; it should be noted that few such comparisons between theoretical and experimental densities of states of *both* filled and empty orbital structures have been reported.[16]

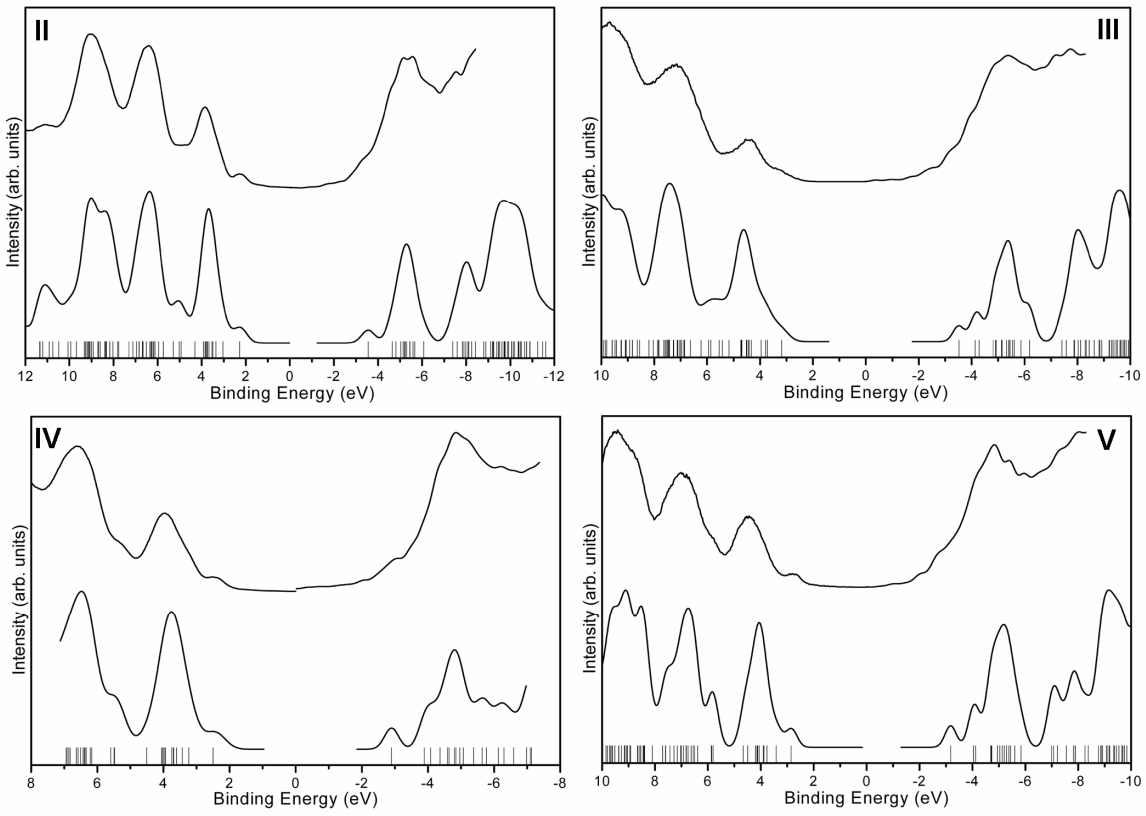

Figure 4.3 Comparison between PES and IPES spectra measured for **II – V**. For each compound, the thin-film [top] and DFT-simulated [bottom] spectra are given; the vertical bars refer to the shifted energies of the molecular orbitals.

The experimentally determined IPs and EAs are given in Table 4.6. These estimates of the adiabatic values are obtained from the onsets of the spectra, with the relatively large error bars at least partially stemming from difficulties associated with accurate determinations of these onsets. The experimental IPs fall in the range 6.05 – 6.78 eV, considerably higher than the solid-state IP values for typical hole-transport (HT) materials such as *N,N'*-diphenyl-*N,N'*-di(3-methylphenyl)-(1,1'-biphenyl)-4,4'-diamine (TPD) (5.38 eV, adiabatic) and NPD (5.5 eV[4, 22]), suggesting a high barrier for hole injection into the siloles from these materials. The EAs (-1.5 – -2.4 eV) may be compared

to values in the range -2.0 to -2.5 eV measured for the widely used electron-transport material tris(quinolin-8-olato) aluminum(III) (Alq_3).[1] This suggests that electron-injection barriers similar to those obtained with Alq_3 could be realized with some of these siloles. The experimental IP and EA values for **II**, **III**, and **IV** are close, within experimental error, whereas **V** is harder to oxidize and easier to reduce than **II – IV**. Additionally, evaluations of the oxidation and reduction energies by cyclic voltammetry, which is a more routine experiment than either PES or IPES, reveal a similar picture: **II – V** are similar to one another in IP and EA, with **V** both significantly easier to reduce and harder to oxidize than **I – IV**.[5] These results are consistent with previous cyclic voltammetry studies upon the influence of 1,1-substituents in which Dhiman *et al*. reported that siloles with electron-withdrawing 1,1-substituents (*e.g.*, chlorine) show higher first oxidation potentials.[7]

Table 4.6 Experimental PES and IPES estimates of thin-film adiabatic IP and EA (eV, from onset) and DFT calculations of gas-phase adiabatic and vertical IP and EA.

	IP			EA		
	PES	DFT		IPES	DFT	
		adiabatic	vertical		adiabatic	vertical
I	-----	6.30	6.54	-----	-0.62	-0.34
II	6.19±0.10	6.19	6.42	-1.85±0.40	-0.78	-0.52
III	6.40±0.10	6.10	6.29	-1.49±0.40	-0.83	-0.58
IV	6.05±0.10	6.23	6.46	-1.93±0.40	-0.85	-0.58
V	6.78±0.10	6.49	6.85	-2.41±0.40	-1.16	-0.86

The adiabatic and vertical gas-phase values for IP and EA from DFT self-consistent-field calculations are included for comparison and reproduce the observed patterns. While the

calculated *gas-phase* values for the IP are similar to those of the experimental *solid-state* PES measurements ($\Delta \sim 0.00 - 0.30$ eV), those for the EA ($\Delta \sim 0.66 - 1.25$ eV) differ rather significantly. These results can be understood in light of the work of Tsiper and Soos.[23] Charge carriers, whether holes or electrons, correspond to molecular ions embedded in a network of neutral molecules that can be thought of as self-consistent polarization clouds.[23] Therefore, a number of factors can influence the polarization effects of the charge carrier, including: crystal packing, intramolecular and intermolecular vibrations, and molecular electrostatic interactions (especially those from neutral molecules containing heteroatoms).[23] In molecular solids, even in the limit of zero-overlap, these electrostatic interactions between neighboring molecules are of considerable importance.[24] For anthracene and perylene-3,4,9,10-tetracarboxylic-3,4,9,10-dianhydride (PTCDA), even when neglecting vibrational parameters, very different polarization energies are found; while anthracene has similar polarization energies for both holes and electrons, the polarization energies for holes and electrons in PTCDA are strikingly different (greater than a 2 eV difference).[23] In addition to the solid-state polarization effects, the rather good agreement between the calculated gas-phase and experimental solid-state IP energies is a rather fortuitous result of the methodology chosen. In general, one would expect that as the level of theory and/or basis set were increased, agreement between the calculated and experimental gas-phase data would converge, while the calculated gas-phase and experimental solid-state data would differ by an amount corresponding to the solid-state polarization energy.

4.3.3 Electronic structure

The calculated highest occupied molecular orbitals (HOMOs) and lowest unoccupied molecular orbitals (LUMOs) – experimentally probed by the PES and IPES measurements, respectively – for **II – V** do not vary drastically in appearance among the different compounds; moreover, they are similar to those reported in other computational studies of siloles.[8, 9, 25] The HOMO is similar to the Hückel HOMO for *cisoid*-butadiene, with some additional antibonding contributions from the HOMOs of 2,5-, and to a lesser extent, 3,4-phenyl groups, see Figure 4.4. The LUMO resembles the LUMO of butadiene with additional in-phase contributions from a silicon-aryl σ*-orbital and from the local LUMOs of the 2,3,4,5-phenyl groups. Significantly, neither HOMO nor LUMO shows any obvious contributions from the π-orbitals of the 1,1-diaryl groups; thus, the variation of the substituents on silicon appears to affect the electronic structure through a principally inductive mechanism. While this has been proposed in previous studies,[9] it has also been suggested that when the 1,1-substituents are phenyl, π-effects are important.[9] However, support for a mainly inductive role of the aryl groups comes from the similar effects of a given substituent on both HOMO and LUMO energies, see Table 4.7. Moreover, the computed IP and EA data suggest slightly lower lying HOMO and LUMO for the thienyl species, **IV**; although thiophene is an electron-rich π-system, it has previously been shown that the 2-thienyl group is inductively somewhat electron-withdrawing.[26]

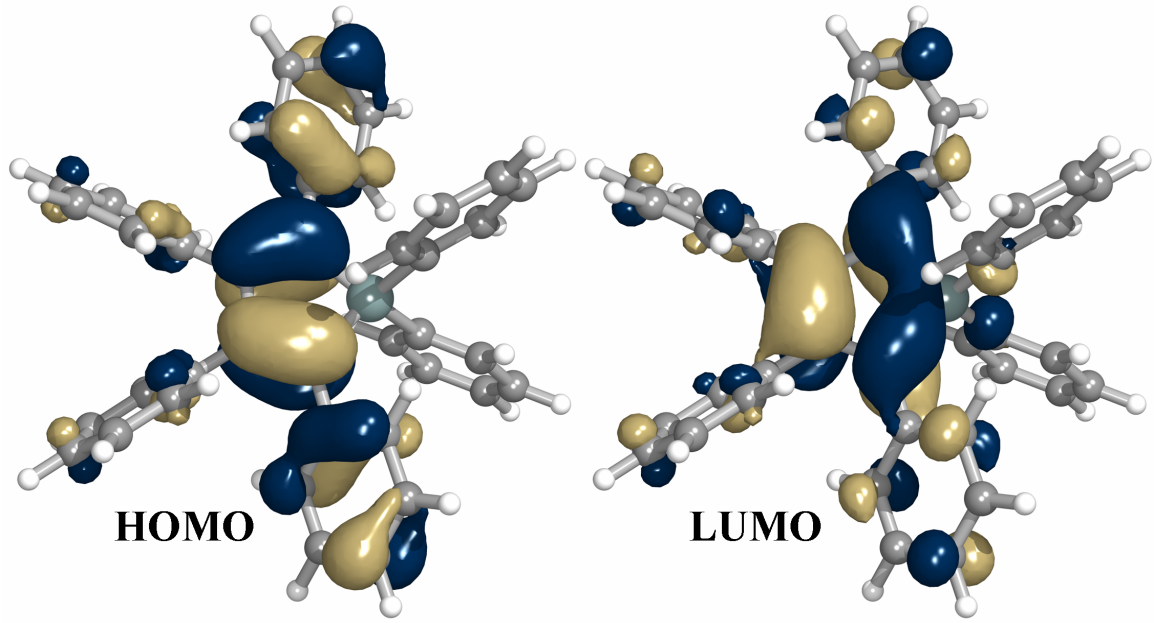

Figure 4.4 B3LYP/6-31G*-calculated highest occupied (HOMO) [left] and lowest unoccupied (LUMO) [right] one-electron molecular orbitals for **II**.

Table 4.7 B3LYP/6-31G*-calculated valence molecular orbital energies (eV) of **I – V**.

	I	II	III	IV	V
LUMO+2	-0.05	-0.41	-0.88	-0.55	-1.08
LUMO+1	-0.27	-0.57	-1.03	-0.75	-1.16
LUMO	-1.59	-1.67	-1.65	-1.74	-2.01
HOMO	-5.29	-5.25	-5.22	-5.29	-5.69
HOMO-1	-6.03	-6.01	-5.77	-6.02	-6.25
HOMO-2	-6.37	-6.33	-5.84	-6.22	-6.60

4.3.4 Intramolecular reorganization energies

Since siloles can show moderate electron mobilities in excess of that seen for Alq_3, we were interested in comparing the barriers to electron transfer between the radical-anion and neutral species in the two systems. We calculated the intramolecular contribution (λ_i) to the total reorganization energy for electron transfer (see Chapter 2), and the corresponding value for hole transfer, from the adiabatic potential surfaces for siloles **I – V**; the results are compared in Table 4.8. The total reorganization energies for electron transfer are approximately 0.5 eV, values comparable with those previously obtained for other siloles at the same level of theory,[25] while those for hole transfer are in the range 0.4 – 0.6 eV. The reorganization energy values for electron transfer are approximately twice that calculated at the same level for Alq_3,[27] while those for hole transfer are approximately four to five times those calculated for pentacene[28] and nearly twice those calculated for N,N'-diphenyl-N,N'-bis(3-methylphenyl)-([1,1'-biphenyl])-4,4'-diamine (TPD).[29, 30] Thus, the differences in electron mobilities that have been seen between siloles and Alq_3 are likely to be due to differences in intermolecular orbital overlap or to morphological effects (such as trapping at grain boundaries), rather than to differences in λ_i. The localized nature of the geometric modifications that occur on both reduction and oxidation of the silole systems are responsible for the relatively large reorganization energy.

Table 4.8 B3LYP/6-31G* intramolecular reorganization energies as determined by ΔSCF.[a]

	neutral/cation			neutral/anion		
	λ_1 (eV)	λ_2 (eV)	λ_i (eV)	λ_1 (eV)	λ_2 (eV)	λ_i (eV)
I[b]	0.21	0.24	0.45	0.24 *0.22*	0.27 *0.28*	0.51 *0.50*
II	0.20	0.22	0.42	0.23	0.26	0.49
III	0.19	0.19	0.38	0.24	0.26	0.50
IV	0.21	0.23	0.44	0.24	0.27	0.51
V	0.25	0.36	0.61	0.26	0.30	0.56

[a] The total intramolecular reorganization energy (λ_i) combines the relaxation energies of the initially neutral molecule (λ_1) and the initially ionized molecule (λ_2) upon electron transfer (polaron hopping). [b] For **I**, values in italics determined by vibrational mode analysis.

To gain further insight into the reorganization energy associated with the electron-exchange reaction between neutral and radical-anion siloles, we explored the contribution of different vibrational modes to the reorganization energy. Since the reorganization energies do not depend strongly upon the substituents on the silicon atom, and since the geometric changes do not extend into this substituent, we investigated the simplest system, **I**; in addition, we also examined the model compound **I',** in which the 3,4-phenyl groups are replaced by hydrogen atoms, in order to reduce the number of degrees of freedom and simplify interpretation. The contribution of normal modes to the reorganization energy can be obtained through the relation:

$$\lambda_{total} = \sum \lambda_i = \sum S_i \hbar \omega_i \tag{4.1}$$

where S is the Huang-Rhys factor (see Chapter 2).[31, 32] Normal mode analysis for **I'** gives a value of 0.51 eV for λ_i, in good agreement with the value (0.47 eV) obtained from the adiabatic potential surfaces, and of similar magnitude to the values in Table 4.8 for **I – V**. Five vibrational modes in **I'** within the neutral potential well comprise 73% of the total relaxation energy, as shown in Table 4.9. Of these five modes, three ring-breathing

modes provide 51% of the total relaxation energy, while rotation of the phenyl rings with respect to the central silole ring makes up 17% of the total relaxation energy. We note that previous experimental evidence from a variety of techniques (solution fluorescence spectroscopy with variable temperatures and solvent viscosities, along with variable temperature NMR experiments) suggests that such a rotational mode plays an important role in the intensity dampening of singlet emission for siloles in solution, and it is thought that restriction of such rotation is responsible for the aggregation-induced emission effects often observed for substituted silole molecules.[33, 34] In the radical-anion potential well, 65% of the total relaxation energy is composed of six vibrational modes. The majority of the relaxation energy contribution (56%) comes from various ring-breathing mode combinations of the silole and phenyl rings, with significant contribution (9%) coming from phenyl-ring rotation with respect to the central silole ring. Thus, for this model system, the majority of the total intramolecular reorganization energy arises from combinations of ring-breathing modes of the central silole ring and the 2,5-substituted phenyl rings.

Table 4.9 Representative vibrational modes corresponding to the relaxation in the neutral and radical-anion potential surfaces of **I'**.

	ω (cm^{-1})	S	energy[a] (eV)	mode description
neutral	29	12.2	0.044	rotation of phenyl rings
	182	0.58	0.013	methyl-silicon-methyl bend
	947	0.12	0.014	ring breathing of silole & phenyl rings
	1536	0.20	0.038	ring breathing of silole & phenyl rings
	1550	0.40	0.077	ring breathing of silole & phenyl rings
anion	21	8.83	0.023	rotation of phenyl rings
	934	0.12	0.014	ring breathing of silole & phenyl rings
	1250	0.19	0.030	ring breathing of silole & phenyl rings
	1485	0.22	0.040	ring breathing of silole & phenyl rings
	1494	0.15	0.028	ring breathing of silole & phenyl rings
	1537	0.07	0.014	ring breathing of silole & phenyl rings
	1646	0.07	0.014	ring breathing of silole & phenyl rings

[a] The energy value represents the contribution of each mode to the total relaxation energy.

Normal mode analysis of **I** reveals a similar picture to that provided by **I'**, though the complexity of the modes involved is much more significant due to the number of intrinsic degrees of freedom in the molecule. Again, λ_i obtained by the normal mode analysis (0.50 eV) is close to that obtained via the adiabatic potential surface analysis (0.51 eV). Here, upwards of fifteen vibrational modes play significant roles in the relaxation processes on the neutral and radical-anion surfaces, Table 4.10. As with **I'**, the predominant vibrations consist of various ring breathing modes and phenyl ring torsions, as well as Me-Si stretches/bends.

Table 4.10 Selected vibrational modes corresponding to the relaxation in the neutral and radical-anion potential surfaces of **I**.

	ω (cm^{-1})	S	energy[a] (eV)	mode description
neutral	24	0.019	6.385	phenyl ring torsion with Me twist
	35	0.007	1.613	phenyl ring torsion with Me twist
	49	0.005	0.823	phenyl ring torsion with Me twist
	70	0.005	0.576	phenyl ring torsion with Me twist
	95	0.006	0.509	Me twist with ring motion
	174	0.008	0.371	Me-Si-Me bend with ring motion
	535	0.006	0.090	C-H modes on Me and phenyls
	685	0.010	0.118	Me-Si-Me bend with ring breathing
	956	0.018	0.152	ring breathing
	1527	0.022	0.116	ring breathing
	1564	0.065	0.335	ring breathing
anion	27	0.019	5.676	phenyl ring torsion with Me twist
	48	0.016	2.689	phenyl ring torsion with Me twist
	58	0.021	2.920	phenyl ring torsion with Me twist
	82	0.007	0.689	phenyl ring torsion with Me twist
	108	0.044	3.286	phenyl ring torsion with Me twist
	179	0.013	0.586	Me-Si-Me bend with ring motion
	678	0.009	0.107	Me-Si-Me bend with ring breathing
	872	0.007	0.065	C-H modes on Me and phenyls
	953	0.017	0.144	ring breathing
	1248	0.017	0.110	ring breathing
	1306	0.011	0.068	ring breathing
	1347	0.012	0.072	ring breathing
	1421	0.041	0.233	ring breathing

[a] The energy value represents the contribution of each mode to the total relaxation energy.

4.3.5 UV/vis absorption and fluorescence spectroscopy

Solution (chloroform) and thin-film UV/vis absorption spectra for the silole systems are shown in Figure 4.5 with the spectral characteristics summarized in Table 4.11. The lowest energy maxima are essentially independent of the identity of the aryl group and are only slightly shifted between the solution and solid state, consistent with previous

observations for other siloles.[35, 36] TDDFT calculations indicate that these transitions can be described as predominantly HOMO → LUMO in character (*i.e.*, π–π* silacyclopentadiene transitions), but somewhat underestimate the transition energies.[37]

Table 4.11 Experimental and TDDFT absorption and experimental emission characteristics for the lowest-lying excited states of **I – V**.

	absorption (eV)[a]		emission (eV)[a]
	experiment	TDDFT	
I	3.43 (3.41)	3.23	2.61 (2.54)
II	3.38 (3.36)	3.10	2.54 (2.53)
III	3.37 (3.38)	3.08	2.53 (2.51)
IV	3.33 (3.31)	3.05	2.51 (2.52)
V	3.30 (3.28)	3.14	2.53 (2.46)

[a] Measured in chloroform; data in thin films are given in the parentheses.

Solution (chloroform) and thin-film PL spectra of the 1,1-substituted siloles **I – V** are shown in Figure 4.5, with emission data provided in Table 4.11. All five siloles show weak blue-green luminescence in solution, with very similar emission spectra peaked around 2.51 – 2.61 eV. Consistent with other siloles,[33, 34] the fluorescence appears to be considerably brighter in the solid state relative to solution; however, the maxima are seen at similar energies (the features seen in the solid-state bands are slightly narrower, but this is presumably attributable to self-absorption).[38]

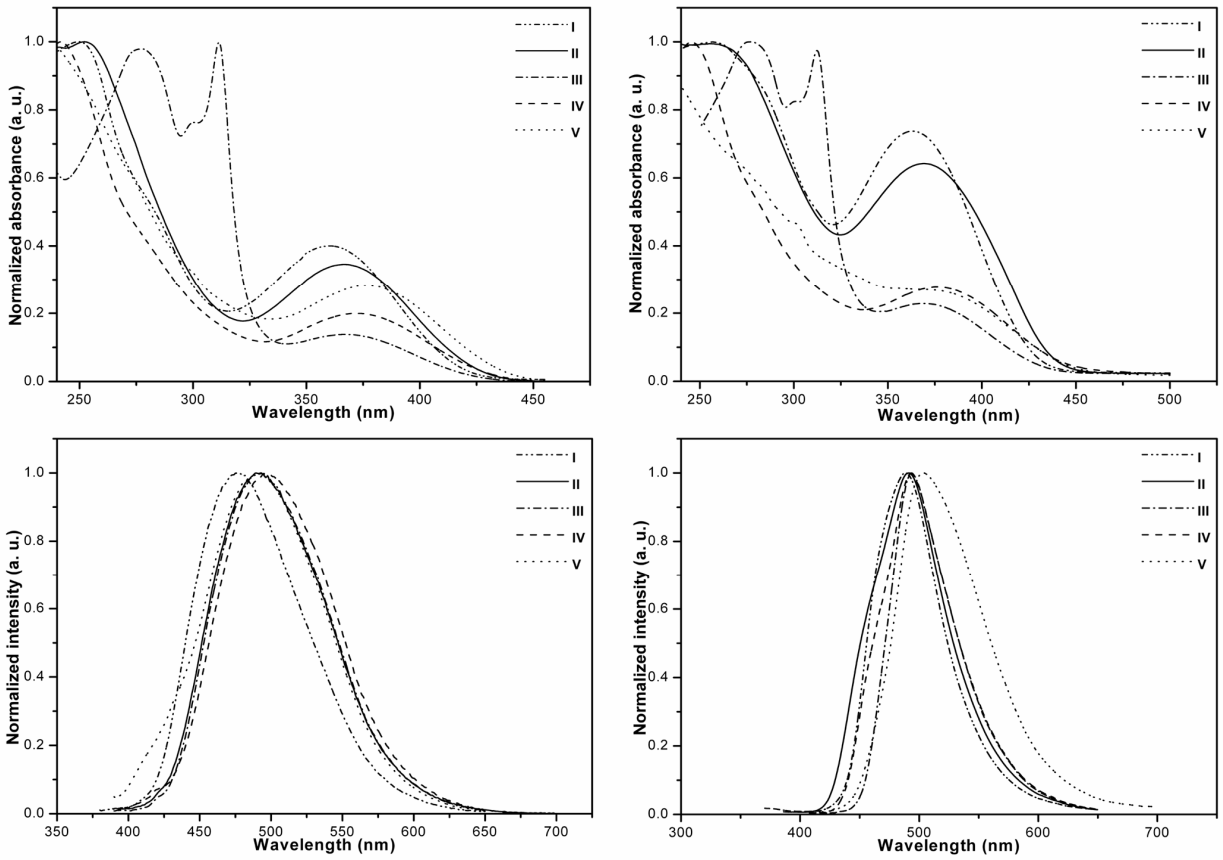

Figure 4.5 Solution (chloroform) [top left] and thin-film [top right] UV/vis absorption spectra and solution (chloroform) [bottom left] and thin-film [bottom right] fluorescence spectra of **I – V**.

From the magnitude of the bulk transport gap (E_t), also known as single-particle gap, and the optical properties, one can estimate the solid-state exciton binding energy (E_B). This is the energy required for photocharge generation of a silole radical anion and silole radical cation from an excited silole molecule (Frenkel exciton), *i.e.*, the energy required for the reaction:

$$M^* + M = M^+ + M^- \tag{4.2}$$

which is given by:

$$E_B = E_t - E_{op} \tag{4.3}$$

where E_{op} is the 0-0 maximum. We evaluated E_t using a procedure previously established by Hill *et al*.[39] E_t is taken as the experimental peak-to-peak HOMO-to-LUMO gap measured by PES and IPES, reduced by 0.8 eV to account for: (i) the increase in polarization from surface to bulk (0.3 eV for the hole state and 0.3 eV for the electron states); and (ii) the loss of energy of the photoemitted electron (PES) and injected electron (IPES) to molecular vibration (2 x 0.1 eV; *i.e.*, providing an approximate correction from vertical to adiabatic values). The experimental values shown in Table 4.12 indicate exciton binding energies in the range 1.0 – 1.7 eV when E_{op} is estimated from the absorption maximum, similar to those estimated by the same method for other organic systems.[39, 40] Values obtained from the DFT adiabatic surface energies and from TDDFT absorption energies are much larger (*ca.* 2 eV), though with a similar variation in energy across the series (0.25 eV); the discrepancy between experimental and DFT estimates of E_B can be attributed at least partly to the neglect in the DFT approach of the solid-state polarization effects that stabilize both cations and anions relative to the gas phase.

Table 4.12 Exciton binding energies as determined by PES/IPES and DFT calculated ionization potentials and electron affinities, and solid-state UV/vis and TDDFT absorption data.

Method		IP (eV)	EA (eV)[a]	E_{op} (eV)[b]	E_t (eV)[c]	E_B (eV)
PES/IPES	I	-----	-----		-----	-----
	II	6.19	-1.85	2.97 *3.36*	4.54	1.57 *1.18*
	III	6.40	-1.49	2.94 *3.38*	5.11	2.17 *1.73*
	IV	6.05	-1.93	2.94 *3.31*	4.32	1.38 *1.01*
	V	6.78	-2.41	2.91 *3.28*	4.57	1.66 *1.29*
DFT/TDDFT	I	6.30	-0.62	3.23	5.88	2.65
	II	6.19	-0.78	3.10	5.0	1.90
	III	6.10	-0.83	3.09	5.9	2.81
	IV	6.23	-0.85	3.04	4.6	1.56
	V	6.49	-1.16	3.14	5.25	2.11

[a] Note that the electron affinities are calculated by subtracting the total energy on the neutral electronic configuration from the energy of the radical-anion electronic configuration. [b] Experimental values for E_{op} estimated from the midpoint of absorption and fluorescence and from the absorption maxima (italics), for direct comparison with the DFT/TDDFT results. [c] Experimental values of the transport gap are obtained as explained in the text

4.4 Conclusion

The density of electronic states for **II** – **IV** obtained from DFT calculations correspond very well to the solid-state PES and IPES data. Of the functional groups examined, only the very strongly electron-withdrawing pentafluorophenyl groups have a significant effect on the IP and EA. The variations in the EA and IP of 1,1-diaryl-2,3,4,5-tetraphenylsiloles appear to be largely dictated by inductive effects. This conclusion is supported by ΔSCF calculations of both IP and EA. Thus, thiophene, despite having an electron-rich π-system, acts as a weakly electron-withdrawing group on the silole skeleton when attached to the silicon atom. Another result of the inductive role played by

the aryl group is that the HOMO-LUMO gap, and, hence, the optical absorption or fluorescence properties, are rather insensitive to the identity of the aryl unit.

We have also used DFT to calculate the reorganization energy associated with the electron-transfer reactions of siloles and their radical cations or anions. These reorganization energies are somewhat larger than for Alq_3, suggesting that this is not the factor determining the higher electron mobilities reported in siloles. From optical data and the transport gap deduced from PES and IPES data, we have been able to estimate exciton binding energies for siloles. Finally, the similarity of the EAs we have measured to that of the widely used Alq_3, combined with the high electron mobilities previously reported for other siloles, suggests these materials could potentially replace Alq_3 in many electron-transport applications; the C_6F_5 derivative, which has the lowest lying LUMO and, therefore, the lowest barrier to electron injection, is particularly promising.

4.5 References

(1) Cahen, D.; Kahn, A., *Adv. Mat.* **2003,** 15, 271.

(2) Alvarado, S. F.; Rossi, L.; Muller, P.; Seidler, P. F.; Riess, W., *IBM J. Res. & Dev.* **2001,** 45, 89.

(3) Mäkinen, A. J.; Uchida, M.; Kafafi, Z. H., *J. Appl. Phys.* **2004,** 95, 2832.

(4) Kahn, A.; Koch, N.; Gao, W. Y., *J. Polym. Sci. B* **2003,** 41, 2529.

(5) Zhan, X.; Risko, C.; Amy, F.; Chan, C.; Zhao, W.; Barlow, S.; Kahn, A.; Brédas, J. L.; Marder, S. R., *J. Am. Chem. Soc.* **2005,** 127, 9021.

(6) Tang, B. Z.; Zhan, X. W.; Yu, G.; Lee, P. P. S.; Liu, Y. Q.; Zhu, D. B., *J. Mater. Chem.* **2001,** 11, 2974.

(7) Dhiman, A.; Zhang, Z. R.; West, R.; Becker, J. Y., *J. Electroanal. Chem.* **2004,** 569, 15.

(8) Ferman, J.; Kakareka, J. P.; Klooster, W. T.; Mullin, J. L.; Quattrucci, J.; Ricci, J. S.; Tracy, J. J.; Vining, W. J.; Wallace, S., *Inorg. Chem.* **1999,** 38, 2464.

(9) Yamaguchi, S.; Jin, R. Z.; Tamao, K., *J. Organomet. Chem.* **1998,** 559, 73.

(10) Mäkinen, A. J.; Uchida, M.; Kafafi, Z. H., *Appl. Phys. Lett.* **2003,** 82, 3889.

(11) Palilis, L. C.; Mäkinen, A. J.; Murata, H.; Uchida, M.; Kafafi, Z. H., *Proceedings of SPIE-The International Society for Optical Engineering* **2003,** 4800, 256.

(12) Mäkinen, A. J.; Uchida, M.; Kafafi, Z. H., *J. Appl. Phys.* **2004,** 95, 2832.

(13) Becke, A. D., *Phys. Rev. A* **1988,** 38, 3098.

(14) Becke, A. D., *J. Chem. Phys.* **1993,** 98, 5648.

(15) Lee, C.; Yang, W.; Parr, R. G., *Phys. Rev. B* **1988,** 37, 785.

(16) Hill, I. G.; Kahn, A.; Cornil, J.; dos Santos, D. A.; Brédas, J. L., *Chem. Phys. Lett.* **2000,** 317, 444.

(17) Frisch, M. J.; Trucks, G. W.; Schlegel, H. B.; Scuseria, G. E.; Robb, M. A.; Cheeseman, J. R.; Zakrzewski, V. G.; Montgomery, J., J.A.; Stratmann, R. E.; Burant, J. C.; Dapprich, S.; Millam, J. M.; Daniels, A. D.; Kudin, K. N.; Strain, M. C.; Farkas, O.; Tomasi, J.; Barone, V.; Cossi, M.; Cammi, R.; Mennucci, B.; Pomelli, C.; Adamo, C.; Clifford, S.; Ochterski, J.; Petersson, G. A.; Ayala, P. Y.; Cui, Q.; Morokuma, K.; Salvador, P.; Dannenberg, J. J.; Malick, D. K.; Rabuck, A. D.; Raghavachari, K.; Foresman, J. B.; Cioslowski, J.; Ortiz, J. V.; Baboul, A. G.; Stefanov, B. B.; Liu, G.; Liashenko, A.; Piskorz, P.; Komaromi, I.; Gomperts, R.; Martin, R. L.; Fox, D. J.; Keith, T.; Al-Laham, M. A.; Peng, C. Y.; Nanayakkara, A.; Challacombe, M.; Gill, P. M. W.; Johnson, B.; Chen, W.; Wong, M. W.; Andres, J. L.; Gonzalez, C.; Head-Gordon, M.; Replogle, E. S.; Pople, J. A. *Gaussian98, Rev. A.11*, 1998.

(18) PES and IPES spectra for **I** were not obtained since **I** was too volatile under the high-vacuum conditions required for the spectroscopy.

(19) Sato, N.; Inokuchi, H.; Silinsh, E. A., *Chem. Phys.* **1987,** 115, 269.

(20) Silinsh, E. A.; Capek, V., *Organic Molecular Crystals: Interaction, Localization, and Transport Phenomena*. AIP Press: New York, 1994.

(21) Anderson, J. D.; McDonald, E. M.; Lee, P. A.; Anderson, M. L.; Ritchie, E. L.; Hall, H. K.; Hopkins, T.; Mash, E. A.; Wang, J.; Padias, A.; Thayumanavan, S.; Barlow, S.; Marder, S. R.; Jabbour, G. E.; Shaheen, S.; Kippelen, B.; Peyghambarian, N.; Wightman, R. M.; Armstrong, N. R., *J. Am. Chem. Soc.* **1998,** 120, 9646.

(22) Gao, W. Y.; Kahn, A., *J. Appl. Phys.* **2003,** 94, 359.

(23) Tsiper, E. V.; Soos, Z. G., *Phys. Rev. B: Condens. Matter Mater. Phys.* **2001,** 64, 195124.

(24) Tsiper, E. V.; Soos, Z. G.; Gao, W. Y.; Kahn, A., *Chem. Phys. Lett.* **2002,** 360, 47.

(25) Risko, C.; Kushto, G. P.; Kafafi, Z. H.; Brédas, J. L., *J. Chem. Phys.* **2004,** 121, 9031.

(26) Fringuel, F.; Marino, G.; Taticchi, A., *J. Chem. Soc. B* **1971**, 2302.

(27) Lin, B. C.; Cheng, C. P.; You, Z.-Q.; Hsu, C.P., *J. Am. Chem. Soc.* **2005,** 127, 66.

(28) Gruhn, N. E.; da Silva, D. A.; Bill, T. G.; Malagoli, M.; Coropceanu, V.; Kahn, A.; Brédas, J. L., *J. Am. Chem. Soc.* **2002,** 124, 7918.

(29) Malagoli, M.; Brédas, J. L., *Chem. Phys. Lett.* **2000,** 327, 13.

(30) Lin, B. C.; Cheng, C. P.; Lao, Z. P. M., *J. Phys. Chem. B* **2003,** 107, 5241.

(31) Barbara, P. F.; Meyer, T. J.; Ratner, M. A., *J. Phys. Chem.* **1996,** 100, 13148.

(32) Pope, M.; Swenberg, C. E., *Electronic Processes in Organic Crystals and Polymers*. 2 ed.; Oxford University Press: New York, 1999.

(33) Luo, J. D.; Xie, Z. L.; Lam, J. W. Y.; Cheng, L.; Chen, H. Y.; Qiu, C. F.; Kwok, H. S.; Zhan, X. W.; Liu, Y. Q.; Zhu, D. B.; Tang, B. Z., *Chem. Commun.* **2001**, 1740.

(34) Chen, J. W.; Law, C. C. W.; Lam, J. W. Y.; Dong, Y. P.; Lo, S. M. F.; Williams, I. D.; Zhu, D. B.; Tang, B. Z., *Chem. Mater.* **2003,** 15, 1535.

(35) It should also be noted that spectra in non-polar solvents (hexane or toluene) showed almost identical absorption maxima, as has been previously reported for other silole systems, see Reference 8.

(36) We attribute the sharp absorption peaks in **III** to π-π* transitions within the fluorenyl groups.

(37) The calculations do not successfully reproduce the slight variations in absorption maxima between the compounds; in particular the experimental maximum for the pentafluorophenyl derivative **V** is slightly red-shifted relative to the phenyl compound, **II**, but is calculated to be slightly blue shifted; these differences may be due to experimental maxima being somewhat shifted from the vertical transition energies due to overlap with the tails of the higher energy (Ph and other aryl π-π*) transitions.

(38) The fact that strong luminescence is observed in the solid state, along with minimal shifts in the luminescence energy, is consistent with previous reports for siloles. These results are in contrast to 'typical' organic emitters that tend to undergo various degrees of aggregation and excimer formation that leads to concentration-dependent electroluminescence quenching, emission band broadening, and bathochromic shifts. The fact that siloles do not undergo these processes has been explained by the quenching of non-radiative decay routes in the solid state, see Reference 34.

(39) Hill, I.; Kahn, A.; Soos, Z.; Pascal, R., *Chem. Phys. Lett.* **2000,** 327, 181.

(40) Knupfer, M., *Appl. Phys. A* **2003,** 77, 623.

CHAPTER 5

BIS-ARYL SUBSTITUTED DIOXABORINES AS ELECTRON-TRANSPORT MATERIALS: A COMPARATIVE DENSITY FUNCTIONAL THEORY INVESTIGATION WITH OXADIAZOLES AND SILOLES

5.1 Introduction

The photoexcited state properties of dioxaborine [2,2-difluoro-1,3,2-oxaoxoniaboratine] derivatives have undergone investigation for a wide variety of functions, including: photocycloaddition and photoinduced electron-transfer reactions[1, 2] and two-photon absorption chromophores for the photodeposition of silver.[3] More recently, dioxaborines have also been envisioned as building blocks for new series of molecular electron-transport materials in organic electronic devices due to their electronic (high electron affinities, reversible electrochemistry) and optical (absorption in the visible range, large fluorescence quantum yields) properties.[4, 5] Recent time of flight measurements have revealed electron mobilities two orders of magnitude larger than tris(quinolin-8-olato) aluminum(III) (Alq_3) for this class of materials.[4]

In this Chapter, we report the results of a preliminary quantum-chemical assessment of bis-aryl substituted dioxaborines and their comparison to oxadiazole and silole model compounds, see Figure 5.1.[6] We use Density Functional Theory to assess the electronic structure, vertical electron affinities, and intramolecular reorganization energies of these

molecules. Our analysis also allows us to directly compare the one-particle molecular orbital properties that are commonly found in organic device literature (*i.e.*, molecular orbital levels aligned relative to the Fermi energy of the electrodes) with (physically observable) properties such as electron affinities.

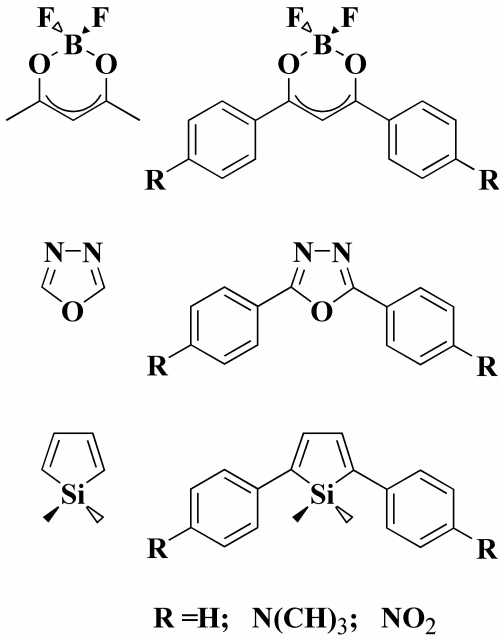

Figure 5.1 Chemical structure of dioxaborine (top), oxadiazole (middle), silole (bottom), and their bis-aryl substitution patterns.

5.2 Theoretical methodology

The systems of interest include dioxaborine bis-aryl substituted at the 1- and 3-positions, and oxadiazole and 1,1-dimethylsilole substituted at the 2-and 5-positions; the aryl substituents are phenyl, p-N,N-dimethylaminophenyl, and p-nitrophenyl, see Figure 5.1.

Geometry optimizations of the neutral and radical-anion electronic configurations were performed by Density Functional Theory (DFT) calculations with the B3LYP functionals and a 6-31G* double-zeta plus polarization basis set. DFT methods have been proven to successfully evaluate the geometric and energetic properties of a number of small-molecule radical-anions with the incorporation of basis sets containing diffuse functions.[7] To account for the proper description of the radical-anion state and provide qualitative estimates of such properties as electron affinity, single-point calculations were carried out with a 6-31+G* basis set for each molecular structure optimized at the 6-31G* level. All DFT calculations were carried out with Gaussian98 (Revision A.11).[8]

5.3 Results and discussion

5.3.1 Molecular orbitals

The DFT-calculated highest occupied π–molecular orbitals for the dioxaborine, oxadiazole, and silole rings fall within a range of 2 eV, see Table 5.1, with the oxadiazole molecular orbital being the most stable. The dioxaborine (-7.68 eV) highest-occupied molecular orbital (HOMO), see Figure 5.2, is characterized by an allylic-like orbital pattern between the three carbon atoms contained within the ring and an antibonding pattern with the oxygen atoms.[5] For oxadiazole (-8.42 eV) and silole (-6.25 eV), the highest π-molecular orbitals reside on the *cis*-diazabutadiene and *cis*-butadiene moieties, respectively, the presence of the nitrogen atoms in oxadiazole pushing the orbital energy down; the bonding – antibonding pattern is consistent with butadiene structures. The

lowest-unoccupied molecular orbitals (LUMO) of the unsubstituted rings lie within a slightly smaller range of energies (~1.5 eV). Importantly, the LUMO energy for dioxaborine lies significantly lower than the oxadiazole and silole equivalents. The dioxaborine LUMO (calculated here to be -2.57 eV) possess the interesting feature of an allylic-like non-bonding orbital among the three carbon atoms contained within the ring. The oxadiazole LUMO (-1.01 eV) is characterized by a bonding interaction between the two nitrogen atoms and an antibonding interaction amongst all other heavy atoms. As described earlier, the silole LUMO (-1.47 eV) reveals the characteristic σ^*–π^* conjugation in the ring due to interaction between the σ^*–orbitals of the two exocyclic σ-bonds on the ring silicon with the π^*–orbital of the butadiene moiety that provides the stable features of the molecular orbital.

Table 5.1 HOMO and LUMO energies for the dioxaborine, oxadiazole, and silole compounds at the B3LYP/6-31+G*//B3LYP/6-31G* level of theory. For each compound, the energy difference from the reference dioxaborine, oxadiazole, or silole ring is given in parentheses.

compound	bis-substituent	HOMO (eV)	LUMO (eV)
dioxaborine	methyl	-7.68 (0.00)	-2.57 (0.00)
	N,N-dimethylaminophenyl	-5.55 (+2.13)	-2.22 (+0.35)
	phenylene	-7.04 (+0.64)	-3.04 (-0.47)
	nitrophenyl	-7.97 (-0.29)	-4.23 (-1.66)
oxadiazole	hydrogen	-8.42 (0.00)	-1.01 (0.00)
	N,N-dimethylaminophenyl	-5.09 (+3.33)	-1.18 (-0.17)
	phenylene	-6.44 (+1.98)	-1.96 (-0.95)
	nitrophenyl	-7.49 (+0.93)	-3.67 (-2.66)
silole	hydrogen	-6.25 (0.00)	-1.47 (0.00)
	N,N-dimethylaminophenyl	-4.47 (+1.78)	-1.50 (-0.03)
	phenylene	-5.46 (+0.79)	-2.04 (-0.57)
	nitrophenyl	-6.45 (-0.20)	-3.45 (-1.98)

a) The energy of the highest π-molecular orbital was taken as the reference value due to the fact that the B3LYP/6-31+G*//B3LYP/6-31G* HOMO was of σ-nature.

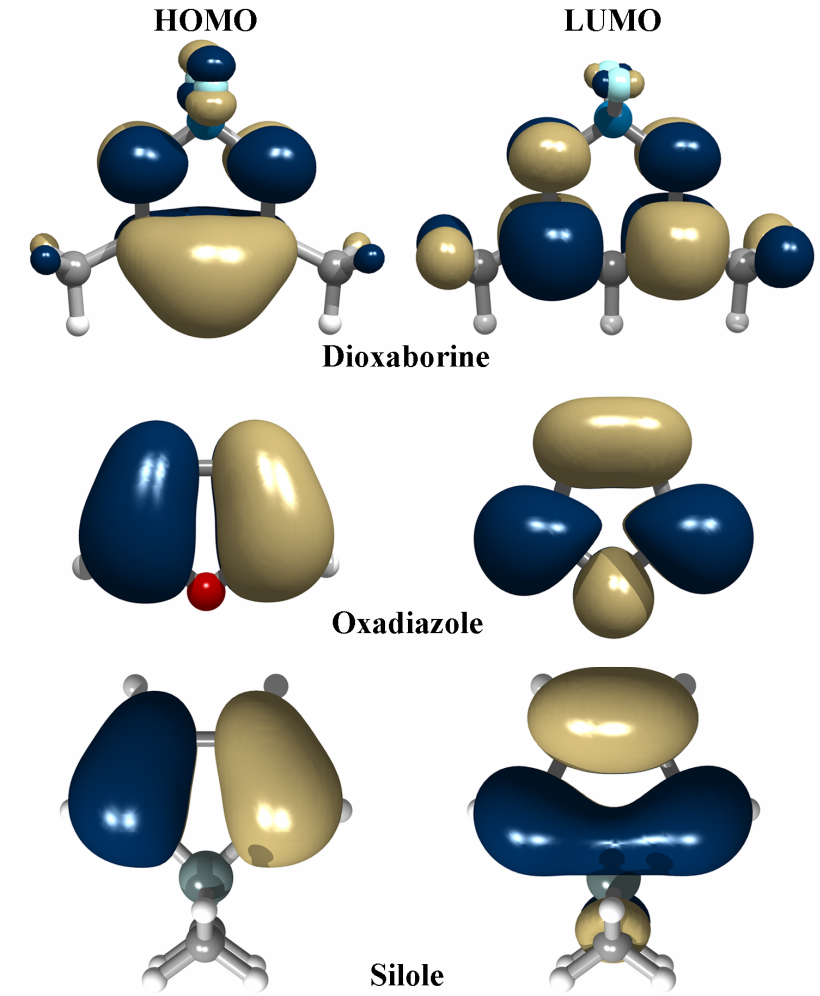

Figure 5.2 B3LYP/6-31+G*//B3LYP/6-31G*-calculated highest occupied (HOMO) [left] and lowest unoccupied (LUMO) [right] molecular orbitals for dioxaborine [top], oxadiazole [middle], and silole [bottom]. Note that the oxadiazole HOMO is taken as the highest π-molecular orbital.

Upon bis-aryl substitution with phenyls, the HOMO energies for the substituted dioxaborine (-7.04 eV), oxadiazole (-6.44 eV), and silole (-5.46 eV) compounds are destabilized relative to the isolated rings, as expected from the increased conjugation. The HOMO wavefunctions are fully delocalized throughout each system, see Figure 5.3; it is observed that each molecular orbital contains a nodal plane between the core ring highest

molecular π-orbital and one of the molecular orbitals derived from the doubly-degenerate benzene HOMOs on the phenyls. The LUMO wavefunctions of the bis-phenyl dioxaborine (-3.04 eV), oxadiazole (-1.96 eV) and silole (-2.04 eV) are stabilized relative to the isolated rings; as with the HOMO wavefunctions, the molecular orbitals are delocalized for each system and there now exists bonding character between the core ring and the substituted phenyl units.

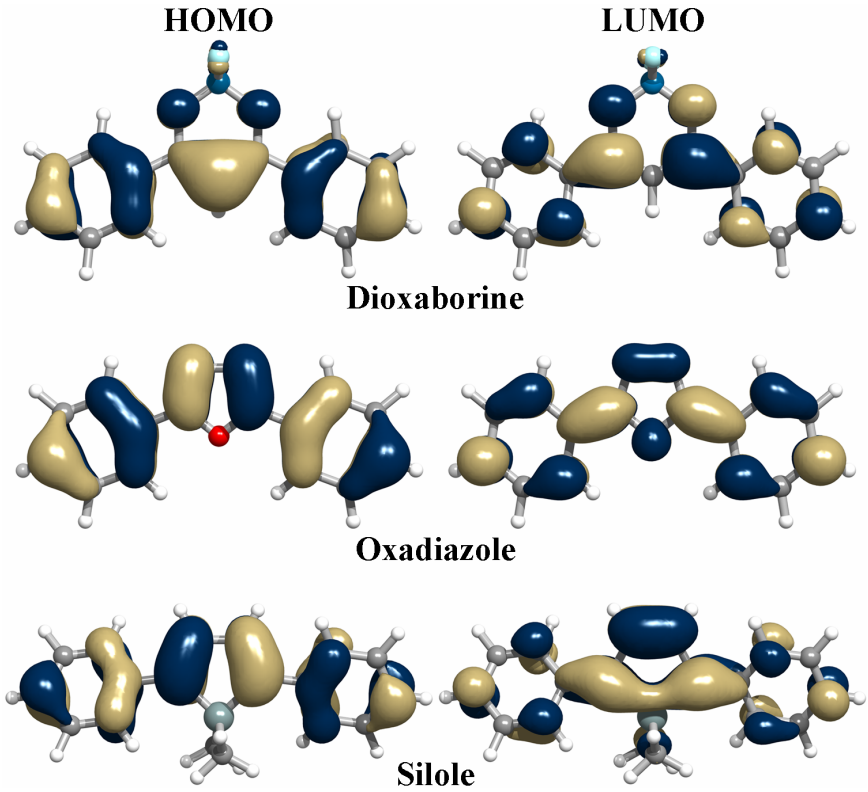

Figure 5.3 B3LYP/6-31+G*//B3LYP/6-31G*-calculated highest occupied (HOMO) [left] and lowest unoccupied (LUMO) [right] molecular orbitals for bis-phenyl substituted dioxaborine [top], oxadiazole [middle], and silole [bottom].

The HOMOs and LUMOs of the bis-donor (p-N,N-dimethylaminophenyl) and bis-acceptor (p-nitrophenyl) substituted structures (as depicted by the representative example of the bis-substituted dioxaborine systems in Figure 5.4) reveal the anticipated opposite effects.[9] Bis-aryl substitution with electron-donating p-N,N-dimethylaminophenyl groups destabilize the HOMO energies considerably, by about 2–3 eV versus the cores, while the effect on the LUMO energies is much smaller, see Table 5.1. This trend is reversed for the electron-withdrawing p-nitrophenyl groups, where the stabilization much more strongly affects the unoccupied levels. This can be rationalized on the basis of the molecular orbitals for which we find a much stronger weight on the p-N,N-dimethylamino substituents in the HOMOs and on the p-nitro substituents in the LUMOs.

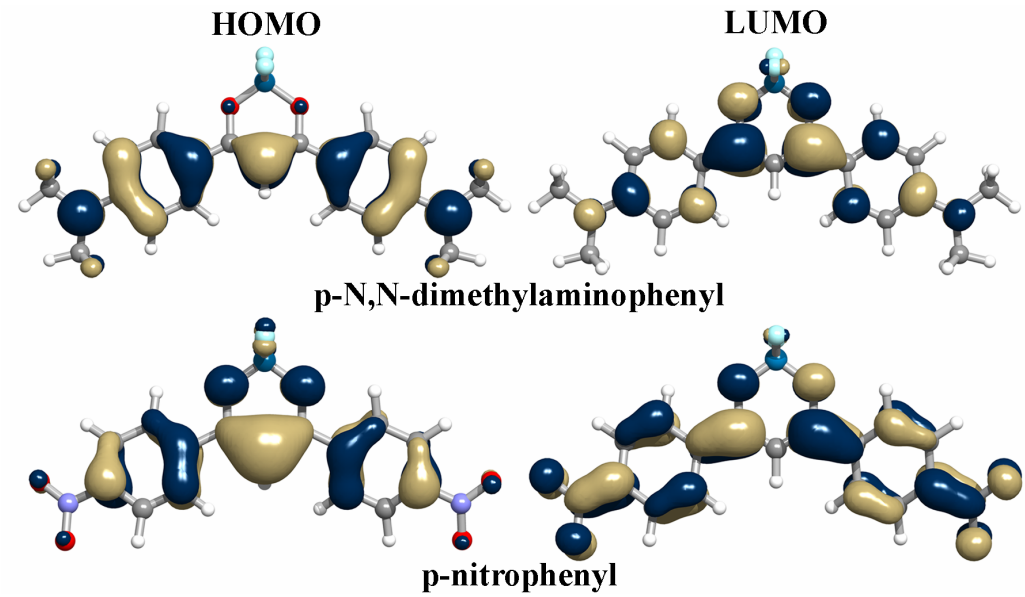

Figure 5.4 B3LYP/6-31+G*//B3LYP/6-31G*-calculated highest occupied (HOMO) [left] and lowest unoccupied (LUMO) [right] molecular orbitals for bis-p-N,N-dimethylaminophenyl substituted [top] and bis-p-nitrophenyl [bottom] substituted dioxaborines.

At this stage, two aspects can be emphasized. First, the results of these electronic-structure calculations indicate that the HOMO and LUMO energies of the dioxaborine, oxadiazole, and silole rings can be tuned on the order of 2 - 3 eV via substitutions as simple as those considered here. Such energy control could potentially allow for the ability to match the Fermi energies of a number of interesting electrode materials. Secondly, the HOMO and LUMO levels for the substituted dioxaborine compounds are consistently more strongly stabilized than their oxadiazole and silole counterparts. These results suggest that dioxaborine-based compounds should exceed oxadiazole- and silole-based systems in both hole-blocking capabilities and overall negative polaron stabilities.

5.3.2 Electron affinities

The electronic structure analysis given above provides a quantitative comparison of the one-electron energy levels often utilized for energy band diagrams of organic device structures. However, the question arises as to what extent do the molecular orbital energies represent an accurate description of the true electron affinities and, hence, actual energetic barriers for carrier injection. To that aim, we have compared the trends obtained from the LUMO energies (that in the framework of Koopmans' theorem,[10] KT, can be viewed as an approximation to electron affinities) and the differences in self-consistent field energies, ΔSCF, obtained for the neutral and radical-anion states. For this discussion, we deal primarily with vertical electron affinities, which are representative of instantaneous processes. Thus, the energy of the radical-anion is calculated at the resultant neutral equilibrium geometry (it is worth noting that the vertical [adiabatic]

electron affinity is defined herein as the energy of the equilibrium neutral geometry subtracted from its energy [energy of the equilibrium radical-anion geometry] on the radical-anion potential energy surface; hence, a negative vertical [adiabatic] electron affinity reflects an energetically stable radical-anion state). Estimations of electron affinities via KT, especially using DFT methods, face a number of potential problems. First, KT neglects energetic effects due to electron reorganization, electron correlation, and vibronic coupling processes.[11] Furthermore, even though Janak's theorem[12] establishes that DFT HOMO and LUMO energies can be regarded as the ionization potential and electron affinities for infinite systems,[13] the validity of Koopmans' DFT[14] is questionable due to the argument that KT cannot apply to DFT methods since *a priori* the Kohn-Sham orbital eigenvalues are auxiliary quantities.[15] Regardless of these potential pitfalls, molecular orbital energies have been successfully utilized in predictions of electron affinities[11] and other energetic properties, even at the DFT level.[13, 15, 16] Additionally, the lower computation cost and the resulting possibility to study increasingly complex systems and the ability to include electron correlation into the formalism make orbital energies obtained from DFT methods even more attractive.[13] It is with this background that we formally evaluate the ΔSCF vertical electron affinities and compare them to molecular-orbital-based estimates for these systems.

Upon initial analysis, the B3LYP/6-31G*//B3LYP/6-31+G*-calculated vertical electron affinities, see Table 5.2, appear to be very consistent with the trends observed for the LUMO energies; the dioxaborine results compare well with those recently reported by Fabian and Hartmann.[5] For each substitution, the calculated vertical electron affinities for

the dioxaborine systems are significantly stabilized versus the oxadiazole and silole counterparts. As is shown in Figure 5.5, the correlation between the ΔSCF and the KT-derived electron affinities is in fact excellent for all bis-aryl substituted systems. Linear regression analysis of the points corresponding to the substituted systems provide a linear fit with a slope very close to one and an offset of 1.32 eV from line through the origin. Such a constant offset has been shown previously with Hartree-Fock methods[11] and, in this case, is probably due to a variety of factors including the DFT methodology in general, as well as the choice of exchange-correlation functionals and basis sets. The unsubstituted dioxaborine, oxadiazole, and silole cores, however, somewhat deviate from this linear regression fit. We attribute this error in the KT-derived electron affinities to the smaller electron count in the unsubstituted systems, which can be expected to increase the negative effect of the frozen-orbital approximation on which KT is based.

Table 5.2 Vertical (VEA) and adiabatic (AEA) electron affinities as determined at the B3LYP/6-31+G*//B3LYP/6-31G* level of theory.

compound	bis-substituent	VEA (eV)[a]	AEA (eV)[a]
dioxaborine	methyl	-0.58	-0.92
	N,N-dimethylaminophenyl	-0.95	-1.27
	phenylene	-1.60	-1.81
	nitrophenyl	-2.95	-3.19
oxadiazole	hydrogen	1.06	+0.92
	N,N-dimethylaminophenyl	0.11	-0.26
	phenylene	-0.53	-0.69
	nitrophenyl	-2.36	-2.54
silole	hydrogen	0.30	+0.06
	N,N-dimethylaminophenyl	-0.28	-0.65
	phenylene	-0.70	-0.95
	nitrophenyl	-2.62	-2.52

[a] Note that the electron affinities are calculated by subtracting the total energy on the neutral electronic configuration from the energy of the radical-anion electronic configuration.

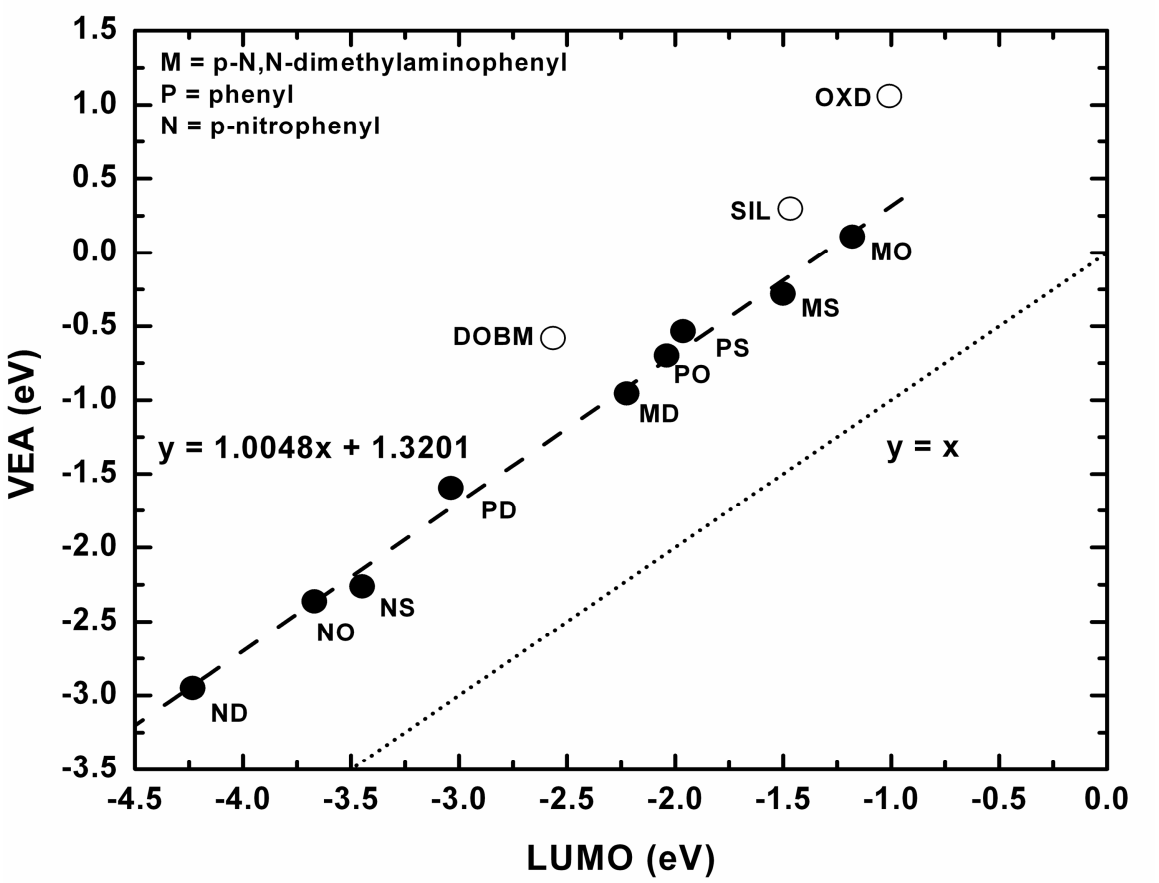

Figure 5.5 B3LYP/6-31+G*//B3LYP/6-31G*-derived vertical electron affinities as a function of the LUMO energies. The core rings are represented by open circles, while the substituted systems are represented by filled circles. The linear regression is conducted exclusively through the filled circles.

Overall, this provides credence, especially for the derived trends obtained and discussed above, in the one-electron molecular orbital picture. A question still remains, however, as to the stability of the radical anions of these compounds versus oxidative electron trapping by molecular oxygen. The calculated adiabatic electron affinity for molecular oxygen at the B3LYP/6-31+G* level is -0.59 eV; this result is in good agreement with previous DFT results.[17, 18] The dioxaborine systems, specifically, favor very well. The calculated adiabatic electron affinity for the dioxaborine ring is -0.92 eV. In the phenyl

(-1.82 eV), bis-substituted p-N,N-dimethylaminophenyl (-1.27 eV), and p-nitrophenyl (-3.19 eV) systems the radical-anion stability is dramatically increased; thus, it may be expected that electron trapping by molecular oxygen is minimal in devices composed of the dioxaborine systems. Though both the oxadiazole and silole rings possess even slightly positive electron affinities, substitution appears to stabilize the molecular structures preventing oxidative trapping by molecular oxygen; in particular, the phenyl and p-nitrophenyl substitutions offer significant stabilization.

5.3.3 Intramolecular reorganization energy

DFT-derived intramolecular reorganization energy results for geometry relaxations between neutral and radical-anion electronic configurations vary rather significantly and, for different substituents, range between 0.3 and 0.7 eV, see Table 5.2. For the unsubstituted systems, the dioxaborine (0.58 eV), oxadiazole (0.50 eV), and silole (0.52 eV) results are very similar. For all three central rings, phenyl substitution provides the smallest overall intramolecular reorganization energy followed by p-nitrophenyl, and p-N,N-dimethylaminophenyl; it is worth noting, however, that the difference in reorganization energies between the phenyl and p-nitrophenyl substitutions is rather small, on the order of 0.01 – 0.05 eV. The phenyl- and nitrophenyl-substituted dioxaborine and oxadiazole present reorganization energies on the order of 0.3-0.37 eV; these values are only slightly larger than that calculated [19, 20] for the widely studied hole-transport material N,N'-diphenyl-N,N'-bis(3-methylphenyl)-([1,1'-biphenyl])-4,4'-

diamine (TPD), 0.29 eV. They are, however, significantly larger than in pentacene, 0.10 eV,[21] which presents a rigid macrocyclic backbone.

Table 5.3 Neutral (λ_1) and radical-anion (λ_2) relaxation energies, and total intramolecular reorganization energy (λ_i), as determined at the B3LYP/6-31+G*//B3LYP/6-31G* level of theory.

compound	bis-substituent	λ_1 (eV)	λ_2 (eV)	λ_i (eV)
dioxaborine	methyl	0.24	0.34	0.58
	N,N-dimethylaminophenyl	0.33	0.31	0.64
	phenylene	0.11	0.22	0.33
	nitrophenyl	0.13	0.24	0.37
oxadiazole	hydrogen	0.36	0.14	0.50
	N,N-dimethylaminophenyl	0.36	0.37	0.73
	phenylene	0.15	0.15	0.30
	nitrophenyl	0.17	0.18	0.35
silole	hydrogen	0.29	0.23	0.52
	N,N-dimethylaminophenyl	0.33	0.37	0.70
	phenylene	0.20	0.25	0.45
	nitrophenyl	0.21	0.25	0.46

5.4 Conclusions

In summary, the electronic structure, electron affinity, and intramolecular reorganization energy results presented here suggest that dioxaborine-based systems should compare favorably with the already successful electron-transport systems based upon oxadiazole and silole chemistry. The HOMO and LUMO levels for the bis-substituted dioxaborine species are consistently more strongly stabilized, indicating the possibility for both favorable hole-blocking and electron-injection properties. In addition, the large electron affinities and comparable intramolecular reorganization energies provide further evidence

that dioxaborine-based systems should be interesting candidates for electron-transport materials. Finally, it has been demonstrated for all three compounds that small chemical modifications in the molecular structure can allow for the tuning of both the HOMO and LUMO energies over a 2-3 eV range.

5.5 References

(1) Chow, Y. L.; Wang, S. S.; Johansson, C. I.; Liu, Z. L., *J. Am. Chem. Soc.* **1996,** 118, 11725.

(2) Chow, Y. L.; Liu, Z. L.; Johansson, C. I.; Ishiyama, J., *Chem. Eur. J.* **2000,** 6, 2942.

(3) Halik, M.; Wenseleers, W.; Grasso, C.; Stellacci, F.; Zojer, E.; Barlow, S.; Brédas, J. L.; Perry, J. W.; Marder, S. R., *Chem. Commun.* **2003**, 1490.

(4) Domercq, B.; Grasso, C.; Maldonado, J. L.; Halik, M.; Barlow, S.; Marder, S. R.; Kippelen, B., *J. Phys. Chem. B* **2004,** 108, 8647.

(5) Fabian, J.; Hartmann, H., *J. Phys. Org. Chem.* **2004,** 17, 359.

(6) Risko, C.; Zojer, E.; Brocorens, P.; Marder, S. R.; Brédas, J. L., *Chem. Phys.* **2005,** 313.

(7) Rienstra-Kiracofe, J. C.; Tschumper, G. S.; Schaefer, H. F.; Nandi, S.; Ellison, G. B., *Chem. Rev.* **2002,** 102, 231.

(8) Frisch, M. J.; Trucks, G. W.; Schlegel, H. B.; Scuseria, G. E.; Robb, M. A.; Cheeseman, J. R.; Zakrzewski, V. G.; Montgomery, J., J.A.; Stratmann, R. E.; Burant, J. C.; Dapprich, S.; Millam, J. M.; Daniels, A. D.; Kudin, K. N.; Strain, M. C.; Farkas, O.; Tomasi, J.; Barone, V.; Cossi, M.; Cammi, R.; Mennucci, B.; Pomelli, C.; Adamo, C.; Clifford, S.; Ochterski, J.; Petersson, G. A.; Ayala, P. Y.; Cui, Q.; Morokuma, K.; Salvador, P.; Dannenberg, J. J.; Malick, D. K.; Rabuck, A. D.; Raghavachari, K.; Foresman, J. B.; Cioslowski, J.; Ortiz, J. V.; Baboul, A. G.; Stefanov, B. B.; Liu, G.; Liashenko, A.; Piskorz, P.; Komaromi, I.; Gomperts, R.; Martin, R. L.; Fox, D. J.; Keith, T.; Al-Laham, M. A.; Peng, C. Y.; Nanayakkara, A.; Challacombe, M.; Gill, P. M. W.; Johnson, B.; Chen, W.; Wong, M. W.; Andres, J. L.; Gonzalez, C.; Head-Gordon, M.; Replogle, E. S.; Pople, J. A. *Gaussian98, Rev. A.11*, 1998.

(9) Cornil, J.; dos Santos, D. A.; Beljonne, D.; Bredas, J. L., *J. Phys. Chem.* **1995,** 99, 5604.

(10) Koopmans, T., *Physica* **1933,** 1, 104.

(11) Staley, S. W.; Strnad, J. T., *J. Phys. Chem.* **1994,** 98, 116.

(12) Janak, J. F., *Phys. Rev. B: Condens. Matter Mater. Phys.* **1978,** 18, 7165.

(13) de Oliveira, M. A.; Duarte, H. A.; Pernaut, J. M.; de Almeida, W. B., *J. Phys. Chem. A* **2000,** 104, 8256.

(14) Levy, M.; Nagy, A., *Phys. Rev. A* **1999,** 59, 1687.

(15) Curtiss, L. A.; Miller, J. R., *J. Phys. Chem. A* **1998,** 102, 160.

(16) Savin, A.; Umrigar, C. J.; Gonze, X., *Chem. Phys. Lett.* **1998,** 288, 391.

(17) Parisel, O.; Ellinger, Y.; GiessnerPrettre, C., *Chem. Phys. Lett.* **1996,** 250, 178.

(18) Tschumper, G. S.; Schaefer, H. F., *J. Chem. Phys.* **1997,** 107, 2529.

(19) Malagoli, M.; Brédas, J. L., *Chem. Phys. Lett.* **2000,** 327, 13.

(20) Lin, B. C.; Cheng, C. P.; Lao, Z. P. M., *J. Phys. Chem. A* **2003,** 107, 5241.

(21) Gruhn, N. E.; da Silva Filho, D. A.; Bill, T. G.; Malagoli, M.; Coropceanu, V.; Kahn, A.; Brédas, J. L., *J. Am. Chem. Soc.* **2002,** 124, 7918.

CHAPTER 6

ELECTRONIC COUPLING IN TETRAANISYLARYLENEDIAMINE MIXED-VALENCE SYSTEMS

6.1 Introduction

In this Chapter, we shift the focus to investigations of the intramolecular electron-transfer properties of organic mixed-valence (MV) compounds. We describe herein three organic systems possessing nearly identical inter-redox site distances that differ only by the nature of the bridging unit – benzene (**1**), naphthalene (**2**), and anthracene (**3**) – see Figure 6.1. These systems are of interest in that ultraviolet photoelectron spectroscopy (UPS), recently shown to be a useful probe for the determination of electronic coupling,[1] and Vis/NIR spectroscopy data suggest that the electronic coupling decreases in the following order of bridging units: benzene > naphthalene > anthracene. [Note: **1** – **3** were synthesized in the group of Professor C. Lambert at the Institut für Organische Chemie, Julius-Maximilians-Universität Würzburg (Würzburg, Germany); the electrochemical, optical studies, and X-ray crystallographic studies were also carried out in the group of Professor Lambert. The UPS investigations were performed under the direction of Dr. N. E. Gruhn at the Center for Gas-Phase Electron Spectroscopy at The University of Arizona.] This finding contradicts the usual expectation that anthracene is superior to benzene as a driving force for electronic communication. Indeed, previous results reported by several groups[2-11] have shown that the replacement of a benzene bridge by

anthracene significantly enhances the electronic communication in both charge-[2-9]and energy-transfer[10, 11] systems. For example, recent electron spin resonance (ESR) studies of bishydrazine MV compounds indicate a significantly lower electron-transfer barrier for systems with anthracene linkers than for those with benzene and naphthalene bridges.[6-9] Additionally, much larger electronic couplings have been found through 9,10-diethynylanthracene bridges than through 1,4-diethynylbenzene spacers in both inorganic[2] and purely organic[4, 5] MV compounds as well as in single-molecule break junctions;[12] 9,10-diethynylanthracene has been shown to yield the largest electronic coupling between porphyrin chromophores.[10, 11]

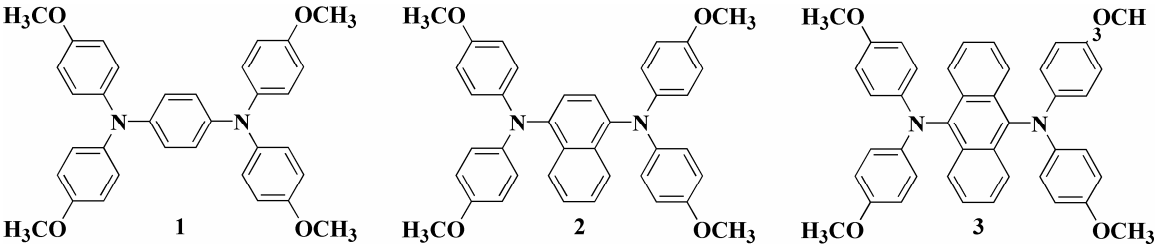

Figure 6.1 Chemical structures of **1** – **3**.

In order to understand the properties of **1** – **3**, we have performed a series of quantum-chemical calculations to further understand the electronic-coupling results provided by the UPS, Vis-NIR, and cyclic voltammetry measurements.[13] The theoretical evidence confirms the empirical results for the tetraanisylarylenediamine MV systems, *i.e.*, the electronic coupling is found to decrease on going from benzene to anthracene bridges.

We explain these results in terms of a super-exchange mechanism and its strong dependence on steric interactions.

6.2 Theoretical methodology

The geometries of **1** – **3** were optimized in the neutral and ground and first-excited radical-cation states. Density Functional Theory (DFT) and the semi-empirical Hartree-Fock Austin Model 1 (RHF-AM1) method were utilized to evaluate the neutral states of the systems. The DFT calculations were carried out using the B3LYP functionals, where Becke's three-parameter hybrid exchange functional is combined with the Lee-Yang-Parr correlation functional,[14, 15] with a 6-31G** split-valence plus double polarization basis set.

UB3LYP/6-31G**, UHF-AM1, and a coupled semi-empirical RHF-AM1/configuration interaction (AM1/CI) method using Complete Active Space Configuration Interaction (CAS-CI) were used for the investigations of the radical-cation electronic states; UB3LYP/6-31G** was used for the description of the first-excited radical-cation state. Relaxation energies were determined through direct calculation of the relevant points on the potential energy surface, as discussed below.[16] Excitation energies for the low-lying excited states have been calculated with time-dependent density functional theory (TDDFT). All AM1-based calculations were carried out using the implementation in the AMPAC 6.55 software package,[17] while the DFT calculations were performed with Gaussian98 (Revision A.11).[18]

6.3 Results and discussion

6.3.1 Geometry

Calculated key geometric parameters for the neutral and ground and first-excited radical-cation states of **1** – **3**, as well as the X-ray crystal structure analysis of **3**, are collected in the Tables 6.1 – 6.6 using the numbering scheme presented in Figure 6.2. The B3LYP/6-31G** results for the neutral structures of **1** – **3** indicate that the geometries for the three systems are comparable, with the most prevalent deviations amongst the structures due to the asymmetric substitution of the naphthylene bridge in compound **2**; the theoretical evaluation of **3** compares very well with the experimental X-ray crystallographic determination, see Table 6.1. The carbon-carbon bond lengths of the phenylene and anthrylene bridges in **1** and **3** are symmetric about the nitrogen-nitrogen axes, while the asymmetric substitution of the naphthylene bridge lowers the symmetry normally realized for isolated naphthalene structures. The larger anthrylene bridge of **3**, through increased steric interactions, produces a large torsional orientation of the *N,N*-di(4-methoxyphenyl)amino groups with respect to the bridge (72° for **3** versus 39° for **1**); these torsion angles thus represent the dihedral angles between the plane defined by the arylene bridge and that defined by the three carbon-nitrogen bonds around the redox site. The theoretical estimates of the dihedral angles are in qualitative agreement with the experimental values of 72° and 74° for **3,** and 54° and 56° for tetraphenylphenylenediamine, a structural analog of **1**.[19] The asymmetric substitution in **2** causes the torsional angles around each redox center to be 49° and 67° (values in between those observed for the phenylene and anthrylene bridges of **1** and **3**), while X-ray crystal

structure determination with very high *R* values gives 35-48° and 62-67° for eight total independent torsional angles. These torsional angles reveal the different landscapes of the 4-methoxyphenyl groups with respect to the naphthylene bridge: one unit is free from steric interactions with the bridge (as with the phenylene bridge) while the other group is hindered by increased steric interactions (as with the anthrylene bridge). Comparable geometries for **1**–**3** are realized at the RHF-AM1 level. The largest departure with respect to the B3LYP/6-31G** results occur for the orientation of the nitrogen atoms; in all three systems at the RHF-AM1 level, the nitrogen atoms are pyramidal with respect to their bound carbon atoms, with the pyramidality in **2** being slightly larger.

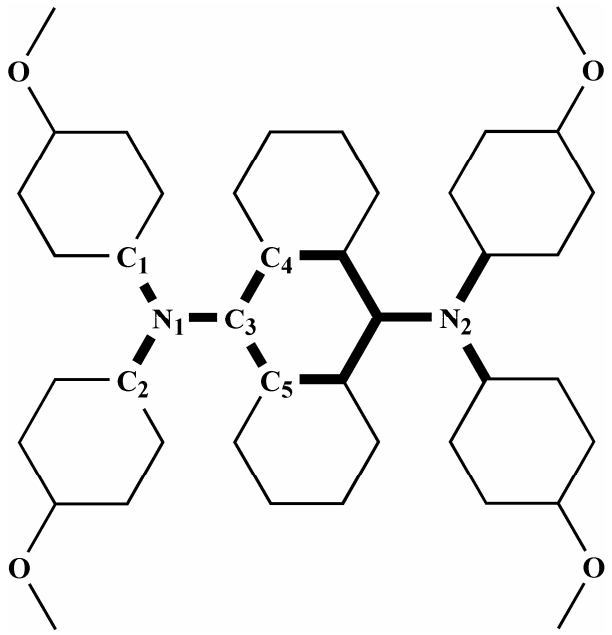

Figure 6.2 Reference numbering scheme utilized for compounds **1 – 3**.

Table 6.1 Selected bond lengths (Å) and angles (°) for the neutral states of **1 – 3** as determined at the B3LYP/6-31G** and RHF-AM1 levels of theory as well as by X-ray crystal structure analysis.

Parameter	B3LYP/6-31G**			RHF-AM1			X-Ray (C_i)
	1	2	3	1	2	3	3
Bond (Å)							
N_1-C_1	1.422	1.425	1.422	1.419	1.425	1.418	1.417(2)
N_1-C_2	1.422	1.423	1.422	1.419	1.424	1.418	1.422(2)
N_1-C_3	1.418	1.428	1.432	1.416	1.429	1.429	1.432(2)
C_3-C_4	1.405	1.383	1.413	1.410	1.388	1.418	1.404(3)
C_3-C_5	1.405	1.436	1.413	1.414	1.442	1.419	1.413(2)
N_1-N_2	5.674	5.698	5.710	5.672	5.704	5.706	5.69
Angle (°)[a]							
C_1-N_1-C_2	120	120	122	118	118	120	121.50(14)
C_4-C_3-N_1-C_1	39	49	72	20	39	63	71.9
C_5-C_3-N_1-C_2	39	67	72	46	75	89	74.3
Angle Sum N	360	358	360	356	351	356	360

[a] Due to the twisted nature of the bridges, the accuracy of the angle measurements is given to the nearest 1°.

Geometry optimizations of the radical-cation structures $\mathbf{1}^+$ – $\mathbf{3}^+$ at the UB3LYP/6-31G** level of theory indicate that all three radical cations possess the same degrees of symmetry as their neutral structures. The bonds between the nitrogens and the bridge carbons shorten considerably in $\mathbf{1}^+$ – $\mathbf{3}^+$, with the extent of change larger for $\mathbf{1}^+$ (0.028 Å) and $\mathbf{2}^+$ (0.025 Å) versus $\mathbf{3}^+$ (0.015 Å). Because of the decrease in these bond lengths, the distance between the two nitrogen redox centers decreases by 0.053 Å, 0.043 Å and 0.024 Å, for $\mathbf{1}^+$, $\mathbf{2}^+$ and $\mathbf{3}^+$**,** respectively. The largest geometric adjustments to the overall radical-cation structures occur for the relative orientation of the 4-methoxyphenyl groups with respect to the bridges. In $\mathbf{1}^+$ and $\mathbf{3}^+$, the geometry relaxations decrease the torsional angles by 10° and 12°, respectively, while the nitrogen atoms remain non-pyramidal with respect to their bridging carbon atoms. The torsional orientation of the 4-methoxyphenyl

groups with respect to the naphthylene bridge in $\mathbf{2}^+$ decreases by 17° for the more sterically hindered group and 9° for the less hindered group. It is worth noting that there is a slight diagonal twisting in the naphthylene and anthrylene bridges of $\mathbf{2}^+$ and $\mathbf{3}^+$.

Table 6.2 Selected bond lengths (Å) and angles (°) for radical-cation states $\mathbf{1}^+ - \mathbf{3}^+$ as determined at the UB3LYP/6-31G** and AM1/CI levels of theory.

Parameter	UB3LYP/6-31G**			AM1/CI[c]		
	1^+ [b]	2^+	3^+	1^+	2^+	3^+
Bond (Å)						
N_1-C_1	1.428	1.426	1.420	1.429	1.431	1.424
N_1-C_2	1.428	1.423	1.420	1.429	1.431	1.425
N_1-C_3	1.390	1.403	1.417	1.366	1.372	1.384
C_3-C_4	1.419	1.400	1.425	1.440	1.431	1.444
C_3-C_5	1.419	1.446	1.425	1.440	1.456	1.444
N_1-N_2	5.621	5.655	5.686	5.608	5.635	5.665
Angle (°)[a]						
C_1-N_1-C_2	118	119	121	117	116	118
C_4-C_3-N_1-C_1	27	40	62	10	20	46
C_5-C_3-N_1-C_2	27	50	62	11	30	46
Angle Sum N	360	362	360	360	359	360

[a]Due to the twisted nature of the bridges, the accuracy of the angle measurements is given to the nearest 1°. [b]Taken from Reference 1. [c] The configuration interaction space for $\mathbf{1}^+$ included the HOMO-5 through LUMO+1, while the space for $\mathbf{2}^+$ and $\mathbf{3}^+$ was limited to the HOMO-2 through LUMO+1. The molecular orbital labels refer to the neutral state designations.

The symmetric, delocalized structures provided by the UB3LYP/6-31G** method are consistent with DFT results reported for other triarylamine-based mixed-valence systems. However, such symmetric structures are provided by DFT even in the case of systems that are experimentally known to localize the excess charge.[20, 21] In order to search for possible charge-localized structures, UHF-AM1 and correlated semi-empirical AM1/CI

methods were used. The UHF-AM1 results indicate that the charge is localized on one side of the molecular architecture for $\mathbf{2}^+$ and $\mathbf{3}^+$; the results are less clear for $\mathbf{1}^+$. However, each UHF-AM1 optimized structure was associated with a large degree of spin contamination ($S^2 \sim 1.8 - 3.2$), thus casting strong doubt on the validity of the method.

For the AM1/CI method, a number of configuration-interaction spaces were explored. These spaces were first limited to the HOMO, SOMO, and LUMO molecular orbitals of the radical cation; larger CI spaces that also included molecular orbitals primarily located on the bridges, were then considered. However, no significant differences in the optimized radical-cation structures were found as a function of the size of the configuration-interaction space chosen for the analysis. In all cases, symmetric, charge delocalized structures consistent with the UB3LYP/6-31G** results were obtained. These results along with the weak solvent dependence of the IV-CT bands[13] strongly point towards the assignment of $\mathbf{1}^+ - \mathbf{3}^+$ to Robin and Day's Class III or at least to Class III-Class II borderline.

6.3.2 Electronic structure

Based on the DFT-computed neutral geometries, the Kohn-Sham energies for the upper occupied molecular orbitals (HOMO to HOMO-5) of **1** – **3** are given in Figure 6.3, together with the energies of the isolated bridge units and the *N,N*-di(4-methoxyphenyl)amine group; Figure 6.4 provides a pictorial representation of the molecular orbitals. While a comparison of the Kohn-Sham orbital energies with those of

the UPS measurements indicates that the application of Koopmans' theorem (KT)[22] leads to absolute IP values that are about 2 eV too low, it is important to note that the energetic splittings between the HOMO and HOMO-1 are in very good agreement with the experimental ΔIP (measured as the energy difference between the first and second ionizations, $\Delta IP = IP_2 - IP_1$)[1] values, see Figure 6.3.

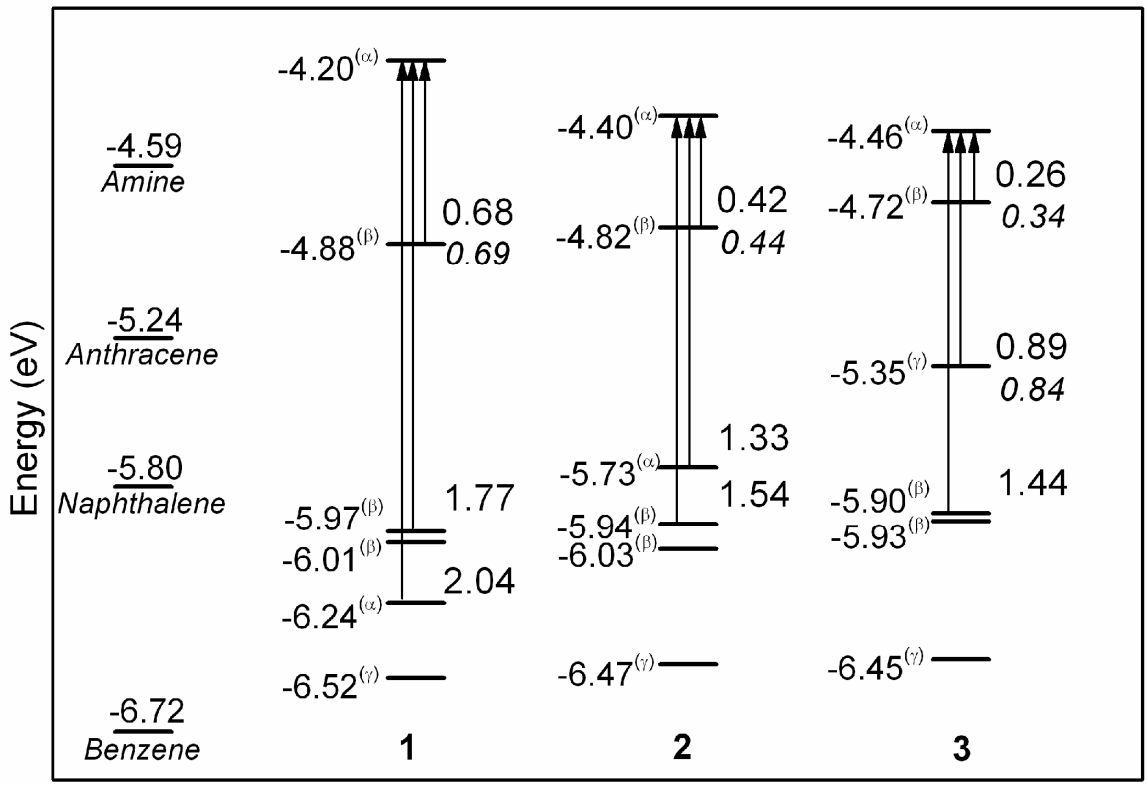

Figure 6.3 B3LYP/6-31G**-derived HOMO through HOMO-5 molecular orbital energies for compounds **1**, **2**, and **3**, as well as the isolated *N,N*-di(4-methoxyphenyl)amine and bridge components. The molecular orbital energies are labeled with superscripts according to the predominant makeup of the orbital structure (see Figure 6.4): (α) amine with strong bridge component; (β) mostly amine; and (γ) mostly bridge. The values given in italics represent the energy separation as determined by UPS.

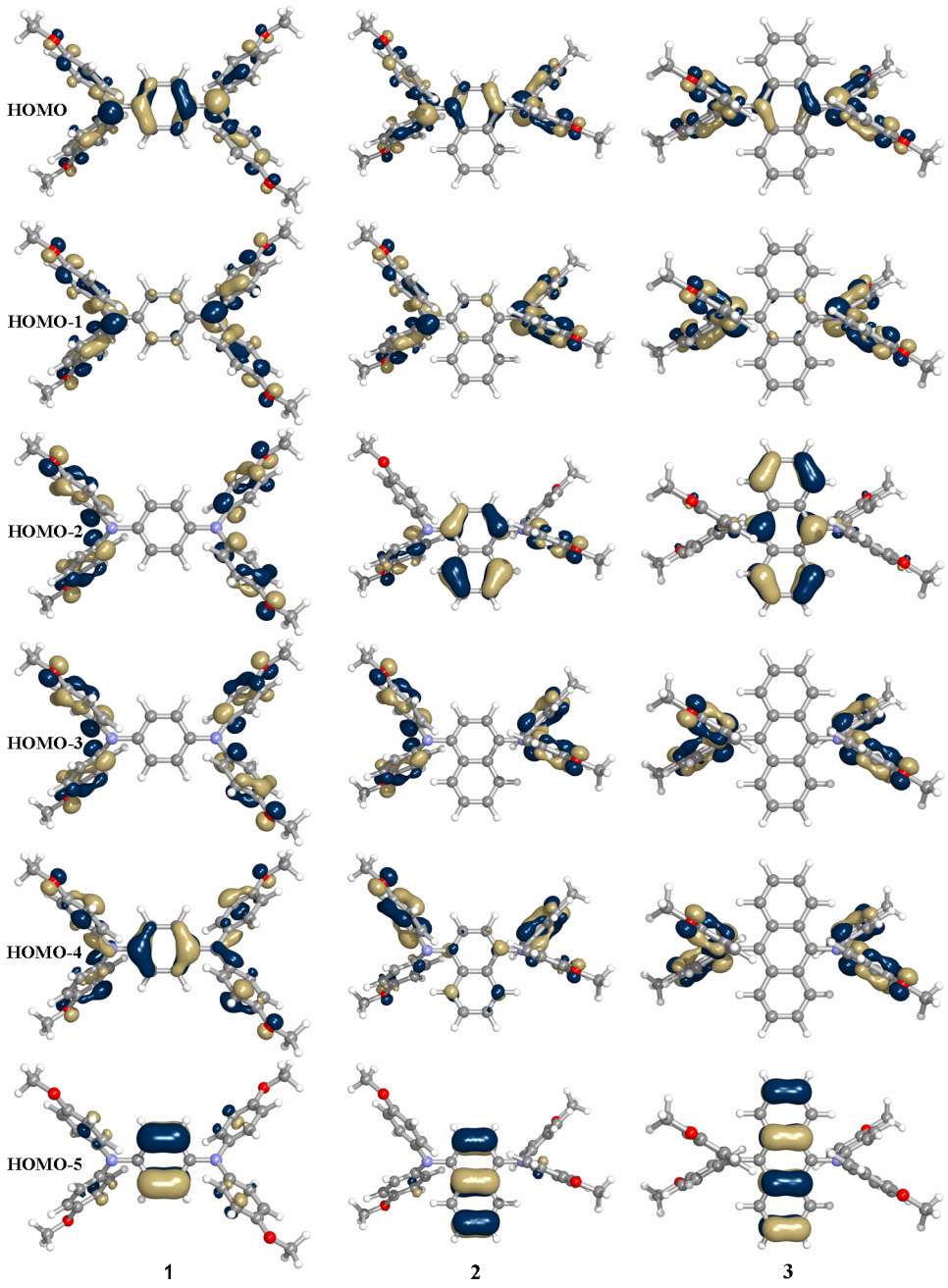

Figure 6.4 Pictorial representation of the B3LYP/6-31G**-derived HOMO through HOMO-5 molecular orbitals in **1**, **2**, and **3**.

The molecular orbitals within the HOMO – HOMO-5 range can be classified into three categories according to their relative localizations on the molecular structure: (i) those

lying on both the amine and bridge components; (ii) those lying predominantly on the amine segments; and (iii) those lying predominantly on the bridge. Consistently across the series, the HOMO (see Figure 6.4) has significant density on both the amine and bridge components while the HOMO-1 lies solely on the amines. In addition, a distinction can be made in the energetic ordering of the next set of amine-based and bridge-character orbitals corresponding to HOMO-2 through HOMO-4. For **1** – **3**, there exists a pair of nearly degenerate amine-based molecular orbitals that maintain similar energies (between -6.03 and -5.90 eV) across the series. In **1**, the next bridge-character orbital lies 0.23 eV below this degenerate pair, while in **2** and **3** the bridge-character molecular orbitals are destabilized versus the degenerate amine orbitals (by 0.21 eV and 0.55 eV, respectively). This picture is in accordance with the UPS data that indicate a peak at *ca.* 8.3 eV for **1** – **3**, which we assign to the amine-based levels, while **2** and **3** have a peak at *ca*. 7.9 eV and 7.28 eV, respectively, that we assign to the bridge-character level. In addition to the concurrence in the energetic splitting of the first two ionization potentials determined via simple Koopmans' theorem analysis of the molecular orbital eigenvalues and the UPS spectra, there is also excellent agreement found through direct B3LYP/6-31G** calculations of the vertical ionization energies at the ΔSCF level. Though there is an approximate 1 eV discrepancy in the absolute values of the ionization potentials, the energy splittings of 0.65 eV, 0.41 eV, and 0.27 eV obtained for **1**, **2**, and **3**, respectively, are nearly identical to those derived from the UPS spectra and demonstrate the reliability of the simple molecular orbital analysis.

For the sake of comparison, we also performed electronic-structure calculations on the hydrazine compounds **N1** – **N3** of Nelsen *et al*., see Figure 6.5.[6-9] These compounds are of interest in that the radical-cations $\mathbf{N1}^+$ and $\mathbf{N2}^+$ are charge localized while the electronic nature of $\mathbf{N3}^+$ is still under debate. At this point it is important to stress that while comparison of the UPS spectra of the neutral **1** – **3** with the electronic properties of $\mathbf{1}^+$ – $\mathbf{3}^+$ is straightforward due to the delocalized nature of $\mathbf{1}^+$ – $\mathbf{3}^+$ and the relatively small changes in geometry upon oxidation, this does not hold for $\mathbf{N1}^+$ – $\mathbf{N3}^+$ where oxidation involves a major reorganization energy and strong changes in geometry. Comparisons of **1** – **3** and **N1** – **N3** are therefore limited to the neutral states and is only valid to some extent for the transition state of the electron in $\mathbf{N1}^+$ – $\mathbf{N3}^+$ as this state has a symmetric geometry but which is not necessarily the same as the neutral **N1** – **N3**.

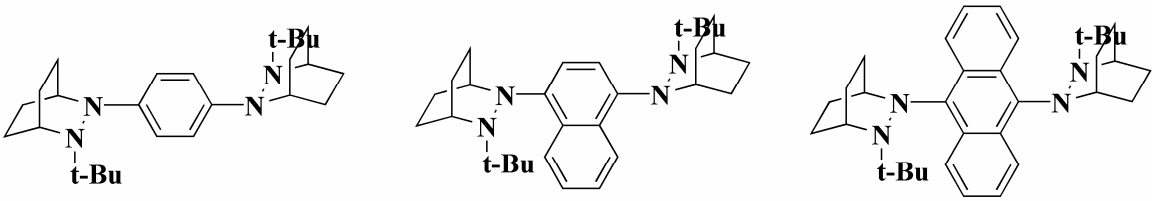

Figure 6.5 Chemical structures of **N1** – **N3**.

The Kohn-Sham energies for the upper occupied molecular orbitals (HOMO to HOMO-5) of **N1** – **N3** are given in Figure 6.6; Figure 6.7 provides a pictorial representation of the molecular orbitals. As with **1** – **3**, the HOMO is distributed across the redox center (*i.e.*, hydrazine) and bridge in **N1** (-4.33 eV), **N2** (-4.27 eV), and **N3** (-4.12 eV); however,

whereas the HOMO energy is stabilized with increasing bridge size in **1** – **3**, there is a slight destabilization in energy for **N1** – **N3**. The HOMO-1 energy, located predominately on the hydrazine units, also slightly destabilizes across the series. The destabilization of both the HOMO and HOMO-1 energies in **N1** – **N3** produce splitting energies that are relatively equal, though the splitting is slightly larger in **N3** (0.67 eV, versus 0.61 eV in **N1** and 0.60 eV in **N2**); such a splitting pattern is drastically different than that for **1** – **3**. Additionally, unlike **1** – **3** where there is a significant reordering of the HOMO-2 to HOMO-4, the HOMO-2 (distributed across the hydrazine and bridge) and HOMO-3 (bridge-based) are consistent in **N1** – **N3**. It is important to note, however, that there is an apparent energy destabilization in the HOMO-2 as the splitting between the HOMO and HOMO-2 decreases by nearly 0.5 eV as the bridge changes from phenylene (1.53 eV) to naphthylene (1.25 eV) over anthrylene (1.05 eV).

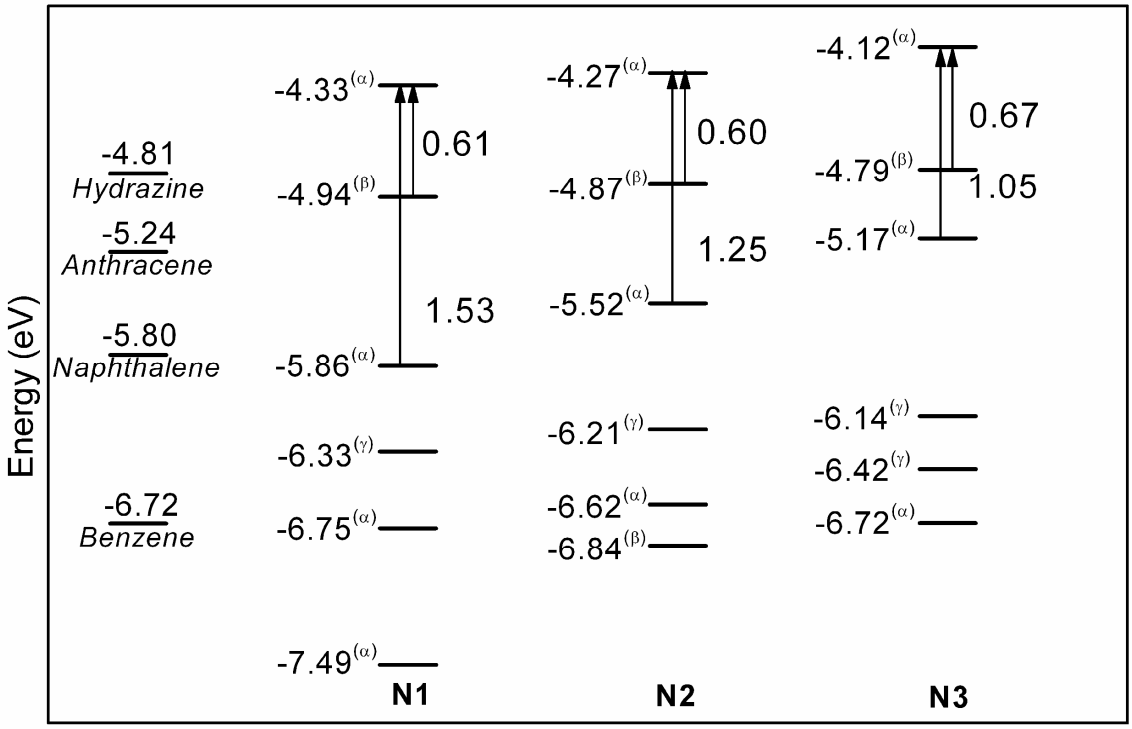

Figure 6.6 B3LYP/6-31G**-derived HOMO through HOMO-5 molecular orbital energies for compounds **N1**, **N2**, and **N3**, as well as the isolated hydrazine and bridge components. The molecular orbital energies are labeled with superscripts according to the predominant makeup of the orbital structure (see Figure 6.7): (α) hydrazine with strong bridge component; (β) mostly hydrazine; and (γ) mostly bridge.

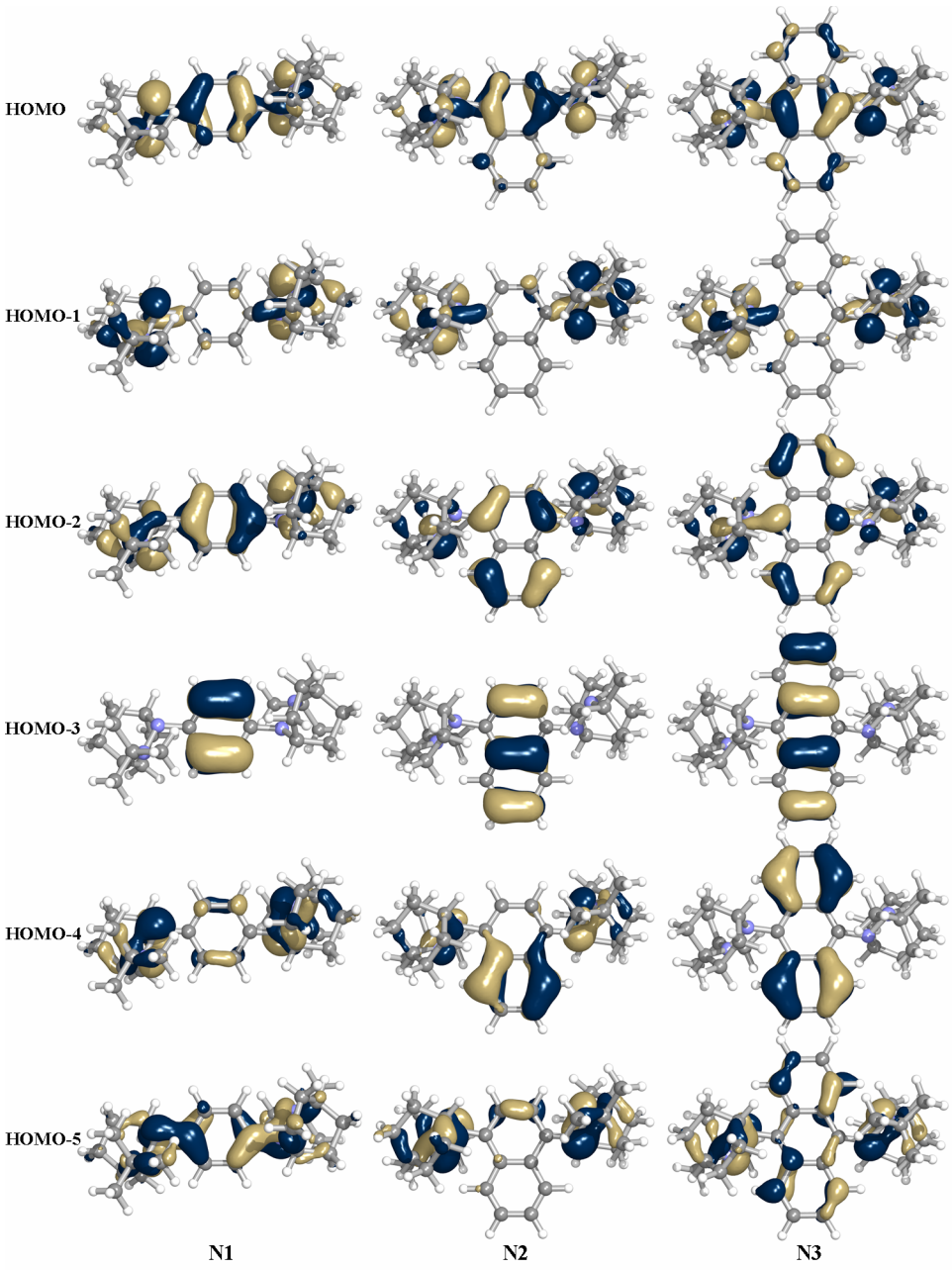

Figure 6.7 Pictorial representation of the B3LYP/6-31G**-derived HOMO through HOMO-5 molecular orbitals in **N1**, **N2**, and **N3**.

The electronic structure results, at least qualitatively, reveal the inherent differences between the two series of compounds **1** – **3** and **N1** – **N3**. The molecular orbital energy

splittings indicate that the Nelsen compounds, at least in the neutral state geometric configuration, should at least be energetically equivalent across the series, while **1** – **3** show a dramatic decrease in splitting with increasing bridge size. Thus, it is not surprising that the two series of compounds reveal different electronic coupling patterns.

The relative orderings of the upper occupied molecular orbitals play a significant role in the electronic transitions that are allowed for $\mathbf{1}^+$ – $\mathbf{3}^+$, as confirmed by TDDFT calculations for the radical cations, see Table 6.3. For $\mathbf{1}^+$ – $\mathbf{3}^+$, the first excitation corresponds to the charge-resonance transition and primarily involves the HOMO-1 → HOMO excitation (the notation for the MOs refers to the neutral ground state). The calculated transition energies agree well with the energies of the experimental optical charge-resonance (CR) bands. The next allowed transition in all three systems is predicted to originate from the quasi-degenerate amine-based molecular orbitals (HOMO-2 and HOMO-3 in $\mathbf{1}^+$, HOMO-3 and HOMO-4 in $\mathbf{2}^+$ and $\mathbf{3}^+$). The calculated energies are again in good agreement with experimental data. However, the TDDFT calculations, in contrast to experiment, predict nearly the same intensity across the series. It is important to mention that in $\mathbf{1}^+$, the third excited state, which arises from the excitation of the bridge-localized HOMO-4, lies very close to the second (quasi-degenerate) excited state. For $\mathbf{2}^+$ and $\mathbf{3}^+$, where the bridge-based molecular orbital is energetically destabilized versus the degenerate amine-based orbitals, the ordering of the respective excited states is inverted. Thus, in $\mathbf{3}^+$, the bridge-localized excited state is located halfway between the charge-resonance (CR) and amine-based states. While optical transition to the bridge-localized state is forbidden in the dipole approximation,

this state might be responsible for the appearance of different scenarios of vibronic interactions in $\mathbf{1}^+ - \mathbf{3}^+$. Therefore, the assignment of the higher-energy bands in these systems and the understanding of the origin of their fine structure require further investigations.

Table 6.3 TDDFT vertical excitation energies (cm^{-1}) and transition dipoles (Debye) of systems $\mathbf{1}^+ - \mathbf{3}^+$ obtained at the UB3LYP/6-31G** radical-cation geometry.

	$\tilde{\nu}_{abs}$ (cm^{-1})	μ (Debye)	configuration[a]
1^+	9290	10.32	HOMO-1 → HOMO (0.87); HOMO → LUMO+1 (0.17)
	15630	2.14	HOMO-2 → HOMO (0.97)
	15900	4.61	HOMO-3 → HOMO (0.97)
	16990	0.00	HOMO-4 → HOMO (0.97)
2^+	7710	9.90	HOMO-1 → HOMO (0.85); HOMO → LUMO (0.19)
	13300	0.72	HOMO-2 → HOMO (0.94); HOMO-4 → HOMO (0.24)
	14820	3.60	HOMO-3 → HOMO (0.96)
	15340	4.01	HOMO-4 → HOMO (0.94); HOMO-2 → HOMO (0.24)
3^+	5730	9.31	HOMO-1 → HOMO (0.80); HOMO → LUMO (0.20)
	9390	0.00	HOMO-2 → HOMO (0.96); HOMO-1 → LUMO (0.10)
	13400	2.49	HOMO-3 → HOMO (0.96)
	13780	4.88	HOMO-4 → HOMO (0.96)

[a] The molecular orbital configurations are labeled in reference to the neutral states.

6.3.3 Electronic coupling

For the sake of comparison, the estimates of the electronic coupling obtained by different methods are collected in Table 6.4. Both the Vis/NIR and UPS estimates point to a large decrease in the electronic coupling when going from $\mathbf{1}^+$ to $\mathbf{3}^+$; the data suggest a decrease in electronic coupling by nearly a factor of two when the phenylene bridge is replaced by an anthrylene bridge. The UPS splitting values are smaller than the splitting values derived from the optical spectra. The discrepancy between the two sets of data is related to the fact that ΔIP is determined at the geometry (see Figure 6.8) of the neutral molecule. Thus, the UPS measurements provide a lower bound of the electronic coupling. In order to obtain more accurate estimates of the electronic coupling, the UPS splitting values should be corrected to account for the relaxation effects that take place on going from neutral to radical-cation states. Within the adiabatic approximation, a simple correction can be obtained. According to Figure 6.8, we can write:

$$V = \left(\frac{\Delta IP}{2} \right) + L^* \tag{6.1}$$

$$L^* = \frac{1}{2}\left(L + \lambda_1 - \lambda_2\right) \tag{6.2}$$

where λ_1 and λ_2 are the relaxation energies of the ground state and first excited state of the radical cation with respect to the geometry of the neutral ground state. The estimated relaxation energies are given in Table 6.5; the values of L for $\mathbf{1}^+$ and $\mathbf{2}^+$ are similar and significantly larger than those for $\mathbf{3}^+$. These differences arise from the extent of geometry modifications observed upon excitation of the radical-cation species: changes in both the

carbon-nitrogen bonds and torsional orientations of the 4-methoxyphenyl groups are dramatically larger for $\mathbf{1}^+$ and $\mathbf{2}^+$ than those observed in $\mathbf{3}^+$, see Table 6.6.

Table 6.4 Electronic coupling parameters (cm^{-1}) as determined from Koopmans' Theorem analysis and experimental UPS and optical data.

	1^+	2^+	3^+
KT-AM1 [a]	2380	1420	950
KT-DFT [a]	2740	1670	1080
UPS (ΔIP/2)	2780	1770	1370
$\Delta IP/2+L^*$	3800	2960	2160
V [b]	4300	3600	2200
exp. $\tilde{\nu}_{abs}/2$	4740	4000	2570

[a]Evaluations were made with respect to the DFT-optimized neutral geometry. [b]From band fitting.[19, 21, 23, 24]

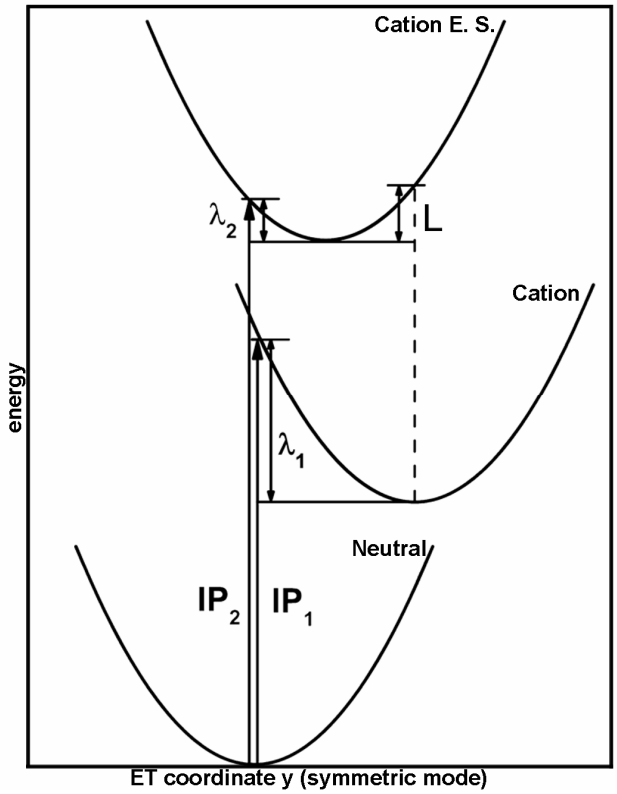

Figure 6.8 Adiabatic potential surfaces along the symmetric vibration mode *y* (the *x* mode is set to zero) of the neutral state, and radical-cation ground and first excited states.

Table 6.5 Intramolecular reorganization energies and correction (*L**) obtained at the UB3LYP/6-31G** level.

	λ_1 (cm^{-1})	λ_2 (cm^{-1})	L (cm^{-1})	L^* (cm^{-1})
1	1090	1200	2160	1020
2	1340	1190	2240	1190
3	940	780	1430	790

Table 6.6 Selected bond lengths (Å) and angles (°) for first-excited radical-cation states of **1**$^{+}$***** – **3**$^{+}$***** as determined at the UB3LYP/6-31G** level of theory.

Parameter	UB3LYP/6-31G**		
	1^{+}*	2^{+}*	3^{+}*
Bond (Å)			
N_1-C_1	1.411	1.414	1.413
N_1-C_2	1.411	1.410	1.413
N_1-C_3	1.435	1.440	1.442
C_3-C_4	1.400	1.379	1.410
C_3-C_5	1.400	1.431	1.410
N_1-N_2	5.670	5.692	5.705
Angle (°)[a]			
C_1-N_1-C_2	122	122	123
C_4-C_3-N_1-C_1	55	67	78
C_5-C_3-N_1-C_2	55	73	78
Angle Sum N	360	360	360

[a] Due to the twisted nature of the bridges, the accuracy of the angle measurements is given to the nearest 1°.

Thus, as seen from Table 6.4, both experimental measurements and electronic-structure calculations concur to demonstrate that the anthracene bridge provides for a significantly smaller electronic coupling than the benzene bridge. We interpret this finding as a result of the influence of steric interactions on the super-exchange mechanism. We believe that these interactions control the electronic communication between the redox centers in **1**$^{+}$ – **3**$^{+}$. For a complete description of the super-exchange interaction, we would need to take the bridge levels explicitly into consideration, preferably by using many-state models. Here, for the purpose of providing a simple, qualitative explanation, we discuss the results obtained in the framework of perturbation theory. If we assume, for the sake of simplicity, that a single pathway contributes to the super-exchange interaction (that likely operates via occupied bridge levels, as they are energetically (see Figure 6.3) the most

favorable), the electronic coupling (V) can be approximated in the tight-binding approximation as:[25]

$$V = \frac{V_B^2}{\Delta E} \tag{6.3}$$

Here, V_B is the electronic coupling between the redox site and the bridge, and ΔE is the energy gap between the relevant states. Since V_B strongly depends on the mutual orientations of the bridge and redox unit, an unfavorable orientation between these two units will diminish the gain in electronic coupling obtained from the decrease in ΔE. For $\mathbf{1}^+$, the twist angle with respect to the bridge is 27°, while for $\mathbf{3}^+$ the twist angle is 62°. Thus, the smaller twist angles in $\mathbf{1}^+$ allow for a stronger interaction and larger electronic coupling. The large twist angle in $\mathbf{3}^+$ significantly reduces the electronic coupling despite a large reduction in ΔE in $\mathbf{3}^+$ with respect to $\mathbf{1}^+$. If the orientations of the p-methoxyphenyl groups in $\mathbf{3}^+$ are forced to be the same as in $\mathbf{1}^+$, the KT estimate of the electronic coupling in $\mathbf{3}^+$ (0.42 eV) is similar to that determined for $\mathbf{1}^+$ (0.48 eV), revealing a significant increase with respect to the value of 0.23 eV found for the optimized geometry of $\mathbf{3}^+$**.** This illustrates that the electronic coupling in $\mathbf{1}^+ - \mathbf{3}^+$ is largely dominated by steric interactions between the p-methoxyphenyl groups and the bridge. In addition, we suggest that a second effect that limits the strength of the electronic coupling in $\mathbf{2}^+$ and $\mathbf{3}^+$ is related to the non-planarity of the naphthylene and anthrylene bridges in these systems.

6.4 Conclusions

In this Chapter, we have investigated the electronic interactions in three organic MV systems inter-redox site distances. The trends in the electronic coupling across the series – which have been estimated by means of gas-phase UPS and Vis/NIR spectroscopy – have been well reproduced by electronic structure calculations. Additionally, a qualitative comparison to a series of compounds that show the opposite trend has been made. Our work provides a first example where an anthracene bridge is found to be less effective in mediating the electronic communication between redox centers than a benzene bridge. This result indicates that the electronic coupling is controlled by a subtle balance between the effects related to the energetics of the bridge and the redox units and to the topology of the bridge-redox center segment.

6.5 References

(1) Coropceanu, V.; Gruhn, N. E.; Barlow, S.; Lambert, C.; Durivage, J. C.; Bill, T. G.; Noll, G.; Marder, S. R.; Brédas, J. L., *J. Am. Chem. Soc.* **2004,** 126, 2727.

(2) Karafiloglou, P.; Launay, J. P., *Chem. Phys.* **2003,** 289, 231.

(3) Fraysse, S.; Coudret, C.; Launay, J. P., *J. Am. Chem. Soc.* **2003,** 125, 5880.

(4) Lambert, C.; Noll, G.; Schelter, J., *Nat. Mater.* **2002,** 1, 69.

(5) Lambert, C.; Amthor, S.; Schelter, J., *J. Phys. Chem. A* **2004,** 108, 6474.

(6) Nelsen, S. F.; Ismagilov, R. F.; Powell, D. R., *J. Am. Chem. Soc.* **1996,** 118, 6313.

(7) Nelsen, S. F.; Ismagilov, R. F.; Powell, D. R., *J. Am. Chem. Soc.* **1997,** 119, 10213.

(8) Nelsen, S. F.; Ismagilov, R. F.; Powell, D. R., *J. Am. Chem. Soc.* **1998,** 120, 1924.

(9) Nelsen, S. F.; Ismagilov, R. F.; Gentile, K. E.; Powell, D. R., *J. Am. Chem. Soc.* **1999,** 121, 7108.

(10) Taylor, P. N.; Wylie, A. P.; Huuskonen, J.; Anderson, H. L., *Angew. Chem. Int. Ed.* **1998,** 37, 986.

(11) Piet, J. J.; Taylor, P. N.; Anderson, H. L.; Osuka, A.; Warman, J. M., *J. Am. Chem. Soc.* **2000,** 122, 1749.

(12) Mayor, M.; Weber, H. B.; Reichert, J.; Elbing, M.; von Hanisch, C.; Beckmann, D.; Fischer, M., *Angew. Chem. Int. Ed.* **2003,** 42, 5834.

(13) Lambert, C.; Risko, C.; Coropceanu, V.; Schelter, J.; Amthor, S.; Gruhn, N. E.; Durivage, J. C.; Brédas, J. L., *J. Am. Chem. Soc.* **2005,** 127, 8505.

(14) Becke, A. D., *Phys. Rev. A: At., Mol., Opt. Phys.* **1988,** 38, 3098.

(15) Becke, A. D., *J. Chem. Phys.* **1993,** 98, 5648.

(16) Brédas, J.; Beljonne, D.; Coropceanu, V.; Cornil, J., *Chem. Rev.* **2004,** 104, 4971.

(17) Semichem *Ampac 6.55*, Shawnee, KS, 1997.

(18) Frisch, M. J.; Trucks, G. W.; Schlegel, H. B.; Scuseria, G. E.; Robb, M. A.; Cheeseman, J. R.; Zakrzewski, V. G.; Montgomery, J., J.A.; Stratmann, R. E.; Burant, J. C.; Dapprich, S.; Millam, J. M.; Daniels, A. D.; Kudin, K. N.; Strain, M. C.; Farkas, O.; Tomasi, J.; Barone, V.; Cossi, M.; Cammi, R.; Mennucci, B.; Pomelli, C.; Adamo, C.; Clifford, S.; Ochterski, J.; Petersson, G. A.; Ayala, P. Y.; Cui, Q.; Morokuma, K.; Salvador, P.; Dannenberg, J. J.; Malick, D. K.; Rabuck, A. D.; Raghavachari, K.; Foresman, J. B.; Cioslowski, J.; Ortiz, J. V.; Baboul, A. G.; Stefanov, B. B.; Liu, G.; Liashenko, A.; Piskorz, P.; Komaromi, I.; Gomperts, R.; Martin, R. L.; Fox, D. J.; Keith, T.; Al-Laham, M. A.; Peng, C. Y.; Nanayakkara, A.; Challacombe, M.; Gill, P. M. W.; Johnson, B.; Chen, W.; Wong, M. W.; Andres, J. L.; Gonzalez, C.; Head-Gordon, M.; Replogle, E. S.; Pople, J. A. *Gaussian98, Rev. A.11*, 1998.

(19) Szeghalmi, A. V.; Erdmann, M.; Engel, V.; Schmitt, M.; Amthor, S.; Kriegisch, V.; Nöll, G.; Stahl, R.; Lambert, C.; Leusser, D.; Stalke, D.; Zabel, M.; Popp, J., *J. Am. Chem. Soc.* **2004,** 126, 7834.

(20) Bally, T.; Borden, W. T., *Rev. Comp. Chem.* **1999,** 13, 1.

(21) Coropceanu, V.; Malagoli, M.; Andre, J. M.; Brédas, J. L., *J. Am. Chem. Soc.* **2002,** 124, 10519.

(22) Koopmans, T., *Physica* **1933,** 1, 104.

(23) Piepho, S. B., *J. Am. Chem. Soc.* **1988,** 110, 6319.

(24) Piepho, S. B., *J. Am. Chem. Soc.* **1990,** 112, 4197.

(25) Creutz, C.; Newton, M. D.; Sutin, N., *J. Photochem. Photobiol., A* **1994,** 82, 47.

CHAPTER 7

MIXED-VALENCE PROPERTIES OF VINYLENE AND PHENYLENE-VINYLENE-LINKED BIS(TRIARYLAMINE)S

7.1 Introduction

While the previous Chapter focused on bis(triarylamine)-based systems that have nearly identical inter-redox site distances, we now look into a series of vinylene- and phenylene-vinylene-linked bis(triarylamine)s, see Figure 7.1, that allow for the investigation of the distance dependence of the MV characteristics;[1-3] these molecular structures are analogous those studied by Lambert *et al*.[4-16] in which the bis(triarylamine) redox sites were linked through ethynylene and phenylene-ethynylene bridges. A complete series of experimental characterizations – including X-ray crystallography, Vis/NIR spectroscopy, cyclic voltammetry (CV), infrared (IR) and Raman vibrational spectroscopy, ^{1}H nuclear magnetic resonance (^{1}H NMR), and electron spin resonance (ESR) spectroscopy – have been performed on the $\mathbf{1}^{n+}$ – $\mathbf{4}^{n+}$ (n = 0, 1, 2) and allow for a thorough theoretical investigation. [Note: The bis(triarylamine) systems were synthesized in the group of Professor S. R. Marder at the Georgia Institute of Technology; all Vis/NIR, CV, IR, Raman, ESR, and NMR investigations were also performed within the Marder group. The X-ray crystallographic data were obtained from the group of Professor T. V. Timofeeva at New Mexico Highlands University.] These systems are attractive in that

distinctive modification of the geometries upon oxidation and strong variations in the electronic coupling across the series allow for definitive categorization of the systems as Robin and Day Class II or Class III. In addition, the structural and electronic properties of $\mathbf{1}^{2+}$ provide an interesting system for the investigation of closed-shell versus open-shell dications.

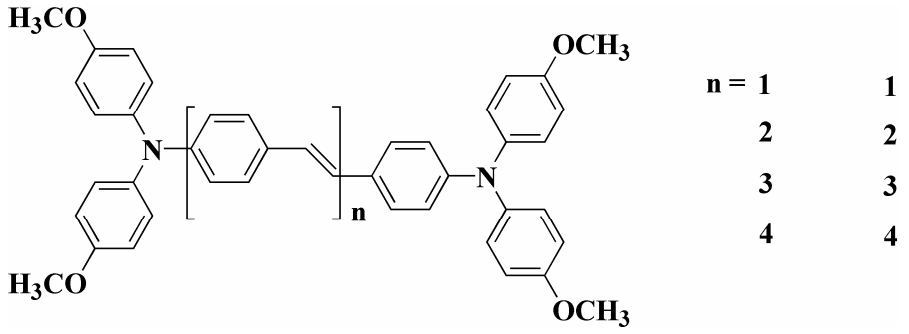

Figure 7.1 Chemical structures of **1** – **4**.

7.2 Theoretical methodology

The geometries of **1** – **4** were optimized in both the neutral and radical-cation states. The semi-empirical Hartree-Fock Austin Model 1 (RHF-AM1) method and Density Functional Theory (DFT) were utilized to evaluate the neutral states of the systems. The DFT calculations were carried out using the B3LYP functionals, where Becke's three-parameter hybrid exchange functional is combined with the Lee-Yang-Parr correlation functional,[17, 18] with a 6-31G* split-valence plus polarization basis set. UHF-AM1 and a

coupled semi-empirical RHF-AM1/configuration interaction (AM1/CI) method using Complete Active Space Configuration Interaction (CAS-CI) were used for optimization of the radical-cation states. While UHF-AM1 predicts asymmetric geometries for each of the molecular systems investigated, the technique suffered from high degrees of spin contamination ($<S^2> \sim 5$). Therefore, only the AM1/CI results are reported. The configuration-interaction (CI) space for the coupled AM1/CI method was restricted to the HOMO-1 and SOMO for each molecular system. In addition, UB3LYP/6-31G* was used for optimization of the geometry of $\mathbf{1}^+$. Excitation energies and transition dipole moments for $\mathbf{1}^+ - \mathbf{4}^+$ were calculated with the correlated semiempirical Zerner's intermediate neglect of differential overlap (ZINDO/CIS) method.[19] The calculations were executed using the radical-cation electronic configuration with the neutral geometry obtained from RHF-AM1. The use of the optimized radical-cation geometries led to large degrees of spin contamination and, hence, unreliable results. All AM1-based calculations were carried out using the implementation in the AMPAC 6.55 software package,[20] while the DFT and ZINDO/CIS calculations were performed with Gaussian98 (Revision A.11).[21]

7.3 Results and discussion

7.3.1 Geometry

Calculated key geometric parameters for the neutral and radical-cation states of **1** – **4**, as well as the X-ray crystal structure parameters of **1** and $\mathbf{1}^+$, are collected in the Tables 7.1 – 7.3, which use the numbering scheme presented in Figure 7.2. In the neutral state, the

nitrogen-carbon bonds within the dianisylamino units of **1** – **4** are of equivalent length [approximately 1.419 Å and 1.425 Å for the RHF-AM1 and B3LYP/6-31G* levels, respectively], while the bridging nitrogen-carbon bonds are significantly shorter [approximately 1.413 Å AM1 and 1.411 Å for the RHF-AM1 and B3LYP/6-31G* levels, respectively]. Within the phenylene-vinylene bridges, there exists the expected bond length alternation (BLA) pattern for such structural motifs. At the RHF-AM1 level of theory, the phenylene-vinylene bridges of neutral **1 – 4** are somewhat twisted in a helical fashion, with dihedral angles of *ca.* 20° between the phenyl rings and the vinylene units; however, planarization of the bridges only costs energy of the order of *kT*. The amine redox centers are slightly pyramidal as the angle sum around the nitrogen atoms is *ca.* 357°. For reference, the RHF-AM1 structures of **1** and **2** are shown in Figure 7.3. At the B3LYP/6-31G* level, there is a slightly less-pronounced twist in the phenylene-vinylene bridges and the redox centers are planar. Both the RHF-AM1 and DFT results match well those of the X-ray structure of **1**.

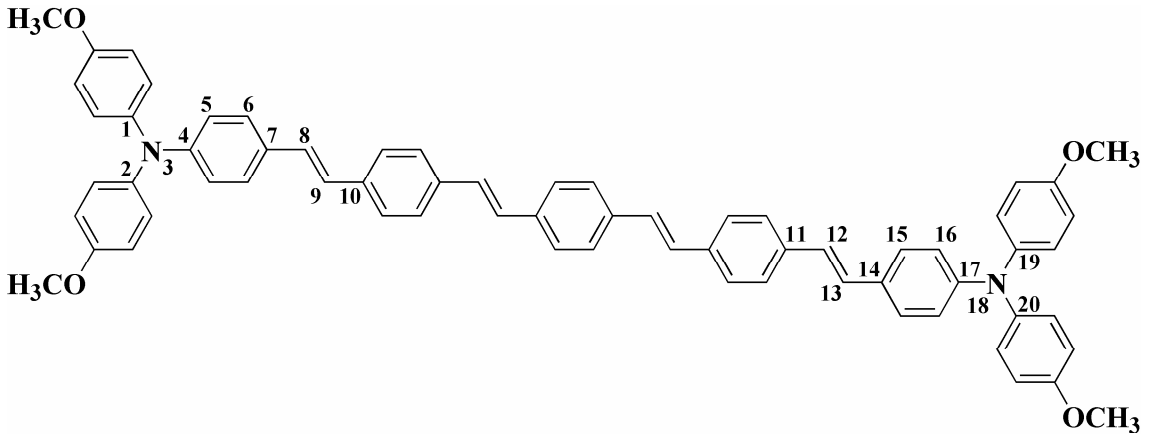

Figure 7.2 Reference numbering scheme utilized for compounds **1 – 4**.

Table 7.1 Selected bond lengths (Å) and angles (°) for the neutral and radical-cation states of **1** as determined at the RHF-AM1, AM1/CI, and B3LYP/6-31G* levels of theory. Data are also provided for the X-ray crystallographic analyses.

	1			1^+		
	X-ray	RHF-AM1	DFT	X-ray	AM1/CI	DFT
Bond (Å)						
$N_3 - C_1$	1.418(5)	1.418	*1.425*	1.424 (4)	1.431	*1.429*
$N_3 - C_2$	1.431(5)	1.418	*1.425*	1.427 (4)	1.431	*1.429*
$N_3 - C_4$	1.391(5)	1.412	*1.413*	1.377 (4)	1.365	*1.388*
$C_4 - C_5$	1.398(5)	1.416	*1.406*	1.411(5)	1.438	*1.418*
$C_5 - C_6$	1.384(5)	1.387	*1.390*	1.389(6)	1.369	*1.378*
$C_6 - C_7$	1.399(5)	1.405	*1.408*	1.405(7)	1.427	*1.419*
$C_7 - C_8$	1.450(5)	1.451	*1.461*	1.488(6)	1.406	*1.436*
$C_8 - C_9$	1.320(7)	1.344	*1.352*	1.316(6)	1.386	*1.370*
$C_9 - C_{10}$	1.450(5)	1.451	*1.461*	1.457(6)	1.406	*1.436*
$C_{14} - C_{15}$	1.384(5)	1.401	*1.411*	1.352(7)	1.423	*1.421*
$C_{15} - C_{16}$	1.375(5)	1.389	*1.386*	1.344(6)	1.370	*1.377*
$C_{16} - C_{17}$	1.378(5)	1.413	*1.410*	1.425(5)	1.437	*1.421*
$N_{18} - C_{17}$	1.391(5)	1.411	*1.413*	1.361(4)	1.365	*1.388*
$N_{18} - C_{19}$	1.418(5)	1.418	*1.425*	1.437(4)	1.431	*1.429*
$N_{18} - C_{20}$	1.431(5)	1.418	*1.425*	1.434(4)	1.431	*1.429*
Angle (°)						
C_1-N_3-C_2	116.1(3)	118.4	*118.9*	117.1(3)	116.7	*117.8*
C_1-N_3-C_4	121.1(3)	119.5	*120.5*	121.2(3)	121.6	*121.1*
C_2-N_3-C_4	122.4(4)	119.7	*120.6*	121.8(3)	121.7	*121.1*
C_{19}-N_{18}-C_{20}	116.1(3)	118.4	*118.9*	116.3(3)	116.7	*117.8*
C_{19}-N_{18}-C_{17}	121.1(3)	119.4	*120.5*	120.5(3)	121.6	*121.1*
C_{20}-N_{18}-C_{17}	122.4(4)	119.6	*120.6*	123.0(3)	121.7	*121.1*

Table 7.2 Selected bond lengths (Å) and angles (°) for the neutral states of **2 – 4** as determined at the RHF-AM1 and B3LYP/6-31G* (*italics*) levels of theory.

	2		3		4	
Bond (Å)						
$N_3 - C_1$	1.419	*1.426*	1.419	*1.426*	1.419	*1.426*
$N_3 - C_2$	1.418	*1.426*	1.419	*1.426*	1.419	*1.426*
$N_3 - C_4$	1.411	*1.411*	1.411	*1.410*	1.411	*1.410*
$C_4 - C_5$	1.416	*1.406*	1.416	*1.407*	1.416	*1.407*
$C_5 - C_6$	1.387	*1.389*	1.387	*1.389*	1.387	*1.388*
$C_6 - C_7$	1.405	*1.408*	1.405	*1.408*	1.405	*1.409*
$C_7 - C_8$	1.451	*1.460*	1.451	*1.460*	1.451	*1.459*
$C_8 - C_9$	1.344	*1.352*	1.344	*1.352*	1.344	*1.352*
$C_9 - C_{10}$	1.452	*1.460*	1.452	*1.460*	1.452	*1.460*
$C_{11} - C_{12}$	1.452	*1.460*	1.452	*1.460*	1.452	*1.460*
$C_{12} - C_{13}$	1.344	*1.352*	1.344	*1.352*	1.344	*1.352*
$C_{13} - C_{14}$	1.451	*1.460*	1.451	*1.460*	1.451	*1.460*
$C_{14} - C_{15}$	1.402	*1.410*	1.405	*1.410*	1.404	*1.410*
$C_{15} - C_{16}$	1.388	*1.386*	1.387	*1.386*	1.388	*1.386*
$C_{16} - C_{17}$	1.414	*1.410*	1.416	*1.411*	1.414	*1.410*
$N_{18} - C_{17}$	1.411	*1.411*	1.411	*1.410*	1.410	*1.410*
$N_{18} - C_{19}$	1.419	*1.425*	1.419	*1.426*	1.418	*1.426*
$N_{18} - C_{20}$	1.419	*1.425*	1.419	*1.426*	1.418	*1.425*
Angle (°)						
C_1-N_3-C_2	118.3	*118.9*	118.3	*118.7*	118.3	*118.9*
C_1-N_3-C_4	119.5	*120.5*	119.5	*120.4*	119.5	*120.4*
C_2-N_3-C_4	119.7	*120.6*	119.7	*120.9*	119.7	*120.7*
C_{19}-N_{18}-C_{20}	118.1	*118.9*	118.0	*118.5*	118.3	*118.7*
C_{19}-N_{18}-C_{17}	119.4	*120.4*	119.4	*120.7*	119.6	*120.6*
C_{20}-N_{18}-C_{17}	119.6	*120.7*	119.6	*120.8*	119.8	*120.7*

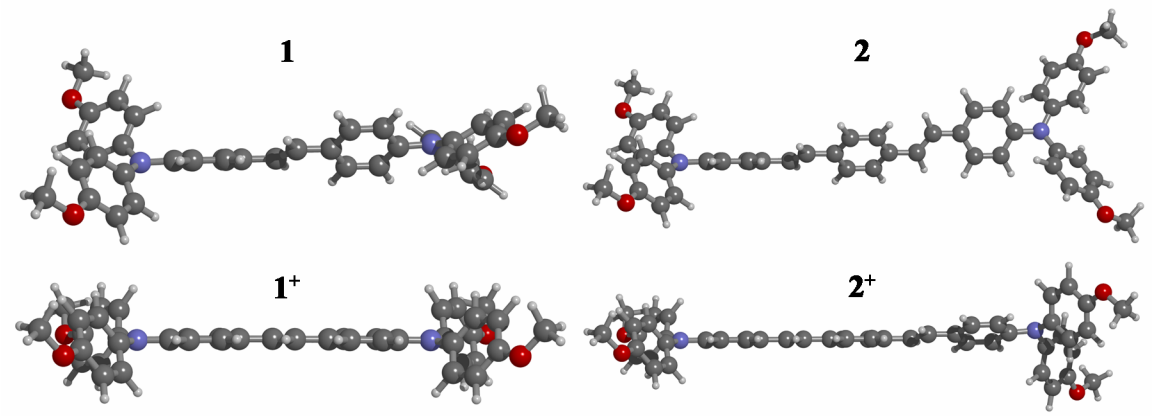

Figure 7.3 Ball-and-stick model of geometries of **1**, **2**, $\mathbf{1}^+$, and $\mathbf{2}^+$ according to RHF-AM1 (neutral) and AM1/CI (radical-cation) levels of theory.

Oxidation to the radical-cation states brings about significant changes relative to the neutral species across the series, see Tables 7.1 and 7.3. $\mathbf{1}^+$ at the AM1/CI level maintains a symmetric structure, however the nitrogen redox center and the bridge planarize. The bridging nitrogen-carbon bonds decrease by 0.046 Å on oxidation, and the carbon-carbon bonds in the stilbene bridge change towards a more quinoid-like arrangement. The net charge is symmetrically distributed over the whole structure. In contrast, the AM1/CI structures of $\mathbf{2}^+ - \mathbf{4}^+$ show definitively broken symmetry; in each case one of the nitrogen centers and a stilbene unit become planar with a similar bond length pattern to $\mathbf{1}^+$, while the remainder of the system maintains a twisted, neutral-like structure. The excess charge is localized solely within the planarized section of the structure. Figure 7.3 shows the AM1/CI structures for $\mathbf{1}^+$ and $\mathbf{2}^+$. Versus their neutral counterparts, not only are the net geometric modifications evident, but also the expected categorization based solely upon the geometric changes: these geometric changes point to $\mathbf{1}^+$ being a potentially Class III system, while $\mathbf{2}^+ - \mathbf{4}^+$ are charge-localized, Class II.

Table 7.3 Selected bond lengths (Å) and angles (°) for the radical-cation states $\mathbf{2}^+ - \mathbf{4}^+$ as determined at the AM1/CI level of theory.

	2^+	3^+	4^+
Bond (Å)			
$N_3 - C_1$	1.433	1.433	1.433
$N_3 - C_2$	1.433	1.433	1.433
$N_3 - C_4$	1.357	1.355	1.354
$C_4 - C_5$	1.445	1.447	1.448
$C_5 - C_6$	1.364	1.363	1.363
$C_6 - C_7$	1.433	1.434	1.435
$C_7 - C_8$	1.404	1.404	1.403
$C_8 - C_9$	1.385	1.382	1.383
$C_9 - C_{10}$	1.417	1.421	1.420
$C_{11} - C_{12}$	1.442	1.455	1.454
$C_{12} - C_{13}$	1.349	1.342	1.343
$C_{13} - C_{14}$	1.446	1.452	1.452
$C_{14} - C_{15}$	1.405	1.400	1.400
$C_{15} - C_{16}$	1.385	1.390	1.390
$C_{16} - C_{17}$	1.417	1.413	1.412
$N_{18} - C_{17}$	1.404	1.412	1.415
$N_{18} - C_{19}$	1.430	1.427	1.426
$N_{18} - C_{20}$	1.429	1.427	1.427
Angle (°)			
C_1-N_3-C_2	116.5	116.5	116.5
C_1-N_3-C_4	121.7	121.8	121.8
C_2-N_3-C_4	121.8	121.8	121.8
C_{19}-N_{18}-C_{20}	115.7	116.1	116.2
C_{19}-N_{18}-C_{17}	118.8	118.3	118.1
C_{20}-N_{18}-C_{17}	119.2	118.8	118.5

X-ray crystal analysis of $\mathbf{1}^+$ also reveals a symmetric structure; thus, UB3LYP/6-31G* analysis of the structure was performed, see Table 7.1. In general, there is excellent agreement between the X-ray, UB3LYP/6-31G*, and AM1/CI results for $\mathbf{1}^+$. Simulations of the IR and Raman vibrational spectra for $\mathbf{1}^+$ at the UB3LYP/6-31G* level, see Figure 7.4, also agree very well with the experimental data. These additional structural characterizations for $\mathbf{1}^+$ again point towards Robin and Day Class III.

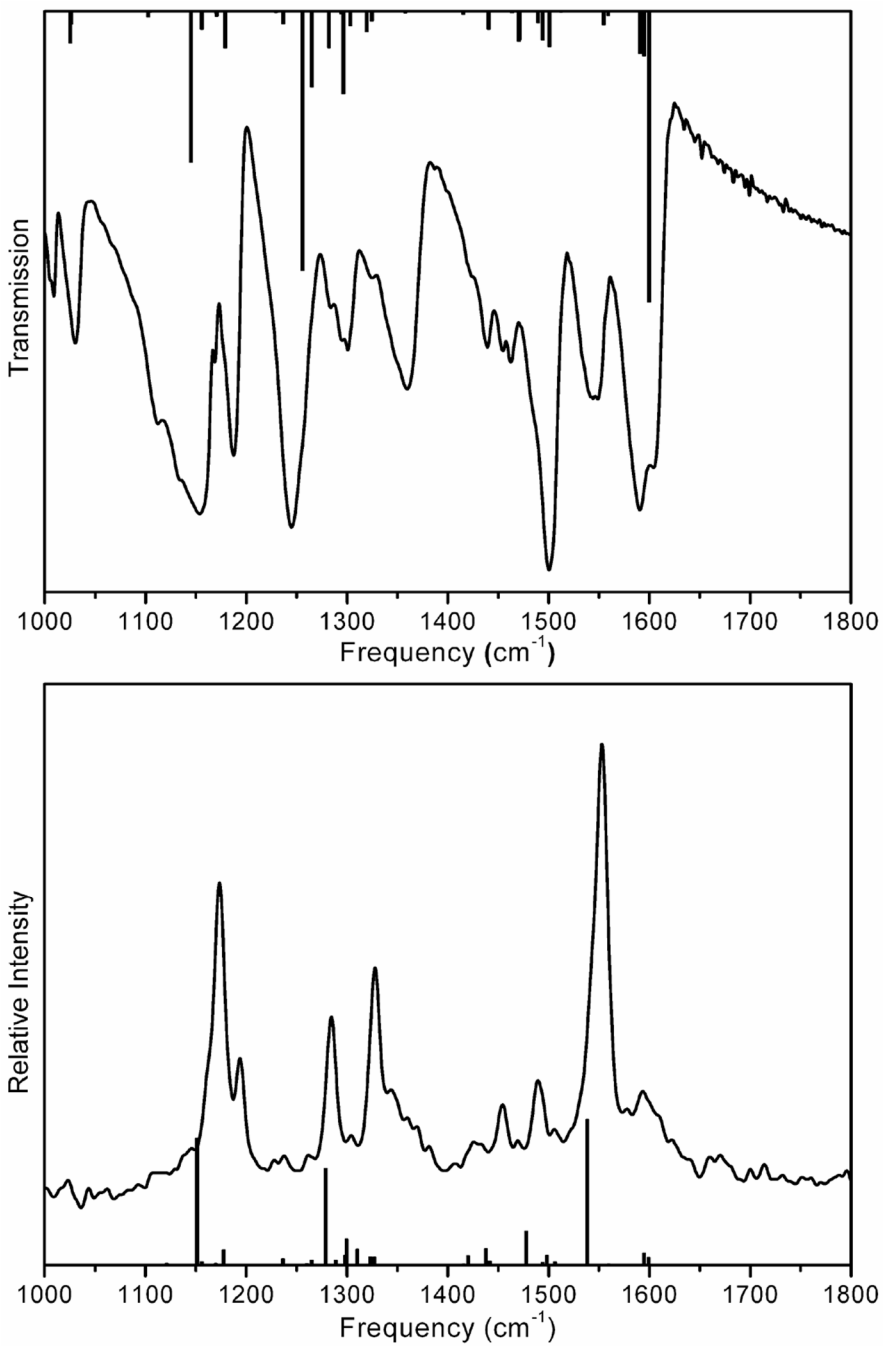

Figure 7.4 Experimental (SbF_6^- salt; KBr pellet) and B3LYP/6-31G* IR [top] and Raman [bottom] spectra of $\mathbf{1}^+$.

7.3.2 Electronic coupling

Theoretical and experimental evaluations of the electronic coupling are listed in Table 7.4. The electronic coupling according to Koopmans' theorem (KT) calculations show similar trends irrespective of the method used: the coupling decreases more-or-less exponentially with inter-redox site distance. However, the values of the couplings are rather sensitive to the details of the method employed, as, to a lesser extent, are the decay constants. A somewhat different trend is suggested by the ZINDO/CIS results. In each case, the calculated transition between the radical-cation ground and first-excited states can be well-described as a HOMO-1 $\rightarrow$ HOMO one-electron transition (using the molecular orbital labels from the neutral electronic configuration), see Table 7.5; the HOMO and HOMO-1 of **1** and **2** are shown in Figure 7.5 and consist of different symmetry combinations of nitrogen p-orbitals, with some contribution from other atoms, particularly from the π-bridging unit in the HOMO. Using the Hush relation for Class III systems (which states that the transition energy between adiabatic potential surfaces for radical-cation ground and excited states at a symmetric geometry [in this case, that of the neutral species] is equal to twice the electronic coupling):

$$2V = \tilde{\nu}_{\max} \tag{7.1}$$

the ZINDO/CIS-calculated coupling decreases rather gradually between $\mathbf{1}^+$ and $\mathbf{3}^+$, and then drops dramatically between $\mathbf{3}^+$ and $\mathbf{4}^+$.

Table 7.4 Electronic coupling parameters (cm^{-1}) as determined from Koopmans' theorem (KT) analysis at varying levels of theory, ZINDO/CIS, and Vis/NIR spectroscopy.

		1^+	2^+	3^+	4^+
KT-AM1		1180	550	260	110
KT-B3LYP/6-31G*		1840	1170	720	440
KT-AM1// B3LYP/6-31G*		1390	800	430	230
ZINDO/CIS		1570	1160	1000	170
Vis/NIR	R_{NN} [a]	1400	700	-----	-----
	$R_{adiabatic}$ [b]	1950	1140	-----	-----
	$V_{Eq.\ 7.1}$ [c]	3040	-----	-----	-----

[a] R_{NN} distance was taken as that of the neutral, RHF-AM1 geometry. [b] $R_{adiabatic}$ estimated from the ZINDO/CIS excitation energies and transition dipole moments, see Table 7.5, which were plugged into the Generalized Mulliken-Hush relation, see Chapter 2. [c] Using Equation 7.1.

Table 7.5 Excitation energies (cm^{-1}) and transition dipole moments (Debye) for compounds $\mathbf{1}^+ - \mathbf{4}^+$ at the ZINDO/CIS level for the neutral RHF-AM1 geometries at the doublet cation electronic configuration.

	excitation energy (cm^{-1})	transition dipole moment, $\mu_{\pm}$ (Debye)
1^+	3140	21.0
2^+	2320	27.6
3^+	2000	32.5
4^+	340	52.4

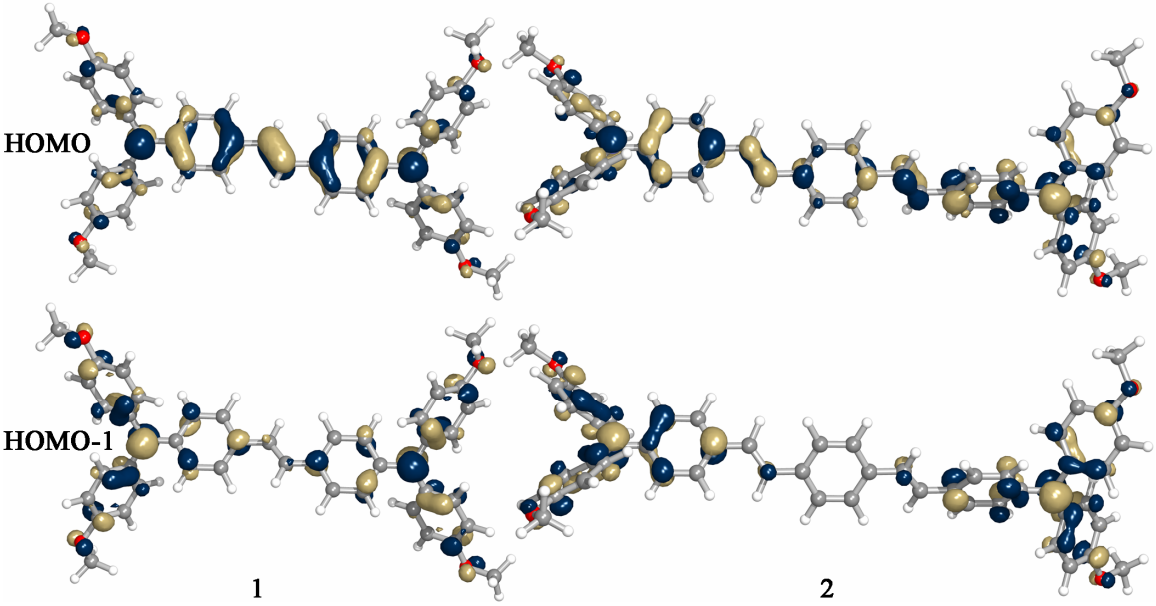

Figure 7.5 Contour plots of the HOMO and HOMO–1 for **1** and **2** obtained at the RHF-AM1 level.

Experimental values of the electronic coupling derived from Vis/NIR data were only determined for $\mathbf{1}^+$ and $\mathbf{2}^+$, see Table 7.4.[1, 3] While $\mathbf{1}^+$ – $\mathbf{4}^+$ all show intense absorption bands in the NIR, only those for $\mathbf{1}^+$ and $\mathbf{2}^+$ can be attributed to intervalence charge-transfer (IVCT) bands; the estimated strengths of the electronic coupling show a similar trend as the theoretical results. In addition, the strong asymmetric nature of the IVCT band for $\mathbf{1}^+$ versus $\mathbf{2}^+$ point towards assignment of $\mathbf{1}^+$ as at least borderline Class II/Class III, if not Class III, and $\mathbf{2}^+$ as Class II. For $\mathbf{3}^+$ and $\mathbf{4}^+$, the IVCT transition is obscured by another NIR band of similar energy and significantly larger absorptivity. Additionally, analogous transitions of nearly twice the absorptivity are observed in dication states $\mathbf{3}^{2+}$ and $\mathbf{4}^{2+}$. Thus, these intense monocation transitions, instead, are assigned to a charge-transfer band from the highest bridge-based orbital to the terminal radical cation; TDDFT results for a single redox center with an extended phenylene-vinylene segment confirm

this assignment. Thus, in $\mathbf{3}^+$ and $\mathbf{4}^+$, the electronic coupling between the redox centers is likely to be small.

In addition to the Vis/NIR spectroscopic results, the relative trends in the strength of the electronic coupling across the series is supported by ESR.[1, 3] The ESR results for $\mathbf{1}^+$ indicate a charge-delocalized system; unfortunately, the room-temperature results for $\mathbf{2}^+ - \mathbf{4}^+$ are poorly resolved. However, ESR of the dication states $\mathbf{1}^{2+} - \mathbf{4}^{2+}$ indicate a transition from strongly coupled redox centers (S = 0) to essentially non-interacting centers (2 × S = ½) in the longer species.

Therefore, the combined theoretical and experimental evaluations of the electronic coupling, combined with the structural analyses, allow for definitive assignment of the molecular structures in the phenylene-vinylene series. While $\mathbf{1}^+$ is a charge-delocalized, strongly-coupled Class III system, $\mathbf{2}^+ - \mathbf{4}^+$ are weaker-coupled, charge-localized systems. In particular, the electronic coupling between redox sites in $\mathbf{3}^+$ and $\mathbf{4}^+$ is very weak.

7.3.3 Dication

Isolation and subsequent formation of crystals allowed for further investigation of $\mathbf{1}^{2+}$, and comparison to $\mathbf{5}^{2+}$ and the Chichibabin hydrocarbon **6**,[22] see Figure 7.6.[2] These systems are of interest in that for radical centers linked by conjugated bridges there are in general two expected, extreme structure types: diamagnetic closed-shell (strong coupling between the redox sites) and paramagnetic biradical (weak coupling between the redox

sites). When the coupling is strong, a quinoidal bond-length alternation pattern is expected through the bridge. ^{1}H NMR spectra and X-ray crystallographic data for $\mathbf{1}^{2+}$ and $\mathbf{5}^{2+}$ appear to provide contrasting evidence as to the expected norm: the ^{1}H NMR spectra point towards diamagnetic, closed-shell electronic states for the two dications, while the X-ray crystallographic structures do not indicate the expected degree of "fully" quinoidal character. Additionally for **6**, a reduced bond-length alternation pattern in the X-ray crystal structure, along with some rather inconclusive ESR data, have lead to some debate as to whether the Chichibabin hydrocarbon is either closed-shell or a biradical.

5

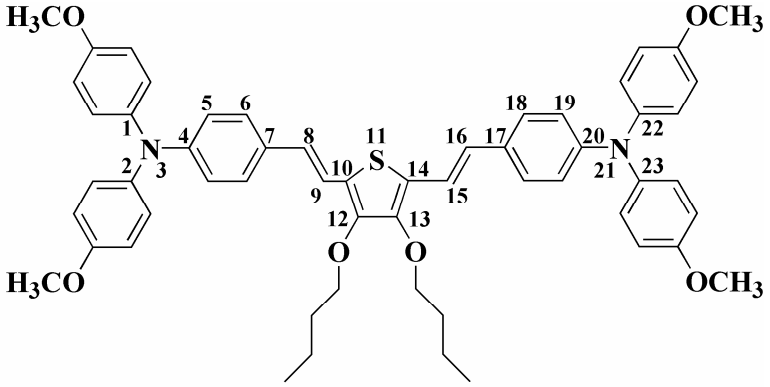

6

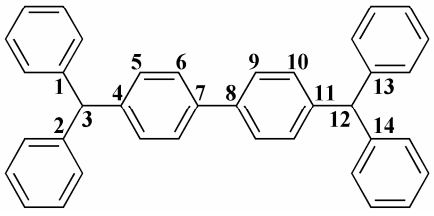

Figure 7.6 Chemical structures and bond numbering of **5** and the Chichibabin hydrocarbon (**6**).

Geometry optimizations of $\mathbf{1}^{2+}$, $\mathbf{5}^{n+}$ (n = 0, 1, 2), and **6** were carried out at the (U)B3LYP/6-31G* level of theory; selected geometric parameters for $\mathbf{1}^{2+}$, $\mathbf{5}^{n+}$, and **6** are collected in Tables 7.6 – 7.9, using the numbering scheme in Figure 7.6. For $\mathbf{1}^{2+}$, $\mathbf{5}^{2+}$, and **6**, calculations were performed for both the closed-shell singlet and open-shell triplet electronic states, as well as the "open-shell singlet" biradical electronic state which was obtained with a broken-symmetry (BS) wavefunction DFT method. It is important to note that the broken-symmetry unrestricted DFT method does not produce a well-defined spin state, but rather a mixture of singlet and triplet states. Open-shell singlet states generally require a multi-configurational self-consistent-field treatment; therefore, these results should be taken with some care.

For $\mathbf{1}^{2+}$, see Table 7.6, the closed-shell, diamagnetic singlet electronic configuration is consistent with that obtained via X-ray crystallography. Both the closed-shell electronic configuration and X-ray structure reveal that there exists a quinoidal "sense" to the structure of the bridge phenylene groups, but that the structure falls well short of the "ideal" quinoidal BLA of *ca*. 0.1 Å; the vinylene bridge of $\mathbf{1}^{2+}$ retains the same sense of BLA as the neutral species, although with a greatly reduced magnitude. Calculations for the open-shell triplet electronic configuration reveal a rather different geometry characterized by more-or-less equal shortening of all carbon-nitrogen bonds on oxidation and by retention of stronger BLA in the vinylene bridge. The BS-wavefunction method suggests that the geometry of the open-shell singlet configuration is intermediate between that of the closed-shell singlet and open-shell triplet. Thus, the experimental data and DFT results are consistent with a closed-shell singlet configuration for $\mathbf{1}^{2+}$.

Table 7.6 Selected bond lengths (Å) and angles (°) for $\mathbf{1}^{2+}$ at the UB3LYP/6-31G* level of theory.

	X-ray	singlet	BS	triplet
Bond (Å)				
$N_3 - C_1$	1.422(6)	1.422	1.413	1.409
$N_3 - C_2$	1.416(6)	1.423	1.414	1.410
$N_3 - C_4$	1.369(6)	1.379	1.407	1.419
$C_4 - C_5$	1.406(7)	1.425	1.411	1.406
$C_5 - C_6$	1.359(7)	1.372	1.383	1.387
$C_6 - C_7$	1.422(6)	1.428	1.416	1.412
$C_7 - C_8$	1.415(7)	1.420	1.450	1.460
$C_8 - C_9$	1.366(9)	1.385	1.362	1.354
$C_9 - C_{10}$	1.415(7)	1.420	1.450	1.460
$C_{14} - C_{15}$	1.422(6)	1.429	1.417	1.413
$C_{15} - C_{16}$	1.359(7)	1.371	1.381	1.385
$C_{16} - C_{17}$	1.406(7)	1.428	1.414	1.409
$N_{18} - C_{17}$	1.369(6)	1.379	1.407	1.419
$N_{18} - C_{19}$	1.416(6)	1.423	1.414	1.410
$N_{18} - C_{20}$	1.422(6)	1.422	1.413	1.409
Angle (°)				
C_1-N_3-C_2	119.8(4)	118.0	119.4	120.1
C_1-N_3-C_4	119.5(4)	121.0	120.3	119.9
C_2-N_3-C_4	120.7(4)	121.0	120.3	120.0
C_{19}-N_{18}-C_{20}	119.8(4)	118.0	119.4	120.1
C_{19}-N_{18}-C_{17}	119.5(4)	121.0	120.3	119.9
C_{20}-N_{18}-C_{17}	120.7(4)	121.0	120.3	120.0

For **5**, there is excellent agreement between the X-ray crystallographic structure and theoretically-derived structure of the neutral electronic configuration, see Table 7.7; the optimized radical-cation structure is provided for reference. The X-ray crystallographic structure of $\mathbf{5}^{2+}$ was less precisely determined than that of $\mathbf{1}^{2+}$, thus the BLA pattern within the bridge phenylene groups is not as well defined; however, the pattern suggested within the vinylene portion points to a similar situation as that for $\mathbf{1}^{2+}$, *i.e.*, the bridge has some quinoidal character, but not the fully-quinoidal character expected. This result is confirmed by the closed-shell, diamagnetic singlet calculation; both the BS-wavefunction

and open-shell triplet electronic structure calculations deviate rather noticeably from the X-ray structure.

Table 7.7 Selected bond lengths (Å) and angles (°) for neutral and radical-cation states of **5** at the (U)B3LYP/6-31G* level of theory.

	neutral X-ray	B3LYP/ 6-31G*	cation UB3LYP/ 6-31G*
Bond (Å)			
$N_3 - C_1$	1.423(3)	1.425	1.432
$N_3 - C_2$	1.412(3)	1.425	1.432
$N_3 - C_4$	1.412(3)	1.412	1.387
$C_4 - C_5$	1.393(4)	1.410	1.421
$C_5 - C_6$	1.380(4)	1.386	1.377
$C_6 - C_7$	1.388(4)	1.411	1.421
$C_7 - C_8$	1.453(3)	1.457	1.432
$C_8 - C_9$	1.332(4)	1.356	1.375
$C_9 - C_{10}$	1.442(4)	1.437	1.413
$C_{10} - C_{12}$	1.366(4)	1.385	1.409
$C_{12} - C_{13}$	1.417(3)	1.427	1.409
$C_{13} - C_{14}$	1.370(3)	1.385	1.407
$S_{11} - C_{10}$	1.728(3)	1.760	1.761
$S_{11} - C_{14}$	1.732(3)	1.760	1.761
$C_{14} - C_{15}$	1.437(3)	1.437	1.414
$C_{15} - C_{16}$	1.321(4)	1.356	1.374
$C_{16} - C_{17}$	1.458(4)	1.457	1.433
$C_{17} - C_{18}$	1.381(4)	1.411	1.420
$C_{18} - C_{19}$	1.385(4)	1.386	1.377
$C_{19} - C_{20}$	1.392(4)	1.410	1.421
$N_{21} - C_{20}$	1.405(3)	1.411	1.387
$N_{21} - C_{22}$	1.428(3)	1.425	1.432
$N_{21} - C_{23}$	1.430(3)	1.425	1.432
Angle (°)			
C_1-N_3-C_2	119.1(2)	118.9	117.7
C_1-N_3-C_4	120.1(2)	120.5	121.1
C_2-N_3-C_4	120.5(2)	120.5	121.1
C_{22}-N_{21}-C_{23}	117.3(2)	118.9	117.7
C_{22}-N_{21}-C_{20}	120.9(2)	120.5	121.2
C_{23}-N_{21}-C_{20}	121.0(2)	120.5	121.2

Table 7.8 Selected bond lengths (Å) and angles (°) for $\mathbf{5}^{2+}$ at the UB3LYP/6-31G* level of theory.

	X-ray	UB3LYP/6-31G*		
		singlet	BS	triplet
Bond (Å)				
$N_3 - C_1$	1.421(9)	1.430	1.422	1.417
$N_3 - C_2$	1.448(9)	1.430	1.422	1.416
$N_3 - C_4$	1.378(9)	1.373	1.391	1.405
$C_4 - C_5$	1.420(9)	1.429	1.421	1.415
$C_5 - C_6$	1.367(10)	1.370	1.376	1.380
$C_6 - C_7$	1.376(10)	1.430	1.423	1.418
$C_7 - C_8$	1.407(10)	1.414	1.432	1.445
$C_8 - C_9$	1.383(9)	1.391	1.375	1.365
$C_9 - C_{10}$	1.371(10)	1.397	1.414	1.426
$C_{10} - C_{12}$	1.416(10)	1.423	1.408	1.398
$C_{12} - C_{13}$	1.392(10)	1.397	1.412	1.423
$C_{13} - C_{14}$	1.395(10)	1.435	1.411	1.397
$S_{11} - C_{10}$	1.750(8)	1.764	1.759	1.757
$S_{11} - C_{14}$	1.766(7)	1.762	1.759	1.756
$C_{14} - C_{15}$	1.383(9)	1.391	1.412	1.427
$C_{15} - C_{16}$	1.385(9)	1.395	1.376	1.364
$C_{16} - C_{17}$	1.414(10)	1.410	1.431	1.446
$C_{17} - C_{18}$	1.385(10)	1.431	1.423	1.418
$C_{18} - C_{19}$	1.385(9)	1.369	1.375	1.380
$C_{19} - C_{20}$	1.443(10)	1.431	1.422	1.415
$N_{21} - C_{20}$	1.373(9)	1.371	1.390	1.405
$N_{21} - C_{22}$	1.441(9)	1.430	1.422	1.416
$N_{21} - C_{23}$	1.399(10)	1.430	1.423	1.416
Angle (°)				
C_1-N_3-C_2	118.1(6)	117.6	118.5	119.2
C_1-N_3-C_4	119.9(6)	121.2	120.8	120.4
C_2-N_3-C_4	121.9(6)	121.2	120.7	120.4
C_{22}-N_{21}-C_{23}	117.8(6)	117.4	118.5	119.2
C_{22}-N_{21}-C_{20}	120.9(6)	121.3	120.8	120.4
C_{23}-N_{21}-C_{20}	121.2(7)	121.3	120.7	120.4

For the Chichibabin hydrocarbon, **6**, see Table 7.9, the features of the X-ray structure – a reduced BLA and long biphenyl bridge bond – have been taken as significant biradical character. The (U)B3LYP/6-31G*-optimized parameters does not allow for the unambiguous assignment of the electronic configuration; the geometric parameters from

the X-ray structure are bracketed by the closed-shell singlet and BS-wavefunction electronic structure calculations, with the BS-wavefunction providing the "better" match. It is interest to note, however, that the closed-shell singlet structure does not show a fully quinoidal structure; the central carbon-carbon bond length is longer than a typical double bond and the BLA in the biphenyl groups is considerably less than 0.1 Å.

Table 7.9 Selected bond lengths (Å) and angles (°) for **6** at the (U)B3LYP/6-31G* level of theory.

	X-ray	singlet	BS	triplet
Bond (Å)				
$C_3 - C_1$	1.482(3)	1.479	1.471	1.465
$C_3 - C_2$	1.457(3)	1.479	1.471	1.465
$C_3 - C_4$	1.429(3)	1.402	1.442	1.463
$C_4 - C_5$	1.424(3)	1.445	1.425	1.415
$C_5 - C_6$	1.371(3)	1.365	1.381	1.388
$C_6 - C_7$	1.420(3)	1.437	1.416	1.408
$C_7 - C_8$	1.448(4)	1.420	1.463	1.480
$C_8 - C_9$	1.420(3)	1.437	1.416	1.408
$C_9 - C_{10}$	1.371(3)	1.365	1.138	1.388
$C_{10} - C_{11}$	1.424(3)	1.445	1.425	1.415
$C_{12} - C_{11}$	1.429(3)	1.402	1.442	1.463
$C_{12} - C_{13}$	1.457(3)	1.479	1.471	1.465
$C_{12} - C_{14}$	1.482(3)	1.479	1.471	1.465
Angle (°)				
C_1-C_3-C_2	117.69(18)	116.6	118.5	120.0
C_1-C_3-C_4	-----	121.7	120.7	120.0
C_2-C_3-C_4	122.07(19)	121.7	120.8	120.0
C_{13}-C_{12}-C_{14}	117.69(18)	116.6	118.5	120.0
C_{13}-C_{12}-C_{11}	-----	121.7	120.7	120.0
C_{14}-C_{12}-C_{11}	122.07(19)	121.7	120.8	120.0
C_6-C_7-C_8-C_9	~ 0.6	9.8	24.3	34.6

It is important to note that in the above electronic-structure calculations that the total energy for the BS-wavefunction state was consistently the most energy stabilized, see Table 7.10, even though the geometric parameters provided by the method did not necessarily predict the experimentally-derived geometry. In general, all three electronic states are within a few *kT* of each other and probably mix readily depending upon the surrounding environment (*e.g.*, temperature, solvent). The proper description of these electronic states requires a multiconfigurational approach.

Table 7.10 Optimized energies (hartrees) and energy splittings (eV) for $\mathbf{1}^{2+}$, $\mathbf{5}^{2+}$, and **6** at the B3LYP/6-31G* level.

		energy (hr)	splitting[a] (eV)
$\mathbf{1}^{2+}$	*singlet*	-2033.22342184	0.17
	BS	-2033.22949390	0.00
	triplet	-2033.22741720	0.06
$\mathbf{5}^{2+}$	*singlet*	-3127.40170528	0.07
	BS	-3127.40424931	0.00
	triplet	-3127.40073782	0.10
6	*singlet*	-1464.87576091	0.14
	BS	-1464.88095919	0.00
	triplet	-1464.87753662	0.09

[a] Energy splitting taken in reference to the BS-wavefunction state energy.

7.4 Conclusions

The MV systems **1** – **4** have been fully characterized experimentally. The AM1/CI-derived geometries predict a charge-delocalized, symmetric geometric structure for $\mathbf{1}^{+}$,

while $\mathbf{2}^{+}$ – $\mathbf{4}^{+}$ are charge-localized, geometrically symmetry-broken structures. Additionally, the theoretically-derived trends of the electronic coupling match well the trends of both the Vis/NIR and ESR spectroscopies. Therefore, $\mathbf{1}^{+}$ can be categorized as a Robin and Day Class III species, while $\mathbf{2}^{+}$ – $\mathbf{4}^{+}$ are Class II. We have also looked into the geometric and electronic structures of $\mathbf{1}^{2+}$ and $\mathbf{5}^{2+}$ and found them to be closed-shell, diamagnetic systems, even though the geometric configurations do not take on the expected fully-quinoidal structure.

7.5 References

(1) Barlow, S.; Risko, C.; Coropceanu, V.; Tucker, N. M.; Jones, S. C.; Levi, Z.; Khrustalev, V. N.; Antipin, M. Y.; Kinnibrugh, T. L.; Timofeeva, T. V.; Marder, S. R.; Brédas, J. L., *Chem. Commun.* **2005**, 764.

(2) Zheng, S.; Barlow, S.; Risko, C.; Kinnibrugh, T. L.; Khrustalev, V. N.; Antipin, M. Y.; Tucker, N. M.; Timofeeva, T. V.; Coropceanu, V.; Jones, S. C.; Brédas, J. L.; Marder, S. R., **2005**, submitted.

(3) Barlow, S.; Risko, C.; Chung, S. J.; Tucker, N. M.; Coropceanu, V.; Jones, S. C.; Levi, Z.; Marder, S. R.; Brédas, J. L., **2005**, submitted.

(4) Lambert, C.; Nöll, G., *J. Am. Chem. Soc.* **1999,** 121, 8434.

(5) Lambert, C.; Nöll, G.; Hampel, F., *J. Phys. Chem. A* **2001,** 105, 7751.

(6) Lambert, C.; Nöll, G.; Schelter, J., *Nat. Mater.* **2002,** 1, 69.

(7) Lambert, C.; Nöll, G., *Chem. Eur. J.* **2002,** 8, 3467.

(8) Lambert, C.; Nöll, G., *J. Chem. Soc. Perkin Trans. 2* **2002**, 2039.

(9) Lambert, C.; Nöll, G., *Synth. Met.* **2003,** 139, 57.

(10) Lambert, C.; Amthor, S.; Schelter, J., *J. Phys. Chem. A* **2004,** 108, 6474.

(11) Lambert, C.; Risko, C.; Coropceanu, V.; Schelter, J.; Amthor, S.; Gruhn, N. E.; Durivage, J. C.; Brédas, J. L., *J. Am. Chem. Soc.* **2005,** 127, 8505.

(12) Coropceanu, V.; Malagoli, M.; André, J. M.; Brédas, J. L., *J. Chem. Phys.* **2001,** 115, 10409.

(13) Coropceanu, V.; Malagoli, M.; André, J. M.; Brédas, J. L., *J. Am. Chem. Soc.* **2002,** 124, 10519.

(14) Coropceanu, V.; Lambert, C.; Nöll, G.; Brédas, J. L., *Chem. Phys. Lett.* **2003,** 373, 153.

(15) Coropceanu, V.; Gruhn, N. E.; Barlow, S.; Lambert, C.; Durivage, J. C.; Bill, T. G.; Nöll, G.; Marder, S. R.; Brédas, J. L., *J. Am. Chem. Soc.* **2004,** 126, 2727.

(16) Szeghalmi, A. V.; Erdmann, M.; Engel, V.; Schmitt, M.; Amthor, S.; Kriegisch, V.; Nöll, G.; Stahl, R.; Lambert, C.; Leusser, D.; Stalke, D.; Zabel, M.; Popp, J., *J. Am. Chem. Soc.* **2004,** 126, 7834.

(17) Becke, A. D., *Phys. Rev. A: At., Mol., Opt. Phys.* **1988,** 38, 3098.

(18) Becke, A. D., *J. Chem. Phys.* **1993,** 98, 5648.

(19) Zerner, M. C.; Loew, G. H.; Kirchner, R. F.; Muellerwesterhoff, U. T., *J. Am. Chem. Soc.* **1980,** 102, 589.

(20) Semichem *Ampac 6.55*, Shawnee, KS, 1997.

(21) Frisch, M. J.; Trucks, G. W.; Schlegel, H. B.; Scuseria, G. E.; Robb, M. A.; Cheeseman, J. R.; Zakrzewski, V. G.; Montgomery, J., J.A.; Stratmann, R. E.; Burant, J. C.; Dapprich, S.; Millam, J. M.; Daniels, A. D.; Kudin, K. N.; Strain, M. C.; Farkas, O.; Tomasi, J.; Barone, V.; Cossi, M.; Cammi, R.; Mennucci, B.; Pomelli, C.; Adamo, C.; Clifford, S.; Ochterski, J.; Petersson, G. A.; Ayala, P. Y.; Cui, Q.; Morokuma, K.; Salvador, P.; Dannenberg, J. J.; Malick, D. K.; Rabuck, A. D.; Raghavachari, K.; Foresman, J. B.; Cioslowski, J.; Ortiz, J. V.; Baboul, A. G.; Stefanov, B. B.; Liu, G.; Liashenko, A.; Piskorz, P.; Komaromi, I.; Gomperts, R.; Martin, R. L.; Fox, D. J.; Keith, T.; Al-Laham, M. A.; Peng, C. Y.; Nanayakkara, A.; Challacombe, M.; Gill, P. M. W.; Johnson, B.; Chen, W.; Wong, M. W.; Andres, J. L.; Gonzalez, C.; Head-Gordon, M.; Replogle, E. S.; Pople, J. A. *Gaussian98, Rev. A.11*, 1998.

(22) Montgomery, L. K.; Huffman, J. C.; Jurczak, E. A.; Grendze, M. A., *J. Am. Chem. Soc.* **1986,** 108, 6004.

CHAPTER 8

SIMULATION OF RESOLVED VIBRONIC STRUCTURE IN CLASS III MV SYSTEMS

8.1 Introduction

As was shown in the two-state, two-mode vibronic model discussed in Chapter 2, symmetric vibrational normal modes play an important role in the shape of the intervalence charge-transfer (IVCT) bands in Robin and Day Class III mixed-valence (MV) systems. When only the diagonal vibronic coupling constant is taken into account, the upper adiabatic surface is displaced with respect to the ground adiabatic surface, see Figure 2.6. The degree of displacement is due to the sensitivity of the molecular geometry to the change in electron distribution upon excitation;[1] thus, a relatively large modification to the molecular geometry leads to a large reorganization energy as well as to a relatively broad IVCT band. Additionally, if the interaction is due to only high frequency vibrational modes, then vibrational structure may be evident in the IVCT band.

In this Chapter, we investigate two such examples of resolved vibrational fine structure in the IVCT bands of Class III organic MV systems. The first system is a phenylene-bridged bis-dioxaborine (**DOB**) radical-anion, see Figure 8.1.[2] Through our studies of dioxaborines as electron-transport materials, we investigated the MV properties of **DOB** to gain insight into the degree of delocalization possible in these systems. The second

example involves a series of arylene-bridged bis-dimethylamines. *N*,*N*,*N'*,*N'*-tetramethyl-p-phenylenediamine (**TMPD**) has been of vast importance in the study of organic radical-cations. Being the first organic radical-cation prepared, it has played a principal role in the application of electron-transfer theory to organic compounds[3-6] and understanding of the mechanisms of photochemistry.[7-10] Related to this structure, *N*,*N*,*N'*,*N'*-tetramethylbenzidine (**TMB**) has also served as an extension of **TMPD** in photochemical studies in solution[11, 12] and heterogeneous solid systems.[13] From the standpoint of organic MV systems, these structures are similar to the triarylamine-based compounds *N*,*N*,*N'*,*N'*-tetra(4-methoxyphenyl)-*para*-phenylenediamine and 4,4'-bis[*N*,*N'*-di(4-methoxyphenyl)amino]biphenyl that have been found to have IVCT bands that suggest strong electronic coupling in the range of Class III.[14] Additionally, *N*,*N*,*N'*,*N'*-tetramethyl-p-tolyldiamine (**TMTD**) was investigated to complete the series. [Note: All Vis/NIR spectroscopic data was collected in the group of Professor S. R. Marder at the Georgia Institute of Technology.]

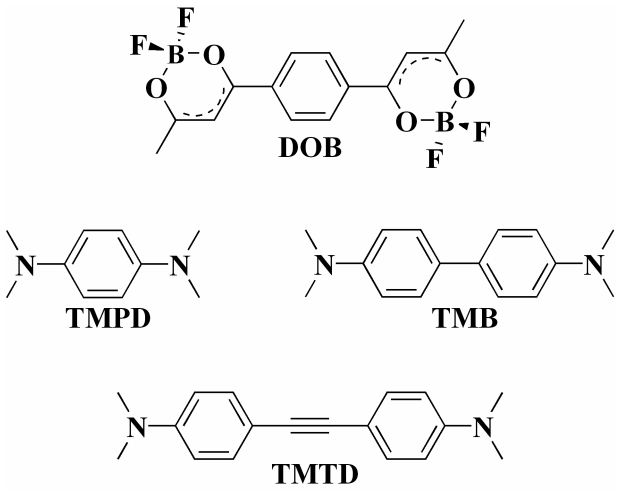

Figure 8.1 Chemical structures of **DOB**, **TMPD**, **TMB**, and **TMTD**.

To simulate the Vis/NIR spectra, we utilized a linear Franck-Condon vibronic model that is given in detail elsewhere.[15] For **DOB**$^{-}$,[2] the model is used to fit the experimental spectrum in order to directly extract optimized vibrational frequencies and Huang-Rhys factors associated with the vibrational modes in the vibronic progression. For **TMPD**$^{+}$, **TMB**$^{+}$, and **TMTD**$^{+}$, Franck-Condon simulation of the spectra were carried out using the vibrational frequencies and Huang-Rhys factors of the optimized first-excited states of the radical-cations.

8.2 Theoretical methodology

The geometry optimizations of the neutral (**DOB**) and radical-anion (**DOB**$^{-}$) ground states were carried out at the Density Functional Theory (DFT) level using the (U)B3LYP functionals, where Becke's three-parameter hybrid exchange functional[16, 17] is

combined with the Lee-Yang-Parr correlation functional,[18] and a 6-31G* split valence plus polarization basis set. The geometry optimization of the first-excited state of the radical-anion (**DOB^{-}***) was determined using symmetry constraints of the radical-anion. The excitation energies of the low-lying excited states have been calculated with time-dependent DFT (TDDFT) and with Zerner's semiempirical intermediate neglect of differential overlap (ZINDO)[19] method supplemented by a single-configuration interaction (CIS) scheme. All DFT calculations were carried out with the Gaussian98 (Revision A.11) suite of programs.[20]

For **TMPD**, **TMB**, and **TMTD**, geometry optimizations of the neutral and radical-cation (**TMPD^{+}**, **TMB^{+}**, and **TMTD^{+}**) ground states were also carried out with DFT. However, due to use of the TURBOMOLE 5.6 software suite[21] for the optimization of these compounds, it is important to note that the B3LYP functional is slightly different than that utilized for the optimization of **DOB**; as well, though the basis set was a Gaussian atomic orbital basis set of split valence plus polarization quality, it is not the same as the Pople 6-31G* basis set. Excitation energies for the low-lying states of the radical-cation species have been calculated at the TDDFT level. With these results, the lowest-lying excited state (**TMPD^{+}***, **TMB^{+}***, and **TMTD^{+}***) was then optimized using analytical TDDFT gradients as described by Furche and Alrichs.[22] Frequency analyses were completed for the optimized geometries to ensure that the geometry was not a transition state. The vibrational modes were utilized to simulate both the first transition of the UPS spectra and the IVCT band of the Vis/NIR spectra; input Huang-Rhys factors, as well as vibrational mode estimates to total intramolecular reorganization energies for excitation,

of the radical cation were obtained using the Dushin program.[23] A scaling factor of 0.9613 for the B3LYP frequencies was utilized for the modeling of the experimental spectra.

8.3 Results and Discussion

8.3.1 DOB

Selected geometric parameters for the neutral and radical-anion ground and first-excited states for **DOB** are listed in Table 8.1, using the reference bond numbering scheme in Figure 8.2. For all three states, there exist two possible rotational isomers: a C_i *anti*-conformation and a C_s *syn*-conformation; the gas-phase C_i *anti*-conformation was, in general, only slightly more stable (~*kT*) than the C_s *syn*-conformation, and the geometric parameters were nearly identical. Within the dioxaborine ring of **DOB**, the bond lengths of the boron-oxygen bond are 1.52 Å, while the ketonic carbon-oxygen bonds are 1.29 Å; the carbon-carbon bonds are also of equivalent length (1.4 Å). The bridging carbon-carbon bond between the dioxaborine ring and the phenylene bridge is 1.48 Å, and the bond-length alternation (BLA) within the phenylene bridge is 0.027 Å. There is an approximate 11° torsion between the dioxaborine and phenylene rings.

Reduction to $\mathbf{DOB}^-$ causes the boron-oxygen bonds to decrease by 0.02 Å to 1.50 Å, while the ketonic carbon-oxygen bonds increase by approximately 0.03 Å. Unlike the neutral state, the carbon-carbon bonds in the dioxaborine are rather different with bond

lengths of 1.375 Å and 1.423 Å, with the longer bond adjacent to the phenylene ring. The bond length of the bridging carbon-carbon bond decreases by 0.045 Å, while the BLA in the phenylene bridge increases to 0.051 Å. The changes across all of the carbon-carbon bonds points towards movement to a quinoidal BLA pattern. Additionally, the dioxaborine and phenylene rings are virtually planar with a dihedral of 2°. Though the *anti*- and *syn*-rotational isomers are energetically similar, the key difference between the two rotamers is the decrease of 10.0 Debye in dipole moment upon going from the *syn*- to *anti*-conformer. Thus, it is expected that solvent polarity should play a role in the actual conformation in solution.

Upon excitation to **DOB^{-}***, very little change occurs in the bonds containing boron. The carbon-carbon bonds of the dioxaborine ring and the phenyl bridge equilibrate with an average change of 0.02 Å. The bridging carbon-carbon bond increases to 1.487 Å, while the BLA in the phenylene bridge becomes virtually negligible (0.007 Å). Hence, the excited-state structure reverts back to a construct containing a higher degree of aromaticity, as in the neutral state. **DOB^{-}*** is also characterized by an increased dihedral angle torsion (~25^{o}) between the dioxaborine rings and phenylene bridge.

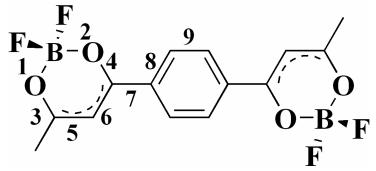

Figure 8.2 Bond numbering scheme for **DOB**.

Table 8.1 Selected bond lengths (Å) and angle (°) for the neutral and radical-anion ground and first-excited states for **DOB** at the B3LYP/6-31G* level of theory.

	DOB		DOB^-		DOB^-*	
Molecular Symmetry	C_i	C_s	C_i	C_s	C_i	C_s
1	1.520	1.522	1.504	1.505	1.502	1.504
2	1.524	1.525	1.498	1.498	1.503	1.504
3	1.290	1.289	1.314	1.314	1.319	1.319
4	1.294	1.293	1.320	1.319	1.321	1.321
5	1.396	1.396	1.375	1.374	1.395	1.395
6	1.399	1.399	1.423	1.423	1.394	1.394
7	1.480	1.480	1.435	1.435	1.487	1.487
8	1.405	1.405	1.426	1.426	1.403	1.403
9	1.388	1.388	1.375	1.375	1.395	1.396
Torsion Angle	11	13	2	2	25	26

The Vis/NIR spectrum for **DOB^-** is shown in Figure 8.3, with the normalized vibronic fit of the low energy band. The charge transfer band consists of well-defined vibrational structure, which strongly points to the assignment of **DOB^-** to Robin and Day's Class III. From the absorption maximum, the electronic coupling is estimated to be 5000 cm^{-1}. TDDFT (6860 cm^{-1}), ZINDO/CIS (5240 cm^{-1}), and KT-DFT (6050 cm^{-1}) estimates point to a similar range, with ZINDO/CIS providing the best reproducibility.

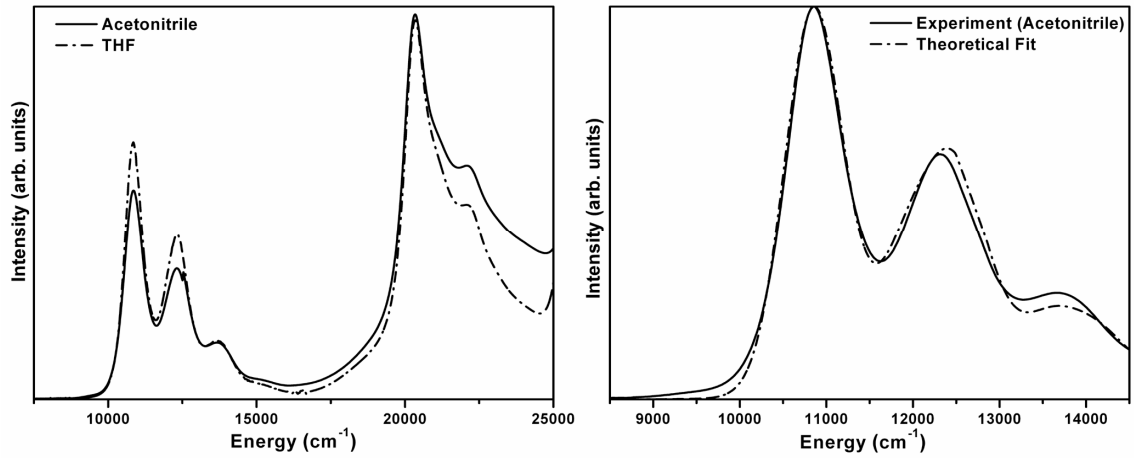

Figure 8.3 Vis/NIR spectra of **DOB**$^-$ in acetonitrile and THF [left] and the IVCT band of **DOB**$^-$ compared to a normzalized fit of the IVCT band [right].

The result of the linear Franck-Condon model is shown in Figure 8.3. The reorganization (relaxation) energy between the ground and excited states of **DOB**$^-$ is dominated by a high energy mode (ν_1) at 1660 cm^{-1}, a frequency in the region of the carbon-carbon stretching modes of the phenylene ring; the best fit yields a contribution to the reorganization energy of λ_1 = 0.102 eV. Contributions from at least two more modes can be modeled with frequencies of 1100 cm^{-1} (ν_2) and 140 cm^{-1} (ν_3) and with respective reorganization energies λ_2 = 0.049 eV and λ_3 = 0.029 eV. This study provided the first instance in which the details of the vibrational normal modes were extracted from the experimental spectrum.[2]

8.3.2 TMPD, TMB, and TMTD

Selected geometric parameters for the neutral and radical-cation ground and first-excited states of **TMPD**, **TMB**, and **TMTD** are given in Tables 8.2 - 8.4, using the reference bond numbering scheme in Figure 8.4. The dimethylamine segments of neutral **TMPD** and **TMTD** possess a slight degree of pyramidal structure as the angle sum around the nitrogen atoms is less than 360° (356.7° and 359.4° for **TMPD** and **TMTD**, respectively). Because of the pyramidal nature, there exist two conformations: C_{2v}, in which all of the methyl groups lie on one side of the phenylene-ring plane, and C_{2h}, in which the methyl groups of the pendant amines lie on opposing sides of the phenylene-ring plane; the bond lengths and angles are identical for these energetically quasi-degenerate conformations. For **TMB**, the twist between the phenylene rings of the biphenylene bridge (33°) reduces the molecular symmetry versus **TMPD**/**TMTD** to C_2. The dimethylamines possess a slight degree of pyramidality (358.8°). The bond lengths in the dimethylamine groups and the phenylene rings are similar across the series.

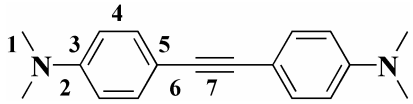

Figure 8.4 Reference bond numbering scheme for TMPD, TMB, and TMTD.

Table 8.2 Selected bond lengths (Å) and angle (°) for the neutral and radical-cation ground and first-excited states of **TMPD** at the B3LYP/SV(P) level of theory.

	TMPD	$TMPD^+$	$TMPD^+$*
Molecular Symmetry	C_{2v}, C_{2h}	D_{2h}	D_{2h}
1	1.446	1.465	1.448
2	1.399	1.357	1.413
3	1.413	1.433	1.414
4	1.395	1.375	1.399
Angle Sum N	356.7	360.1	360.0

Table 8.3 Selected bond lengths (Å) and angle (°) for the neutral and radical-cation ground and first-excited states of **TMB** at the B3LYP/SV(P) level of theory.

	TMB	TMB^+		TMB^+*
Molecular Symmetry	C_2	D_2	D_{2h}	D_{2h}
1	1.447	1.462	1.462	1.456
2	1.389	1.359	1.359	1.382
3	1.417	1.431	1.431	1.422
4	1.394	1.378	1.377	1.389
5	1.408	1.426	1.427	1.415
6	1.484	1.451	1.452	1.492
Angle Sum N	358.8	360.0	360.1	360.1

Table 8.4 Selected bond lengths (Å) and angle (°) for the neutral and radical-cation ground and first-excited states of **TMTD** at the B3LYP/SV(P) level of theory.

	TMTD	$TMTD^+$	$TMTD^+$*
Molecular Symmetry	C_{2v}, C_{2h}	D_{2h}	D_{2h}
1	1.449	1.462	1.458
2	1.385	1.359	1.377
3	1.419	1.433	1.426
4	1.391	1.377	1.386
5	1.412	1.427	1.418
6	1.426	1.397	1.422
7	1.222	1.234	1.225
Angle Sum N	359.4	360.0	360.1

Upon oxidation, the molecular symmetries of **TMPD**$^+$ and **TMTD**$^+$ transform to D_{2h} as the dimethylamine groups lose their pyramidal structure. The methyl-nitrogen bonds lengthen, while the bridging nitrogen-phenylene bonds significantly shorten. Within the phenylene rings, the BLA increases significantly, while the acetylene unit of **TMTD**$^+$ undergoes a decrease in BLA; these structural changes mark the expected progression towards a quinoidal structure upon oxidation. The calculated geometries of **TMPD** and **TMPD**$^+$ are comparable to the previous computational results at the B3LYP/6-31G* level of Brouwer[8] and the crystallographic results of de Boer and Vos[24] and Ikemoto et al.[25] Oxidation of **TMB** planarizes the dimethylamine units, as in the case of **TMPD**$^+$/**TMTD**$^+$ described above, and thus increases the molecular symmetry. Two possible geometric structures of relatively equivalent energies – D_2 and D_{2h} molecular symmetry – are possible. Such results have been previously described by both DFT calculation and time-resolved resonance Raman spectroscopy, with the D_{2h} form proposed empirically;[10, 11] for the D_2 form, the dihedral angle between the phenylene units decreases to 15°; all bond lengths are equal for the two conformations. Within the dimethylamine groups, the methyl-nitrogen bonds are found to lengthen; the bridging nitrogen-phenylene bonds shorten. Within the pheneylene units of the biphenylene bridge, the carbon-carbon bonds take on a more quinoidal-like structure and the bridging carbon-carbon bond shortens considerably with respect to the neutral molecule. These geometric changes for oxidation lead to rather significant intramolecular reorganization energies for the three compounds, with the total energy decreasing from **TMPD** (0.386 eV) to **TMB** (0.367 eV) over **TMTD** (0.262 eV).

To describe the relaxation processes of the photoabsorption of the radical cation and simulate the IVCT, we need to be concerned with the description of the first-excited state of the radical cation. In the lowest excited states, B3LYP geometry optimization of **TMPD^{+}*** leads to the same D_{2h} molecular symmetry group with planar dimethylamine groups. TDDFT analysis of the vertical excitation energies, see Table 8.5, reveals that there are two close lying states at 2.32 eV (B_{2u}) and 2.58 eV (B_{1g}) that upon relaxation could equilibrate to the lowest-lying state. In the B_{2u} state, the methyl-nitrogen bonds shorten to lengths very similar to those observed in the neutral ground state, while the bridging nitrogen-phenylene bonds lengthen to distances longer than observed in both the neutral (by 0.014 Å) and radical-cation (by 0.056 Å) ground states. The phenylene ring adjusts back to the more aromatic-like structure of the neutral state with a BLA of 0.015 Å. In the B_{1g} state, the methyl-nitrogen bonds shorten slightly, while the bridging nitrogen-phenylene bond lengths increase; in the phenylene ring, the BLA reverses relative to the other described states. It is worth noting at this time that the B_{2u} state optimized to be the lowest excited state of the radical-cation; additionally, frequency analysis of the B_{1g} state produces one negative frequency indicating that this state potentially possesses broken molecular symmetry. The results for **TMTD^{+}*** reveal that the D_{2h} symmetry group is retained in the lowest-lying first excited state which transforms as B_{1g}. The bond length changes make the molecule structure closer to that observed for the neutral state.

Table 8.5 First five excited state energies of **TMPD**$^+$, **TMB**$^+$, and **TMTD**$^+$ as determined by TDDFT.

	transition energies (eV)
$TMPD^+$	2.32, 2.58, 3.78, 4.13, 4.15
TMB^+	1.54, 2.30, 2.44, 2.92, 3.28
$TMTD^+$	1.39, 2.41, 2.41, 2.45, 2.48

Use of the planar D_{2h} structure for **TMB**$^+$ reveals in TDDFT a first-excited state that is of B_{2u} symmetry. The methyl-nitrogen bond lengths fall in between those found for the neutral and radical-cation ground states, while the bridging nitrogen-phenylene bonds are closer in length to those observed for the neutral structure. The phenylene units within the bridge, though they fall between the observed bond lengths for the neutral and radical-cation ground states, are closer to those observed in the neutral structure; the single bond of the biphenyl unit lengthens considerably versus the radical-cation ground state. These geometric changes for excitation lead to small intramolecular reorganization energies for the three compounds, with the energy decreasing from **TMPD**$^+$ (0.362 eV) to **TMB**$^+$ (0.138 eV) over **TMTD**$^+$ (0.101 eV).

The Vis-NIR absorption spectra for **TMPD**$^+$, **TMB**$^+$, and **TMTD**$^+$ are presented in Figure 8.5. In all three cases, the charge-transfer band consists of well-defined vibrational structure; as with **DOB**$^-$, this vibrational structure strongly points to the assignment of all three radical-cations to Robin and Day's Class III. Alignment of the charge-transfer bands, reveals that as the bridge length is increased, the absorption spectra decreases in width. According to the two-state, two-mode vibronic model, this indicates that as the bridge length is increased, the total displacement of the geometry decreases. This result is

confirmed by the decrease in the intramolecular reorganization energy as derived by the adiabatic potential analyses.

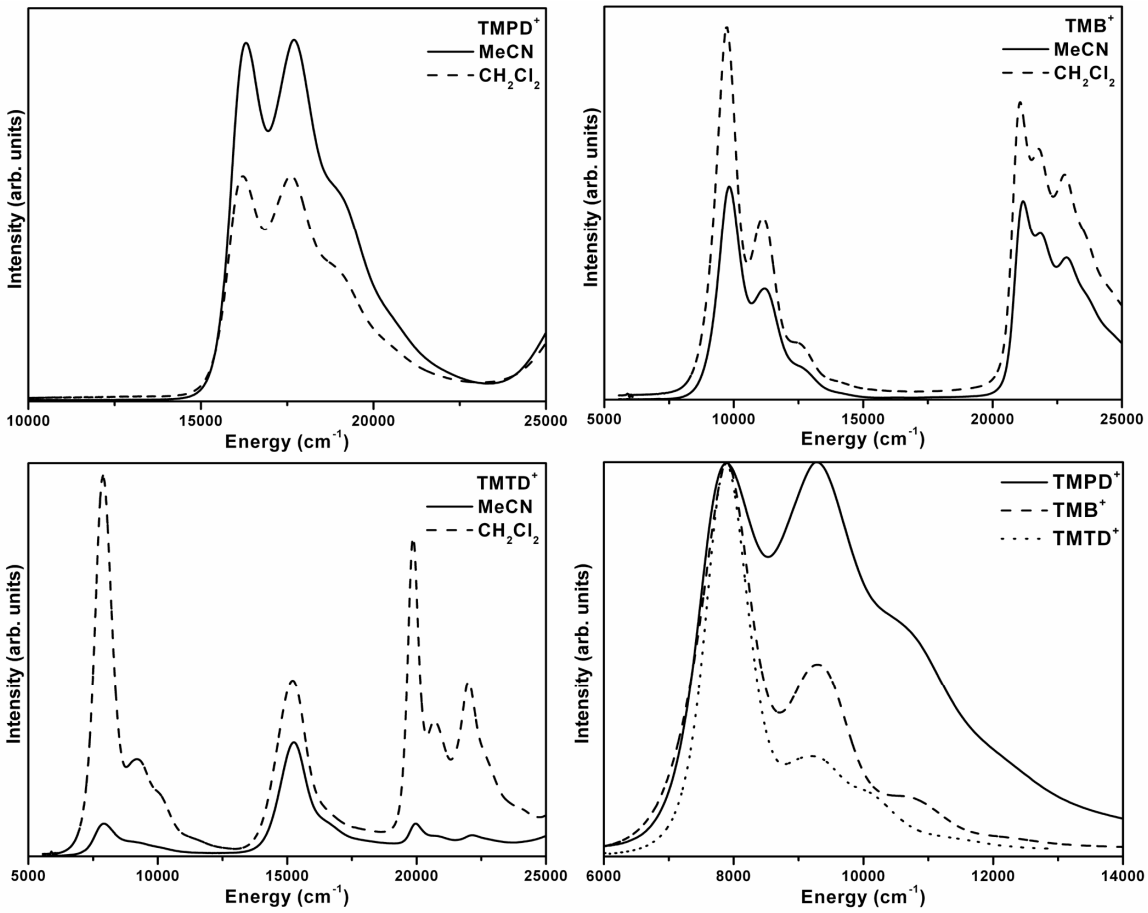

Figure 8.5 Vis/NIR spectra of a) **TMPD**$^+$, b) **TMB**$^+$, and c) **TMTD**$^+$, along with a stacked view of the IVCT bands of the three molecules.

The IVCT bands of **TMPD**$^+$, **TMB**$^+$, and **TMTD**$^+$ have been modeled using the calculated vibrational modes of the first excited state of the radical-cation, see Figure 8.6; similar simulations are observed using the radical-cation ground state vibrational modes. Excellent agreement is found for all three systems. The IVCT transition in **TMPD**$^+$ is

dominated by one low frequency mode at 306 cm^{-1} (S=0.28) and one high frequency mode at 1602 cm^{-1} (S=0.35); modes at 929 cm^{-1}, 1122 cm^{-1}, 1197 cm^{-1}, and 1289 cm^{-1} also contribute; the total reorganization energy determined by the normal mode analysis is 0.365 eV. Increasing the bridge by one phenylene unit to form **TMB**$^{+}$, reveals that the IVCT again has one low (212 cm^{-1}, S=0.29) and one high (1586 cm^{-1}, S=0.14) mode that predominately contribute to the relaxation process. However, as can be seen from the Huang-Rhys factors and total reorganization energy (0.141 eV), the role of the high-frequency mode is severely diminished versus that displayed in **TMPD**$^{+}$. In the IVCT transition of **TMTD**$^{+}$, the high-frequency mode disappears and only a single low-frequency mode at 181 cm^{-1} remains as the dominate mode of relaxation; the total reorganization energy is 0.103 eV. The continuous decrease in the role of the high-frequency modes points to lower reorganization energies and smaller geometric displacements as the bridge length is increased. These results confirm those provided by the adiabatic potential analysis.

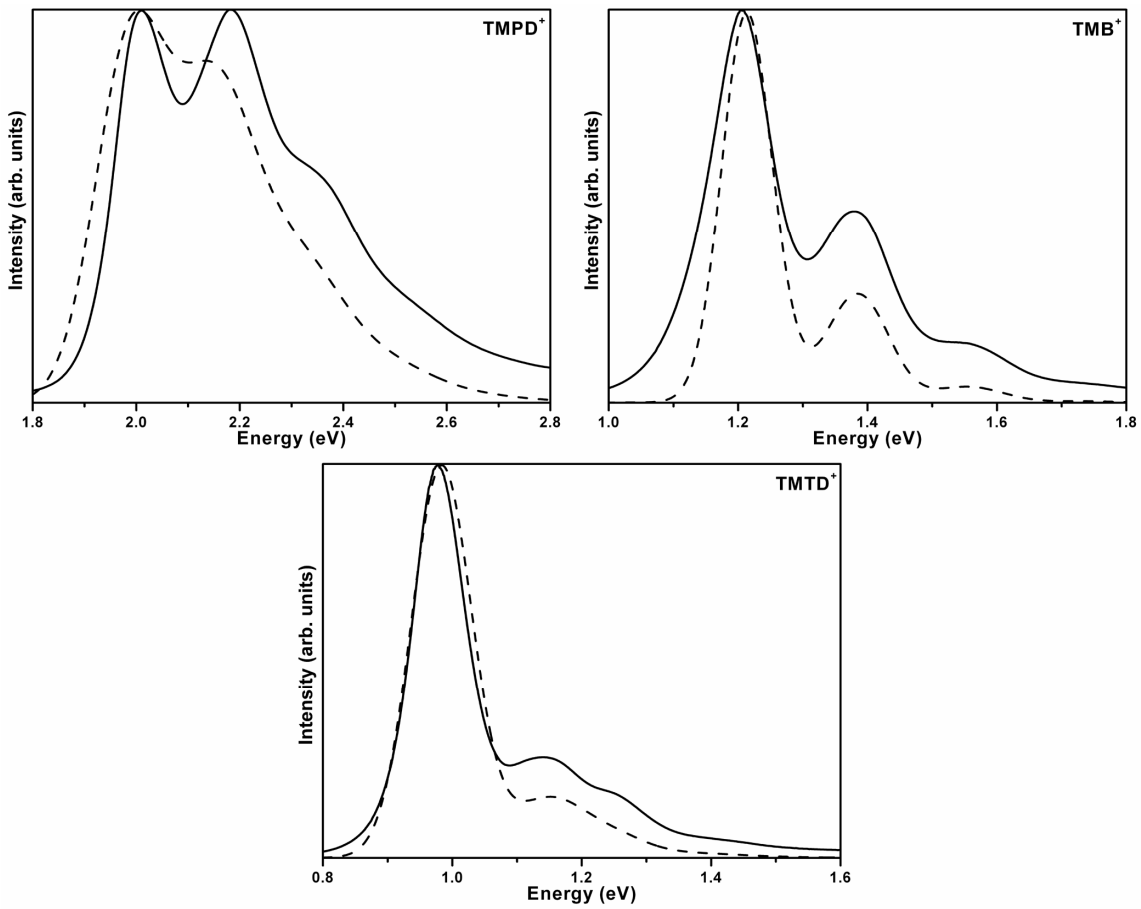

Figure 8.6 Experimental and simulated IVCT spectra for a) **TMPD**$^+$, b) **TMB**$^+$, and c) **TMTD**$^+$.

The **TMPD**$^+$, **TMB**$^+$, and **TMTD**$^+$ series also allows for investigation of the distance dependence of the electronic coupling between the dimethylamine redox centers. As shown in Table 8.6, the electronic coupling decreases by roughly 40% between **TMPD**$^+$ and **TMB**$^+$ with the addition of an extra phenylene ring to the bridge; further addition of the alkyne linkage in **TMTD**$^+$ further decreases the coupling by an additional 10%. The general trend is reproduced by TDDFT estimates, though the estimated drop in electronic coupling between **TMB**$^+$ and **TMTD**$^+$ is not as large. We note that the Koopmans' Theorem (KT) DFT estimate fails to predict the correct trend between **TMB**$^+$ and

TMTD^{+}; this failure reveals the need for configuration interaction provided by the TDDFT methodology to properly describe the electronic coupling in these systems.

Table 8.6 Electronic coupling (cm^{-1}) as determined from Koopmans' theorem (KT) analysis at the B3LYP/SV(P) level of theory, TDDFT, and Vis/NIR spectroscopy.

	$TMPD^{+}$	TMB^{+}	$TMTD^{+}$
KT-DFT	7400	3630	3770
TDDFT	9360	6210	5600
Vis/NIR	8100	4860	3940

8.4 Conclusions

In this Chapter, we have used a linear vibronic model to both fit and simulate Class III IVCT bands with well-resolved vibronic progressions. For **DOB**$^{-}$, we provided the first instance in which the details of the vibrational normal modes were extracted from the experimental spectrum. For **TMPD**$^{+}$, **TMB**$^{+}$, and **TMTD**$^{+}$, we successfully utilized parameters from optimizations of the first-excited state to simulate the IVCT bands. These results support Hush's prediction on the role of symmetric vibrations in Class III compounds.

8.5 References

(1) Coropceanu, V.; Malagoli, M.; André, J. M.; Brédas, J. L., *J. Am. Chem. Soc.* **2002,** 124, 10519.

(2) Risko, C.; Barlow, S.; Coropceanu, V.; Halik, M.; Brédas, J. L.; Marder, S. R., *Chem. Commun.* **2003**, 194.

(3) Nelsen, S. F.; Ismagilov, R. F.; Powell, D. R., *J. Am. Chem. Soc.* **1996,** 118, 6313.

(4) Nelsen, S. F.; Ismagilov, R. F.; Powell, D. R., *J. Am. Chem. Soc.* **1997,** 119, 10213.

(5) Nelsen, S. F.; Tran, H. Q.; Nagy, M. A., *J. Am. Chem. Soc.* **1998,** 120, 298.

(6) Lu, J.; Wen, X.; Wu, L.; Liu, Y.; Liu, Z., *J. Phys. Chem. A* **2001,** 105, 6971.

(7) Bourkba, A.; Poizat, O.; Buntinx, G.; Deffontaine, A., *J. Mol. Struct.* **1988,** 175, 1.

(8) Brouwer, A. M., *J. Phys. Chem. A* **1997,** 101, 3626.

(9) Guichard, V.; Bourkba, A.; Lautie, M. F.; Poizat, O., *Spectrochim. Acta, Part A* **1989,** 45, 187.

(10) Poizat, O.; Bourkba, A.; Buntinx, G.; Deffontaine, A.; Bridoux, M., *J. Chem. Phys.* **1987,** 87, 6379.

(11) Boilet, L.; Buntinx, G.; Lapouge, C.; Lefumeux, C.; Poizat, O., *Phys. Chem. Chem. Phys.* **2003,** 5, 834.

(12) Boilet, L.; Buntinx, G.; Lefumeux, C.; Poizat, O., *J. Phys. Chem. A* **2003,** 107, 8506.

(13) Ranjit, K.; Kevan, L., *Phys. Chem. Chem. Phys.* **2001,** 3, 2921.

(14) Lambert, C.; Noll, G., *J. Am. Chem. Soc.* **1999,** 121, 8434.

(15) Malagoli, M.; Coropceanu, V.; da Silva Filho, D. A.; Brédas, J. L., *J. Chem. Phys.* **2004,** 120, 7490.

(16) Becke, A. D., *Phys. Rev. A: At., Mol., Opt. Phys.* **1988,** 38, 3098.

(17) Becke, A. D., *J. Chem. Phys.* **1993,** 98, 5648.

(18) Lee, C.; Yang, W.; Parr, R. G., *Phys. Rev. B: Condens. Matter Mater. Phys.* **1988,** 37, 785.

(19) Zerner, M. C.; Loew, G. H.; Kichner, R. F.; Mueller-Westerhoff, U. T., *J. Am. Chem. Soc.* **1980,** 102, 589.

(20) Frisch, M. J.; Trucks, G. W.; Schlegel, H. B.; Scuseria, G. E.; Robb, M. A.; Cheeseman, J. R.; Zakrzewski, V. G.; Montgomery, J., J.A.; Stratmann, R. E.; Burant, J. C.; Dapprich, S.; Millam, J. M.; Daniels, A. D.; Kudin, K. N.; Strain, M. C.; Farkas, O.; Tomasi, J.; Barone, V.; Cossi, M.; Cammi, R.; Mennucci, B.; Pomelli, C.; Adamo, C.; Clifford, S.; Ochterski, J.; Petersson, G. A.; Ayala, P. Y.; Cui, Q.; Morokuma, K.; Salvador, P.; Dannenberg, J. J.; Malick, D. K.; Rabuck, A. D.; Raghavachari, K.; Foresman, J. B.; Cioslowski, J.; Ortiz, J. V.; Baboul, A. G.; Stefanov, B. B.; Liu, G.; Liashenko, A.; Piskorz, P.; Komaromi, I.; Gomperts, R.; Martin, R. L.; Fox, D. J.; Keith, T.; Al-Laham, M. A.; Peng, C. Y.; Nanayakkara, A.; Challacombe, M.; Gill, P. M. W.; Johnson, B.; Chen, W.; Wong, M. W.; Andres, J. L.; Gonzalez, C.; Head-Gordon, M.; Replogle, E. S.; Pople, J. A. *Gaussian98, Rev. A.11*, 1998.

(21) Ahlrichs, R.; Bär, M.; Baron, H.-P.; Bauernschmitt, R.; Böcker, S.; Deglmann, P.; Ehrig, M.; Eichkorn, K.; Elliott, S.; Furche, F.; Haase, F.; Häser, M.; Horn, H.; Hättig, C.; Huber, C.; Huniar, U.; Kattannek, M.; Köhn, A.; Kölmel, C.; Kollwitz, M.; May, K.; Ochsenfeld, C.; Öhm, H.; Schäfer, A.; Schneider, U.; Sierka, M.; Treutler, O.; Unterreiner, B.; von Arnim, M.; Weigend, F.; Weis, P.; Weiss, H. *Turbomole*, 5.6; 2003.

(22) Furche, F.; Ahlrichs, R., *J. Chem. Phys.* **2002,** 117, 7433.

(23) Reimers, J. R., *J. Chem. Phys.* **2001,** 115, 9103.

(24) de Boer, J. L.; Vos, A., *Acta Crystallogr., Sect. B: Struct. Sci.* **1972,** B 28, 835.

(25) Ikemoto, I.; Katagiri, G.; Nishimura, S.; Yakushi, K.; Kuroda, H., *Acta Crystallogr., Sect. B: Struct. Sci.* **1979,** 35, 2264.

CHAPTER 9

PERSPECTIVES

9.1 Synopsis

By progressing through fundamental scientific and engineering studies, the field of organic electronics has undergone tremendous growth – from the fledgling discovery of conductance in polyacetylene to commercially-available electronic and optoelectronic devices – over the past three decades. It is from this standpoint of investigating fundamental chemical and physical phenomena with an eye on the future that the work performed within this Dissertation was performed. One of the key hurdles that still hinder further advancement in these technologies is the ability to transport charges through a thin film of organic material in a consistently efficient manner. Therefore, it is important that there is a true understanding of the electron-transfer process on a molecular level so that the desired macroscopic properties can be obtained.

In this Dissertation, we have utilized electronic-structure techniques to investigate a number of molecular systems for both intermolecular and intramolecular electron-transfer properties. Our initial focus was on non-rigid, π-conjugated molecular systems that have amorphous solid-state properties used as the electron-transport layer in semiconductor applications. First, for siloles, we examined two chemically similar structures that have

rather different solid-state electronic and optical properties. Though the calculated gas-phase investigations did not provide any discernable distinctions as to why the materials behave differently in the solid state, we were able to provide one of the first thorough investigations of a number of quantum-chemical properties of siloles as they relate to electron-transport materials and point toward the need to gain further understanding of these materials in the solid state. In addition, an investigation into a series of 1,1-diaryl substituted siloles led to an understanding of the solid-state ionization potential and electron affinities. We were also able to provide insight into the purely inductive effects that 1,1-substituents have on the electronic structure of the silole systems, as well as to gain a thorough understanding through vibrational mode analysis of the large intramolecular reorganization energies for the reduction of siloles.

We have also introduced preliminary studies on model dioxaborine compounds, which have recently garnered attention as electron-transport materials. In this work, we showed that simple substitution patterns can drastically affect the electronic structure of these attractive materials, thus allowing for the potential to design materials with varying electronic properties. In addition, we performed a direct comparison of the DFT-calculated LUMO energies with the physically observable electron affinity. The linear relationship between the two parameters provides some credence to the use of these LUMO energies as approximate values for electron affinity, even though it is still more beneficial and accurate to determine directly the electron affinity.

Our second focus was on the investigation of organic mixed-valence compounds. These systems are of interest in that they allow for studies of the borderline region between weak and strong electronically-coupled (*i.e.*, Robin and Day Class II and Class III) systems where there is the possibility for the Born-Oppenheimer approximation to break down. Our first examination centered on tetraanisylarylenediamines that have nearly identical inter-redox site distances. The work provided a first example of where an anthracene bridge was found to be less effective in the mediation of electronic communication between redox centers than a benzene bridge; the calculated results reproduced well the trends produced by gas-phase UPS and Vis/NIR spectroscopy. These results showed that the electronic coupling is controlled by a subtle balance between the effects related to the energetics of the bridge and the redox units and to the topology of the bridge-redox center segment.

We then studied a series of vinylene- and phenylene-vinylene-bridged mixed-valence systems as a means to assess the effects of distance on electronic coupling. For these systems, analysis of the calculated geometric structures and electronic coupling, whose trends matched well those determined by ESR and Vis/NIR spectroscopies, allowed for definitive Robin and Day categorization. Additionally, the isolation of dication species allowed us to investigate the transitions from open-shell diradical to closed-shell systems.

Finally, we simulated a series of Class III intervalence charge-transfer bands that show vibronic progression. The simulations, for both a radical-anion and a series of radical-cations, showed the importance of symmetric vibrational normal modes in the

delocalization of the excess charge. The investigation of the dioxaborine provided the first example of an organic MV species in which the details of the vibrational normal modes coupled to the electron transfer were extracted from the IVCT spectrum.

9.2 Future considerations

Even though the majority of the empirical evidence used as benchmarks within this work was either obtained in solution or solid-state media, the calculated molecular properties were all generated under the assumption of gas-phase conditions. Such an assumption ignored influences due to solvent/solid-state polarization, interfaces (*e.g.*, solid-state metal-organic and organic-organic interfaces, or an organic film exposed to air), and conformation variability due to solvent and/or packing effects. An ideal scenario would be to obtain the individual properties of a molecule as it is a part of its dynamic surroundings; implementation of such a rectification is generally too complex and computationally expensive at this time. However, there are currently many ongoing efforts within theoretical/computational chemistry and physics to address one-by-one these complex issues. Thus, even implementation of some of the more simple models of these physical influences may make the conclusions made within this Dissertation more physically significant.

More specifically for the characterization of electron-transport molecules, especially those that are designed to have amorphous solid-state properties, it would be good to be able to evaluate the molecular properties under various packing motifs that are involved

in the solid state. The molecular systems in amorphous structures can be found within numerous packing situations depending on the orientation and distance of the surrounding molecules. Such differences in packing can influence polarization effects, excited-state separation/recombination properties, and electronic communication through intermolecular overlap of the individual wavefunctions. Each of these properties has a profound effect on the capability of the system to transport electrons. Therefore, use of merged quantum-mechanical and molecular mechanical and/or dynamical techniques to investigate a single molecule under the influence of numerous other molecules in a large cell could provide an initial step.

For organic-mixed valence systems, there is a definite need to be able to expand the two-state model to a three-state model. The third state would account for electronic properties of bridge-localized states that can assist in delocalization of the charge. In addition, one of the major difficulties in the calculation of the electronic coupling of organic MV systems is that the distinction between the redox center and bridge is difficult due to a mixture of the electronic states of the different components. As shown in Chapter 7, use of different values of inter-redox site distances can lead to very different estimates of the electronic coupling. Though this difficulty cannot be avoided, it is important that all possible variations be utilized so as to show the influences of the different estimations. Finally, as with the electron-transport materials, it would be ideal to determine the electronic properties of MV systems under the influence of solvent polarization so as to address the issue of solvent effects on charge (de)localization. Potentially, this could be performed via the simple cavity models that are available in commercial computational

packages as well as to use combined quantum-mechanical and molecular mechanical and/or dynamical techniques where the molecular system could be placed in a cell of 'real' solvent molecules.

With such additional procedures, the obtained theoretical results should correspond more precisely with the physical reality of the molecular systems. The application of such theoretical methodology will also provide a better capability to design molecular systems with specific properties before they are synthesized. Therefore, the challenge lies ahead to not only accurately interpret and understand the results from these methodologies, but also to continue to design better models for the description of such complex and interesting systems.